

Some pages of this thesis may have been removed for copyright restrictions.

If you have discovered material in Aston Research Explorer which is unlawful e.g. breaches copyright, (either yours or that of a third party) or any other law, including but not limited to those relating to patent, trademark, confidentiality, data protection, obscenity, defamation, libel, then please read our [Takedown policy](#) and contact the service immediately (openaccess@aston.ac.uk)

THE UNIVERSITY OF ASTON IN BIRMINGHAM

(U.K.)

THE INTERACTION OF FAST NEUTRONS WITH SHIELDING
AND FUSION BLANKET MATERIALS

A thesis submitted for the degree of
DOCTOR OF PHILOSOPHY

By

IBRAHIM ISMAIL ALI BASHTER

B.Sc. (Hons.), M.Sc.

JUNE, 1985.

DEPARTMENT OF MATHEMATICS
AND PHYSICS

" The University of Aston in Birmingham"
(U.K.)

THE INTERACTION OF FAST NEUTRONS WITH SHIELDING
AND FUSION BLANKET MATERIALS

A thesis submitted for the degree of
DOCTOR OF PHILOSOPHY

By

Ibrahim Ismail Ali Bashter

1985

SUMMARY

In the present work the neutron emission spectra from a graphite cube, and from natural uranium, lithium fluoride, graphite, lead and steel slabs bombarded with 14.1 MeV neutrons were measured to test nuclear data and calculational methods for D - T fusion reactor neutronics.

The neutron spectra measured were performed by an organic scintillator using a pulse shape discrimination technique based on a charge comparison method to reject the gamma rays counts. A computer programme was used to analyse the experimental data by the differentiation unfolding method.

The 14.1 MeV neutron source was obtained from $T(d,n)^4He$ reaction by the bombardment of T - Ti target with a deuteron beam of energy 130 KeV. The total neutron yield was monitored by the associated particle method using a silicon surface barrier detector.

The numerical calculations were performed using the one - dimensional discrete - ordinate neutron transport code ANISN with the ZZ - FEWG 1/ 31 - 1F cross section library. A computer programme based on Gaussian smoothing function was used to smooth the calculated data and to match the experimental data.

There was general agreement between measured and calculated spectra for the range of materials studied. The ANISN calculations carried out with $P_3 - S_8$ calculations together with representation of the slab assemblies by a hollow sphere with no reflection at the internal boundary were adequate to model the experimental data and hence it appears that the cross section set is satisfactory and for the materials tested needs no modification in the range 14.1 MeV to 2 MeV. Also it would be possible to carry out a study on fusion reactor blankets, using cylindrical geometry and including a series of concentric cylindrical shells to represent the torus wall, possible neutron converter and breeder regions, and reflector and shielding regions.

KEYWORDS : NEUTRON - SHIELDING, FUSION BLANKET, SPECTRUM MEASUREMENT,
TRANSPORT CALCULATIONS, LITHIUM FLUORIDE.

DEDICATED TO MY WIFE

AND MY SON AHMAD

ACKNOWLEDGEMENTS

I wish to express my sincere gratitude to my supervisor, Dr. P.N. Cooper, for his invaluable advice and constant encouragement throughout this work.

My thanks are also due to Mr. J. Phull and Mr. T. Kennedy for their help. Thanks should go to the members of the Physics Workshop and the members of the Computer Centre, at Aston University, for the help they offered.

I would like to thank the University of Zagazig in Egypt for granting me a study - leave. Also thanks to the Egyptian Education Bureau in London for the financial support throughout the whole work.

Finally, I wish to express my thanks to my wife, for the sacrifices made throughout this work and to my son, Ahmad, a constant source of pleasure and encouragement for the future.

CONTENTS

		Page No.
	<u>SUMMARY</u>	i
	<u>ACKNOWLEDGEMENTS</u>	ii
	<u>LIST OF TABLES</u>	vii
	<u>FIGURES</u>	vii
<u>CHAPTER 1</u>	<u>INTRODUCTION</u>	1
<u>CHAPTER 2</u>	<u>INTERACTION OF NEUTRONS WITH MATTER</u>	
2.1	Introduction	7
2.2	Neutron Sources	8
2.2.1	Radioactive Sources	8
2.2.2	Fast Neutrons From Accelerators	9
2.2.2.1	Accelerators	9
2.2.2.2	Accelerator Sources	11
2.2.3	Reactor Sources	15
2.3	Neutron Energy Classification	16
2.4	Neutron Scattering	17
2.4.1	Elastic Scattering, $X(n,n)X$	18
2.4.2	Inelastic Scattering, $X(n,n')X$	20
2.5	Absorption, $X(n,\gamma)Y$	23
2.6	Charged Particles Reactions, $X(n,b)Y$	24
2.7	The $(n,2n)$ Reaction	25
2.8	The $(n,3n)$ Reaction	27
2.9	Nuclear Fission	27
<u>CHAPTER 3</u>	<u>NEUTRON SPECTROMETER</u>	
3.1	Introduction	31

3.2	The Scintillator	32
3.3	The Photomultiplier Tube	35
3.4	Discrimination Between Neutron and Gamma	37
3.4.1	The Method Of Discrimination	38
3.4.2	Description Of The Circuit	39
3.5	Calibration Of The Spectrometer	44
3.5.1	Spectrometer Linearity	48
3.5.2	The Relation Between Recoil Proton And Electron Pulse	50
3.5.3	Neutron Efficiency	51
3.5.4	Shape Correction Factor (B)	53
3.6	The Unfolding Method	55
<u>CHAPTER 4</u>	<u>NEUTRON PRODUCTION AND MONITORING</u>	
4.1	Introduction	63
4.2	Neutron Production	63
4.2.1	The Target	63
4.2.2	The $T(d,n)^4He$	64
4.3	The Alpha Particle Detector	67
4.3.1	The Associated Particle Technique	68
4.3.2	The 14.1 MeV Neutron Yield	68
4.3.3	The Silicon Surface Barrier Detector	72
<u>CHAPTER 5</u>	<u>CALCULATION METHODS</u>	
5.1	Introduction	79
5.2	Derivation Of The Neutron Transport Equation .	80
5.3	Approximation Solutions To The Transport Equation	84
5.3.1	Spherical Harmonics	85

5.3.2	P_1 Approximation	86
5.3.3	P_N Approximation	88
5.3.4	Numerical Methods	90
5.3.4.1	The Discrete Ordinates S_N Method	90
5.3.4.2	The Monte Carlo Method	92
5.3.4.3	The Moments Method	93
5.3.5	The ANISN Code	93
5.4	Smoothing Of Calculated Spectra	97
5.4.1	Smoothing Function	98
5.4.2	Smoothing Computer Programme	100

CHAPTER 6 SHIELDING MATERIALS AND EXPERIMENTAL ASSEMBLIES

6.1	Introduction	102
6.2	Nuclear Fuel Materials	102
6.3	Shielding, Coolant And Blanket Materials	103
6.4	Moderator And Reflector Materials	104
6.5	The Steel Frame	106
6.6	Uranium And Lithium Fluoride Assemblies	107
6.7	Graphite Assemblies	117
6.8	Lead Assemblies	120
6.9	Steel Assembly	125

CHAPTER 7 RESULTS AND DISCUSSIONS

7.1	Introduction	127
7.2	Neutron Spectrum From Unshielded 14.1 MeV Source	128
7.3	Neutron Spectra From Uranium Slabs	130
7.4	Neutron Spectra From LiF Slabs	136
7.5	Neutron Spectra From A Mixture Of LiF And Uranium Slabs	148
7.6	Neutron Spectra From Multilayer Assemblies of U And LiF Slabs	156

7.6.1	Neutron Spectra At The Surface Of Samples Containing LiF On Top Of U	156
7.6.2	Neutron Spectra At The Surface Of Samples Containing U On Top Of LiF	168
7.6.3	Neutron Spectra At The Surface Of Samples Containing LiF Between Two Slabs Of Uranium ..	178
7.6.4	Neutron Spectra At The Surface Of Samples Containing Uranium Between Two Slabs Of LiF ..	182
7.6.5	Neutron Spectra At The Surface Of Samples Containing Multilayers Of LiF And Uranium ...	186
7.7	Neutron Spectra From The Graphite Assemblies .	189
7.7.1	Neutron Spectra From The Graphite Cube	189
7.7.2	Neutron Spectra From The Graphite Slabs	192
7.7.3	Neutron Spectra At The Surface Of Samples Containing Uranium On Top Of Graphite Slabs ..	200
7.7.4	Neutron Spectra At The Surface Of Samples Containing LiF On Top Of Graphite Slabs	207
7.7.5	Neutron Spectra At The Surface Of Samples Containing Lif And Uranium Mixture On Top Of Graphite Slabs	214
7.8	Neutron Spectra From The Lead Assemblies	228
7.8.1	Neutron Spectra From The Lead Slabs	229
7.8.2	Neutron Spectra At The Surface Of Samples Containing LiF On Top Of Lead Slabs	234
7.9	Neutron Spectra From The Steel Slabs	247

CHAPTER 8

CONCLUSIONS

8.1	Introduction	252
-----	--------------------	-----

8.2	Neutron Detection	253
8.3	Calculation Methods And Cross Section Set ...	253
8.4	Calculations And Experiments Compared	257
8.5	Further Work And Improvements	258
8.6	Conclusions	259

APPENDICES

<u>APPENDIX 1</u>	NSPEC Programme	260
<u>APPENDIX 2</u>	SMOOTH Programme	262
<u>APPENDIX 3</u>	ANXSEC Programme	263

<u>REFERENCES</u>	266
-------------------	-------	-----

<u>LIST OF TABLES</u>	Table (3.1) Proton Pulse Size (P) As Calculated From Equations (3.5) And (3.6) ...	52
	Table (3.2) PSI Values Used In " NSPEC " Programme	60
	Table (5.1) Neutron Energy Boundaries For The 34 Groups Fast Neutron Data Derived From 37 - 21 Groups ZZ - FEWG 1/ 31 - 1F Cross Section Library	94
	Table (5.2) Angular Quadrature Constants	95

FIGURES

Figures are, in general, placed below the page where they are first mentioned and discussed.

CHAPTER 1

INTRODUCTION

For over three decades the major thrust of controlled thermonuclear research has been directed towards the achievement of the plasma conditions of density, confinement, and temperature necessary to produce substantial amounts of power by nuclear fusion. At the same time it has been recognized that the realization of fusion as a safe, reliable and economic source of power would require extensions in available technologies and the development of new technologies, as well as a successful demonstration of the necessary plasma conditions. The first comprehensive assessment of the technological requirements for fusion power was performed by Spitzer et al⁽¹⁾ in 1954. This study identified a number of technological areas for future study including magnetic - field production, neutronics, lithium corrosion, tritium recovery and fuel injection. These areas of technology are still relevant to fusion power. During the period 1954 - 1967 a number of studies of fusion power appeared in the literature⁽²⁻⁸⁾. An excellent review of all this work is provided by Rose⁽⁹⁾. This time period was marked by a lack of positive scientific results that precluded the initiation of any major efforts in fusion power technology.

During the years 1968 - 1971 significant progress in plasma performance was achieved in several experimental facilities. Within the years 1972 - 1975 a number of groups completed rather comprehensive conceptual design studies of fusion power plants. It is emphasized that

these studies are neither definitive nor exhaustive; they are rather, self - consistent descriptions of approaches to fusion power based on extrapolations and assumptions in the areas of plasma physics and technology ⁽¹⁰⁾. Since that date many studies were performed by groups in all countries with fusion programmes to satisfy the technological requirements for fusion reactor ⁽¹¹⁻¹⁸⁾.

The fusion reactor concepts can be classified to four types ; the theta - pinch ⁽¹⁹⁾, the Tokamak ⁽²⁰⁻²³⁾, the mirror ^(24,25), and the inertial confinement ⁽²⁶⁻²⁸⁾ concepts. The required technology is divided into three principal areas of concern : (a) the power balance, that is, the unique power handling requirements associated with the production of electrical power by fusion ⁽²⁹⁻³¹⁾, (b) reactor design, focusing primarily on the requirements imposed by a tritium - based fuel cycle ⁽³²⁻³⁴⁾, thermal - hydraulic considerations ^(35,36), and magnet systems ⁽³⁷⁻⁴⁰⁾, and (c) materials considerations, including surface erosion ⁽⁴¹⁾, radiation effects ⁽⁴²⁾, materials compatibility ⁽⁴³⁾, and neutron - induced activation ⁽⁴⁴⁻⁴⁷⁾.

The effect of nuclear heating and radiation damage will require that a substantial amount of radiation shielding be placed between the breeding blanket and the superconducting coils in mirror and Tokamak reactors. Depending on the magnitude of the neutron wall - loading, the shielding requirements will be set either by heating considerations or by radiation damage considerations ⁽⁴⁸⁾. In reactor design studies there

should be model experiments, simple with respect to geometry and material composition, to facilitate the interpretation of differences between measured and calculated quantities. These studies have usually been based on one - dimensional radiation transport calculations. The effects of penetrations and other geometrical irregularities will be very important in shield design⁽⁴⁹⁾, and therefore, multidimensional radiation transport calculations will be required in any realistic shielding design. Also, it is expected that, the effects of nuclear data uncertainties will be important in shield design⁽⁵⁰⁻⁵²⁾.

The purpose of this work is to conduct both experimental and theoretical studies of the energy distribution of neutrons emerging from some shielding materials. These materials are chosen that could be of possible interest to the fusion reactor programme for use in breeding blankets. These materials are lithium fluoride, graphite, lead, steel and natural uranium (^{238}U).

Lithium fluoride was chosen as a fuel (for tritium breeding), blanket coolant, heat removal and neutron slowing down. A large number of conceptual fusion reactor designs have been proposed⁽⁵³⁻⁵⁷⁾ using different heat exchange media, of which lithium, lithium fluoride and $\text{LiF} - \text{BeF}_2$ eutectic mixture (66 % : 34 % by weight) called Flibe⁽⁵⁸⁾ have been widely considered.

The importance of fast neutron spectral measurements in graphite comes from the fact that graphite is used in some conceptual designs of

fusion reactors as a reflector of fast neutrons into lithium blankets to increase tritium breeding, as a shield for the superconducting magnets and to improve the neutron economy in the system⁽⁵⁹⁻⁶³⁾. Several attempts were made in the last few years to measure and calculate the fast neutron distributions in unreflected lithium^(12,64), in lithium with graphite reflector⁽⁶⁵⁻⁶⁹⁾ and in graphite⁽⁷⁰⁻⁷²⁾. Generally, it was found that, concerning the lithium, it can be concluded that, there is agreement, more or less, between calculations and experiments. The situation is different for graphite. There are discrepancies of tens or even hundreds of percent between calculation and experiment⁽⁷³⁾. These discrepancies make it necessary to improve the experimental and computational efforts in order to resolve the discrepancy. In the present research a graphite sphere and slabs were chosen to check the accuracy of calculation and experiments spectra.

Lead and graphite were chosen because most of the common design of fusion reactors include at least one of these materials for shielding and to increase tritium breeding. For example, shield composition used in some fusion reactors blanket designs are ; lead + graphite^(74,75), lead⁽⁷⁶⁾ and lead + B₄C + structural steel⁽⁷⁷⁾. In the recent years, increasing attentions has been devoted to the use of the eutectic Li₁₇Pb₈₃ as liquid breeder / coolant material for experimental and commercial fusion power reactors^(78,79). Measured and calculated neutron spectra from lead slabs were performed using ANISN - one dimensional code⁽⁸⁰⁾ and Monte Carlo code⁽⁸¹⁾

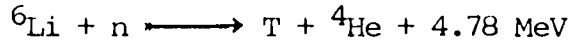
Iron is an important structural and shielding material in fast

breeder reactors and is also being used in the design of fusion reactor blankets. Most of the earlier experimental and theoretical studies were confined to the measurement and calculations of neutrons leaking out from various iron assemblies⁽⁸²⁻⁸⁸⁾.

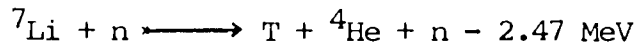
The uranium was chosen in the present work due to its potentially useful application in the fusion and the fusion - fission reactors. It has a high atomic weight and so is a good fast neutron and gamma ray shielding material. The neutrons can be multiplied through fission in a heavy element blanket (^{238}U), surrounding the fusion plasma. The concepts which involve the use of fusion produced neutrons to ultimately produce fission are called the fusion - fission hybrids⁽⁸⁹⁾. The conceptual design of these fusion - fission reactors requires the use of accurate codes and cross sections. Given the complexity of the designs, the codes and cross sections can be only be checked against measurements of single materials in a simple geometry. The measured and calculated neutron spectra from uranium⁽⁹⁰⁾, iron - uranium⁽⁹¹⁾ and lithium fluoride - uranium⁽⁵⁵⁾ have been reported.

The first fusion reactors will use the $\text{T}(d,n)^4\text{He}$ reaction because of its relatively low ignition temperature due to the reaction resonance at 110 KeV and large energy release⁽⁹²⁾. For this reaction, the energy extracted is associated with the neutron and is transferred to a heat exchange medium surrounding the plasma as the neutron slows down. Since tritium does not naturally occur, the choice of heat exchange material is dictated by the need to include lithium in it, so that tritium can be

bred by the two reactions ;



and



The choice of measuring techniques for the determination of fast neutron spectra produced from the interaction of 14 MeV source neutrons with blanket materials is limited. For measurements two groups of methods could be used⁽⁹³⁾; (a) activation detector⁽⁹⁴⁾, (b) proton recoil detector⁽⁹⁵⁾. The NE - 213 proton recoil liquid scintillator was used in this work as a fast neutron spectrometer based on proton recoil spectrum measurement and unfolding procedure to obtain the neutron spectrum.

Fast neutrons of 14 MeV energy were produced with the aid of a low energy electrostatic accelerator using the D - T reaction, thus reproducing the neutron energy spectrum emitted from a hot plasma.

For calculation purposes the ANISN one dimensional transport code was chosen using the ZZ - FEWG 1 / 31-1F cross section library, that has only become available as this work start. This set was seemingly originally produced for calculating the radiations from nuclear weapons. This set contains a wide variety of elements suitable for both shielding and fusion blanket studies. Part of this work is to see if this data set could be used satisfactory for thin shields.

CHAPTER 2

INTERACTION OF NEUTRONS WITH MATTER

2.1 Introduction

The behaviour of neutrons in matter is quite different from that of either charged particles or gamma rays. Since the neutrons are uncharged, no coulomb forces come into play with either the orbital electrons or the nuclei. Thus, for neutrons to affect matter, they must either enter the nucleus or come sufficiently close to it for the nuclear forces to act⁽⁹⁶⁾.

If, in a collision with a nucleus, the total kinetic energy of the system is conserved, the reaction is called an elastic scattering which may be written as $X(n,n)X$, where X is the target nucleus. After re-emission of a neutron if the target is left in an excited state, the process is called inelastic scattering and written as $X(n,n')X^*$. If instead of being scattered the neutron is absorbed by the nucleus, it induces a nuclear reaction which leads to a different residual nucleus and new end products. When the end product is a capture gamma ray ${}^A_ZX(n, \gamma){}^{A+1}_ZX$, where ${}^{A+1}_ZX$ is an isotope of the target nucleus, the reaction is called radiative absorption. Particle reactions, which occur when a particle (or particles) emerges, are written as ${}^A_ZX(n,p){}^A_{Z-1}Y$, ${}^A_ZX(n, \alpha){}^{A-3}_{Z-2}Y$, etc. At high energies, reactions such as $(n,2n)$, $(n,3n)$ or fission may take place.

The importance of the neutron energy in the interaction of neutrons

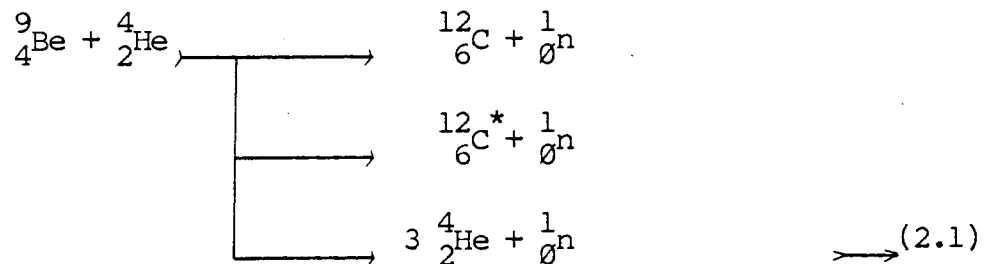
with matter makes necessary a classification of neutrons according to their energies. The attenuation of neutrons in shields is determined by the probabilities that these neutron interactions will occur in the shield materials⁽⁹⁷⁾.

2.2 Neutron Sources

Basically, there are three neutron source types; radioactive sources, accelerator sources and reactor sources.

2.2.1 Radioactive Sources

Radioactive sources are mixtures of an alpha emitter, such as radium, polonium or americium, with some light elements, e.g., beryllium, boron or lithium. A widely used mixture is that of Am - 241 and beryllium. The reaction may be represented by:



The neutrons produced by the interaction of alpha particles with beryllium have fairly high energies, ranging from 5 to 12 MeV or more, depending on the energy of the incident alpha particles. Such a source is polyenergetic, since the neutrons do not all have the same (or nearly the same) energies⁽⁹⁸⁾. The neutron spectrum of Am - Be source will be shown in chapter (3).

The highest yield is obtained from Californium - 252. This decays by spontaneous fission as well as by alpha particle emission in which the nucleus breaks up into two roughly equal halves and a few surplus neutrons, since the daughter nuclides cannot contain the neutron excess of the parent. The half - life for fission is about 85.5 years, but Cf - 252 also decays by alpha emission, with a half - life of 2.73 years, and this shorter time determines the useful life of the source which has an effective half - life of 2.65 years. The neutron yield is about 2.3×10^6 n/s. μ g (99).

2.2.2 Fast Neutrons From Accelerators

Accelerators are machines which use electric or electric and magnetic fields to accelerate charged particles up to high energies. They include linear accelerators, Van de Graaff generators, Cyclotrons and Synchrotrons. By bombarding various thin targets with variable energy protons or deuterons from accelerators and observing the monoenergetic neutrons at different angles, the entire neutron energy range from a few kilo electron volts to 20 MeV can be covered.

2.2.2.1 Accelerators

The early Van de Graaff generators were capable of accelerating charged particles to a few MeV, but some present - day machines attain energies of from 12 to 20 MeV. It can supply up to tens of micro ampere current of accelerated protons or deuterons whose energy can be varied continuously from a few hundred kilo electron volts to the maximum energy of the machine. This charged particle current focused and has spread in energy of only about 2 keV.

Cockroft - Walton accelerators range from 50 to 500 keV. They can produce currents of several hundred micro ampere of charged particles with only a few kilo electron volts spread in energy. This type used to accelerate deuterons towards a tritium target is an intense source of 14 MeV neutrons. In both the Van de Graaff and Cockroft - Walton machines, the high potential is generated by electrostatic devices and applied to the discharge tube containing the ion to be accelerated .

In the linear accelerators, the energies of the charged particles are increased by a series of phased pulses arranged to give the ions an extra push at the right moment of time. The accelerator tubes (drift tubes) are narrow cylinders connected alternately to a source of high frequency potential. The frequencies required for protons are much higher than for heavy ions and it is now possible to accelerate protons up to about 50 MeV. The linear accelerator for electrons is different from the proton accelerator. It consists of a tube down which an electromagnetic wave progresses. The tube is really a wave - guide and contains apertures spaced according to the required velocity of the travelling wave and the size of the tube.

Cyclotrons range from a few to about 40 MeV, and the external beams are of fixed energy. It consists of an electron beam ion source which ionizes gas fed to it (Hydrogen, deuterium or helium). These ions travel in a magnetic field within two hollow conductors (dees) inside a closed vessel under high vacuum. The magnetic field passes across the dees perpendicular to the path of ions. The two dees are fed with a high power radiofrequency. The magnetic field causes the ions to move in a semi - circular path through one dee and if they get to the gap at the peak of the radiofrequency they will be accelerated. If the time spent

in the other dee is half a cycle, then they will be accelerated again in reaching the gap and so on .

For an ion of mass m and charge e moving in a circular path of radius r with speed v in a magnetic field of flux density B , $m v^2 / r = B e v$ or $v = r B e / m$. The path length in one dee is $2 \pi r / 2 = \pi r$. The period $T = 2 \pi r / v = 2 \pi m / B e$. The period is therefore independent of speed and radius provided that the particles are non - relativistic, and is thus the same for all particles of the same m/e . A constant radiofrequency is therefore used. The ion is always in phase once the frequency and magnetic field correctly adjusted, so that the energy is increased each time the ion passes a gap. When the ion has reached the maximum radius, it is led out by a channel some 60° long curved to follow the path of the ions with outer plate at a negative potential (- 50 kV) to draw the ions away from the magnetic field .

Since the maximum velocity at circumference = $B e R / m$, where R is the radius of the dees, $E = m v^2 / 2 = (B R e)^2 / 2 m$. Therefore E is proportional to R^2 for a given particle. The maximum energies of a particles from a fixed - frequency cyclotron are about 10, 20 and 40 MeV for protons, deuterons and alpha - particles respectively. The limit is set by the relativistic mass increase as well as mechanical engineering difficulties and expense⁽¹⁰⁰⁾. The ${}^9\text{Be}(d,n){}^{10}\text{B}$ reaction has been used as neutron source using this type of machine. The neutrons are produced by deuterons of 10 - 20 MeV on a thick target⁽¹⁰¹⁾.

2.2.2.2 Accelerator Sources

Neutrons are obtained from the charged particles beams of the

various accelerators by a variety of (p,n) and (d,n) reactions. The most common (p,n) reactions are those on lithium and tritium and the most useful (d,n) reactions are those on deuterium and tritium.

i- The $T(p,n)^3\text{He}$ Reaction

Since tritium has become readily available, the $T(p,n)^3\text{He}$ reaction has gradually replaced the $^7\text{Li}(p,n)^7\text{Be}$ reaction as a neutron source in the 0.6 - 4 MeV energy range. In this range a second group of neutrons in the $^7\text{Li}(p,n)^7\text{Be}$ reaction complicates the situation. The $T(p,n)^3\text{He}$ reaction is endoergic by 0.764 MeV so that the laboratory threshold is 1.019 MeV.

Near the threshold, because of the centre - of - mass motion, neutrons will emerge in the forward direction in a narrow cone. As the proton energy is increased, this cone opens until at a laboratory energy of 1.148 MeV the cone finally includes all directions. From 1.019 MeV to 1.148 MeV the cone is directed forward, and any angle in the cone will have two energy groups of neutrons up to a neutron energy of about 300 keV at 0° . The lower energy group, however, is much less intense. Just at threshold the two groups coincide in energy, giving neutrons of 63.9 KeV. Monoenergetic neutrons with energies > 300 KeV can be obtained at 0° . Since there are no known excited states of ^3He up to many MeV, these neutrons are truly monoenergetic.

ii. The $D(d,n)^3\text{He}$ Reaction

It has a positive Q - value (3.267 MeV). Thus relatively high

energy neutrons can be obtained from low - energy accelerators. Using a thick target for incident deuteron energies up to 400 KeV the neutron spectrum at 90° is approximately monoenergetic with an energy of about 2.5 MeV and 1 milliampere beam of deuterons will produce about 10^9 n/sec. from this target. With deuteron energies > 500 KeV it is necessary to use a thin target to get monoenergetic neutrons. At these higher energies the angular distribution is peaked some what in a forward direction and neutrons are usually taken at 0° . The total cross section rises up to 1.0 MeV deuteron energy and is approximately constant for higher energies. Since there are no excited state of ^3He , this $\text{D}(d,n)^3\text{He}$ source can supply monoenergetic neutrons up to 10 MeV⁽¹⁰²⁾.

iii. The $\text{T}(d,n)^4\text{He}$ Reaction

Because the coulomb barrier between the incident deuteron and the light target nuclus is relatively small, the deuterons need not be accelerated to a very high energy in order to create a significant neutron yield. These reactions are widely exploited in " neutron generators " in which deuterium ions are accelerated by a potential of about 100 - 300 kV. Because the incident particle energy is then small compared with the Q - value (17.6 MeV), all neutrons produced are of about the same energy (14 MeV). A 1 milliampere beam of deuterons will produce about 10^{11} n/s for a thick tritium target⁽¹⁰³⁾. Using thin targets and higher deuteron energies, neutrons from 12 to 20 MeV can be obtained by observing neutrons at various angles .

From figure (2.1) it is obvious that, with incident particles up to

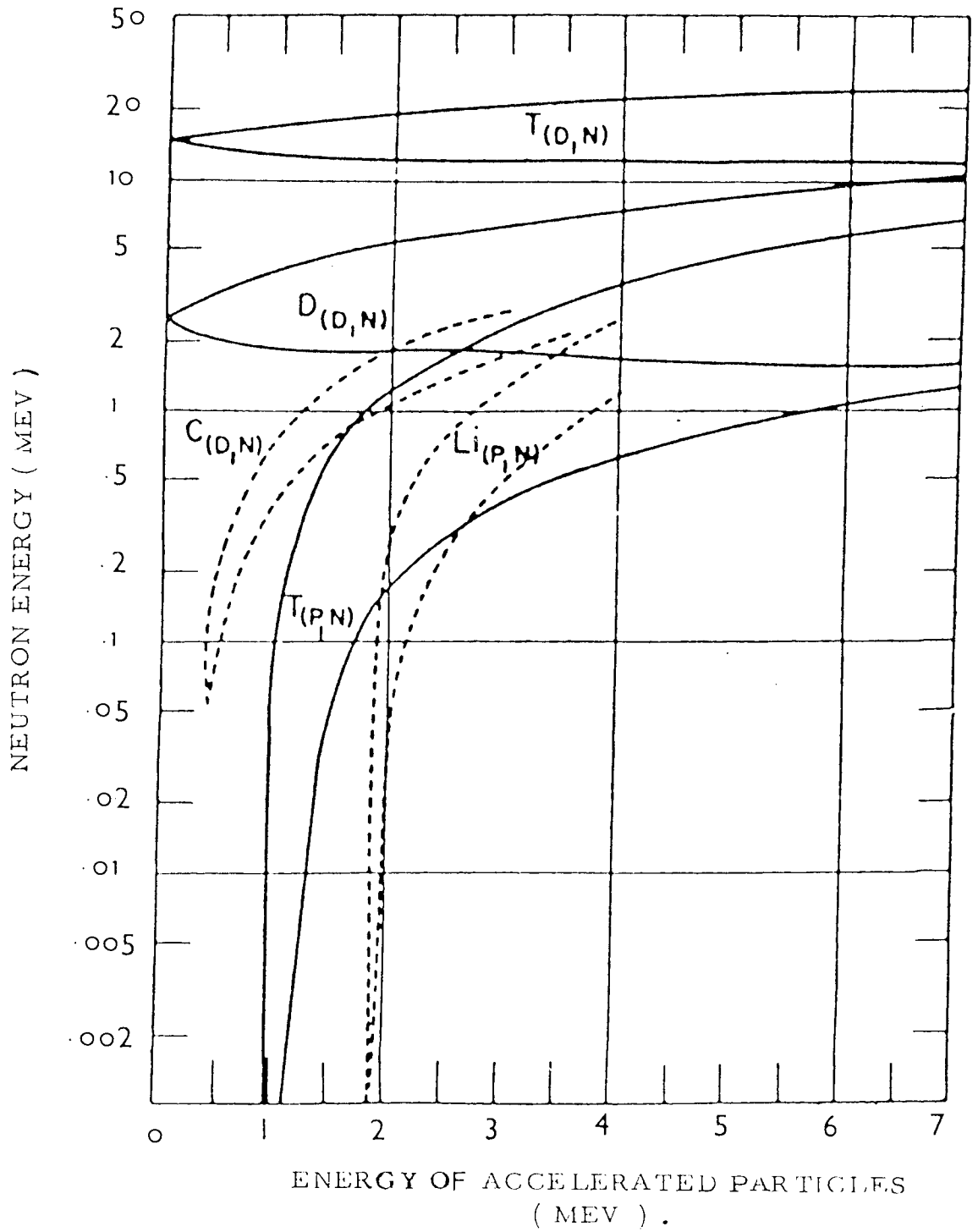


FIG. 2.1 ENERGIES OF NEUTRONS EMITTED AT 0° AND 180° FOR THE MOST IMPORTANT MONOENERGETIC (p,n) AND (d,n) REACTIONS. (THE LOWER CURVE THE 180° ENERGY).

7 MeV, neutrons of all energies up to 22 MeV, except the small range from 10 to 12 MeV, can be obtained from these previous sources⁽¹⁰²⁾.

2.2.3 Reactor Sources

Nuclear reactors are based on the process of neutron induced fission. The fission products emit neutrons which are classed as "prompt" if the time between fission and emission is not measurable, or "delayed" if it is measurable.

The neutrons emitted at the time of fission of ^{235}U from its fission fragments are distributed in energy from 0.075 MeV (or lower) to about 17 MeV. The distribution of these "prompt" neutrons is quite closely described by⁽¹⁰⁴⁾:

$$N(E) dE = 0.484 \sinh \sqrt{2E} e^{-E} dE \quad \longrightarrow \quad (2.2)$$

where $N(E) dE$ is the number of neutrons of energy E to $E + dE$ per fission neutron emitted.

A simple approximate expression that is good to 15 per cent from $E = 4$ to 12 MeV is :

$$N(E) dE = 1.8 e^{-0.75} dE \quad \longrightarrow \quad (2.3)$$

Some of the fission products decay radioactively by neutron emission. These "delayed" neutrons are of lower energy than the "prompt" neutrons and are much less numerous.

Generally, reactors can be used as sources of fast neutrons, with energies of about 17 MeV, but these are not so monoenergetic as accelerator produced neutrons. Consequently, reactors are more often used as sources of thermal neutrons. They produce these in very large numbers compared with other neutron sources and fluxes of the order of 10^{14} n/cm²s. can be attained. Compared with radioactive and accelerator sources, reactors are high intensity sources of thermal neutrons.

2.3 Neutron Energy Classification

Neutrons are usually classified according to either energy or velocity. A common classification is :

High - energy	> 10 MeV		
Fast	10 MeV	to	10 keV
Intermediate	10 keV	to	100 eV
Slow	100 eV	to	1 eV
Thermal(Maxwellian)	0.025 eV (average at 300 k ^o)		
Epi - cadmium	> 0.4 eV		

As neutrons traverse matter, they lose energy by a series of collisions, and like gas molecules eventually come into thermal equilibrium with the surroundings. The term "thermal neutron" refers to a neutron in equilibrium at the temperature of its surroundings. When in equilibrium, the neutron energies will have a Maxwellian distribution about the mean. This value is calculated from the Boltzmann equation,

$$\bar{E} = 3kT / 2 \quad \longrightarrow (2.4)$$

where $kT/2$ is ergs energy for each degree of freedom,
 k is Boltzmann constant (8.61×10^{-11} MeV K^{-1}),
 T is absolute temperature.

Convenient expressions relating temperature and velocity to neutron energy are :

$$T = 1.159 \times 10^4 E \quad \longrightarrow (2.5)$$

$$v = 13.83 \sqrt{E} \quad \longrightarrow (2.6)$$

where E is in electron volts, v in km / sec , and T in K° .

The epi - cadmium neutron is included in the classification because of the importance of cadmium as a neutron absorber. Cadmium has a very large absorption cross section for neutrons up to about 0.4 eV, but is relatively transparent at energies about this value. Hence, epi- cadmium neutrons are those capable of passing through a cadmium absorber⁽¹⁰⁵⁾.

2.4 Neutron Scattering

Neutrons undergo two main types of reactions with atomic nuclei; there are (1) scattering, in which the neutron interacts with, and transfers some or all of its energy to the nucleus, but the neutron remains free after the process, and (2) absorption (or capture), in which a neutron enters the nucleus but other particles leave. Scattering is of two types ; elastic and inelastic, the principles of conservation of energy and momentum applying in both.

2.4.1 Elastic Scattering, X(n,n)X

Elastic collisions of neutrons with nuclei are of two general types. Resonance scattering involves capture of the neutron to form a compound nucleus followed by emission of another (scattered) neutron, whereas in potential scattering there is apparently no compound nucleus formation. In either case, the struck nucleus remains in its lower energy (ground) state and the interaction with the nucleus can be treated as a " billiard ball " type of collision. The behaviour can thus be analyzed by means of the familiar laws of mechanics, based on the principles of the conservation of both energy and momentum. The amount of energy lost by a neutron in each elastic scattering collision depend upon the mass number of the nucleus target (A) and the angle of scatter. Mathematically, for an incident neutron energy E_0 , the energy, $E (\theta)$, of a neutron scattered at an angle θ (in center of mass system) is given by:

$$E(\theta) / E_0 = \frac{A^2 + 2A \cos \theta + 1}{(A + 1)^2} \longrightarrow (2.7)$$

The relationship between the scattering angle Φ (in laboratory - system) and θ is given by :

$$\cos \Phi = \frac{A \cos \theta + 1}{\sqrt{A^2 + 2 A \cos \theta + 1}} \longrightarrow (2.8)$$

Therefore, elastic neutron scattering in laboratory system is described by :

$$E(\Phi) = E_0 \frac{A^2 + \cos 2\Phi + 2 \cos \Phi \sqrt{A^2 - \sin^2 \Phi}}{(A+1)^2}$$

or

$$\frac{E(\Phi)}{E_0} = \frac{(A^2 + 1) - 2 \sin^2 \Phi + 2 \cos \Phi \sqrt{A^2 - \sin^2 \Phi}}{(A+1)^2} \quad \rightarrow (2.9)$$

At $\Phi = 180^\circ$,

$$\frac{E(180)}{E_0} = \frac{A^2 + 1 - 2 \times 0 + 2(-1)A}{(A+1)^2} = \left(\frac{A-1}{A+1}\right)^2 \quad \rightarrow (2.10)$$

To make a comparison between different materials, it is convenient to measure energy loss for head-on collisions in which θ or $\Phi = 180^\circ$ and energy loss is a maximum. From equation(2.7) or (2.10) we get :

$$\Delta E_{\text{Max}} = E_0 \frac{4A}{(A+1)^2} \quad \rightarrow (2.11)$$

It can be seen that much more energy can be lost by the neutrons if the scattering nucleus is light. A neutron may lose a maximum of less than 2 per cent in a collision with a ^{238}U nucleus but about 28 per cent with a carbon nucleus and all its energy in a single collision with a hydrogen nucleus.

The average neutron energy loss per elastic collision is given in terms of a quantity called the logarithmic energy decrement ξ , defined by :

$$\xi = \frac{E \int \Delta(\ln E) dn}{n} \quad \rightarrow (2.12)$$

Where n is the number of scattered neutrons,

$$dn / n = - dE / \Delta E_{\max}$$

$\Delta (\ln E)$ is the average change in logarithm of the neutron energy after a single elastic scattering process.

ξ can be given by :

$$\xi = 1 - \left[\frac{(A-1)^2}{2A} \ln \left(\frac{A+1}{A-1} \right) \right] \longrightarrow (2.13)$$

Except for small value of A, equation (2.13) can be written as:

$$\xi = 2 / [A + (2 / 3)] \longrightarrow (2.14)$$

Using the above relationships, we find that the average number of collisions, n , to slow down a neutron of a given initial energy, E_{ni} , to a prescribed final energy, E_{nf} , in elastic scatter is given by :

$$n = [\ln (E_{ni} / E_{nf})] / \xi \longrightarrow (2.15)$$

Equations (2.13) and (2.15) show that the smaller the nucleus, the better moderator it makes from the point of view of a neutron slowing down per collision⁽¹⁰⁶⁾.

2.4.2 Inelastic Scattering , $X(n,n')X^*$

Inelastic scattering occurs when the nucleus is raised to an excited (virtual) state and emits one or more photons of gamma

radiation, called inelastic scattering gamma rays, in addition to a neutron. Since light elements commonly have excited energy levels one MeV or more apart, the slowing down process is usually considered as taking place by elastic scatter only. With heavy nuclei the energy levels are only about 0.1 MeV apart and inelastic scatter is more prominent. Generally, only fast neutrons engage in inelastic scattering where, because of the energy of the gamma rays, the emergent particles have less kinetic energy and momentum than the incident particles⁽¹⁰⁷⁾.

Let E_1 be the total kinetic energy of the neutron and target nucleus before collision and E_2 the kinetic energy after collision, then if E_γ is the energy emitted as gamma radiation, it follows that :

$$E_1 = E_2 + E_\gamma \quad \longrightarrow \quad (2.16)$$

In inelastic scattering kinetic energy is not conserved. Nevertheless, there is conservation of momentum, so that, if E_γ were known, the mechanics of the process could be solved. Since kinetic energy of the target nucleus is, in general in laboratory system, negligible in comparison with that of the neutron, it follows that, in an inelastic collision, the initial energy of the neutron (laboratory system) must exceed the minimum excitation energy of the target nucleus.

For elements of moderate and high mass number, the minimum excitation energy is usually from 0.1 to 1 MeV. Hence, only a neutron with energy exceeding this amount can be inelastically scattered as a result of nuclear excitation. With decreasing mass number of the

nucleus there is a general tendency for the excitation energy to increase, so that the neutrons must have higher energies if they are to undergo inelastic scattering. The threshold energy for such scattering in oxygen, for example, is about 6 MeV, and in hydrogen the process does not occur at all. Exception to the foregoing generalization are the "magic" nuclei, heavy nuclei of this type, e.g., lead (82 protons) and bismuth (126 neutrons), which behave like light nuclei with respect to inelastic scattering.

Another general rule relating to inelastic scattering is that the relative probability of its occurrence, as against radiative capture or other processes following neutron absorption, increases with increasing neutron energy. This is because the separation of the excited levels of a nucleus is smaller at high excitation energies, there are consequently more excited state, in a given energy range, which the nucleus can occupy after expulsion of a neutron. The probability of the emission of a neutron by the compound nucleus increases correspondingly.

The energy of the inelastic scattering gamma rays depends, of course, upon the value of energy released as gamma radiation in the particular case, and upon whether it is emitted as one or more photons. For inelastic scattering by elements of low mass number, the total gamma rays energy must be high, e.g., several MeV, where as for heavy elements it will usually be lower⁽¹⁰⁸⁾.

Inelastic scattering in shields can be useful since it degrades neutrons to energies below the inelastic threshold, however, light materials must still be used to further degrade the neutrons by elastic scattering.

2.5 Absorption, $X(n, \gamma)Y$

For neutrons below the inelastic scattering threshold, the only reactions that occur with appreciable cross section are elastic scattering and radiative absorption. Exceptions to this are some particle reactions in very light nuclei and fission in the very heavy nuclei. Since elastic scattering serves only to alter the direction and degrade the energy of the neutrons, ultimately, except for the cases just mentioned, the neutrons are captured with emission of one or more gamma rays.

Upon capture of a slow neutron, the resultant compound nucleus has an excitation approximately equal to the binding energy of the neutron (about 8 MeV). The nucleus may release this energy with the emission of a single gamma ray and go to its ground state. However, if the nucleus has some energy levels intermediate between about 8 MeV and its ground state, it may instead emit several lower energy gamma rays in cascade while going to the lowest state. In light nuclei and in the so called "magic" nuclei, the average level spacing is large, and gamma ray transitions are often directly to the ground state.

The existence of capture gamma rays greatly complicates the shielding problem since merely slowing down and capturing the neutrons is no longer sufficient. Owing to the (n, γ) reaction, neutrons can give rise to new sources of energetic gamma rays at the point of capture. One means of suppressing capture gamma rays is to include small quantities of a material, such as boron, which has a very high cross section for thermal neutron capture via an (n, α) reaction. Even this results in a gamma ray, $E_\gamma = 0.47$ MeV in about 95 % of the reactions.

2.6 Charged Particles Reactions, X(n,b) Y

The principal reactions of this type are the (n,p) and (n,α) reactions. The kinetic energy available to the emitted charged particle and the recoil nucleus, b, is ;

$$E_p = Q + E_n \longrightarrow (2.17)$$

Where E_n is the energy of the incident neutron.

If the reaction is exoergic ($Q > 0$), it may occur even with thermal neutrons. If it is endoergic ($Q < 0$), there will be a threshold in the laboratory system,

$$E_{th} = |Q| \frac{(A + 1)}{A} \longrightarrow (2.18)$$

Where A is the mass number of the target nucleus.

For a given value of E_p , proton emission will always be more probable than alpha emission because of the lower height of the barrier for the proton.

There are a number of (n,p) and (n,α) reactions for slow neutrons on light nuclei, notably the reactions ${}^6\text{Li} (n, \alpha) {}^3\text{H}$ with $Q = 4.785$ MeV, the ${}^{10}\text{B}(n, \alpha) {}^7\text{Li}$ with $Q = 2.791$ MeV, and ${}^{14}\text{N} (n,p) {}^{14}\text{C}$ with $Q = 0.626$ MeV. The first two reactions have large thermal cross sections. Such reactions have a cross section that obeys the $1/v$ law for a considerable range above thermal, since the first resonance will be at

a relatively high energy for light nuclei with large level spacing. The $^{10}\text{B}(n, \alpha) ^7\text{Li}$ reaction, for example, follows the $1/v$ law up to 10 KeV.

For heavier nuclei, the greater height of the coulomb barrier prevents appreciable emission of charged particles with low energies. Hence, even through the reaction may be exoergic, the cross section for (n, p) and (n, α) process will be extremely small for slow and intermediate neutrons, becoming appreciable only in the MeV range. Generally the cross sections increase rapidly with energy approaching a constant, which is small because of competition with other processes, after the barrier height has been exceeded.

2.7 The $(n, 2n)$ Reaction

This reaction is a two stage process; after an inelastic scattering the residual nucleus may be left in a state of excitation sufficiently high to permit the emission of a neutron. The observed result is two scattered neutrons (of different energies) for each incident neutron and a residual nucleus of mass number $A - 1$ for a target nucleus of mass number A , with Z unchanged. The residual nucleus is frequently radioactive, uaually a positron emitter.

In order to emit a neutron, the nucleus remaining after the inelastic scattering must have an excitation energy at least equal to the separation energy of a neutron from the target nucleus. The Q - value of the $(n, 2n)$ reaction is equal to the binding energy of the "loosest" neutron in the target nucleus. As in other reactions, the

threshold energy in the laboratory system is equal to $E_{th} = |Q|[(A+1)/A]$. The separation energy of a neutron is at the same time the threshold energy for the (γ, n) reaction on that nucleus, so that (γ, n) and $(n, 2n)$ Q - values are neglecting signs identical. The threshold of the $(n, 2n)$ reactions are thus well known from nuclear mass data or from reaction energetics. They are highest for lighter elements (10 to 20 MeV) and around 5 to 7 MeV for the heaviest elements.

Nuclei which contain a loosely bound neutron, thus have a low $(n, 2n)$ threshold. One of the most important examples of this kind is beryllium - 9 , whose $(n, 2n)$ threshold is only 1.8 MeV. Beryllium is sometimes used in substantial quantities in reactors, and when this is the case special attention must be given to this reaction .

If there is no appreciable competition with charged particle emission, as in the case for heavier charged particle emission, for heavier elements and not too far above the $(n, 2n)$ threshold, the $(n, 2n)$ cross section as a function of energy and nuclear temperature may be obtained by integration over all emitted neutrons. The result is :

$$\sigma_{(n,2n)} = \sigma_c \left\{ 1 - \left[1 + \frac{(E_n - E_{th})}{T} \right] \exp - \left[\frac{E_n - E_{th}}{T} \right] \right\} \gg (2.19)$$

Where E_n is the energy of the incident neutron.

Just above threshold, equation (2.19) gives⁽¹⁰²⁾;

$$\sigma_{(n,2n)} \text{ is } \sim (E_n - E_{th})^2$$

The (n,2n) cross section rises rapidly above its threshold at the expense of the inelastic cross section, since the bulk of the inelastic neutrons are now included as part of the (n,2n) reaction. This situation is illustrated in figure (2.2), where the inelastic and (n,2n) cross sections are shown for ^{238}U .

2.8 The (n,3n) Reaction

The relationship of the (n,3n) reaction to the (n,2n) reaction is similar to that of the (n,2n) reaction to inelastic scattering. Thus a third neutron will be emitted provided the nucleus retains sufficient excitation energy after the emission of the second neutron in the (n,2n) reaction. The (n,3n) cross section therefore rises from the (n,3n) threshold at the expense of the (n,2n) cross section, as indicated in figure (2.2).

The (n,3n) threshold is high (11 MeV to 30 MeV). If a nucleus has a low (n,2n) threshold, it does not necessarily follow that its (n,3n) threshold will also be low. For instance, while the (n,2n) threshold of ^9Be is only 1.8 MeV, its (n,3n) threshold is 21 MeV. The origin of this disparity lies in the fact that; although it may require only a small amount of energy to remove one neutron from a nucleus it may take considerably more energy to remove a second neutron⁽¹⁰⁹⁾.

2.9 Nuclear Fission

Fission occurs only with certain heavy nuclei, and hence the repulsive force within the nucleus is an important contributory factor.

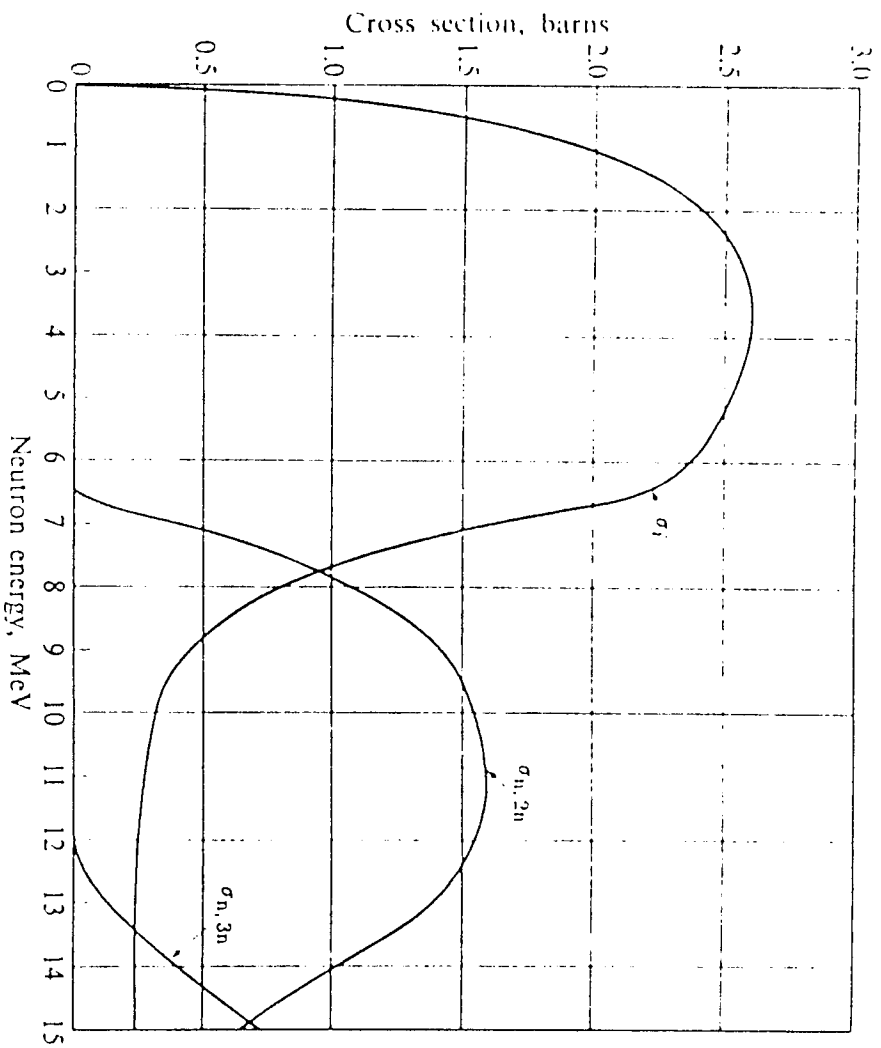
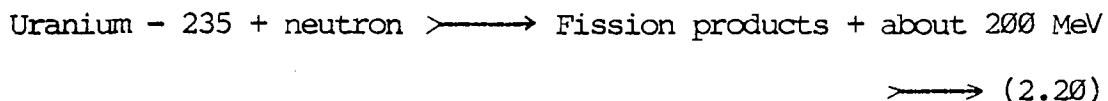


FIG. 2.2 THE INELASTIC , (n, 2n) AND (n, 3n) CROSS SECTIONS OF U - 238 .

When fission occurs, the excited compound nucleus formed after absorption of a neutron breaks up - into two lighter nuclei, called fission fragments. Nuclides such as ^{233}U , ^{235}U and ^{239}Pu are fissionable by neutrons of all energies, they are called fissile nuclides. Thorium - 232 , uranium - 238 and neptunium - 237 required fast neutron for fission. Once the fission reaction has been started in a few nuclei by means of an external source of neutrons, it can be maintained in other nuclei by the neutrons produced in the reaction. It is only with the fissile nuclides mentioned above that a selfsustaining chain is possible. ^{232}Th and ^{238}U cannot support a fission chain because the fission probability is small even for neutrons with energies in excess of the threshold of 1 MeV, and inelastic scattering soon reduces the energies of many neutrons below the threshold value.

The liberation of neutrons in the fission reaction can be explained as follows. In the compound nucleus ^{236}U formed when a ^{235}U nucleus captures a neutron, the ratio of neutrons to protons is nearly 1.57 ; consequently, when this nucleus splits into two parts, with mass numbers in the range of roughly 95 to 140 , the average neutron to proton ratio in the instantaneous products must have the same value. This ratio is too large for stability in nuclei of intermediate mass. Consequently, if these nuclei, produced in fission, have sufficient excitation energy, they can expel neutrons, thereby tending to become more stable. The actual number of neutrons released in this manner is too small, however, to confer the stability on the resulting fission fragments. The latter still have too high a ratio of neutrons to protons and so, they are radioactive, exhibiting negative beta decay. The fission fragments undergo, on the average, four stages of radioactive decay before stable

nuclei are formed. The fission reaction may be represented by :



The general term, fission products, is applied to the complex, highly radioactive, mixture of nuclides consisting of fission fragments and their various decay products.

The distribution of the fission energy for ^{235}U is given as :

Kinetic energy of fission fragments	168 MeV
Instantaneous gamma ray energy	7 MeV
Kinetic energy of fission neutrons	5 MeV
Beta particles from fission products	7 MeV
Gamma rays from fission products	6 MeV
Neutrinos	10 MeV

The 10 MeV energy of the neutrinos accompanying the beta radioactivity is not available for power production because the interaction between these particles and matter is extremely weak⁽¹⁰⁸⁾.

CHAPTER 3

NEUTRON SPECTROMETER

3.1 Introduction

Many organic crystals, liquids and plastics scintillate when bombarded with nuclear radiation⁽¹¹⁰⁻¹¹²⁾. Light is emitted in response to either primary or secondary ionization induced by the radiation. A number of these scintillations are widely used for detecting nuclear radiation because they exhibit good detection efficiency. They have high response and ability to provide exact information on number, time of arrival and energy of nuclear particles. Some can distinguish between particles by the shape of light pulses⁽¹¹⁸⁾.

The response of these organic materials is usually critically dependent upon the specific ionization of the detected particles. Some of these scintillators respond to ionizing particles by emitting a light pulse which is sum of a short (a few ns) and a long (several μ s) decay time component.

The response of organic scintillators to electrons is quite linear with particle energy above about 100 keV. Furthermore, linear extrapolations of the electron response from higher energies generally pass within a few KeV of the origin⁽¹¹⁴⁾. However, organic scintillators response to heavier ionizing radiation is generally nonlinear with a light output, which is less than that for electrons of the same energy.

Neutrons and gamma rays can be detected by scintillators because they collide with particles in the scintillator material and cause them to recoil. In organic materials, gamma rays interact primarily with atomic electrons by the Compton effect whereas neutrons scatter elastically from the nuclei of the atoms in the scintillator. Organic scintillators are good neutron detectors since they contain light elements whose nuclear recoils can easily be detected. Neutrons can be distinguished from gamma rays by the pulse shape discrimination (PSD) technique^(115,116) .

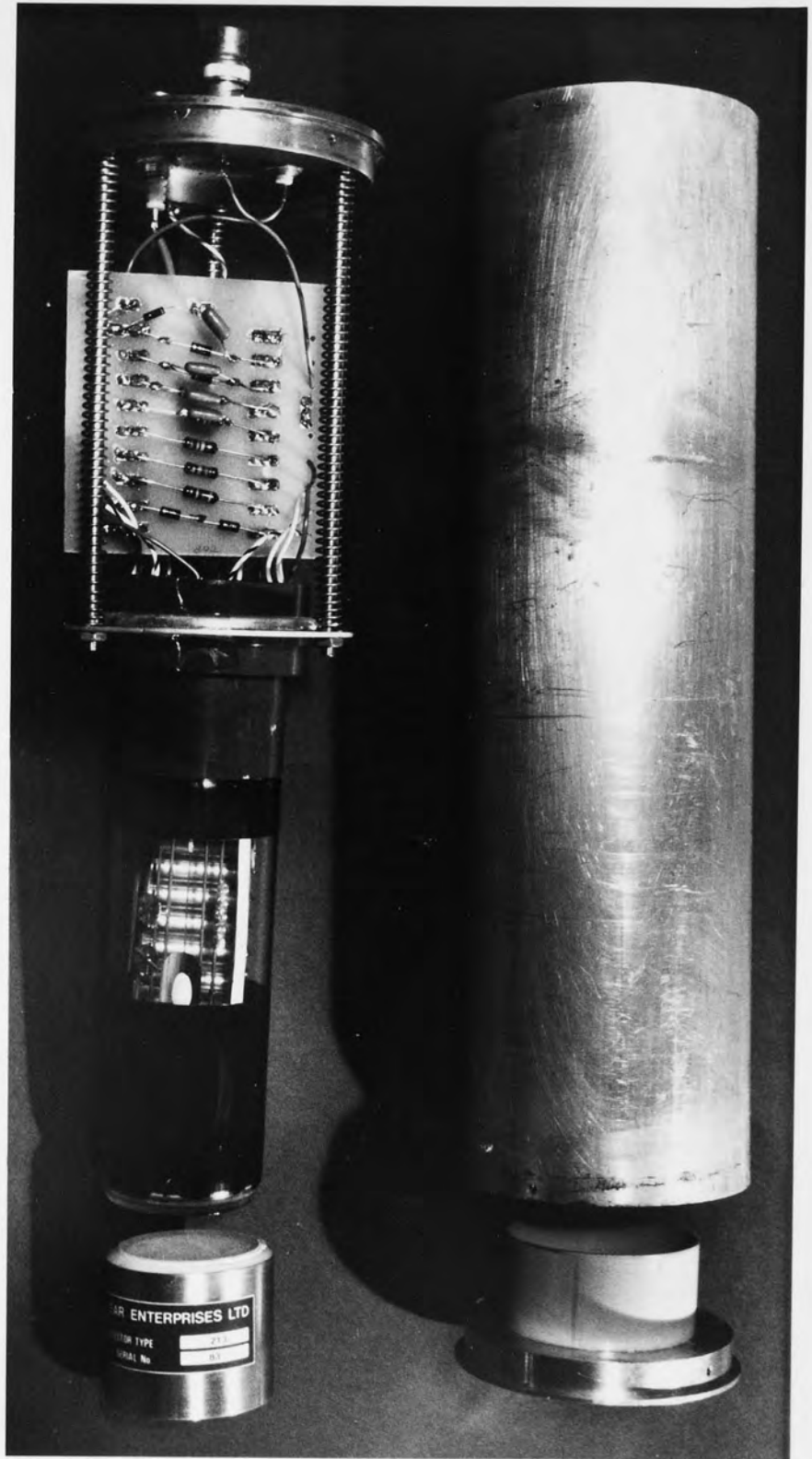
3.2 The Scintillator

A 40 mm by 40 mm diameter cylinder of NE - 213 scintillator was chosen because it offers a good compromise between efficiency and resolution. This scintillator is made with xylene, activators, and POPOP as a wave shifter. Naphthalene is added to enhance the slow component of light emission. This is important for achieving a good pulse shape discrimination capability^(117,118). The scintillator was commercially prepared encapsulated in an aluminium BA1 cell 40 mm x 40 mm with a hidden expansion volume and was bubbled with pure nitrogen to remove the undesirable oxygen which selectively quenches the slow component of light emission.

This type of scintillator has the following parameters :

Chemical composition	= CH _{1.213}
Density	= 0.874 gm.cm ⁻³
N _H (the number of hydrogen nuclei)	= 0.0482x10 ²⁴ atoms cm ⁻³

FIG. 3.1 THE PHOTOMULTIPLIER TUBE AND THE NE-213 SCINTILLATOR DETECTOR.



$$N_C(\text{the number of carbon nuclei}) = 0.0398 \times 10^{24} \text{ atoms cm}^{-3}$$

The NE - 213 scintillator has the following characteristics :

- 1- It has an enhanced emission of delayed light that gives it good pulse shape discrimination capabilities.
- 2- Being a liquid, NE - 213 is isotropic in response to neutrons and is not sensitive to mechanical or thermal shock.
- 3- Carbon recoils and alpha particles from 14 MeV neutrons on NE - 213 produce only about half the pulse height that is produced with stilbene, when normalizing to the largest hydrogen recoil pulses.⁽¹¹⁹⁾
- 4- It has greater hydrogen content than stilbene.
- 5- Its scintillation processes permit discrimination from gamma rays based on the pulse rise time - pulse shape discrimination⁽¹²⁰⁻¹²²⁾.

The response of a scintillation detector (scintillator plus photomultiplier tube) to radiation, depends on several geometrical factors including the size and shape of the scintillator, the quantity of the light reflector and location of the scintillation within the scintillator⁽¹²³⁾.

Figure (3.1) presents a photograph of the scintillator and photomultiplier tube used in this work .

3.3 The Photomultiplier Tube

Using an NE - 213 scintillator requires a gain of the order 10^6 due to the small light output. In order to preserve a good timing resolution, it is desirable to operate the photomultiplier tube (PMT) as near the recommended voltage as possible. These requirements can be met by a 14 stages photomultiplier tube type 56AVP. This type has a high degree of time definition and a good timing resolution.

When radiation is incident on the scintillator, a fraction of the energy loss transfers by ionisation and excitation. Ionisation and excitation cause the generation of light photons radiated in all directions. Those photons which strike the photocathode, generate photoelectrons. Photoelectrons are accelerated towards the first dynode by a potential between this dynode and the photocathode. To maximise the amount of light striking the photocathode, the scintillator is usually coated with a reflector. In the BAL cell a diffuse internal reflector is provided.

From the first dynode, several secondary electrons are ejected for each incident electron. These electrons, in turn, are accelerated towards the second dynode. Using the dynode chain in figure (3.2), a very high gain in the number of electrons can be obtained, that eventually appear on the anode. The dark current in the photomultiplier tube must be low in order to measure low energy neutrons.

Since a linear signal is required from the anode and peak currents of 50-100 mA may occur, space charge saturation of the photomultiplier signal in the later dynodes is a problem. To overcome this problem a

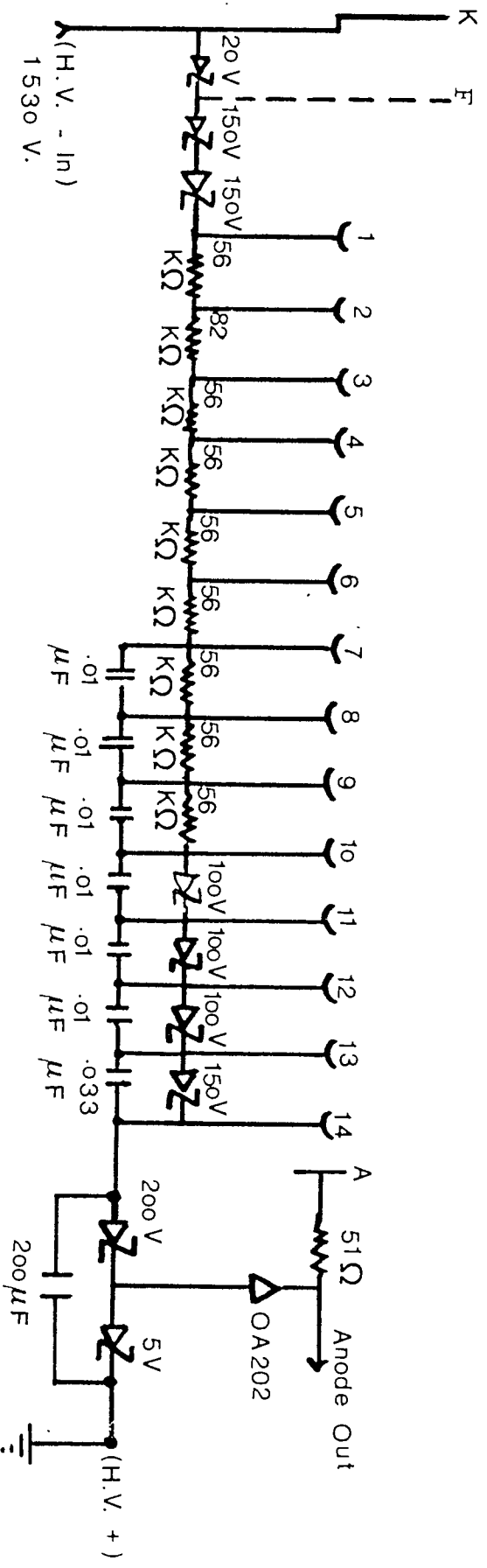


FIG. 3.2 DYNODE CHAIN OF THE PHOTOMULTIPLIER TUBE TYPE 56AVP .

fixed high potential between the anode and the last dynode (200 V), and between the tenth dynode and the fourteenth dynode (100, 100, 100 and 150 volts respectively) are used. The use of zener diodes enables the overall voltage and so the gain to be changed without running into space charge saturation and high count rates can be accommodated. If only resistors are used, when the dynode voltage is adjusted to obtain the desired gain, the top dynodes may have insufficient voltage across them during the pulse to remove the electrons rapidly, thus causing saturation

3.4 Discrimination Between Neutron And Gamma

There are two common methods of pulse shape discrimination. The first one is based on integrating the charge contained in the initial portion of the pulse and comparing it with the charge obtained by integrating the entire pulse^(124,125). This method, which is known as charge comparison was originally developed by Brooks⁽¹¹⁵⁾ for scintillator pulses. The second one is to integrate the pulse and to differentiate between the different rise times obtained after the integration by the zero crossing method⁽¹²⁶⁻¹³⁰⁾. This method was first described by Alexander⁽¹¹⁶⁾.

Initially measurements were made using the zero crossing method but with the equipment available the degree of discrimination obtained was not adequate over a sufficient energy range. Equipment for the charge comparison method was then obtained and the measurements were repeated.

There is another method based on taking the ratio of digitized signal derived by getting a portion of the fast and slow components of each pulse, separately⁽¹³¹⁾.

Many papers have been written on the subject of pulse shape discrimination. Few of them have presented information in such a way that direct comparisons can be made between the various methods employed. If results are given in terms of energy, then comparison can only be made if the scintillator / photomultiplier conversion efficiency is given. Bertolaccini et al.⁽¹³²⁾ have described a simple method to determine this. Adams and White⁽¹³³⁾ describe a complete instrument based on the charge comparison method providing all the necessary outputs such as particle identification, fast timing, integrated signal for multichannel analyser use, "low level" show bias and outputs to an oscilloscope to give a display showing neutron and gamma. This instrument has been successfully employed in a wide variety of experiments involving neutron energies from about 100 keV up to 20 MeV. Within this energy range, the experimental problems of discrimination have been solved.

3.4.1 The Method Of Discrimination

This method has been employed before in pulse shape discriminators from the Harwell "2000" series and used two linear gated integrators⁽¹³⁴⁾. Recently, greatly improved performance and reduction in volume has been obtained in a commercial production version manufactured by Link Systems, model 5010.

A simplified block diagram and waveforms are shown in figures (3.3) and (3.4) respectively. The principle is that the anode current of the photomultiplier is integrated for a time T_1 (25 ns) and then held. A second integrator opens coincidentally with the first but continues integrating for time T_2 (500 ns). The outputs of the integrators are so weighted that when they are compared, the output of the comparator indicates a neutron (if the output of integrator 2 exceeds that of integrator 1), and a gamma ray (if the reverse is true). This can be represented by the following :

If $K_1 Q_1 > K_2 (Q_1 + Q_2)$, then a gamma ray is indicated and,

If $K_1 Q_1 < K_2 (Q_1 + Q_2)$, a neutron is indicated ,

Where Q_1 is the charge collected in the time T_1 ,
 $(Q_1 + Q_2)$ is the charge collected in time T_2 ,
 K_1 and K_2 are the normalising weights.

3.4.2 Description Of The Circuit

With reference to figure (3.3), the signals from the detector are delayed in a 30 ns delay cable. At the same time a X1 buffer amplifier drives a start discriminator which "enables" the constant fraction discriminator and the signal emerging from the enabling AND gate triggers the gate generators 1 and 2. The linear gate and integrators 1 and 2 integrate the input signal for 25 ns and 500 ns respectively. These waveforms are shown in figure (3.4). At the end of the longer of

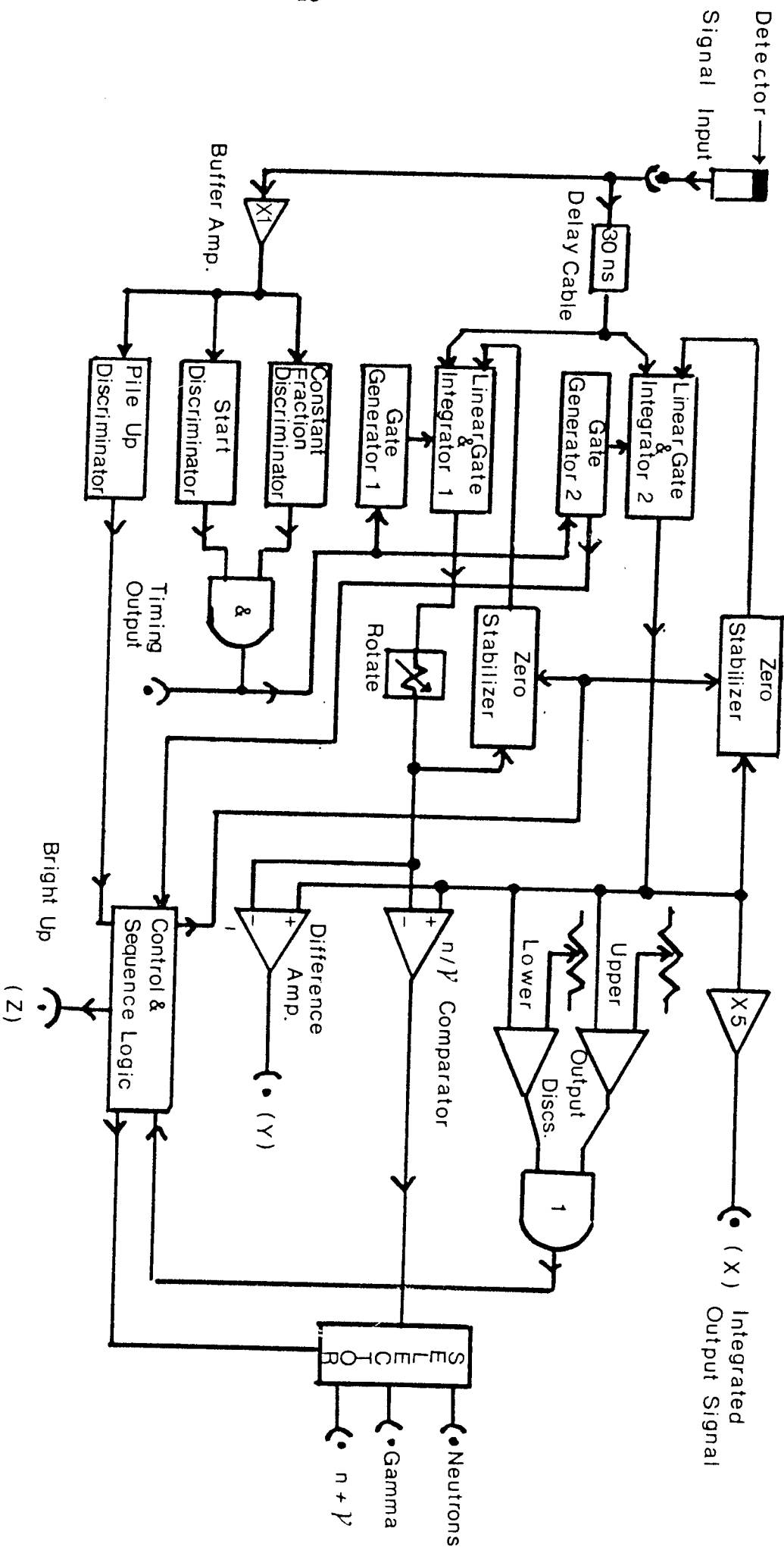


FIG. 3.3 SIMPLIFIED BLOCK DIAGRAM OF THE PSD-5010.

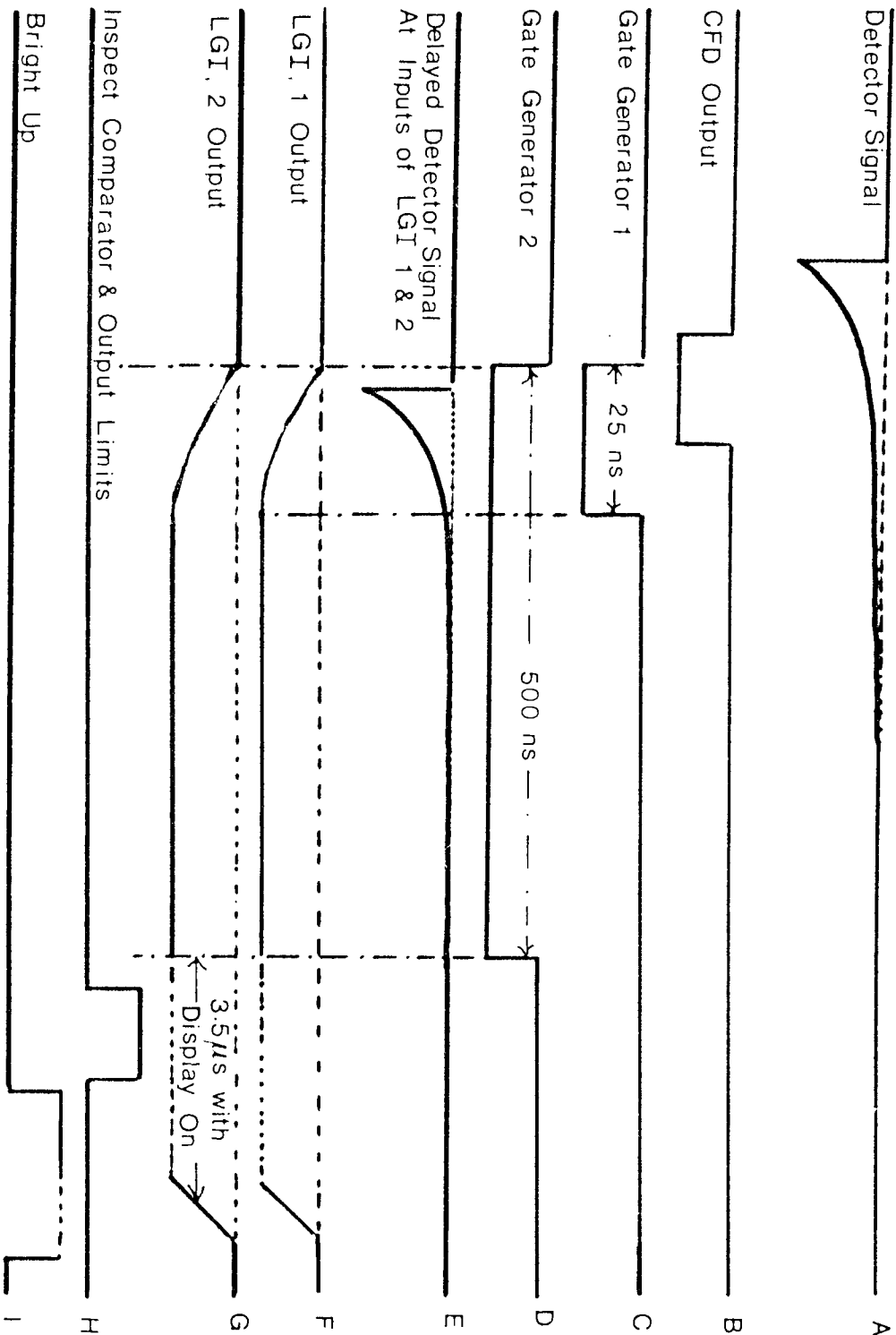
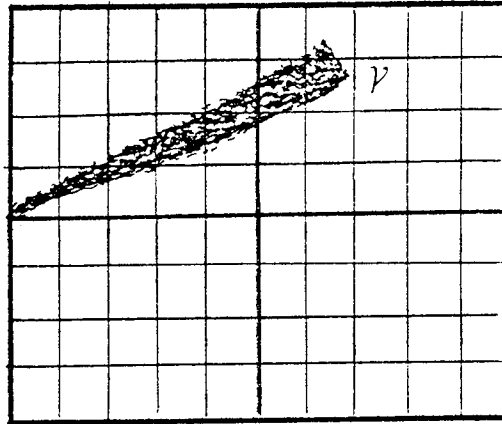


FIG. 3.4 LINEAR GATE AND INTEGRATOR WAVEFORMS.

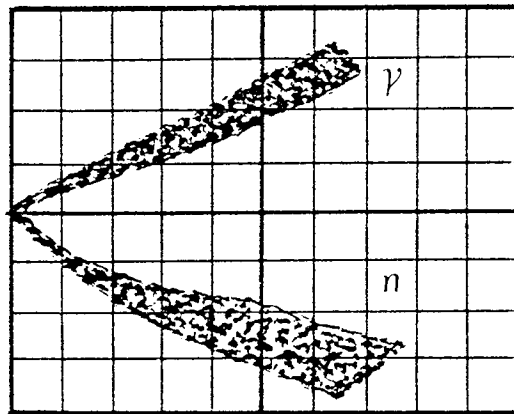
the two integrator time periods (gate 2), the control and sequence logic will perform the following operations :

- 1- The state of the comparator is inspected to see whether the output of the linear gate and integrator LGI(1) is greater or less than the output of LGI(2). The result of this inspection determines whether the event is classified as a gamma ray or neutron.
- 2- The upper and lower output discriminators are inspected, and only those events, falling between these limits, are allowed to indicate outputs.
- 3- If an output occurs from the pile - up discriminator during the gate generator 2 period, the present event is rejected and no output occurs.
- 4- The zero - stabiliser oscillator triggers periodically if no detector signal is present. The stabilisers maintain the zero pedestal level of the integrators at a preset value.
- 5- Bright up signals (Z) are provided for the cathode ray tube (CRT) display of the difference (Y) and total energy (X) outputs.

All the setting up can be done with the aid of the oscilloscope display. However, the circuits built into the instrument to drive a standard oscilloscope are not shown on the diagram. The loci of the events will be displayed, as in figure (3.5), when the display switch is set to NEUTRON + GAMMA. When the display switch is set to NEUTRON, only



(A)



(B)

FIG. 3.5 SKETCH OF OSCILLOSCOPE DISPLAY SHOWING :
A- GAMMAS.
B- GAMMAS + NEUTRONS.

those events identified as such will have "bright up". Thus the SEPARATION level between neutrons and gamma rays can, easily, be adjusted. The ROTATE control has the effect of varying the weight K_1 . Its effect on the display is to rotate the neutron and gamma ray loci about their zero energy origin.

The output pulses from pulse shape discriminator, PSD - 5010, (NEUTRON OUTPUT) are increased in length by an external pulse stretcher to 3 μ s and are used to gate a 512 channels multichannel analyser (MCA). The INTEGRATED OUTPUT signal passed through an attenuator to the input of a fast amplifier used as an inverter. The inverted output signals are fed to the input of the multichannel analyser . Figure (3.6) shows a block diagram of the circuit used for neutron detection.

The output data is listed on punched paper tape which is input to the Aston University ICL 1904S Computer. Computer programme (NSPEC) is then used to analyse the data for obtaining the neutron spectrum. This programme uses the differentiation method to unfold the spectrum (see section 3.6).

Figure (3.7) shows the pulse height spectrum produced by 14.1 MeV neutrons from an unshielded target as obtained on multichannel analyser . Figure (3.8) presents a photograph of the measuring system with the control panel of the SAMES Accelerator.

3.5 Calibration Of The Spectrometer

The first step in obtaining neutron spectra from pulse height

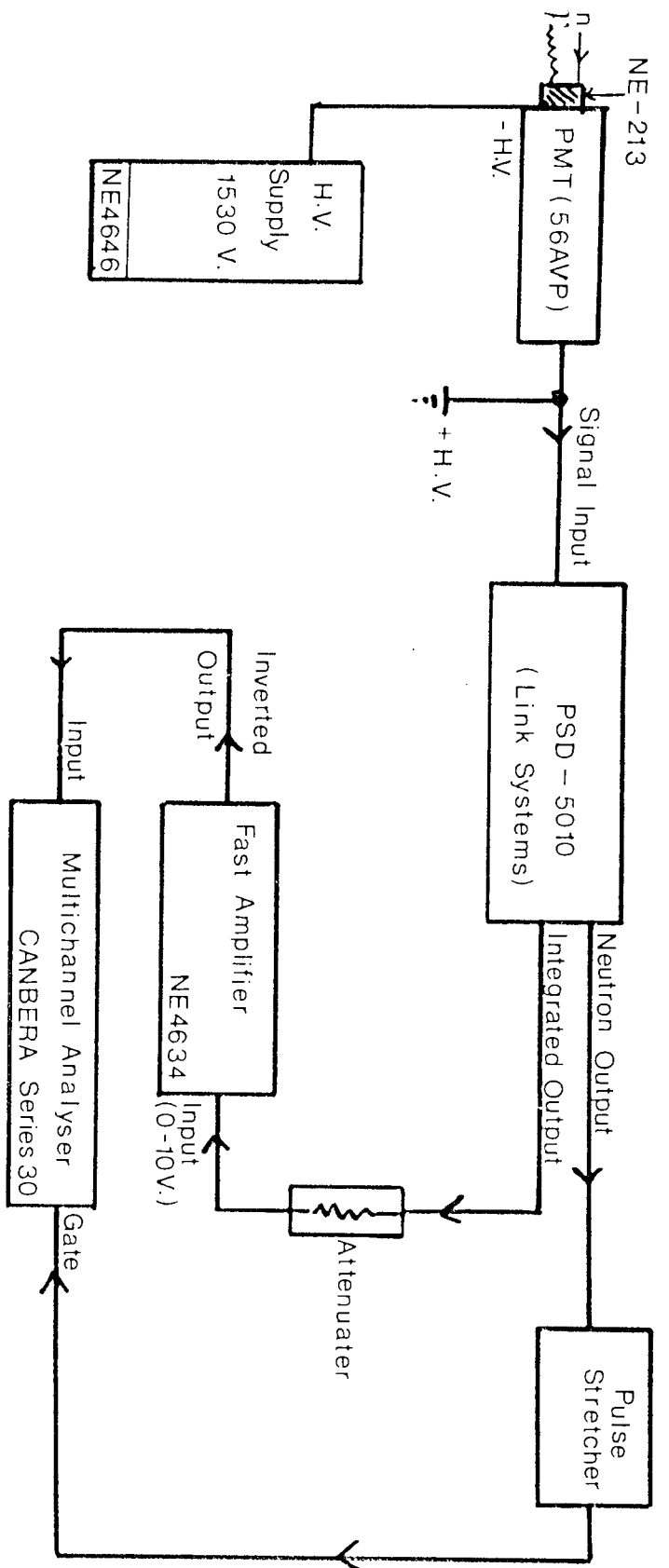


FIG. 3.6 THE BLOCK DIAGRAM OF THE CIRCUIT USED FOR NEUTRON DETECTION .

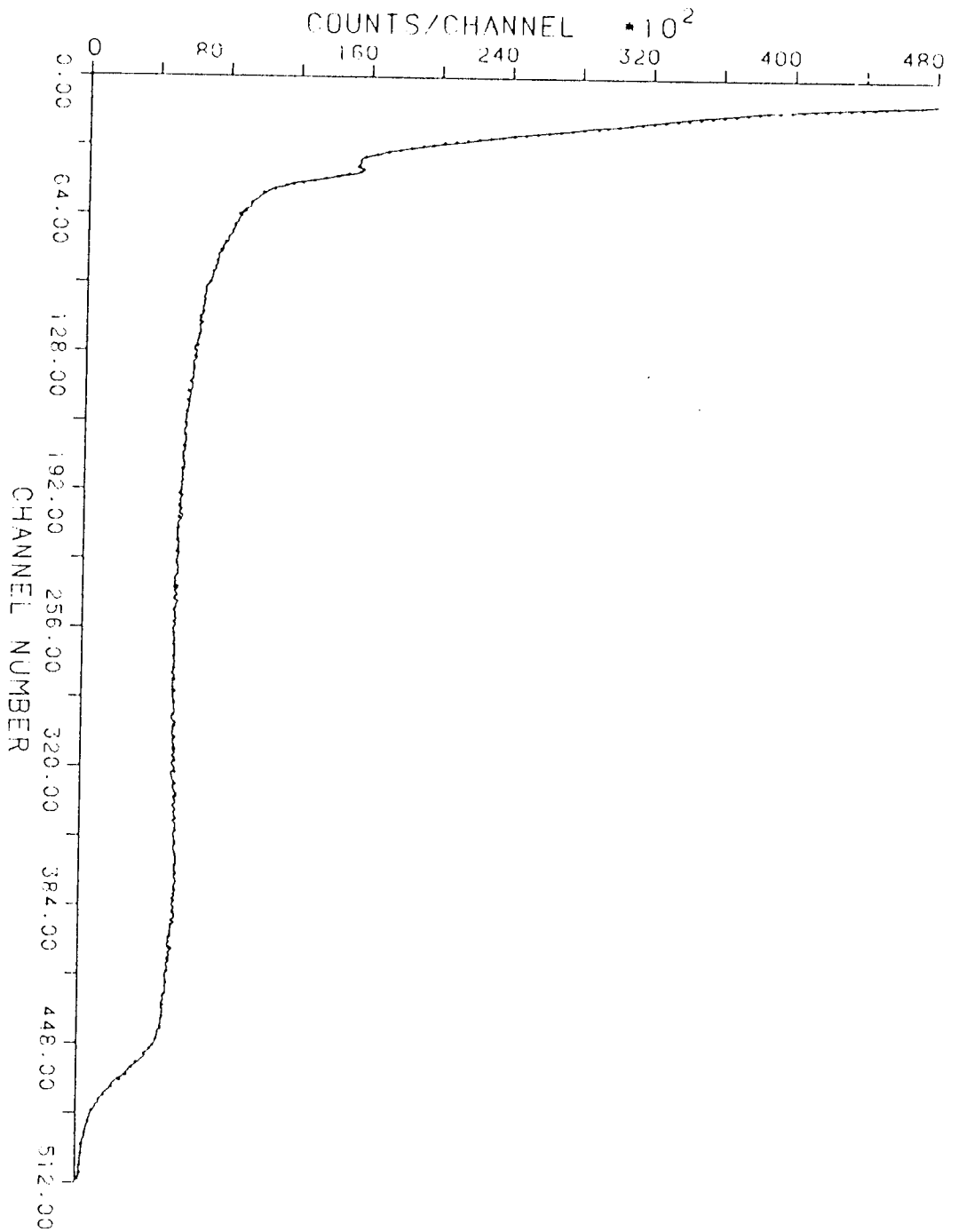


FIG. 3.7 THE PULSE HEIGHT SPECTRUM OF THE 14.1 MEV
NEUTRONS FROM AN UNSHIELDED TARGET AS OBTAINED
ON THE MULTICHANNEL ANALYSER.

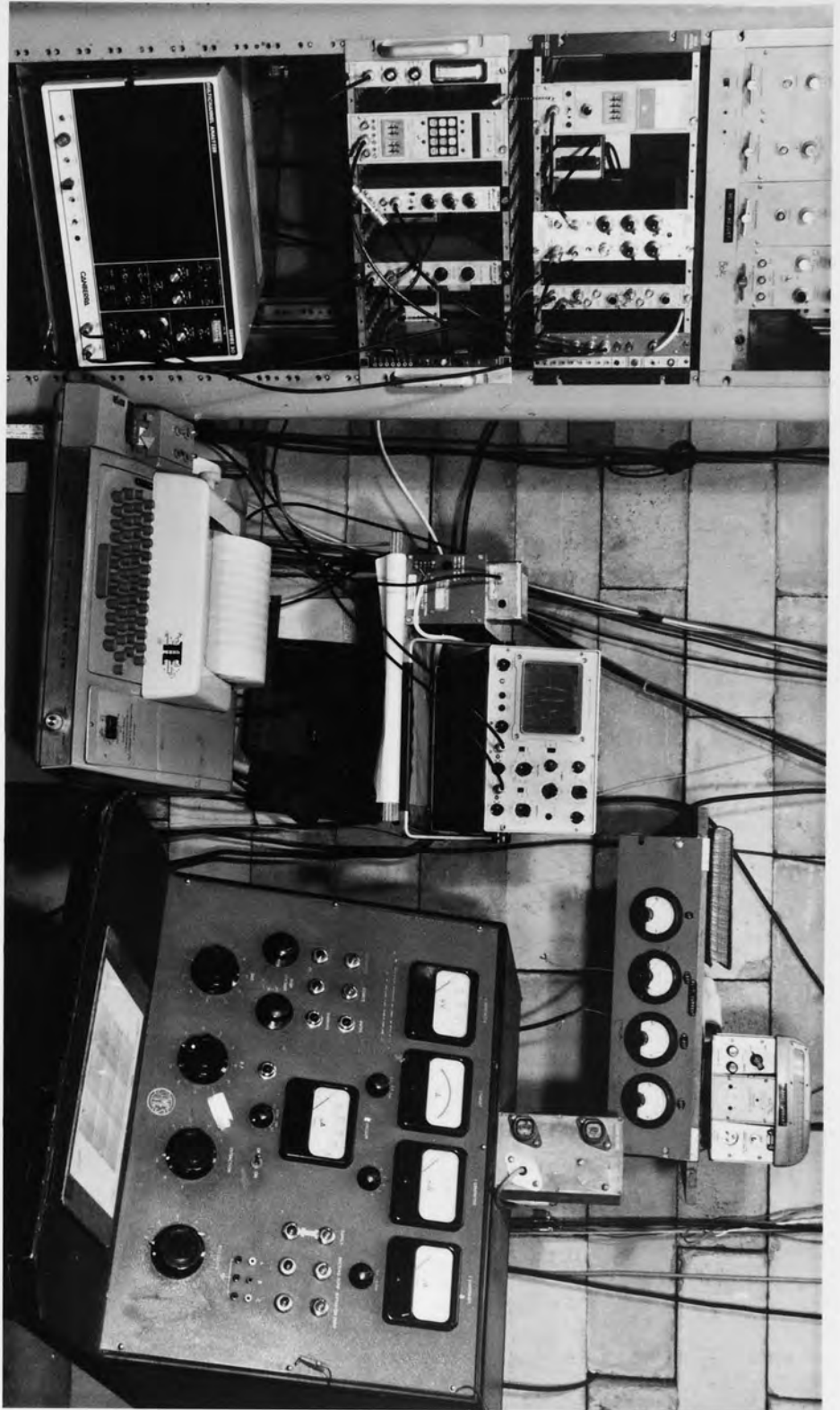


FIG. 3. 8 THE MEASURING SYSTEM WITH PANEL OF SAME'S ACCELERATOR.

distributions is to convert them to energy distributions of the recoil protons. Since the scintillation response to electrons is linear with respect to their energies, the response due to other particles can be given in terms of electron equivalence. Broek and Anderson⁽¹³⁵⁾ show the calibration of their detector as a relation between proton energy and electron energy for equal scintillation pulse height. This relation was obtained by the concurrent calibration with gamma sources (for electrons) and mono - energetic neutrons (for recoil protons). An advantage of determining the proton versus electron response is that calibration against changes in the gain of the equipment can be readily accomplished with gamma ray sources to test the linearity of the spectrometer.

3.5.1 Spectrometer Linearity

The spectrometer linearity is tested by means of gamma ray sources ^{22}Na , ^{137}Cs , ^{54}Mn and ^{60}Co . Figure (3.9) demonstrates the electron (gamma ray) response of our system. Here, the half height channel number, of the measured Compton distribution from a number of reference gamma ray sources, is plotted as a function of the electron energy assigned to that half height, assuming that the half height corresponds to the Compton edge. That is given by⁽¹³⁶⁾ :

$$E_c = E_\gamma / [1 + (0.51 / 2 E_\gamma)] \quad \longrightarrow (3.1)$$

Where E_γ is the energy of the gamma quantum in MeV.

It can be seen that, there is a linear relationship between light

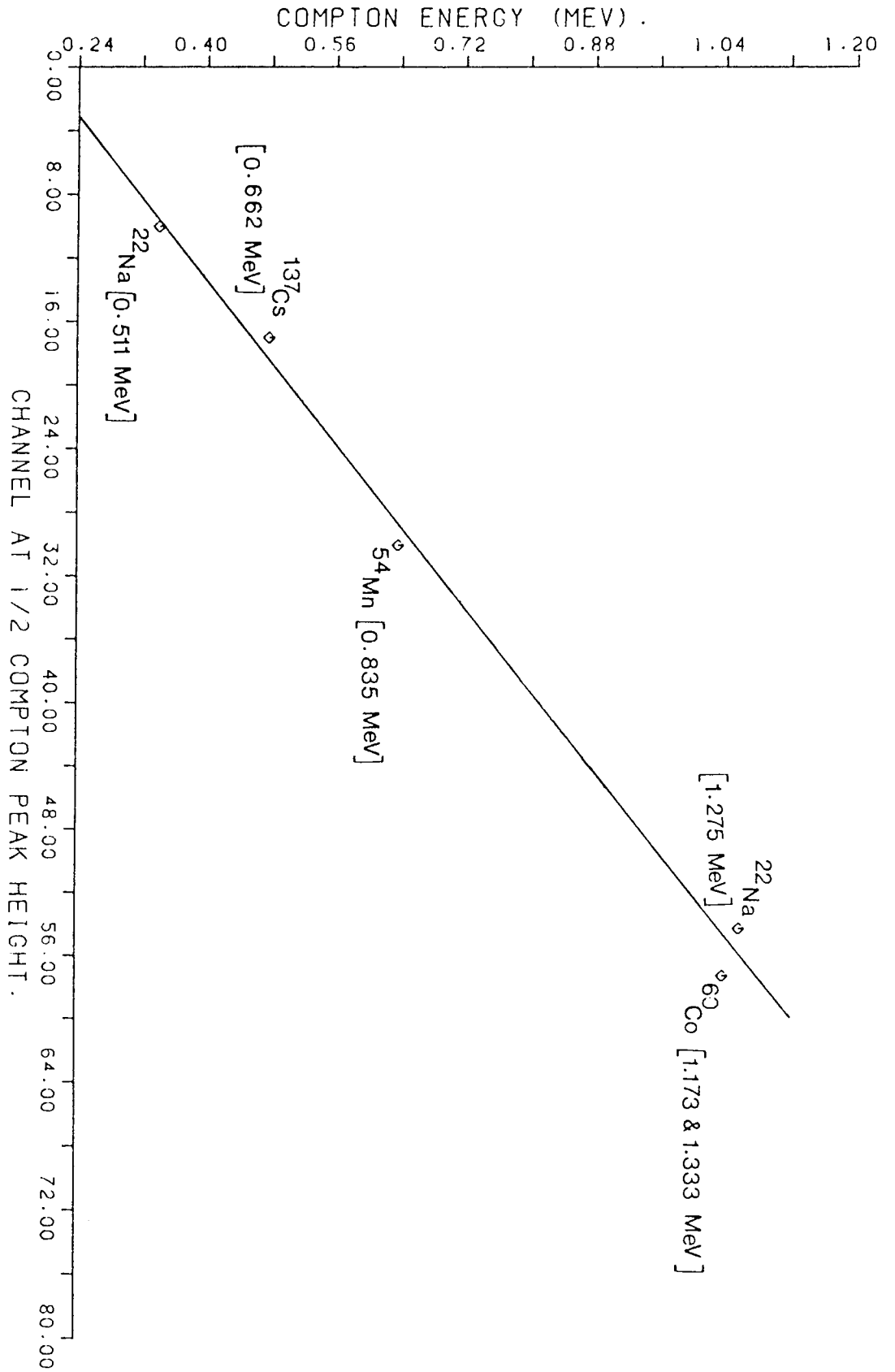


FIG. 3.9 THE LINEARITY OF THE SPECTROMETER.

output and electron energy. The intercept with the energy axis being at 0.14 MeV, is due to a zero - offset of the multichannel analyser used. This only checks the linearity over a limited range. It would require gamma radiation up to about 8 MeV to check the linearity over the whole of the neutron pulse height range.

Since high energy gamma rays are not available for calibrating the system, the position of the 14.1 MeV peak is identified from the half height of the 14.1 MeV edge of the integrated pulse height distribution and equated to an electron energy 7.7355 MeV using equation (3.5) below . This sets the energy scale and forces the 14.1 MeV peak to the correct energy .

3.5.2 The Relation Between Recoil Proton And Electron Pulse

The relation between the pulse height and energy of the recoil proton can be expressed by giving the pulse height in terms of equivalent electron energy as follows^(137,138) :

$$\text{For } E_e < 2.17 \text{ MeV , } E_p = 3.13 (E_e)^{2/3} \text{ MeV } \longrightarrow (3.2)$$

$$\text{For } E_e > 2.17 \text{ MeV , } E_p = (1.59 E_e + 1.8) \text{ MeV } \longrightarrow (3.3)$$

$$\text{For } E_e = 2.17 \text{ MeV , } E_p = 5.25 \text{ MeV } \longrightarrow (3.4)$$

E_e is equivalent electron energy corresponding to the same pulse size and is proportional to pulse height.

It is convenient to relate the pulse size (P) to the recoil proton energy (E_p) from equations (3.2) and (3.3). Since the light output from an electron is proportional to energy (except for very low energies) ,i.e, E_e proportional to pulse height, hence :

$$\text{For } E_p > 5.25 \text{ MeV , } E_e = 0.6289 (E_p - 1.8) \longrightarrow (3.5)$$

$$\text{For } E_p < 5.25 \text{ MeV , } E_e = (E_p)^{3/2} \times 0.1806 \longrightarrow (3.6)$$

The computer calculation uses table (3.1) of E_e calculated for $E_p = 0.2 , 0.4 , 0.6 , \dots, 16.0 , 16.2 , 16.4 \text{ MeV}$.

3.5.3 Neutron Efficiency

The efficiency of a cylindrical scintillator, for detecting a parallel beam of neutrons incident normally on the cylindrical end by a single scattering on hydrogen, is given by⁽¹⁰¹⁾ :

$$\epsilon_n = (N_H \sigma_{n,H} / a) [1 - \exp (- aL)] \longrightarrow (3.7)$$

Where N_H is the number of hydrogen atoms per cm^3 .

$\sigma_{n,H}$ is the neutron - proton cross section .

L is the detector length in cm .

a is the quantity ($N_H \sigma_{n,H} + N_C \sigma_{n,C}$)

N_C is the number of carbon atoms per cm^3 .

$\sigma_{n,C}$ is the total neutron - carbon cross section .

Table (3.1) Proton Pulse Size (P) As Calculated From Equations (3.5) And (3.6)

E_p (MeV)	$P=E_e$ (MeV)						
0.2	0.0162	0.4	0.0457	0.6	0.0839	0.8	0.1292
1.0	0.1806	1.2	0.2374	1.4	0.2992	1.6	0.3655
1.8	0.4361	2.0	0.5108	2.2	0.5893	2.4	0.6715
2.6	0.7571	2.8	0.8462	3.0	0.9384	3.2	1.0338
3.4	1.1322	3.6	1.2336	3.8	1.3378	4.0	1.4448
4.2	1.5545	4.4	1.6669	4.6	1.7818	4.8	1.8992
5.0	2.0192	5.2	2.1415	5.4	2.2641	5.6	2.3899
5.8	2.5157	6.0	2.6414	6.2	2.7672	6.4	2.8930
6.6	3.0188	6.8	3.1446	7.0	3.2703	7.2	3.3961
7.4	3.5219	7.6	3.6477	7.8	3.7735	8.0	3.8992
8.2	4.0250	8.4	4.1508	8.6	4.2766	8.8	4.4024
9.0	4.5281	9.2	4.6539	9.4	4.7797	9.6	4.9055
9.8	5.0313	10.0	5.1570	10.2	5.2828	10.4	5.4086
10.6	5.5344	10.8	5.6602	11.0	5.7859	11.2	5.9117
11.4	6.0375	11.6	6.1633	11.8	6.2891	12.0	6.4148
12.2	6.5406	12.4	6.6664	12.6	6.7922	12.8	6.9180
13.0	7.0437	13.2	7.1695	13.4	7.2953	13.6	7.4211
13.8	7.5469	14.0	7.6726	14.2	7.7984	14.4	7.9242
14.6	8.0500	14.8	8.1758	15.0	8.3015	15.2	8.4273
15.4	8.5531	15.6	8.6789	15.8	8.8047	16.0	8.9304
16.2	9.0562	16.4	9.1819				

$\sigma_{n,H}$ and $\sigma_{n,C}$ are evaluated at the neutron energy.

The neutron scattering cross section for hydrogen can be expressed according to Wasson's equation⁽¹³⁹⁾ as :

$$\sigma_{n,H} = \frac{5.603 \pi}{1 + 7.417 E + 0.1105 E^2} + \frac{0.8652 \pi}{1 + 0.2427 E + 0.0028 E^2} \text{ barns / atom} \quad \longrightarrow (3.8)$$

The cross sections for carbon $\sigma_{n,C}$ were taken from Ref. (140).

The efficiency ϵ_n was calculated by using equation (3.7) for neutron energies up to 15.8 MeV, and plotted in figure (3.10).

3.5.4 Shape Correction Factor (B)

The shape correction factor (B), which removes most of the effect of second scattering of neutrons by hydrogen and the loss of recoil protons through the wall of the detector; is⁽¹³⁵⁾:

$$B = 1 - 0.78 \frac{R_m}{L^*} + 0.09 N_H \sigma_{n,H} L + 0.077 N_H \sigma_{n,H}^* r \quad \longrightarrow (3.9)$$

Where $\sigma_{n,H}^*$ is the value of $\sigma_{n,H}$ at 0.068 E .

L^* is the scintillator thickness in mg/cm^2 .

L is the scintillator thickness in cm .

r is the scintillator radius in cm .

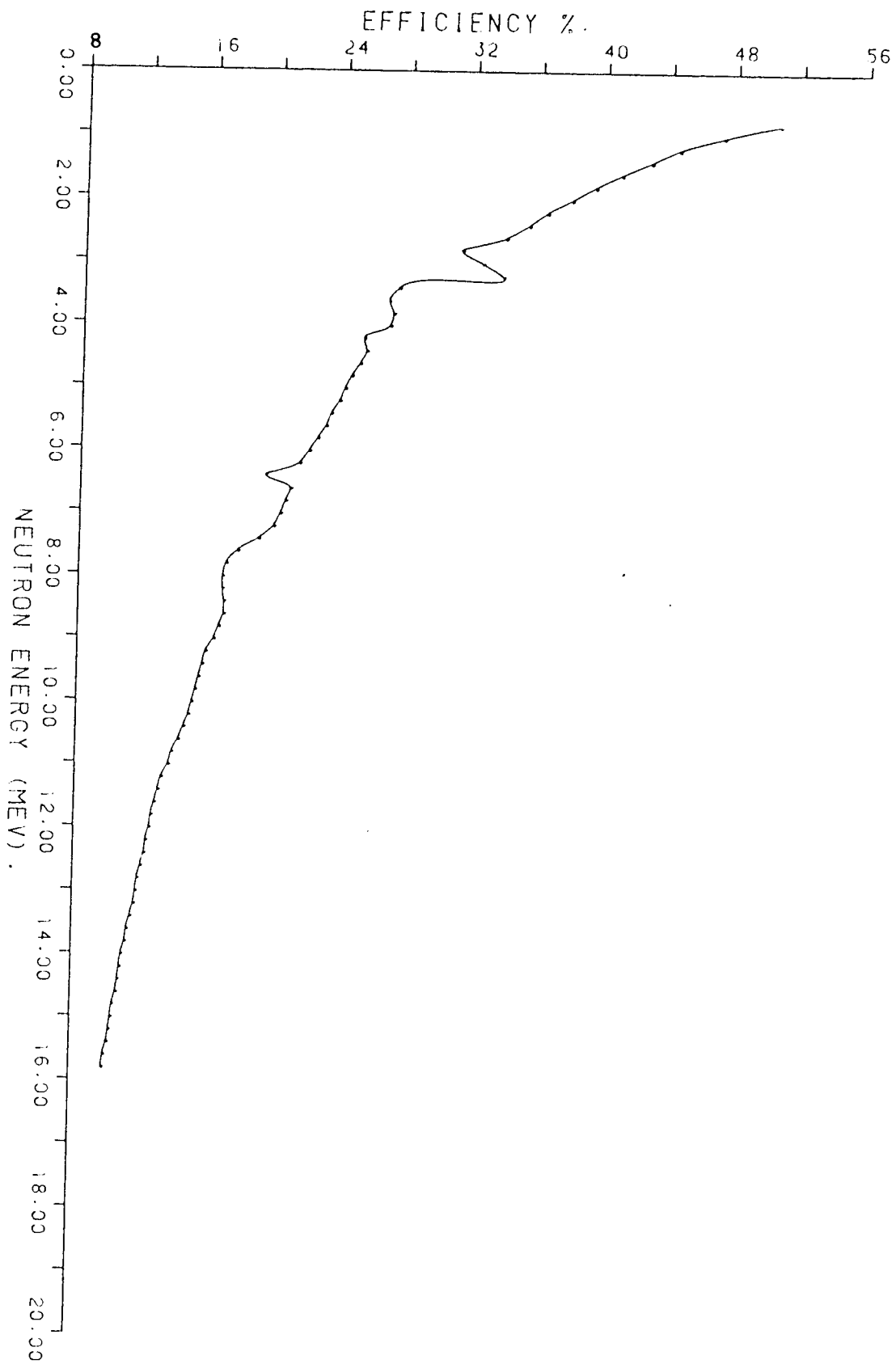


FIG. 3.10 NEUTRON DETECTOR EFFICIENCIES FOR NE-213 (4X4 CM.).

R_m is the range in the scintillator of a proton which receives the full neutron energy, in mg/cm^2 .

From ranges of protons in NE - 213 given by Schutter⁽¹⁴¹⁾, R_m was obtained as :

$$R_m = 1.7382 (E + 0.15045)^{1.8194} \text{ mg}/\text{cm}^2 \longrightarrow (3.10)$$

This formula reproduces measured values to within two per cent. The magnitude of the neutron peak derived from the pulse - height spectrum produced by monoenergetic neutrons is corrected by this factor. The effect of the distortions upon the low - energy tail of the neutron spectrum is neglected. This is because the two effects, for which the correction is made, tend to cancel each other for certain sizes and shapes. It is possible, then, to make a choice to minimize this correction. Hence, the closer the value of B is to unity, the less is uncertainty due to the method of derivation^(142,143).

Figure (3.11) shows the relation between shape correction, B, and neutron energy up to 15.8 MeV.

3.6 The Unfolding Method

The experimental data given by the spectrometer measurements do not produce directly the desired information on the energy distribution of the recorded particles. An appropriate analysis or unfolding method must be used for measuring pulse amplitude distribution in order to evaluate real neutron spectra.

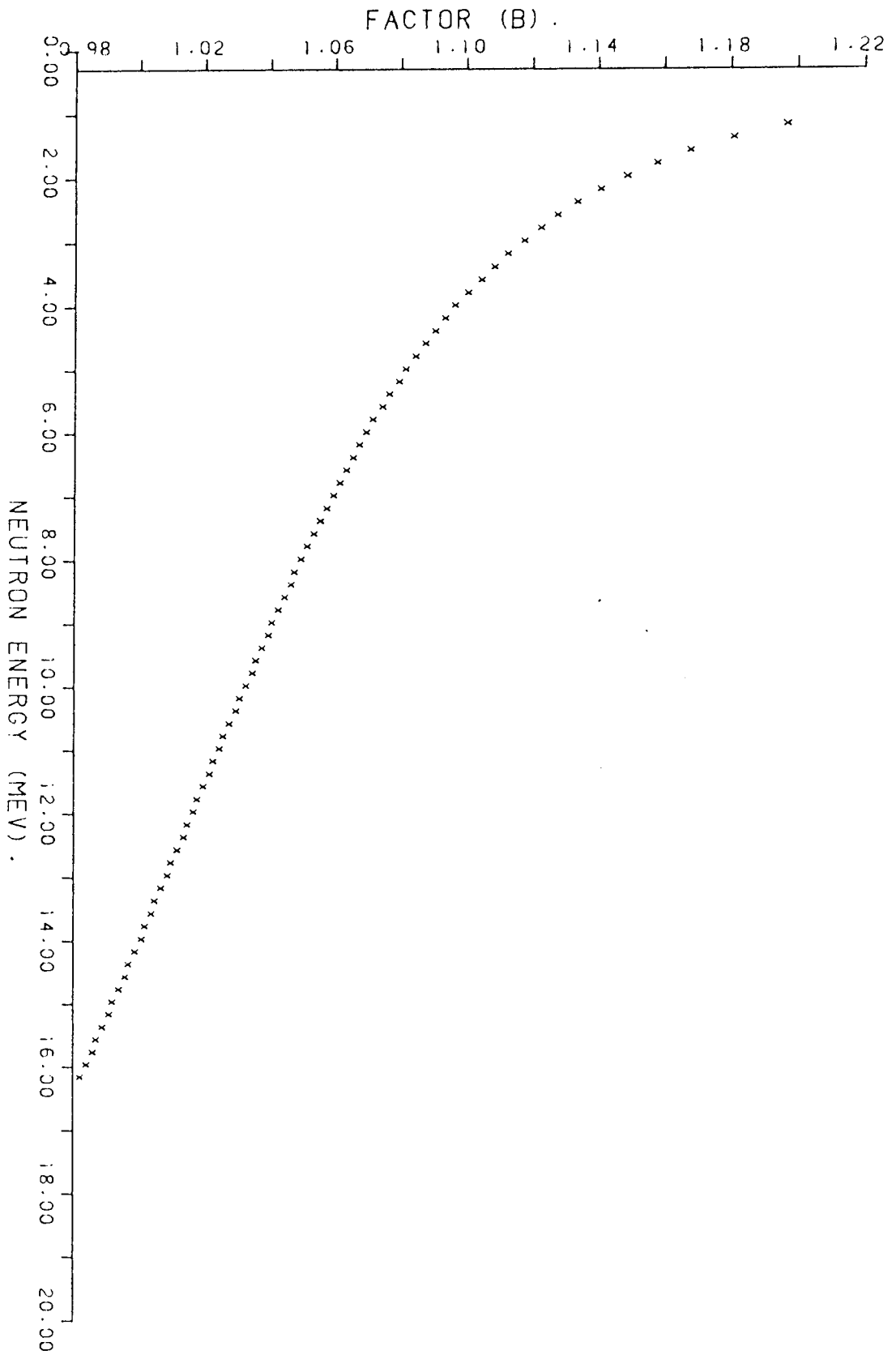


FIG. 3.11 SHABE CORRECTION FACTOR FOR THE NE-213 SINTILLATOR.

The number of recoil protons with energy (E), in a unit energy interval, due to a number of neutrons (ϕ_0), of energy (E_{on0}), is :

$$N (E) = \epsilon_n A \phi_0 / E_{on0} \longrightarrow (3.11)$$

Where ϵ_n is the efficiency of the scintillator [Equation (3.7)] .

A is the cross section area of the detector .

In the case of neutrons with a complicated energy spectrum, ϕ_n , recoil protons of energy, E, will be generated by neutrons of different energies $E_n \geq E$. Hence, the number of recoil protons in a unit energy interval is :

$$N_p (E) = \int_E^{\infty} (\epsilon_n \phi_n A / E_n) d E_n \longrightarrow (3.12)$$

Differentiation of equation (3.12) with respect to E_n , is :

$$\frac{d N_p (E)}{d E} = \frac{\epsilon_n A \phi_n}{E_n}$$

or

$$\phi_n = \left(\frac{E_n}{\epsilon_n A} \right) \left[\frac{d N_p (E)}{d E} \right] \longrightarrow (3.13)$$

This means that, the neutron spectrum can be calculated from the energy distribution of the recoil protons by differentiation.

Naturally, the real pulse amplitude distribution, even for

monoenergetic neutrons, could not be described analytically. For this reason, numerical methods have to be used for the determination of the derivative.

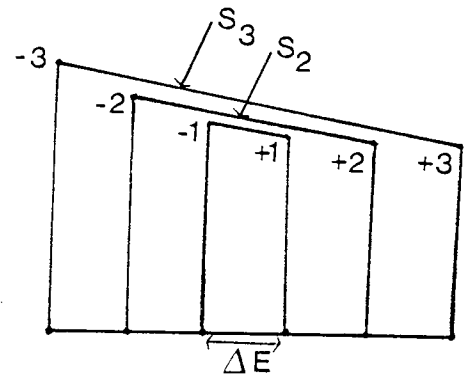
The counts in the spectrum could be grouped into proton energy bins, content C_i . Assuming a " perfect spectrum ", the number of counts per (ΔE) proton width is :

$$C_i = \Sigma \frac{\epsilon_n \phi_n A}{E_n} \Delta E$$

$$C_i - C_{i+1} = \frac{\epsilon_n \phi_n A}{E_n} \Delta E$$

or

$$\phi_n = \frac{C_i - C_{i+1}}{\Delta E} \frac{E_n}{\epsilon_n A} \quad \longrightarrow \quad (3.14)$$



A more complicated differentiation function is used to get better results on a curve. In this case, the differential is expressed over six adjacent points. The slope of the points - 3 and + 3 is S_3 :

$$S_3 = \frac{C_{i-3} - C_{i+3}}{5 \Delta E} \quad \longrightarrow \quad (3.15)$$

For the points -2 , +2 the slope is :

$$S_2 = \frac{C_{i-2} - C_{i+2}}{3 \Delta E} \quad \longrightarrow \quad (3.16)$$

The weighted average slope of the curve is :

$$\begin{aligned} \bar{S} &= \frac{1}{8} (5 S_3 + 3 S_2) \\ &= \frac{C_{i-3} + C_{i-2} - C_{i+2} - C_{i+3}}{8 \Delta E} \quad \longrightarrow (3.17) \end{aligned}$$

The NSPEC programme, using equation (3.17), is used to obtain a neutron spectrum .

Equation (3.13) does not include the shape correction factor. However, to use this equation, the shape correction factor (B) must be included in order to get the following final form :

$$\Phi_n (E) = \phi_n / \Delta E = \frac{E_n}{\epsilon_n A B} \frac{dN_p}{dE} \frac{1}{\Delta E} \quad \longrightarrow (3.18)$$

Which is modified to :

$$\Phi_n (E) = \Psi_n \frac{C_{n-3} + C_{n-2} - C_{n+2} - C_{n+3}}{8 \Delta E^2} \quad \longrightarrow (3.19)$$

With

$$\Psi_n = \frac{E_n}{\epsilon_n A B} \quad \longrightarrow (3.20)$$

Where Ψ_n is the spectrum conversion factor.

The Ψ_n values were calculated using equation (3.20) and listed in table (3.2).

Table (3.2) PSI Values Used In "NSPEC" Programme

E_n (MeV)	PSI						
0.8	0.105	1.0	0.143	1.2	0.184	1.4	0.225
1.6	0.271	1.8	0.318	2.0	0.370	2.2	0.425
2.4	0.482	2.6	0.545	2.8	0.640	3.0	0.662
3.2	0.681	3.4	0.895	3.6	0.970	3.8	1.018
4.0	1.082	4.2	1.209	4.4	1.264	4.6	1.345
4.8	1.433	5.0	1.522	5.2	1.608	5.4	1.707
5.6	1.798	5.8	1.907	6.0	2.023	6.2	2.150
6.4	2.464	6.6	2.346	6.8	2.463	7.0	2.572
7.2	2.709	7.4	2.913	7.6	3.217	7.8	3.444
8.0	3.579	8.2	3.675	8.4	3.741	8.6	3.847
8.8	4.007	9.0	4.185	9.2	4.420	9.4	4.566
9.6	4.731	9.8	4.916	10.0	5.087	10.2	5.280
10.4	5.498	10.6	5.722	10.8	5.996	11.0	6.234
11.2	6.511	11.4	6.746	11.6	6.998	11.8	7.234
12.0	7.430	12.2	7.674	12.4	7.893	12.6	8.127
12.8	8.402	13.0	8.632	13.2	8.898	13.4	9.175
13.6	9.458	13.8	9.754	14.0	10.048	14.2	10.301
14.4	10.590	14.6	10.882	14.8	11.180	15.0	11.483
15.2	11.799	15.4	12.130	15.6	12.467	15.8	12.829

To check the proper functioning of the liquid scintillation spectrometer as well as the computer programme for unfolding of the proton energy spectrum, a neutron spectrum of an Am - Be neutron source of neutron emission 2.5×10^6 n/s was measured. The source is supplied by Amersham International, U.K. The result showed an agreement with the measurements of Lorch⁽¹⁴⁴⁾ and Chuang et al.⁽¹⁴⁵⁾ as shown in figure (3.12). The slight difference in the intensities at the observed peaks can be attributed to the different compositions of the sources in the given cases.

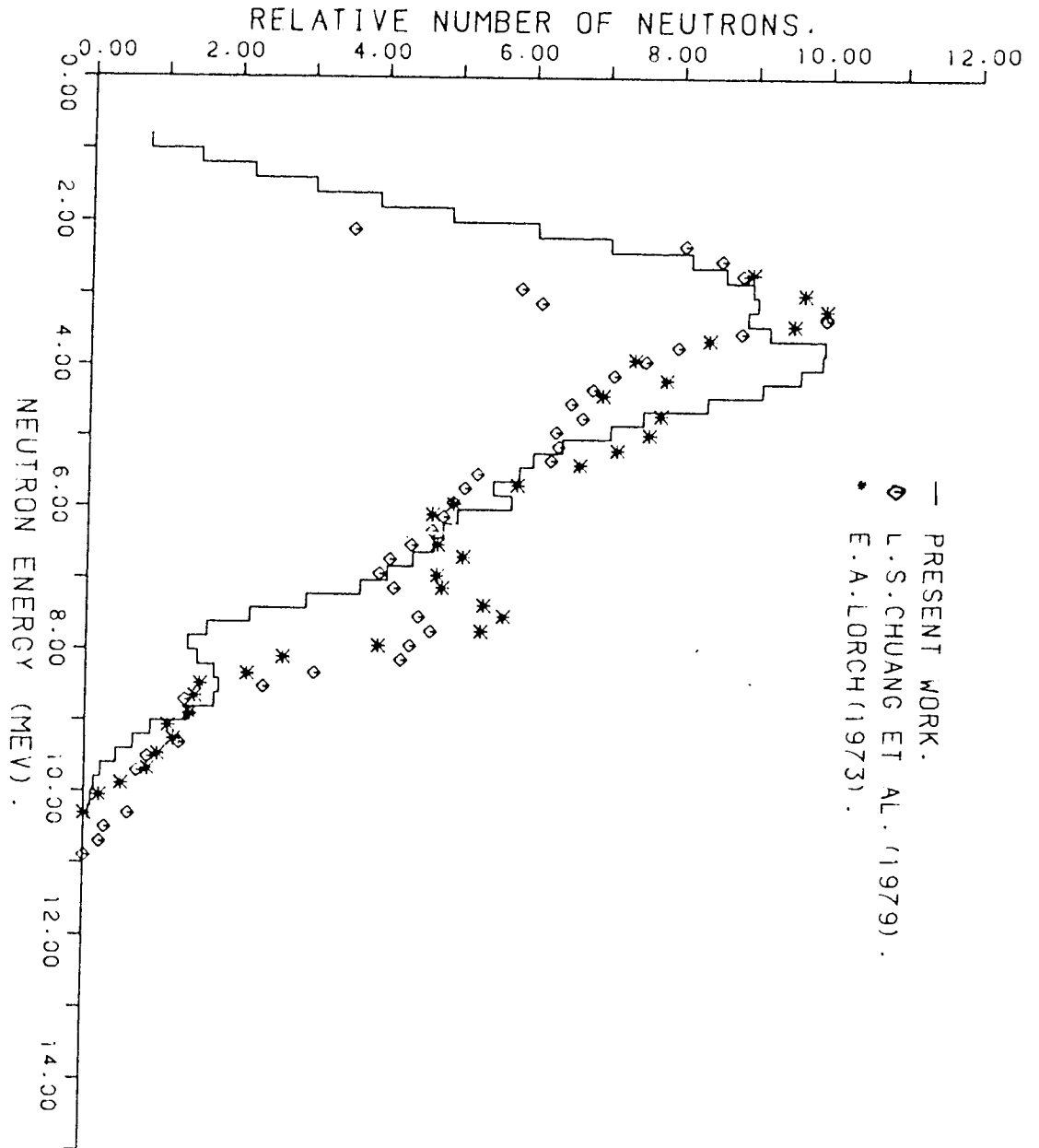


FIG. 3.12 AM-BE NEUTRON SPECTRUM.

CHAPTER 4

NEUTRON PRODUCTION AND MONITORING

4.1 Introduction

Neutrons were produced from the $T(d,n)^4\text{He}$ reaction. With a deuteron beam of energy 130 KeV incident on the tritium target, neutrons of 14.1 MeV can be obtained at an angle of 90° to the beam.

The intensity of the neutron source was monitored by detecting alpha particles associated with neutrons by a silicon surface barrier detector.

4.2 Neutron Production

The 14.1 MeV neutron source was obtained from $T(d,n)^4\text{He}$ reaction by the bombardment of tritium - titanium target with a deuteron beam of energy 130 KeV, using a SAMES type J accelerator. The accelerating voltage is produced by an electrostatic generator which is housed in hermetically sealed unit in a hydrogen atmosphere. The generator can deliver 2 milliampere at + 150 KV with a stability of $\pm 1\%$ (146)

4.2.1 The Target

The tritium target used in this work was the type TRT51 manufactured by Amersham International U.K. It has a copper backing disk of 2.86 cm diameter and 0.025 cm thickness, a very thin evaporated layer of titanium in which the tritium is absorbed of 2.54 cm diameter and

1.09 mg/cm² thickness⁽¹⁴⁷⁾. A stainless steel diaphragm covers the target and exposes a 5 mm diameter area to approximate a point source. Only a small part of the target is struck at any one time by the deuteron beam, and the target can be rotated to expose new areas to the deuterons.

4.2.2 The T(d,n)⁴He Kinematics

The T(d,n)⁴He reaction has a Q - value of 17.59 MeV. This high Q - value and its resonance at 110 keV with a peak cross section of more than 5 barns [figure (4.1)], allows the production of high flux of fast neutrons even with low energy accelerators. The reactions T(d,np)T and T(d,2n)³He become energetically possible above a deuteron energy of 3.7 and 5.0 MeV respectively⁽¹⁴⁸⁾.

By using the laws of conservation of energy and momentum, it is possible to compare the energy and the angle of emitted particles in the T(d,n)⁴He reaction. This reaction produces a neutron (of mass m_n) and alpha particles (of mass m_α), when a deuteron (of mass m_d and energy E_d) is incident on the triton (of mass m_t). The expression for the neutron energy (E_n) in the laboratory system is given by :

$$E_n = \frac{m_d m_n}{(m_d + m_t)^2} E_d \cos^2 \phi + \frac{m_\alpha [\mu E_d + Q]}{(m_\alpha + m_n)} \pm \frac{2 \sqrt{m_d m_n}}{(m_d + m_t)} \cos \phi$$

$$\times \sqrt{\frac{m_\alpha E_d [\mu E_d + Q]}{(m_\alpha + m_n)} - \frac{m_d m_n}{(m_d + m_t)^2} E_d^2 \sin^2 \phi} \quad \text{--- (4.1)}$$

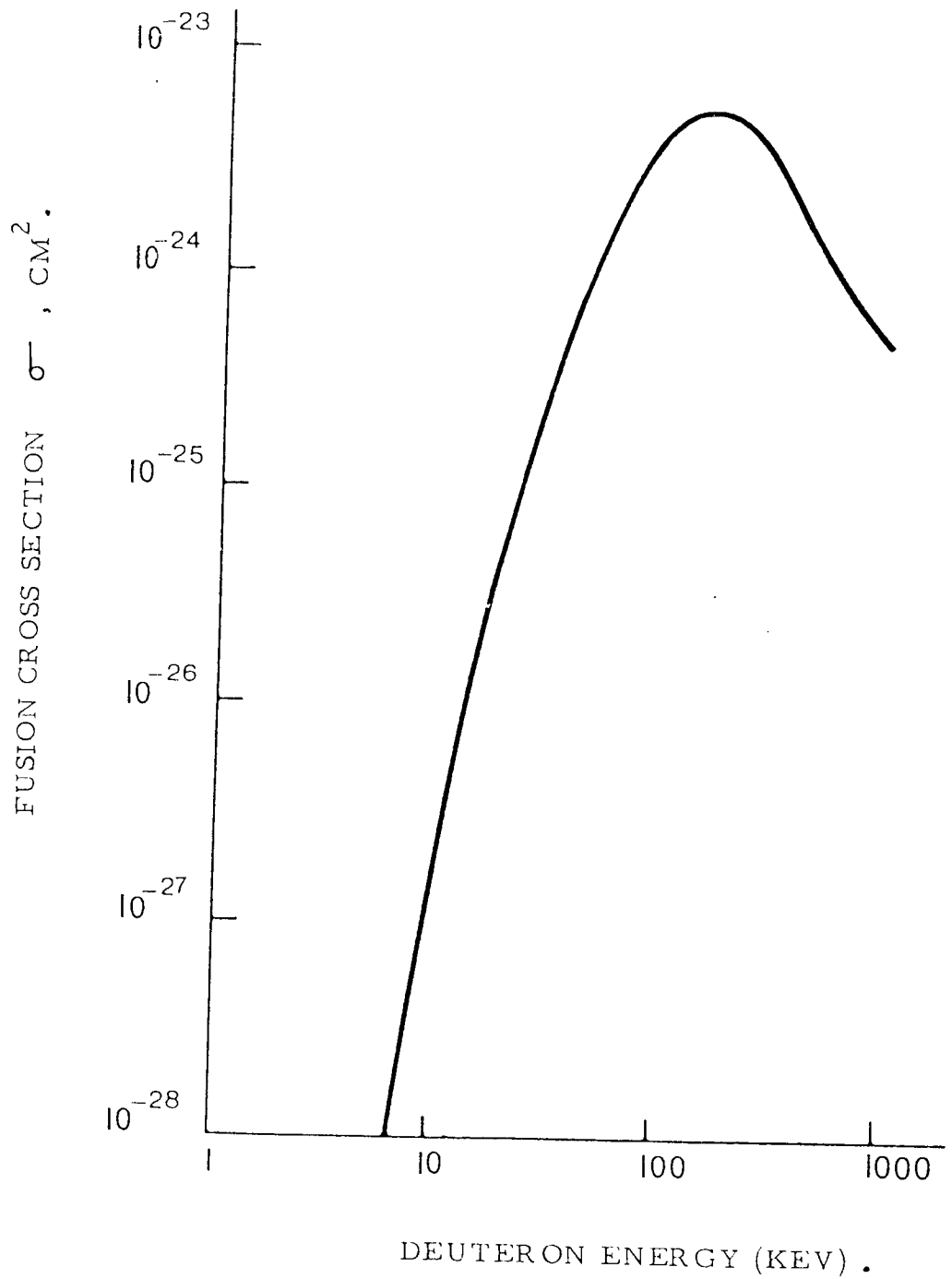


FIG. 4.1 THE TOTAL CROSS SECTION FOR D-T REACTION .

Where ϕ is the angle with respect to incident beam in laboratory system.

$$\mu = m_t / (m_t + m_d)$$

To get the alpha particle energy (E_α) for various deuteron energies as a function of neutron angle in laboratory system, interchange m_n and m_α in equation (4.1).

The total neutron yield per detected alpha particle can be calculated by^(149,150).

$$N = \frac{4\pi}{\Delta\Omega_\alpha} \frac{\int_0^{E_d} \frac{\sigma_{cm}(\theta, E)}{dE/dx} dE}{\int_0^{E_d} \frac{\sigma_{cm}(\theta, E)}{dE/dx} \frac{d\omega_{cm}}{d\omega_{lab}} dE}$$

$$= \frac{4\pi}{\Delta\Omega_\alpha} \cdot R_\alpha \quad \longrightarrow \quad (4.2)$$

Where $\Delta\Omega_\alpha$ is the solid angle subtended by the alpha detector

$\sigma_{cm}(\theta, E)$ is the differential cross section for the D - T reaction in the center of mass system.

dE/dx is the rate of energy loss of deuterons in the target material.

$d\omega_{cm}/d\omega_{lab}$ is the solid angle conversion factor from the centre

of mass system to the laboratory system for the detected alpha particles.

R_α is the anisotropy factor.

Implicit in the derivation of this expression are the following assumptions :

- 1- The reaction products are isotropically distributed in the centre of mass system for the incident deuteron energies below 200 KeV⁽¹⁵¹⁾.
- 2- dE/dx is fairly well known in the region $0 < E < E_d$.
- 3- Uniform loading of tritium atoms to a depth at least equal to the range of incident deuterons.
- 4- No scattering of incident deuterons.

The kinematics details, tables and figures of energies of the reaction products, and the equations for converting from one system of coordinates to the other are given in several works⁽¹⁵⁰⁻¹⁵⁵⁾.

4.3 The Alpha Particle Detector

In using the $T(d,n)^4He$ reaction as a source of monoenergetic neutrons, the neutron flux is often determined by counting the associated alpha particle⁽¹⁵⁶⁻¹⁵⁸⁾ Several investigators have pointed out potential problems with this procedure due to charged particles from



other reactions⁽¹⁵⁹⁻¹⁶²⁾. When a titanium tritide target is so employed, it must expect build up of deuterium from ion bombardment and ^3He from tritium beta decay. Reactions produced by the deuteron bombardment of such a target include $\text{T}(d,n) ^4\text{He}$, $\text{D}(d,p) ^3\text{H}$, $^3\text{He}(d,p) ^4\text{He}$ and $\text{D}(d,n) ^3\text{He}$. The aim of this work has been to make an accurate count of the alpha particles associated with the first reaction using a silicon surface barrier detector.

4.3.1 The Associated Particle Technique

The associated particle technique has been used for neutron flux measurements for many years, being already well established by Barschall et al⁽¹⁶³⁾. The principle of the technique is that for certain neutron producing reactions there is a one for one relation between the emitted neutron and a recoiling charged particle reaction product, with the directions of emission related by simple kinematic considerations. The most important of these reactions are, $\text{T}(p,n) ^3\text{He}$, $\text{D}(d,n) ^3\text{He}$ and $\text{T}(d,n) ^4\text{He}$. Since the charged reaction product, ^4He or ^3He , can be measured with virtually 100 % efficiency over a well defined solid angle, the number of associated neutrons is known. The main advantage in this method is, since the alpha particle and neutron are not ejected at the same angle in space, the neutron flux can be continuously measured while the experiments is in progress⁽¹⁰¹⁾.

4.3.2 The 14.1 MeV Neutron Yield

An absolute determination of the total 14.1 MeV neutron yield can be achieved by monitoring the associated alpha particles. This method

required one to determine the number of alpha particles emitted into a well - defined solid angle and then multiply these numbers by a factor N [Equation (4.2)], which is defined as the number of neutrons produced in the target per alpha particles passing through the detector. From equation (4.2) it can be seen that, when one multiplies R_{α} by the experimentally determined alpha counts, C_{α} , the result represent the number of alpha particles that would have passed through the same solid angle in the centre of mass system. It can be shown that, $(4\pi / \Delta\Omega_{\alpha})$ is simply a geometry factor (G), which represents the ratio of the total number of particles emitted to the number of particles passing through the solid angle subtended by the detector operation. Thus the total number of alpha particles produced, Y_{α} , can be obtained from ;

$$\begin{aligned}
 Y_{\alpha} &= C_{\alpha} R_{\alpha} (4\pi / \Delta\Omega_{\alpha}) \\
 &= C_{\alpha} N \qquad \qquad \qquad \longrightarrow (4.3)
 \end{aligned}$$

Also

$$Y_n = Y_{\alpha} = C_{\alpha} (G) R_{\alpha} \qquad \qquad \qquad \longrightarrow (4.4)$$

Where Y_n represents the total neutron yield.

The value of R_{α} will be altered if deuterons are scattered before interacting with tritium. This error is very difficult to estimate, but it would be minimized for the 90° alpha detector location. This small error will be ignored at low accelerating potentials. A complete analysis of the total creditable cumulative error made by Fewell⁽¹⁵⁴⁾.

The R_{α} value used for the 90° alpha detector position is 1. The 90° detector is almost insensitive to both deuteron beam and Ti-T target

conditions. The 90° detector yields very good accuracy in all cases where geometry considerations are negligible. Therefore, in this work, the 90° detector location was chosen. In this case, equation (4.4) gives:

$$\begin{aligned} Y_n &= C_\alpha G \\ &= C_\alpha (4 \pi / \Delta \Omega_\alpha) \\ &= C_\alpha [16 R^2 / D^2] \end{aligned} \quad \longrightarrow (4.5)$$

Where $\Delta \Omega_\alpha$ is the solid angle subtended by the detector of a diameter D at a distance R from the source.

The value of the geometry factor, G, was calculated to be 1.482×10^5 . The value was used in the computer programme NSPEC (Appendix 1) written for analysis of the data to normalize all the measurements to the same source strength.

Benveniste and Zenger^(149,150) have discussed the effect on calculated total alpha particle yield of anisotropy in the centre of mass differential cross section for T - D reaction, of uncertainties in dE/dx at low energies and of deuteron scattering in the target. These effects are generally $\ll 1\%$, the error in the neutron yield being minimised for an alpha detector at 90° to the deuteron beam. They conclude that non - uniformity of tritium loading in the target contributes the most serious error to the computed yield. Ruby and Crawford⁽¹⁵⁶⁾ have extended the calculation of Benveniste and Zenger to cover a wide range of deuteron energy and angle of associated particle.

Some work reported by Gunnerson and James⁽¹⁵⁷⁾ presents evidence suggesting that in the case of a typical Ti-T target there is invariably a surface layer depleted in tritium and a fall off in density towards the back of the titanium layer. Variations of this kind in the loading factor could effect the computed neutron yield by as much as 2 % depending on the alpha particle angle and the incident deuteron energy. Fieldhouse⁽¹⁶⁴⁾ has discussed a technique for measuring this effect.

However, there is another source of error in this type of measurement. The tritium being radioactive, decay by beta - emission to ^3He . A one year old tritium target thus has approximately 6 % ^3He content with the result that there is a background in the alpha particle detector from the reaction $^3\text{He} (d,p) ^4\text{He}$. The alpha particles from this reaction have approximately the same energy as those from the $\text{T} (d,n) ^4\text{He}$ reaction. The error caused by the contribution of the $^3\text{He} (d,p) ^4\text{He}$ reaction is minimized by using a new target and with a deuteron energy close to the resonance region of the tritium reaction⁽¹⁵⁹⁾.

In addition, the influence of protons from the $\text{D} (d,p) \text{T}$ reaction as a result of deuteron build up in the target must be taken into account⁽¹⁶⁰⁾. By using a single channel analyser with upper and lower level such contribution, if any, can be discriminated⁽¹⁶¹⁾. Also a very thin foil of aluminium (0.0015 mm) was used to cut out light and to prevent both the beta - particles and scattered deuterons from reaching the detector, but not the alpha particles⁽¹⁶⁵⁾. The range of 3.5 MeV alpha particles in aluminium is 4.5 mg/cm^2 , i.e., 0.016 mm.

Finally, under positively charged deuteron bombardment, electrons are ejected from the target assembly. To prevent these electrons back streaming to the accelerator, a suppressor electrode was inserted between the target and the beam tube and this was maintained at about - 150 volts, thus reflecting the secondary electron back to the target.

4.3.3 The Silicon Surface Barrier Detector

The silicon surface barrier detector used has a sensitive surface evaporated with a thin layer of gold. The circular silicon wafer is mounted in an insulating ring whose back and front surface are metallized. The front surface of this ring is grounded to a metal case, and thereby to a connector. The back surface is connected to the centre electrode of the connector which is supplied with positive potential bias (18 volts) and gives a negative output signal.

When a charged particle passes through the field region, it creates electrons and holes which are swept apart by the strong electric field in the silicon. The motion of these charge carriers induces a sudden change in voltage between the front and back electrodes. The size of this voltage change is given approximately by :

$$\Delta V = k \left(E_L / A_C \right) \left(V_a \right)^{1/2} \quad \longrightarrow \quad (4.6)$$

Where ΔV is the voltage change, in mV.

k is a constant for particular detector.

E_L is the energy lost by particle in barrier region, in MeV.

A_c is the active counting area, in cm^2 .

V_a is the applied bias voltage, in volts.

Hence the pulse size is related to bias voltage if the detector is used with a voltage sensitive amplifier. A charge sensitive amplifier is more usually used and this eliminates the effect of detector bias voltage and cable capacitance.

The depth of the depletion region, in cm, is given by

$$D = L (V_a)^{1/2} \longrightarrow (4.7)$$

Where L is a constant for the particular material.

The depth of sensitive region is D plus an additive constant involving the diffusion rate of the charge carriers and the clipping time in the pulse amplifier.

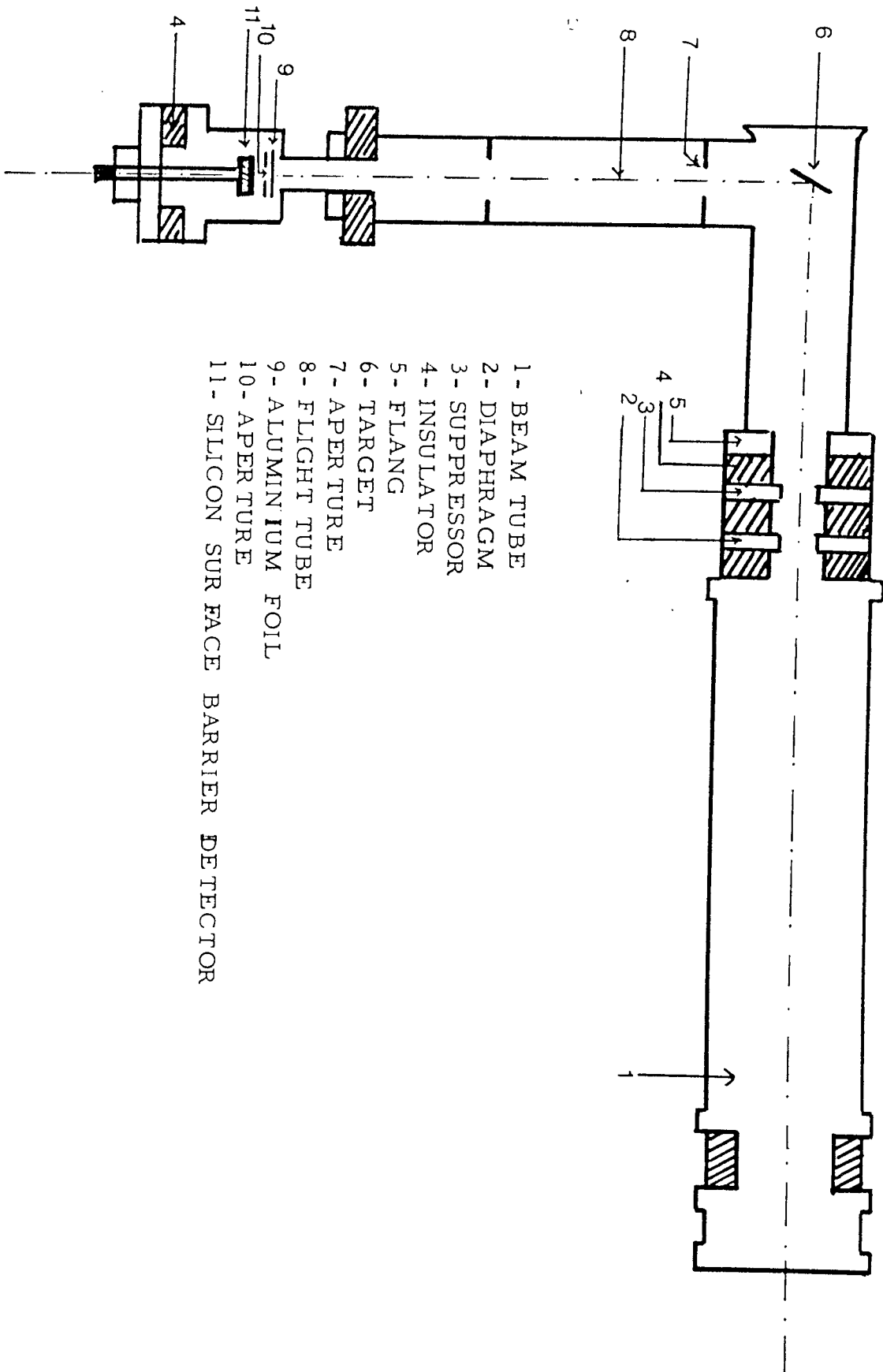
The characteristics of this counter can be varied by choice of basic starting material and the applied bias. An alpha particle or fission fragment detector which is very insensitive to gamma rays and neutrons, can be made by producing a barrier whose depth just exceeds the range of the particle of interest. A detector with a large fission fragment to alpha particle pulse height ratio, can be obtained by making the barrier depth less than the alpha particle range.

The main characteristics of this type of detector are :

- 1- It has 100 % detection efficiency for alpha particles for any case where the energy lost in the sensitive region is much larger than the noise level⁽¹⁶⁶⁾.
- 2- It has low sensitivity to background gamma rays and neutrons⁽¹⁶⁷⁾.
- 3- It has linearity over a wide energy range and is not affected by magnetic fields.
- 4- It has very good energy resolution, good stability and freedom from drift, excellent timing characteristics, very thin entrance window, and simplicity of operation⁽¹⁶⁸⁾.
- 5- It has a fast response time.
- 6- It is compact, light and has low voltage operation, low power consumption and reliability⁽¹⁶⁸⁾.

The silicon surface barrier detector used was placed at the end of a flight tube at a distance 38.5 cm from the target and was covered by a diaphragm with an aperture of 4 mm diameter. The target was inclined at 45° to the direction of both the incident deuteron beam and the axis of the flight tube [figure (4.2)].

A block diagram of the electronics used for detecting and counting the alpha particles is shown in figure (4.3). The output pulses from the detector are applied to a charge sensitive preamplifier. The output



- 1 - BEAM TUBE
- 2 - DIAPHRAGM
- 3 - SUPPRESSOR
- 4 - INSULATOR
- 5 - FLANG
- 6 - TARGET
- 7 - APERTURE
- 8 - FLIGHT TUBE
- 9 - ALUMINIUM FOIL
- 10 - APERTURE
- 11 - SILICON SURFACE BARRIER DETECTOR

FIG. 4.2 THE BEAM TUBE AND THE ALPHA - PARTICLE FLIGHT TUBE

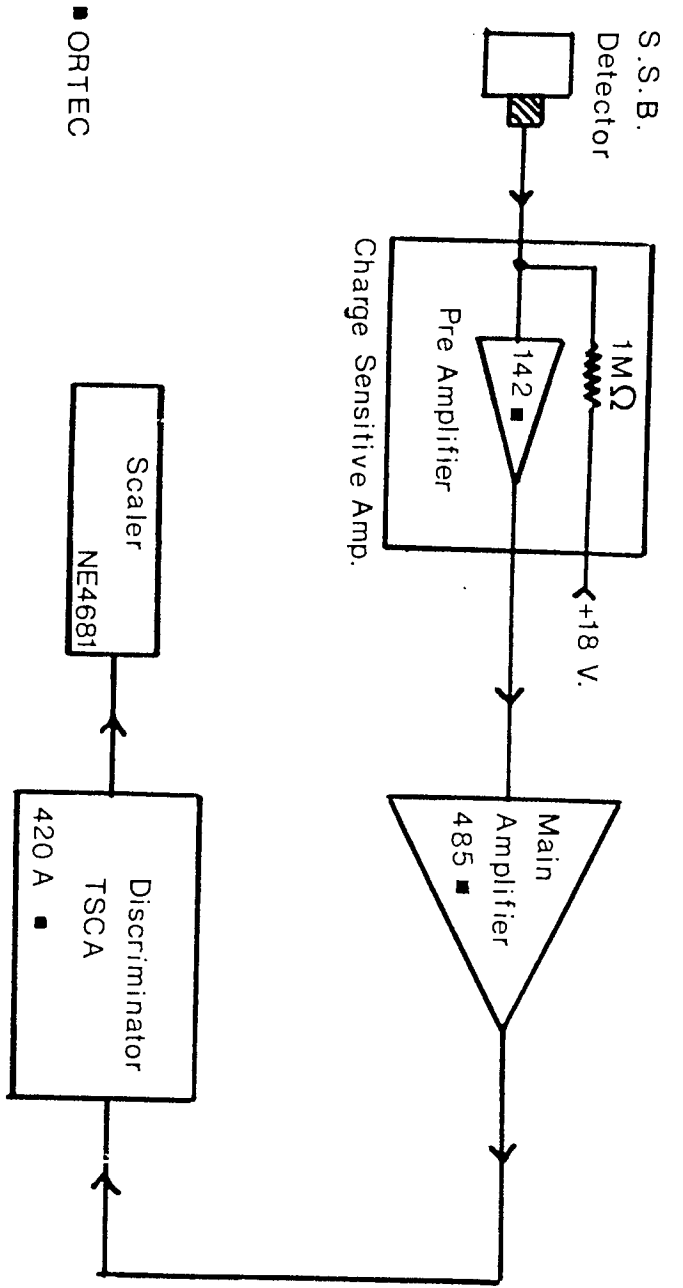


FIG. 4.3 THE CIRCUIT OF ALPHA - PARTICLE DETECTOR .

pulses are fed to a main amplifier, type Ortec - 485 . After amplification the signals are passed through a timing single channel analyser, Ortec - 420A used as a simple discriminator to get only the associated alpha particles from T (d,n)⁴He reaction, then to a scaler (NE - 4681). Figure (4.4) shows the associated particle spectrum obtained at a deuteron energy of 130 keV .

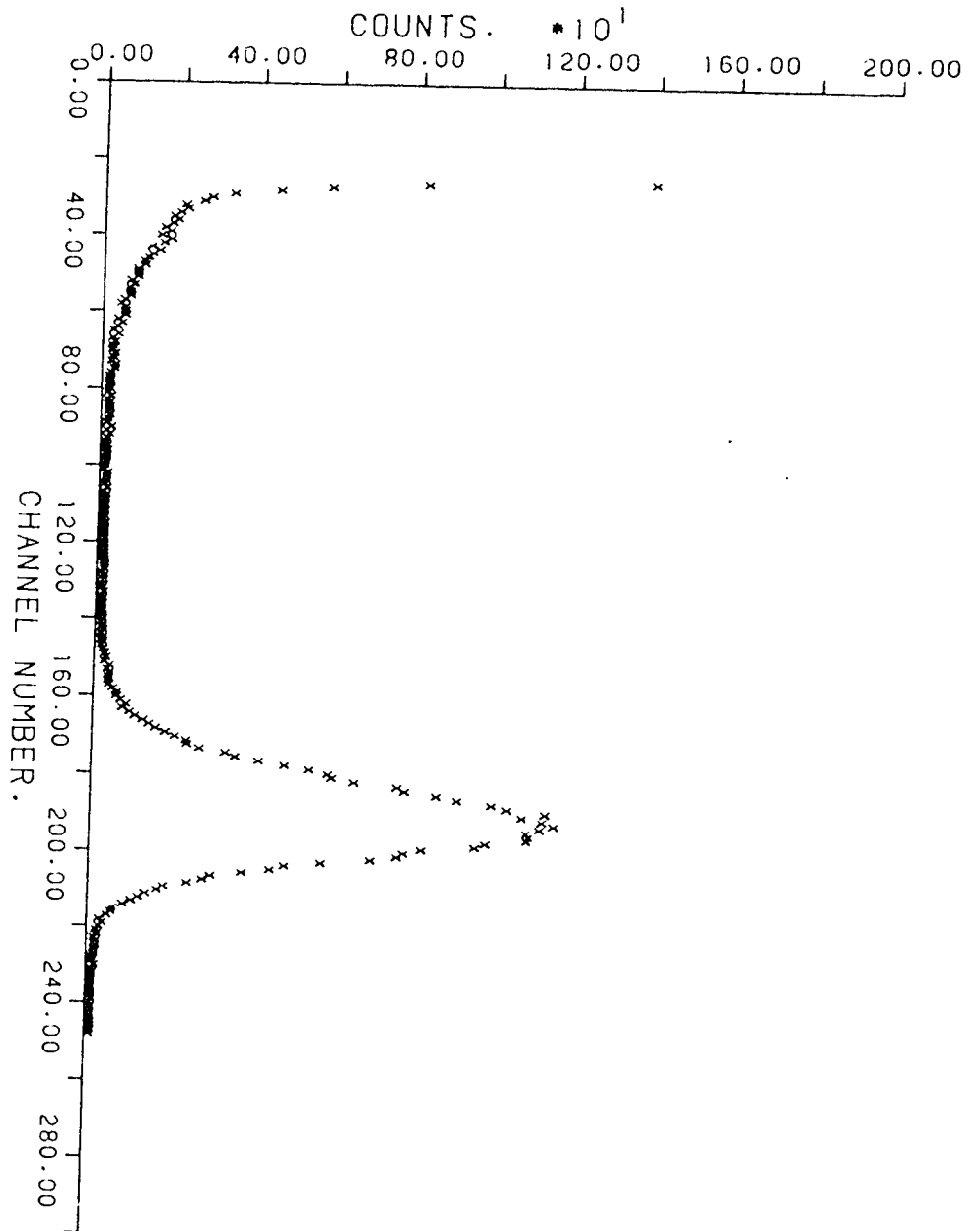


FIG. 4.4 ALPHA PARTICLE SPECTRUM FROM $D(T,n)^4\text{He}$ REACTION USING A SILICON SURFACE BARRIER DETECTOR.

CHAPTER 5
CALCULATION METHODS

5.1 Introduction

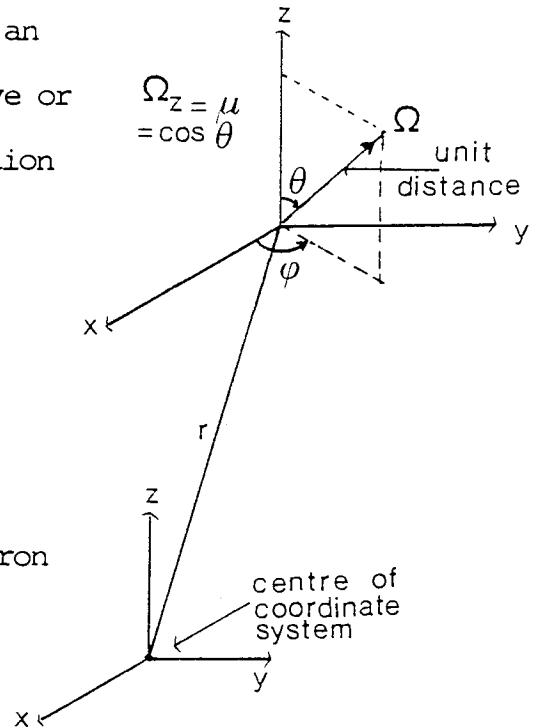
Neutrons move about in a reactor or in reactor shields in complicated, zigzag path due to repeated collisions with nuclei. Therefore, neutrons that were originally in one part of a reactor and moving in a particular direction with a particular energy appear at a later time in another part of the system, moving in another direction with some other energy. The neutrons in this case are said to have been transported from the first region and energy to the second, and the study of this phenomenon is known as transport theory⁽¹⁰⁹⁾.

In shielding studies, it is required to solve the appropriate form of the transport equation, which is applicable to both neutrons and gamma rays in order to determine the distribution of the particles (neutrons and photons) in energy and space.

The purpose of this chapter is to derive the transport equation and then show some approximations to it for some cases of interest in shielding studies. For calculation purpose the ANISN one dimensional transport theory code was chosen. The results obtained by ANISN code were smoothed by a computer programme based on Gaussian smoothing function for comparison with the experimental data. The derivation of this equation is described.

5.2 Derivation Of The Neutron Transport Equation

A neutron balance is made for neutrons in a given volume element having a specified angular direction vector, Ω , and lethargy, U , at a given time, t . The time rate of change for neutrons having the above specifications arises from an accumulation (or depletion) due to convective or flow changes, loss by scattering and absorption collisions, input from other appropriate scattering collisions, and generation from a source.



The time rate of change of the neutrons in a volume element which move with the neutron stream in the direction $d\Omega$ at Ω in a lethargy interval dU at U at time t is :

$$\left[\frac{\partial N (r, \Omega, U, t)}{\partial t} + v \Omega \cdot \nabla N (r, \Omega, U, t) \right] d\Omega dU$$

→ (a)

Where $v\Omega$ is the vector velocity (v is the scalar speed),

$N (r, \Omega, U, t)$ is the angular density at position r and time t per unit lethargy per unit solid angle.

The first term is the time rate of the change at a given position, and the second term is the net convective loss.

Losses by absorption and scattering of the specified neutrons per unit volume per unit time are given by the product of the angular neutron flux Φ , i.e., $\nu N (r, \Omega, U, t)$, and total macroscopic absorption and scattering cross section for neutrons of lethargy U , $\Sigma(U)$:

$$\nu N (r, \Omega, U, t) \Sigma(U) \longrightarrow (b)$$

Neutrons from different angular directions and from higher speeds at the position, r , may scatter into the appropriate direction and lethargy. Consider another set of neutrons at the same field point, r , and at the same time, t , whose velocity is determined by the parameters Ω^* and U^* , and call this set $N (r, \Omega^*, U^*, t)$. The number of scattering collisions with this set is ;

$$[\nu^* N (r, \Omega^*, U^*, t) \Sigma_s (U^*)] d\Omega^* dU^*$$

Where $\Sigma_s (U^*)$ is the macroscopic scattering cross section at a lethargy, U^* , and ν^* is the corresponding neutron speed.

Let $F d\Omega dU$ represent the probability that a neutron scattered from dU^* at U^* and $d\Omega^*$ at Ω^* will end up in dU at U and $d\Omega$ at Ω . Only elastic scattering is considered.

$$\text{The product of } \Omega^* \cdot \Omega = \cos \theta = \mu_0$$

Where μ_0 is the cosine of the scattering angle, and Ω^* represents the direction before collision and Ω after collision. The scattering function, F , is dependent upon the lethargy change, $U - U^*$, and as a consequence of assumptions of an isotropic and homogenous medium, is dependent on μ_0 . The total number of neutrons scattered at point r and time t from all other possible energies and directions to the lethargy, U , and angular direction, Ω , is :

$$\int_0^U dU^* \int d\Omega^* \int v^* N(r, \Omega^*, U^*, t) \Sigma_s(U^*) F(\mu_0, U - U^*) d\Omega^* \longrightarrow (c)$$

If an isotropic source term is included, this designation is used :

$$S(r, U, t) \longrightarrow (d)$$

Here the implications are that the source is instantaneous and monoergic

The total time rate of change of N is equal to the loss by absorption and scattering plus the source generation and plus the influx of scattered neutrons. Using definitions a, b, c and d, and to simplify the representation put $S(r, \Omega, t) = S$, $N = N(r, \Omega, U, t)$, $N^* = N(r, \Omega^*, U^*, t)$ and $F(\mu_0, U - U^*) = F$, the time dependent transport equation is :

$$\begin{aligned} \frac{\partial N}{\partial t} + \frac{v}{U} \Omega \cdot \nabla N + v N \Sigma(U) \\ = \int_0^U dU^* \int d\Omega^* v^* N^* \Sigma_s(U^*) F + S \longrightarrow (5.1) \end{aligned}$$

Equation (5.1) may also be expressed in terms of the angular flux Φ and energy E, thus ;

$$\frac{1}{v} \frac{\partial \Phi}{\partial t} + \Omega \cdot \nabla \Phi + \Sigma \Phi = \iint \Sigma_s F \Phi^* d\Omega^* dE^* + S \quad (5.2)$$

Equations (5.1) and (5.2) represent the basic transport equations. Differential equations of this type containing the function desired in an integral term are called integro - differential equations.

The integro - differential equation for monoergic neutrons is written as :

$$\frac{\partial N}{\partial t} (r, \Omega, t) + v \Omega \cdot \nabla N(r, \Omega, t) + v N(r, \Omega, t) \Sigma = \int v N(r, \Omega^*, t) d\Omega^* \Sigma_s F(\mu_0) + S(r, \Omega, t) \quad (5.3)$$

Where $F(\mu_0)$ is the scattering function for the monoenergetic neutrons.

Solutions for this equation are considered for the following conditions :

- a - Steady state, i.e, $\partial N / \partial t = 0$
- b - Plane symmetry (one - dimensional, movement in z - direction)
- c - Isotropic source .

The gradient of $N(z, \mu)$ for the one - dimensional case is ;
 $[\partial N(z, \mu) / \partial z] k$, where k is a unit vector in the z -
direction. Further, the velocity , v , reduces to $v \Omega_z k$ or
 $v \mu k$. With these relations, $v \Omega \cdot \nabla N(z, \mu)$ is written as :

$$v \mu \frac{\partial N(z, \mu)}{\partial z} k \cdot k = v \mu \frac{\partial N(z, \mu)}{\partial z} \quad \text{---} \quad (e)$$

Conditions a, b, c, d and equation e lead equation (5.3) to the one
- velocity equation as :

$$v \mu \frac{\partial N(z, \mu)}{\partial z} = - N(z, \mu) v \Sigma + \int N(z, \mu^*) v \Sigma_s F(\mu_0) d\Omega^* + S(z) \quad \text{---} \quad (5.4)$$

In the notation used, μ is the cosine of the angle formed by the
direction of the neutron and the z - axis, whereas μ_0 is the cosine of
the scattering angle for a neutron with any initial direction , Ω^* ,
before collision and direction Ω after collision. It may be shown
that ;

$$\mu_0 = \mu \mu^* + \sqrt{1 - \mu^2} \sqrt{1 - \mu^{*2}} \cos(\varphi - \varphi^*)$$

5.3 Approximation Solutions To The Transport Equation

The method to obtain an approximate solution of the transport
equation involves the assumption that the scattering function, $F(\mu_0)$,
and the angular neutron density, $N(z, \mu)$, can be expressed in a
series of spherical harmonics, separating the spatial and angular
dependencies. This approach is given below.

5.3.1 Spherical Harmonics

If a function satisfies the Laplace equation $\frac{\partial^2 f}{\partial x^2} + \frac{\partial^2 f}{\partial y^2} + \frac{\partial^2 f}{\partial z^2} = 0$, its first derivatives are continuous in a region R, and satisfy the conditions on the boundary of R, the function is said to be harmonic with R. A harmonic function is called a "spherical solid harmonic" if it satisfies Euler's theorem on homogenous functions $x (\partial f / \partial x) + y (\partial f / \partial y) + z (\partial f / \partial z) = \nu f$. The degree of homogeneity is expressed by ν . A property of the harmonic utilized is the relation that⁽¹⁶⁹⁾:

$$\int P_l(\mu) d\Omega \int N(z, \mu^*) F(\mu_0) d\Omega^* = F_l N_l(z)$$

For the case of a plane symmetry or a spherically symmetrical distribution, only one angle need be specified to indicate the direction. Thus for these conditions, the expansion in terms of the zonal spherical harmonics results in the use of the Legendre polynomials. For more complex geometry where two angles are needed to characterize the direction, the general form of spherical harmonic expansion is utilized.

The following expansions are assumed for $F(\mu_0)$ and $N(z, \mu)$:

$$F(\mu_0) = \sum_{l=0}^{\infty} [(2l+1)/4\pi] F_l P_l(\mu_0) \quad \text{---} (5.5)$$

$$N(z, \mu) = \sum_{l=0}^{\infty} [(2l+1)/4\pi] N_l(z) P_l(\mu) \quad \text{---} (5.6)$$

Where

$$F_l = \int F(\mu_0) P_l(\mu_0) d\Omega_0$$

$$N_l = \int N(z, \mu) P_l(\mu) d\Omega$$

If the angular distribution of neutrons is not highly anisotropic, or at least, if the very anisotropic portions constitute only a very small part of the region to be considered, only the first few terms of the Legendre polynomials are required for a good approximation. As more terms are obtained, the accuracy of the result would be expected to improve.

5.3.2 P₁ Approximation

The diffusion theory is derived by retaining only two terms. What is implied is that a "minimum" of anisotropy is assumed, for otherwise no neutron current would result. The limiting conditions for diffusion theory implied that⁽¹⁷⁰⁾:

- 1- The region considered is far from source, sinks, or boundaries (in terms of mean free path, λ)
- 2- The properties of the medium do not change appreciably within a distance comparable to a mean free path.
- 3- The probability of capture is small compared to scattering .

The transport solution would be expected to hold rigorously if these conditions are fulfilled .

The P₁ approximation retains the terms for $l = 0$ and $l = 1$ and neglects all others. The two P₁ equations for one dimensional transport equation are :

$$\nu \frac{dN_1(z)}{dz} = -\nu \Sigma N_0(z) + \nu \Sigma_s N_0(z) + S_0(z) \quad \text{---} (5.7)$$

$$\nu \frac{dN_0(z)}{3 dz} = -\nu \Sigma N_1(z) + \nu \Sigma_s F_1 N_1(z) \quad \text{---} (5.8)$$

Where $N_0(z) = 2\pi \int_{-1}^{+1} N(z, \mu) d\mu$, i.e, the neutron density .

$$N_1(z) = \int \mu N(z, \mu) d\Omega$$

$$F_1 = \int \mu_0 F(\mu_0) d\Omega_0 = \bar{\mu}_0 = \overline{\cos\theta}$$

Equation (5.7) is derived by integrating equation (5.4) over all values for $d\Omega$. The second equation (5.8) is obtained by multiplying equation (5.4) through by μ and integrating the transport equation once again over all values for $d\Omega$.

A simplification made in equation (5.8) is $\Sigma = \Sigma_s$, and by differentiating it with respect to z , N_1 is eliminated :

$$\frac{\nu d^2 N_0(z)}{3 \Sigma_s dz^2} = -(1 - F_1) \frac{d N_1 \nu}{dz}$$

Substituting in equation (5.7) to eliminate dN_1 / dz , and put the flux

$$\Phi = \nu N_0 \quad , \quad \text{and} \quad \Sigma_a = \Sigma - \Sigma_s ;$$

$$\left(\frac{d^2 \Phi}{dz^2} \right) / [3 \Sigma_s (1 - F_1)] - \Sigma_a \Phi + S_0(z) = 0 \quad \text{---} (5.9)$$

This equation is an approximate solution to the monoergic transport equation, with the additional assumption that the capture is weak, and $\Sigma_s = \Sigma$. Upon comparison with diffusion theory, the important conclusion is that the proper diffusion constant for the elementary diffusion theory is :

$$D = \frac{1}{3 \Sigma_s (1 - F_1)} = \frac{\lambda_s}{3 (1 - \cos \theta)} \longrightarrow (5.10)$$

Where λ_s is the scattering mean free path.

Weinberg and Noderer⁽¹⁷¹⁾ have presented a detailed discussion on the limitations of the solutions to the transport equation.

5.3.3 P_N Approximation

The P₁ approximation leads to the ordinary diffusion theory. The higher the P_N approximation, the better and more accurate results obtained through the use of the higher spherical harmonics. The spherical harmonic method is illustrated for the monoergic Boltzmann equation for the case of plane geometry and isotropic scattering with constant cross sections. Equation (5.4) is rewritten as ;

$$\mu \partial \Phi(z, \mu) / \partial z + \Phi(z, \mu) / \lambda = c / v \int_{-1}^{+1} \Phi(z, \mu^*) d \mu^* + Q / 2$$

Where $\Phi(z, \mu) = v N(z, \mu)$, $\lambda = 1 / \Sigma$, $c = \frac{\Sigma_s}{\Sigma}$,
 $\Sigma = \Sigma_a + \Sigma_s$ and Q is the total source strength, .

Multiply this equation by $(2n + 1) P_n (\mu) d\mu$ and integrate from $\mu = -1$ to $+1$;

$$\begin{aligned} & \frac{(n+1) d \Phi_{n+1}(z)}{d z} + \frac{n d \Phi_{n-1}(z)}{d z} + \frac{(2n+1) \Phi_n(z)}{\lambda} \\ & = \left[\frac{C \Phi_0(z)}{\lambda} + Q \right] \delta_{0,n} \qquad \longrightarrow (5.11) \end{aligned}$$

Where $\delta_{0,n} = 1$ for $n = 0$ and $\delta_{0,n} = 0$ for $n \neq 0$.

The solution to the homogeneous system of equations given by equation (5.11) with $Q = 0$ is of the form ;

$$\Phi_n(z) = g_n \exp(\nu z/\lambda) \qquad \longrightarrow (5.12)$$

If the first four equations are retained in the set given by equation (5.11), and the term involving $\Phi_4(z)$ is neglected, the solution obtained is called the P_3 approximation. Just the odd - numbered approximations are used, for they yield more reliable results than the even - numbered ones from the stand point of correctly presenting the oscillatory nature of the angular neutron density, and in the determination of the boundary conditions at an interface⁽¹⁷²⁾. The first $N+1$ equations contain $N+1$ unknowns, namely $\Phi_0, \Phi_1, \Phi_2, \dots, \Phi_n$, where $n = 0, 1, 2, \dots, N$, and are used to determine the P_N approximation.

5.3.4 Numerical Methods

Many of the diffusion problems met in practice cannot be solved by the analytical techniques discussed above. The problems must be handled by numerical methods. With the advent of modern high speed computing machinery, it has become possible to make computations using the transport equation as well as the diffusion equation, and a large number of programs, or codes, have been developed to handle a variety of problems with these equations. Numerical methods generally fall into two broad categories, namely, numerical integration and Monte Carlo. The first category consist of a large number of techniques for numerically integrating a differential or integral equation⁽¹⁰⁹⁾ The discrete ordinates S_N method is commonly used for one and two dimensional calculations. For more complex shield geometries, where a three dimensional treatment is required, the Monte Carlo method is preferred. In some cases, the overall analysis may be simplified by using the S_N method in part of the calculation and the Monte Carlo method in another part. Other combinations of procedures for solving the transport problem are also possible. A large number of computer codes have been developed to meet the various needs and situations arising in shield design⁽¹⁷³⁻¹⁷⁶⁾.

5.3.4.1 The Discrete Ordinates S_N Method

The discrete S_N method is a general numerical procedure for solving the neutron transport equation, and has been presented by Carlson⁽¹⁷⁷⁾. An alternative to expressing the spatial distribution of the neutron angular flux Φ in terms of Legendre polynomials is to employ the method

of discrete ordinates⁽¹⁷⁸⁾. In this procedure the angular flux is considered in a limited number of directions, and it is assumed to vary in a linear manner between these discrete directions. The symbol S stands for " segments " and N is the number of directions. The accuracy attainable increases with N because a better approximation to the actual angular flux distribution is possible, but so does the complexity of the computations. The S_N expression in terms of discrete directions applies only to the angular neutron flux distribution in space. As in the P_N treatment, however, allowance for anisotropic scattering is made by an expansion as a sum of spherical harmonics (or Legendre polynomials) of the cosine of the scattering angle.

With the approximation just described, the transport equation can be written in multigroup form. The set of coupled group equations can then be expressed in finite difference form and solved. Both inner and outer iteration schemes are used as may be required. There are some minor differences in the group constants, especially in the transfer cross sections, these depend on the number of terms retained in the Legendre expansion of the anisotropic scattering⁽¹⁰⁸⁾. Computer codes, e.g , DTF-IV⁽¹⁷³⁾ are available for solving the multigroup S_N equations with various approximations for the anisotropic scattering.

The S_N method has a number of useful applications in reactor analysis, especially in situations where diffusion theory is a poor approximation. An example is criticality calculations for small fast reactors. Another application is in the adjustment of cross sections, especially for fast neutron systems. This is done by comparing the

results of S_8 (or S_{16}) calculations with those obtained from integral experiments. In shielding calculations, the discrete ordinates method is now commonly used for one dimensional shielding calculations , e.g , by the ANISN code⁽¹⁷⁴⁾, and, to some extent, for two dimensional calculations, e.g , by the DOT code⁽¹⁷⁵⁾

5.3.4.2 The Monte Carlo Method

The Monte Carlo method is a numerical procedure for solving mathematical problems based on statistical theory. Features in common for all Monte Carlo calculations are⁽¹⁷⁰⁾:

- 1- Description of the physical process.
- 2- Formulation of the probability model.
- 3- Definition of the basic estimating random variable.
- 4- Construction of sampling distributions, using random numbers.
- 5- Processing of samples and statistical analysis of data .

Neutron transport problems can be solved numerically by the Monte Carlo method⁽¹⁷⁹⁾. However, the procedure requires extensive computer time since it is necessary to follow the histories of many neutrons through a large number of collisions in order that the results may have statistical significance. A great advantage of this technique is that a three - dimensional problem can be solved with little more effort than for a similar problem in one dimension. The Monte Carlo method may be employed in homogenization calculations and to check the results given by simpler but more approximate procedures. For complex geometries in shielding studies, use of the Monte carlo technique, e.g , by the MORSE

code⁽¹⁷⁶⁾ is necessary.

5.3.4.3 The Moments Method

The moments method for solving the transport equation is not used directly in reactor analysis since an infinite homogeneous medium must be assumed. It has been utilized, however, to study the penetration of neutrons and gamma rays through various shielding materials. The results of such calculations have been used in the analysis of reactor shields⁽¹⁰⁸⁾.

5.3.5 The ANISN Code

In the present work the calculation of neutron spectra were performed by the ANISN code which was used on the CDC 7600 at UMRCC. The cross section data used was from a new set, the "ZZ - FEWG 1 / 31-1F Cross Section Library". This is a coupled 37 neutron groups (19.6 MeV to the thermal region with a minimum energy of 1×10^{-5} eV) and 21 gamma ray groups (14 MeV to 10 keV). The cross sections contain angular distributions in P_3 form and are suitable for use with ANISN code. To reduce the amount of unnecessary information produced, cross sections for groups 4 to 24 (14.2 MeV to 52.5 keV) were extracted, by using a programme ANXSEC (Appendix 3), from this data for use in the calculations not involving fissile materials which used groups 4 to 37 .

ANISN is a one dimensional transport theory programme using the multigroup discrete ordinates method of solution. Calculations were made for the 34 groups covering the range 14.2 MeV to 10^{-5} eV [table (5.1)] using $P_3 S_8$ approximation to the angular distributions. Table (5.2) represents the angular quadrature constants used in every

Table (5.1) Neutron Energy Boundaries For The 34 Groups
Fast Neutron Data Derived From 37 - 21 Groups
ZZ - FEWG 1/ 31 - 1F Cross Section Library.

Group No.	Boundaries (MeV)		E(MeV)
1	14.2	13.8	0.4
2	13.8	12.8	1.0
3	12.8	12.2	0.6
4	12.2	11.1	1.1
5	11.1	10.0	1.1
6	10.0	9.05	0.95
7	9.05	8.19	0.86
8	8.19	7.41	0.78
9	7.41	6.38	1.03
10	6.38	4.97	1.41
11	4.97	4.72	0.25
12	4.72	4.07	0.65
13	4.07	3.01	1.06
14	3.01	2.39	0.62
15	2.39	2.31	0.08
16	2.31	1.83	0.48
17	1.83	1.11	0.72
18	1.11	5.5E-1 *	0.56
19	5.5E-1	1.58E-1	0.392
20	1.58E-1	1.11E-1	0.047
21	1.11E-1	5.25E-2	0.0585
22	5.25E-2	2.48E-2	0.0277
23	2.48E-2	2.19E-2	2.90E-3
24	2.19E-2	1.03E-2	0.0116
25	1.03E-2	3.35E-3	6.95E-3
26	3.35E-3	1.23E-3	2.12E-3
27	1.23E-3	5.83E-4	6.47E-4
28	5.83E-4	1.01E-4	4.82E-4
29	1.01E-4	2.90E-5	7.20E-5
30	2.90E-5	1.07E-5	1.83E-5
31	1.07E-5	3.06E-6	7.64E-6
32	3.06E-6	1.13E-6	1.93E-6
33	1.13E-6	4.14E-7	7.16E-7
34	4.14E-7	1.00E-11	4.14E-7

* Read as 5.5×10^{-1} .

Table (5.2) Angular Quadrature Constants

Cosine (COS.)	Weight (WT.)	WT.x COS.
- 9.75900 E-01	0.00000	0.00000
- 9.51190 E-01	6.04938 E-02	- 5.75411 E-02
- 7.86796 E-01	9.07407 E-02	- 7.13944 E-02
- 5.77350 E-01	1.37037 E-01	- 7.91184 E-02
- 2.18218 E-01	2.11728 E-01	- 4.62029 E-02
2.18218 E-01	2.11728 E-01	4.62029 E-02
5.77350 E-01	1.37037 E-01	7.91184 E-02
7.86796 E-01	9.07407 E-02	7.13944 E-02
9.51190 E-01	6.04938 E-02	5.75411 E-02

calculation. Slabs and sphere calculations are possible and the 14.1 MeV neutron source was represented by a shell source of neutrons in the forward direction at the lower face of the shield.

Various options are available within ANISN. Slab calculations are for semi - infinite slabs with a uniformly distributed source. Therefore a shell source at the inner boundary is a poor representation of the finite experimental slab assemblies which have a point neutron source at 14 cm below the lower face. Space and radiation levels did not permit the point source to be placed at a long distance, for example 1 meter, below the slabs, which would have been a closer approximation to the ANISN slab calculations.

A choice is allowed in ANISN of including reflection at a boundary or omitting it. For the outer boundary there should be no reflection. When calculating the case of the graphite cube this was taken to be a hollow sphere for calculation purposes. Attempts to include a point source at the centre of the internal cavity (assumed to be otherwise empty) failed, probably because the source needs to be embedded in a scattering medium, so a radially directed shell source was used at the inner radius of the sphere. In addition reflection was assumed at the inner boundary to allow for the uniform neutron distribution in the central cavity.

Closer agreement with experiment was obtained for the slab cases by again using a spherical calculation model with an inner cavity of radius 14 cm and a shell thickness equal to the slab thickness. Since in the real slab case neutrons will escape from the lower boundary and not be

reflected, no reflection was assumed at the inner boundary of the sphere, which effectively means that neutrons entering the inner cavity are lost. Hence this calculation model was thought to be a better approximation to the finite experimental slabs than the slab option in ANISN, and as will be seen in chapter 7 reasonable agreement is obtained in most cases.

Some difficulty was experienced in using ANISN for source calculations with systems containing uranium. The additional production of neutrons by fission involves further iterations to reach a converged result and in many cases adequate convergence was not obtained. On increasing the maximum number of iterations some oscillation in the fluxes was observed and this did not seem to converge to a steady value within a finite number of iterations. All the cases without uranium converged rapidly. No explanation has been discovered so far for this behaviour with uranium. As will be seen in chapter 7, the uranium calculations can still be compared with experiment although the comparison is not always as good as for non - multiplying shields.

The ANISN programme (written at Oak Ridge) was obtained from NEA data bank, as was also the cross section data.

5.4 Smoothing Of Calculated Spectra

The experimental spectra are presented as histograms with a bin width of 0.2 MeV. As can be seen from Table (5.1) all of the energy groups above 0.158 MeV used in the calculations are wider than this and consequently direct comparison between calculated and experiment is not

possible. In order to present the calculated spectra in a form similar to the measured spectra a smoothing technique was applied to the calculated results.

The contents of each energy bin in the calculations were first equally divided among 0.1 MeV wide sub - intervals, where each group was approximated in width to a multiple of 0.1 MeV. From Table (5.1) it can be seen that group number 1 will be divided into 4 sub - intervals, group 2 into 10 , group 6 into 10 , group 10 into 14 sub - intervals and so on, down to group 17 .

5.4.1 Smoothing Function

The contents of each sub - interval we then assumed to be spread over a Gaussian function with a standard deviation assumed proportional to the square root of the energy. At 14 MeV the standard deviation was found to be experimentally $S = 0.64$ MeV and hence ;

$$S = 0.171 \sqrt{E} \quad \text{MeV} \quad \longrightarrow \quad (5.13)$$

The square root variation was chosen since it is a measure of the standard deviation of the signal size, although not an exact measure due to the non - linearity of light output with energy. Sources of lower energy monochromatic neutrons were not available for experimental determination of the actual variation, but since the measured spectra have a relatively smooth variation it was felt that the standard deviation would not have a marked effect on shape at lower energies.

The Gaussian distribution was assumed to exist only within the range $+ 3S$ to $- 3S$, and the distribution of the contents of a $\emptyset.1$ MeV wide sub - interval (index i) into the $\emptyset.1$ MeV wide bins of the smoothed spectrum (index k) was calculated as follows :

$$G_k = \frac{C_i}{\sqrt{2\pi} S} \int_{E_k - 0.05}^{E_k + 0.05} \exp \left(- \frac{(E_i - E_k)^2}{2 S^2} \right) dE \quad \text{-----} \quad (5.14)$$

Where E_k is the central energy of the particular bin.

This integral was performed numerically by a Simpson's integration as follows :

$$G_k = \frac{C_i}{\sqrt{2\pi} S} \frac{0.05}{3} \left[\exp \left(- \frac{(\Delta E_{k-0.05})^2}{2 S^2} \right) + 4 \exp \left(- \frac{\Delta E_k^2}{2 S^2} \right) + \exp \left(- \frac{(\Delta E_{k+0.05})^2}{2 S^2} \right) \right] \quad \text{-----} \quad (5.15)$$

where

$$\Delta E_k = |E_k - E_i| \quad \text{-----} \quad (5.16)$$

and the integral was carried out within the range $E_i - 3S \leq E \leq E_i + 3S$.

This was carried out for each sub - interval (i) in turn and the G values were summed into the $\emptyset.1$ MeV wide bins in order to obtain the smoothed spectrum. Finally, since bins $\emptyset.1$ MeV wide were used instead of the $\emptyset.2$ MeV wide bins of the experimental distribution, the contents of adjacent pairs of bins were summed to produce a histogram equivalent to the experimental one in detail.

5.4.2 Smoothing Computer Programme

The method described in section (5.4.1) was written as a computer programme SMOOTH which is listed in Appendix 2. By making the substitution

$$Z = (0.1)^2 / 2 S^2 \quad \text{and} \quad J = \Delta E_k / 0.1$$

the Simpson integration [Equation (5.15)] becomes ;

$$G_k = G_{i+J} = G_{i-J}$$

$$= 0.00665 \left[\frac{C_i}{S} \right] \left[\exp(-[J-0.5]^2 Z) + 4 \exp(-J^2 Z) + \exp(-[J+0.5]^2 Z) \right]$$



(5.16)

where J ranges in unit steps from 0 to NMAX , which is set by a maximum width of 3S for the Gaussian. Due to symmetry only half the distribution needs to be calculated apart from the central section (for J = 0), thus reducing the number of computing operations.

Figure (5.1) shows the calculated neutron spectra emitted from 8.9 cm thick graphite with and without smoothing.

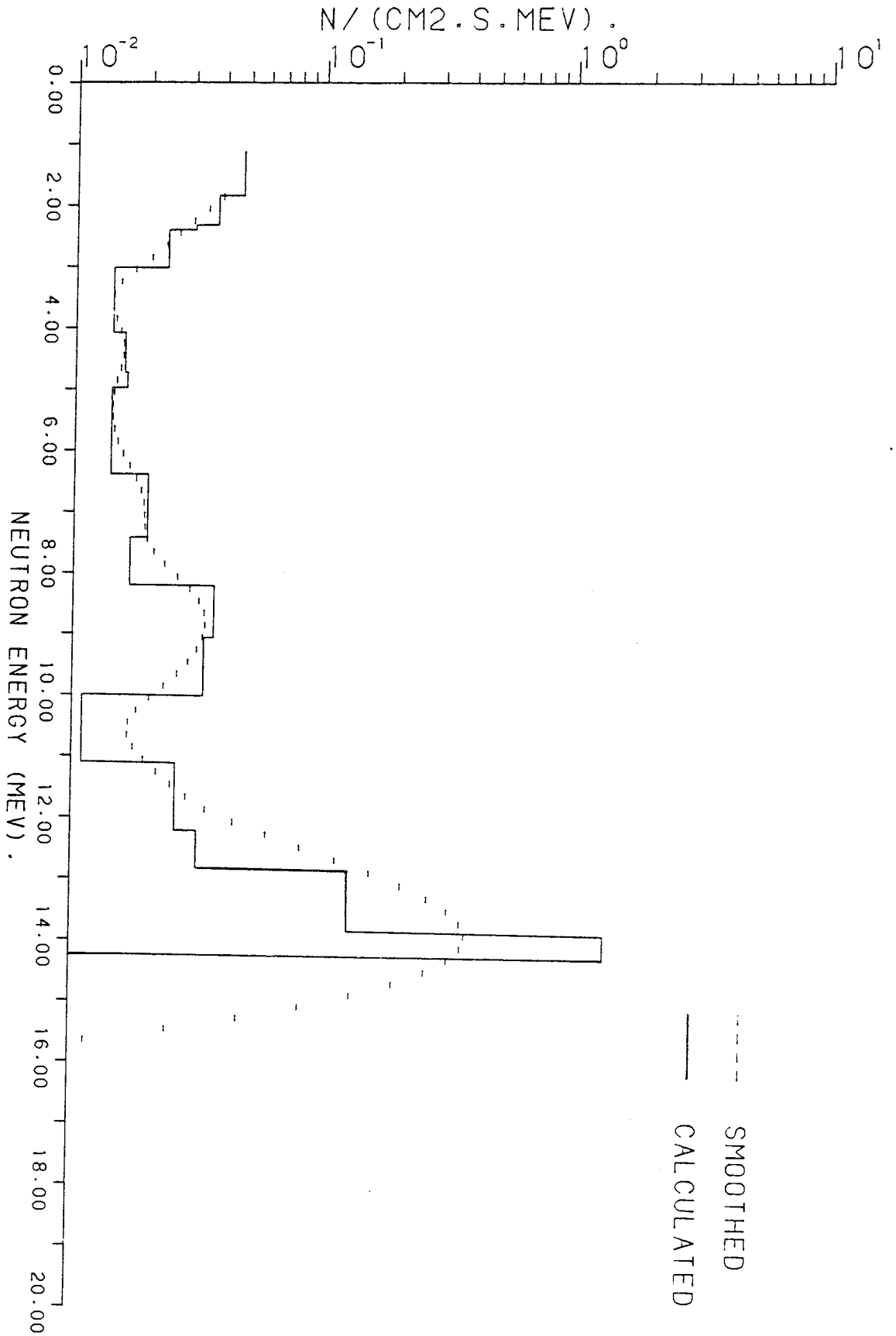


FIG. 5.1 CALCULATED SPECTRA EMITTED FROM 8.9 CM THICK GRAPHITE SLAB WITH AND WITHOUT SMOOTHING.

CHAPTER 6

SHIELDING MATERIALS AND EXPERIMENTAL ASSEMBLIES

6.1 Introduction

The primary components and materials of nuclear fusion reactors will consist of nuclear fuels, structural materials, moderator, reflector and blanket materials, coolant, shields, nonsuperconducting or superconducting magnet systems.

The materials selected for the fusion reactor shielding materials in this work are natural uranium, lithium fluoride, graphite, lead and steel. All materials were shaped as slab assemblies and the graphite only was shaped as a cube. A point source of 14.1 MeV neutrons was located at 14 cm below the slab assemblies while the cube assembly, source was at the centre.

A steel frame was designed to carry the assembly materials and to support them horizontally, so that there was a minimum of additional scattering material near the assemblies.

6.2 Nuclear Fuel Materials

Nuclear fusion fuel and fertile materials for the generation of nuclear fusion energy are deuterium (^2D), tritium (T), helium (^3He) and lithium (^6Li and ^7Li) respectively.

The primary nuclear fusion fuel reactions are $D - T$, $D - D$ and $D - {}^3\text{He}$. The neutrons and protons produced from these three cycles can, respectively, be utilized to breed T and ${}^3\text{He}$ with fertile material ${}^6\text{Li}$.

6.3 Shielding, Coolant And Blanket Materials

The shielding materials for use in a nuclear fusion reactor fall into three groups according to their purposes⁽¹⁸⁰⁾:

- 1- Heavy and moderately heavy elements to attenuate the gamma and X - rays and to slow down fast neutrons inelastically.
- 2- Light elements or hydrogenous substances to scatter and slow down neutrons elastically.
- 3- Light materials containing boron to capture neutrons with little secondary gamma ray emission.

The most common shielding materials for use in nuclear fusion reactors are likely to be lead, steel, concretes, boron and hydrogenous substances for the thermal and biological shieldings. Many shielding materials often used in nuclear fission reactors can well be applied to nuclear fusion reactors.

The candidates for first wall or structural materials are austenitic stainless steel, nickel alloy, niobium alloy, vanadium alloy and titanium alloy or combination of stainless steel - niobium alloy and stainless steel - vanadium alloy.

Good heat transfer and thermal (physical) properties are the basic requirements of a fusion reactor coolant. Therefore, the coolant should have high thermal conductivity, large specific heat, low melting point, high boiling point, low density, low viscosity and little corrosiveness, that is, the coolant must be compatible with the structural, channel, and piping materials of the nuclear fusion reactor. The materials selected for the fusion reactor coolant material are Li , LiF, LiF-BeF₂, Li₂Be F₄, He or H₂O . The coolants for use in the primary coolant loop and the secondary coolant loop of nuclear fusion power plant will be different.

The blanket materials could include some of the following ; Li , BeF₂ , ²³⁸U or liquid Li-Pb⁽⁷⁸⁾.

The coolant - blanket materials are Li and Li-Pb eutectic alloy in the liquid form, LiF-BeF₂(or Li₂BeF₄) in the fused or molten salt form, and LiO , LiAl , LiAlO₂ and Li₇Pb₂ in the solid form of blanket material only (because of their high melting points). The first wall and coolant blanket can be either integrated or detachable in the D - T fusion reactor design, Figure (6.1).

6.4 Moderator And Reflector Materials

The chief function of a moderator in a fusion reactor is to slow down fast neutrons from high energy to thermal energy and so convert kinetic energy into heat. The function of a reflector is to reflect

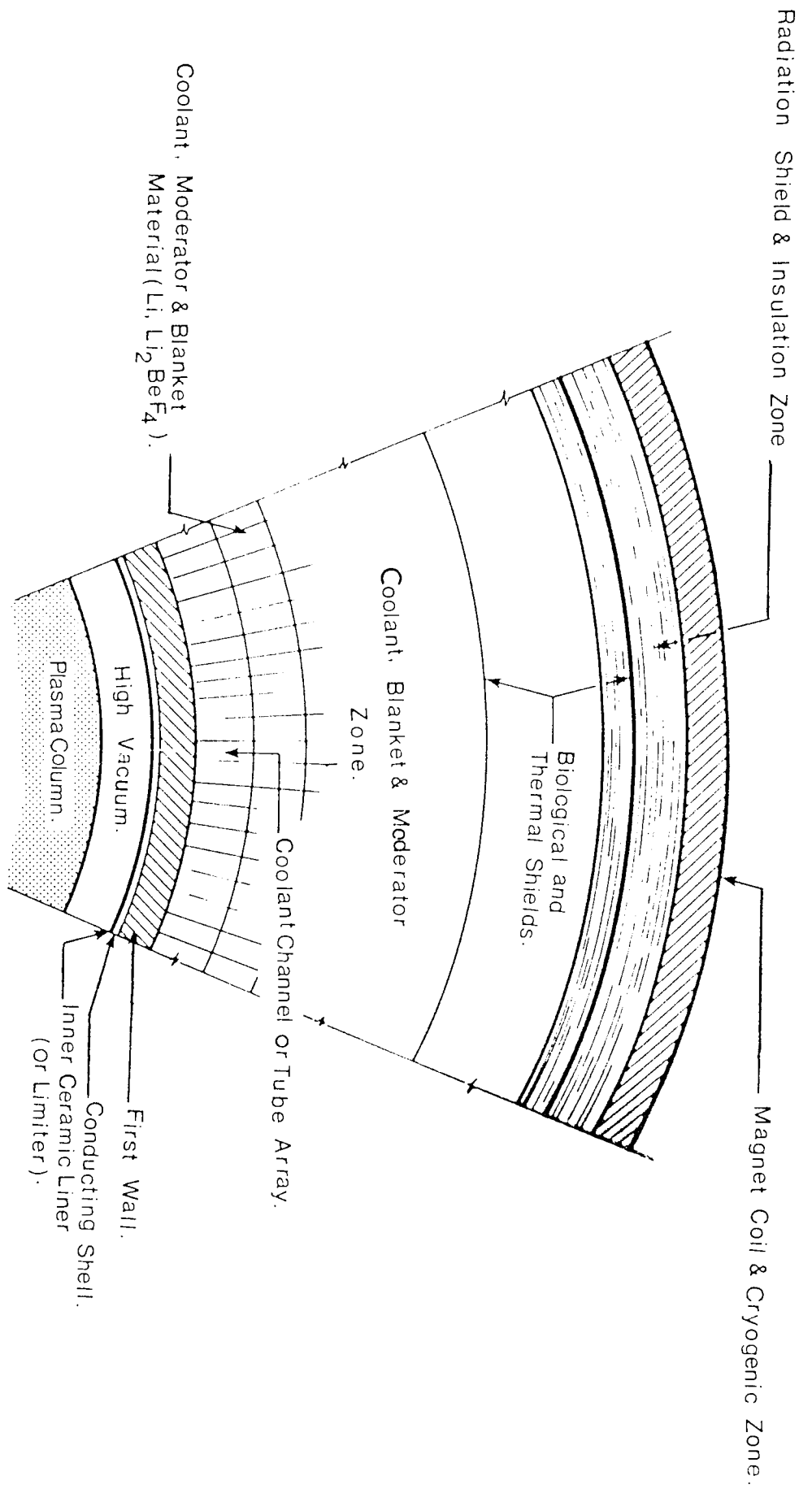


FIG. 6.1 TYPICAL CROSS SECTION OF CONTROLLED THERMONUCLEAR REACTOR USING A CHANNEL - BANK COOLANT SYSTEM OUT SIDE THE FIRST - WALL.

escaping neutrons back into the source and so increase the production of tritium from neutron reaction in lithium. The major moderator - reflector materials are LiF , BeF₂ , Li , H₂O and graphite .

In the fast nuclear fission reactor, moderator materials must be excluded from the blanket and core since they reduce breeding of plutonium. In a nuclear fusion reactor, however, the moderator, reflector, and blanket materials can exist together. For instance, liquid ⁶Li , a light element, can moderate and slow down the energetic fusion neutron, reflect it, and finally absorb it to carry out the breeding reaction for tritium production. In fact, liquid ⁶Li is also a very important coolant in the conceptual controlled nuclear fusion reactor (CNFR) system. Further, in the case of a hybrid fusion - fission reactor, the energetic neutrons passing through the slowing down and thermalization process may be absorbed in the fertile material, depleted uranium, of the fission reactor blanket to breed new fissile fuel, instead of being absorbed, by lithium - 6.

6.5 The Steel Frame

The material media under investigation were supported horizontally with a steel frame such that the lower surface of slab assemblies was 14 cm above the neutron source. In addition it could support the roughly spherical assembly such that the source was at its centre.

The steel frame, made from steel angles of 5 and 7.5 cm width, consists of two main parts. The lower one is 107 cm above the floor and 104 cm width. It is used separately for the rough sphere assembly and

the beam tube penetrates in the assembly as shown in figure (6.2). The upper one has two horizontal aluminium angles to carry the slab assemblies 53.3 cm high from the upper surface of the lower part and permits the slab to be a maximum of 62.2 cm width . Figure (6.3) shows the slab assembly, the neutron detector (standing on the surface and exactly above the source) and the steel frame.

6.6 Uranium And Lithium Fluoride Assemblies

Natural uranium (U) and lithium fluoride (LiF) materials are contained inside cylindrical aluminium cans 86.4 cm overall length and 82 cm effective length with a wall thickness of 0.915 mm. The inner and outer diameters are 29.54 and 31.37 mm respectively. The density of uranium is 18.7 gm cm^{-3} and the average density of LiF powder inside the tube is about 0.78 gm cm^{-3} which is much lower than the density of LiF crystals (2.635 gm cm^{-3}).

The assembly was designed with the tubes touching each other horizontally arranged in layer. The first layer consists of 19 tubes, second one of 18 tubes, third one 19 tubes and so on. The tube layers were supported by the upper part of the frame to build up the effective thickness required. The effective thickness calculated for 2 up to 8 layers of tubes were 5.4, 8.2, 10.9, 13.6, 16.3, 19 and 21.7 cm respectively. Figure (6.4 A) shows a cross section of the four layers assembly and the effective thickness calculated as an example. This thickness is the maximum value in case of U or LiF assemblies. Figures (6.5) and (6.6) represent the U and LiF assemblies used in this work.

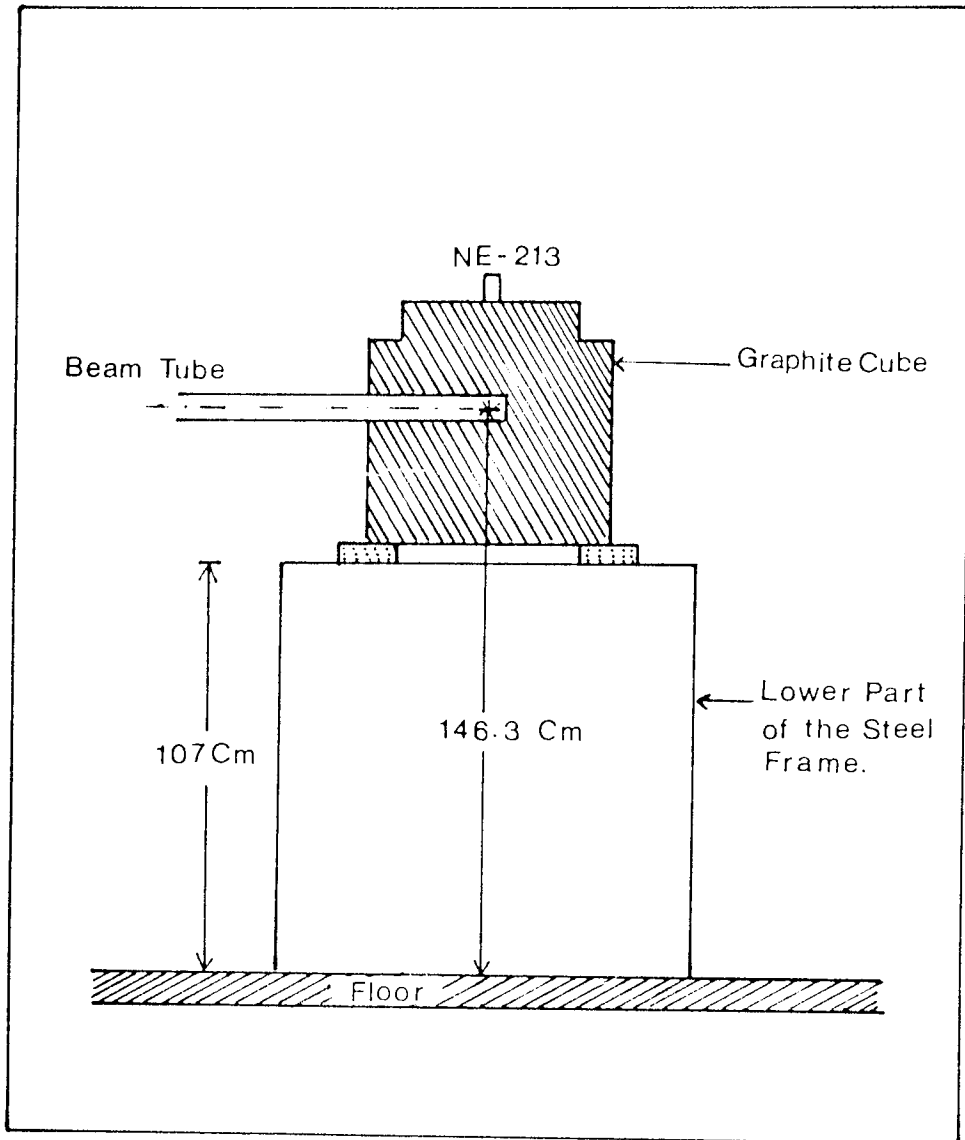


FIG. 6.2 THE STEEL FRAME (LOWER PART), GRAPHITE CUBE, THE BEAM TUBE AND THE NEUTRON DETECTOR.

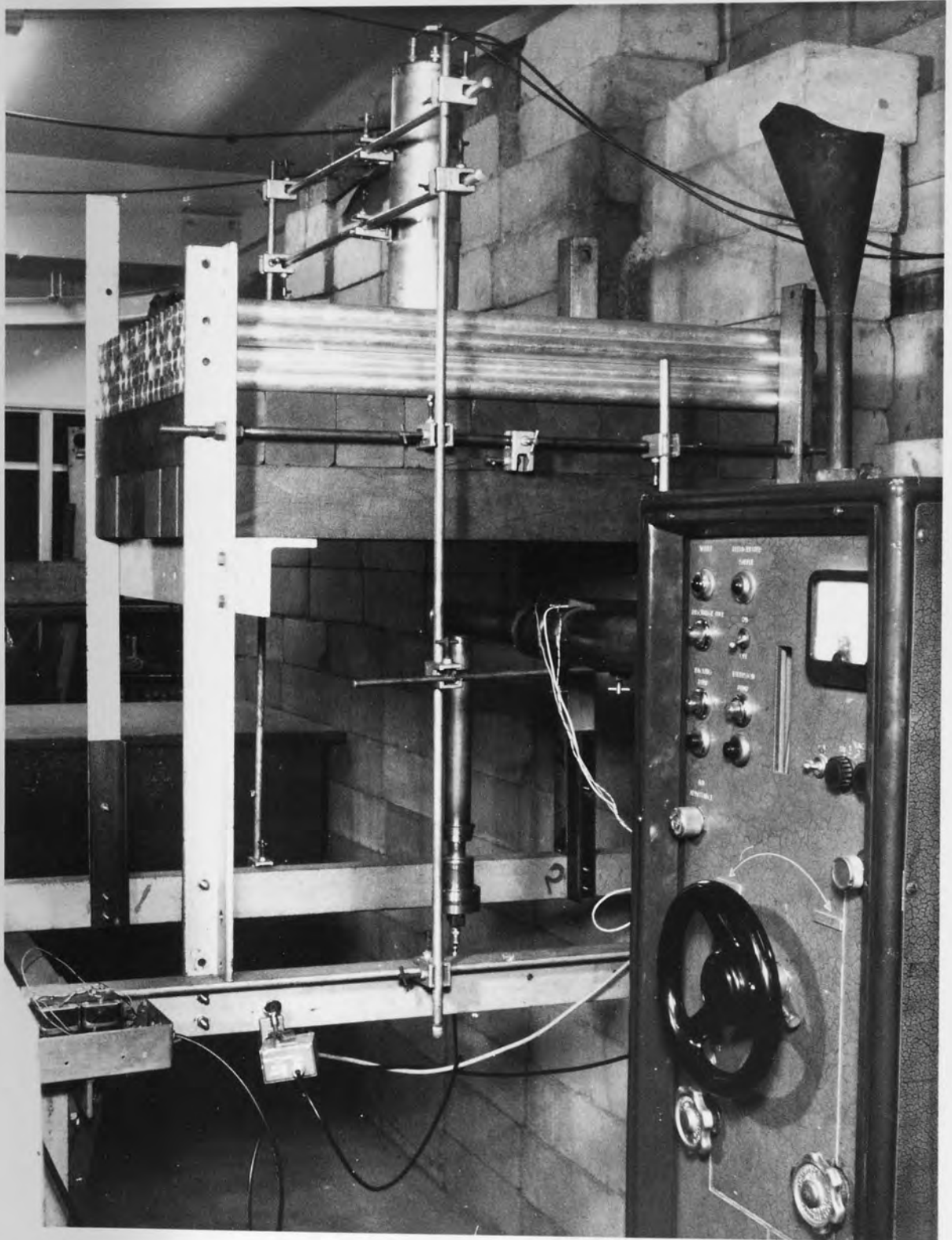


FIG. 6.3 THE SLAB ASSEMBLY (10.9 Cm. URANIUM ON TOP OF 17.8 Cm. THICK GRAPHITE), THE NEUTRON DETECTOR, THE STEEL FRAME, THE BEAM TUBE AND SAMES ACCELERATOR.

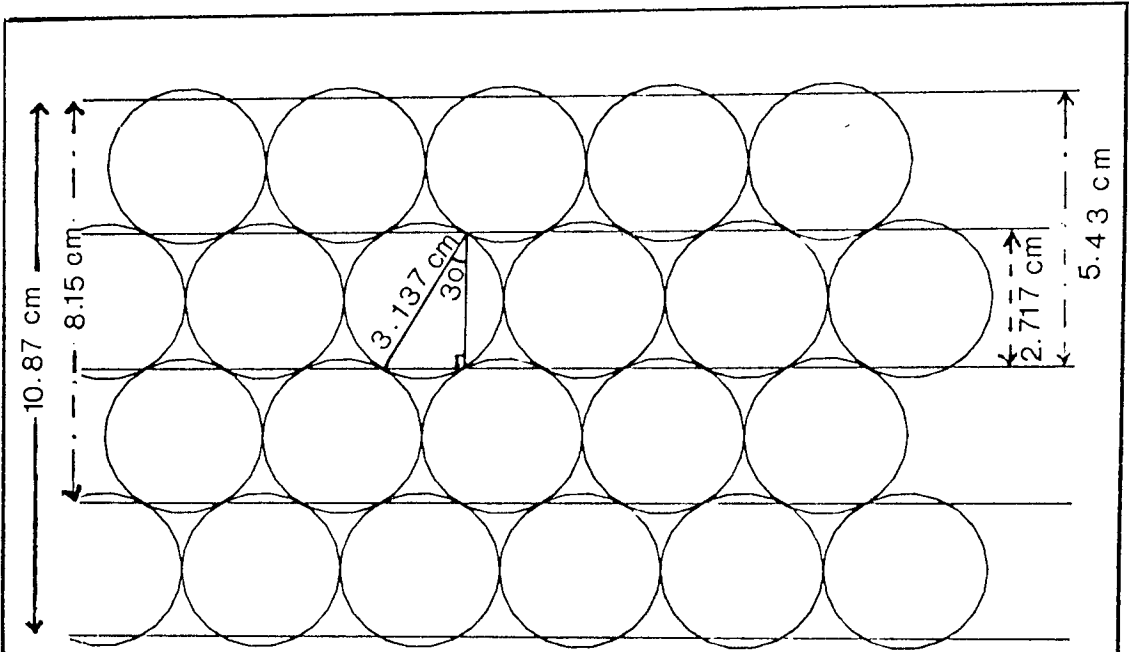


FIG. 6.4A A CROSS SECTION OF FOUR LAYERS ASSEMBLY (U OR LiF) AND THE EFFECTIVE THICKNESSES USED IN BOTH U AND LiF ASSEMBLIES .

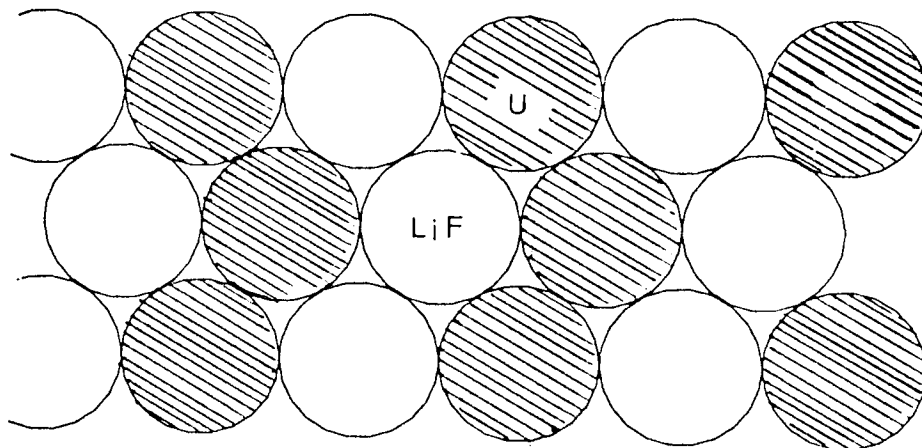


FIG. 6.4B THE HOMOGENEOUS ASSEMBLY FOR URANIUM AND LITHIUM FLUORIDE .

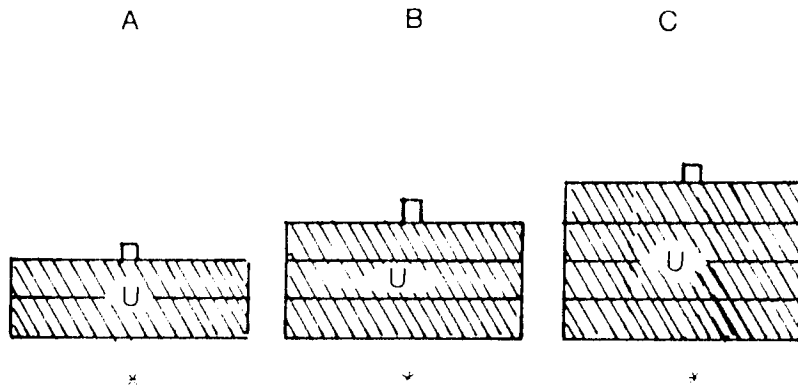


FIG. 6.5 URANIUM ASSEMBLIES WITH;
(A) 5.4, (B) 8.2 AND (C) 10.9 Cm.
THICK.

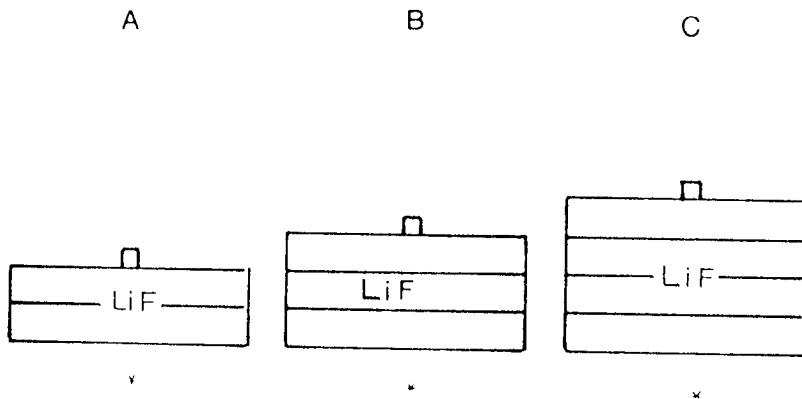


FIG. 6.6 LiF ASSEMBLIES WITH;
(A) 5.4, (B) 8.2 AND (C) 10.9 Cm.
THICK.

The homogeneous media for U and LiF were constructed by putting U and LiF tubes horizontally alternately in each layer as shown in figure (6.4 B) up to a maximum effective thickness of 21.7 cm . Figure (6.7) represents these assemblies in diagrammatic form.

Multilayers assemblies of U and LiF were built up by using different thicknesses from these two materials with different arrangements. Using 5.4 cm thickness of U on bottom with 5.4, 8.2 and 10.9 cm LiF on top, 10.9, 13.6 and 16.3 cm assembly thicknesses respectively were constructed as shown in figure (6.8 A, B and C). Similarly, 8.2 and 10.9 cm thickness uranium with the same thicknesses above of LiF mentioned before gave assemblies with thicknesses up to 21.7 cm. Figure (6.9) shows a block diagram of the samples containing 8.2 cm uranium, while figure (6.10) presents the cases used 10.9 cm thickness uranium. In the same manner and by interchanging U and LiF in the previous arrangements, assemblies of LiF on the bottom and uranium on top can be constructed with thickness up to 21.7 cm also. This is shown in figure (6.11 A, B and C) for samples contained 5.4 cm LiF on bottom with 5.4 , 8.2 and 10.9 cm uranium on top. In the samples contained 8.2 and 10.9 cm LiF on bottom with the same thicknesses of U mentioned before, figures (6.12) and (6.13) show these cases respectively.

Other multilayers assemblies for U and LiF were built up by putting 5.4, 8.2 or 10.9 cm thick LiF between two layers of uranium 5.4 cm thick each as shown in figure (6.14). Similarly, using 5.4, 8.2 or 10.9 cm thickness of uranium between two layers of LiF, 5.4 cm thick each, were used to construct assemblies with thicknesses up to 21.7 cm as shown in figure (6.15 A, B and C).

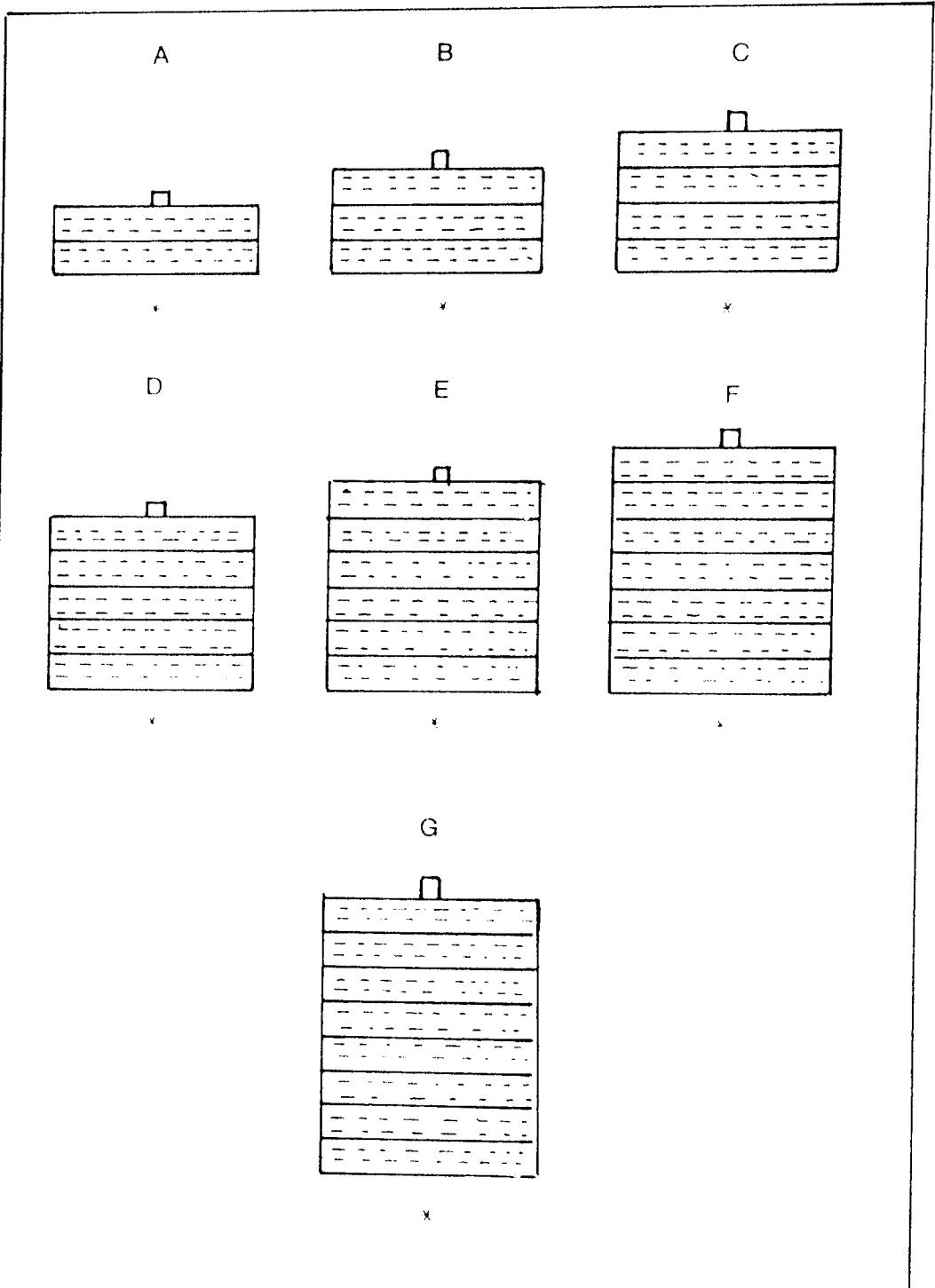


FIG. 6.7 SLABS OF URANIUM AND LiF MIXTURE WITH; (A) 5.4, (B) 8.2, (C) 10.9, (D) 13.6, (E) 16.3, (F) 19 AND (G) 21.7 Cm.THICK.

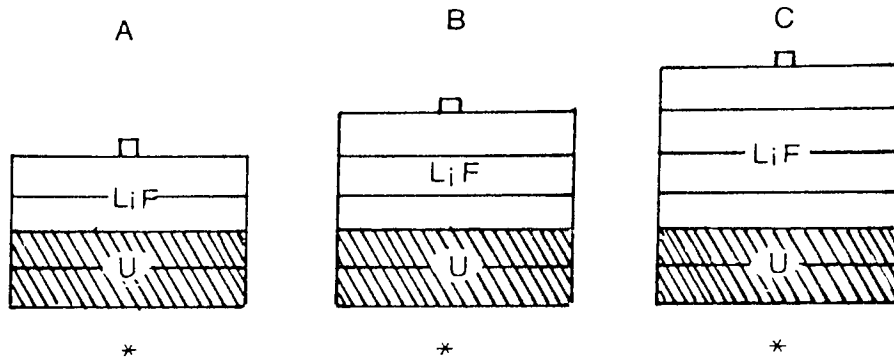


FIG. 6,8 SAMPLES CONTAINING 5.4 Cm URANIUM ON BOTTOM AND (A) 5.4, (B) 8.2 AND (C) 10.9 Cm LiF ON TOP .

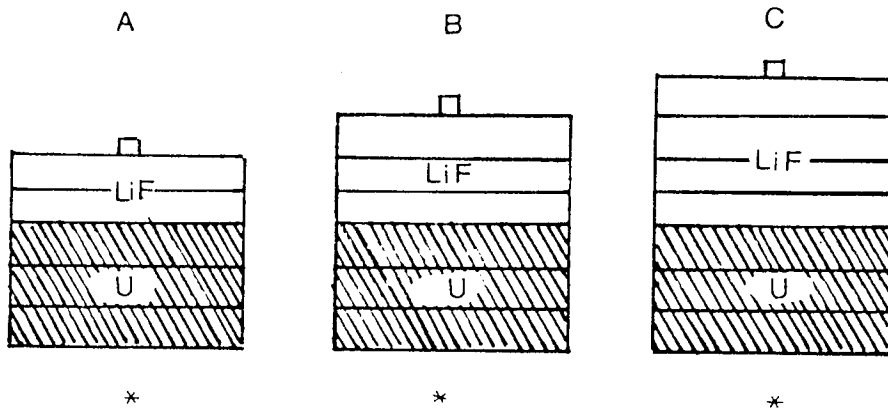


FIG. 6.9 SAMPLES CONTAINING 8.2 Cm URANIUM ON BOTTOM AND (A) 5.4, (B) 8.2 AND (C) 10.9 Cm LiF ON TOP .

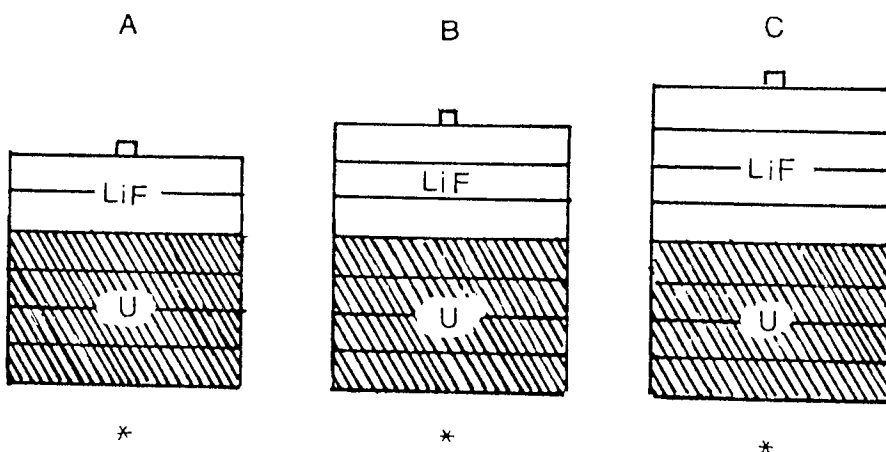


FIG. 6.10 SAMPLES CONTAINING 10.9 Cm URANIUM ON BOTTOM AND (A) 5.4, (B) 8.2 AND (C) 10.9 Cm LiF ON TOP.

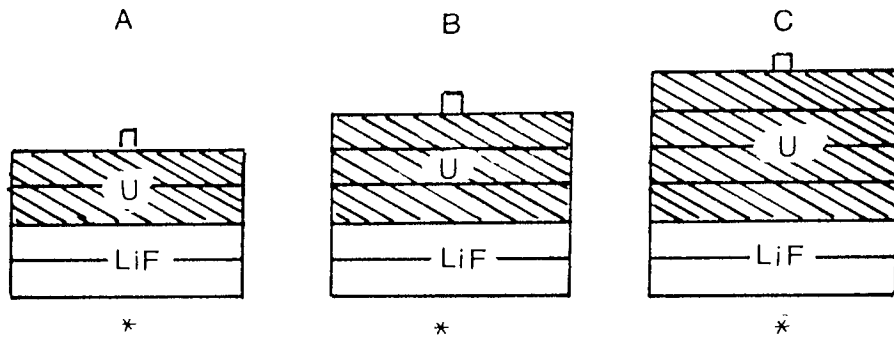


FIG. 6.11 SAMPLES CONTAINING 5.4 Cm LiF ON BOTTOM AND (A) 5.4, (B) 8.2 AND (C) 10.9 Cm URANIUM ON TOP.

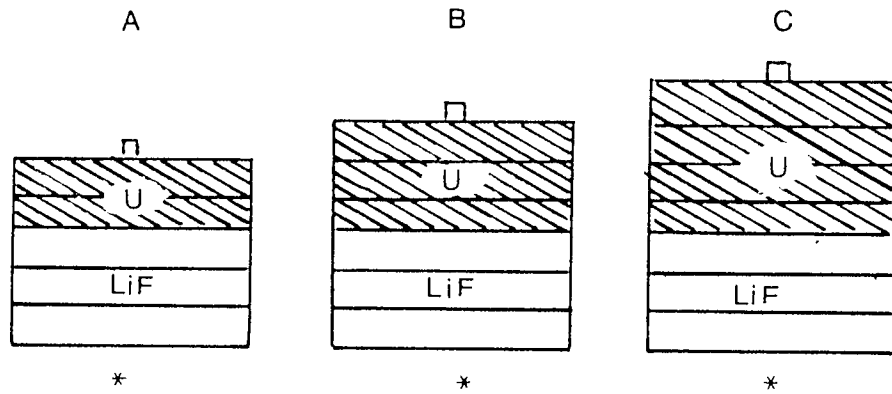


FIG. 6.12 SAMPLE CONTAINING 8.2 Cm LiF ON BOTTOM AND (A) 5.4, (B) 8.2 AND (C) 10.9 Cm URANIUM ON TOP.

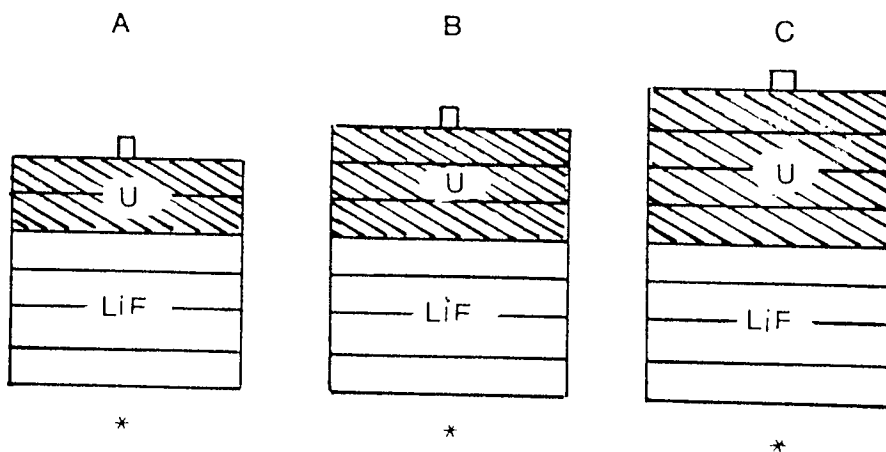


FIG. 6.13 SAMPLES CONTAINING 10.9 Cm LiF ON BOTTOM AND (A) 5.4, (B) 8.2 AND (C) 10.9 Cm URANIUM ON TOP.

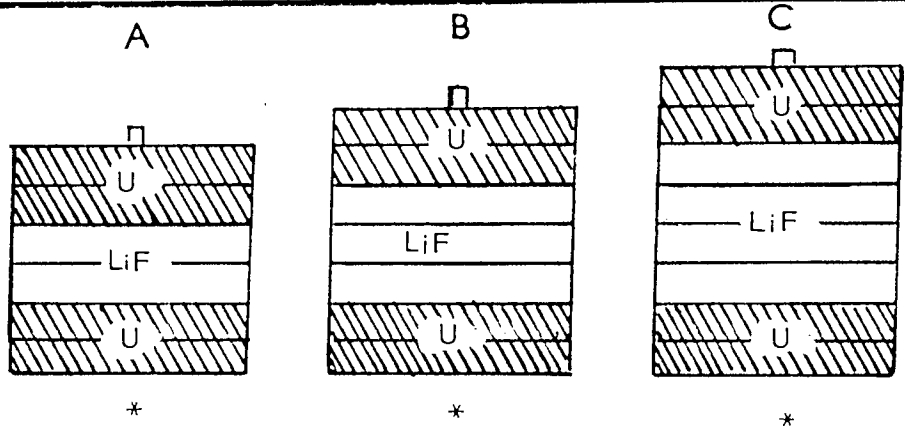


FIG. 6.14 SAMPLES CONTAINING (A) 5.4, (B) 8.2 & (C) 10.9 Cm LiF BETWEEN 2 LAYERS OF U 5.4 Cm EACH.

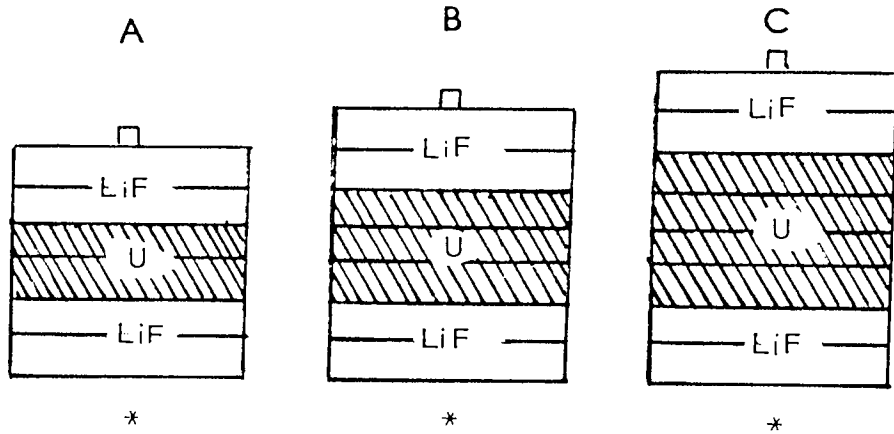


FIG. 6.15 SAMPLES CONTAINING (A) 5.4, (B) 8.2 & (C) 10.9 Cm U BETWEEN 2 LAYERS OF LiF 5.4 Cm THICK EACH.

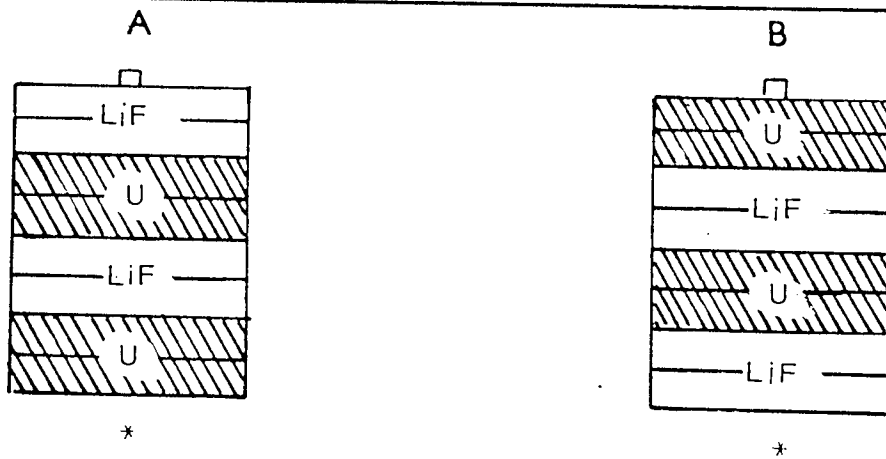


FIG. 6.16 SAMPLES CONTAINING (A) 5.4 Cm U, 5.4 Cm LiF, 5.4 Cm U AND 5.4 Cm LiF, (B) 5.4 Cm LiF, 5.4 Cm U, 5.4 Cm LiF AND 5.4 Cm U FROM BOTTOM TO TOP.

Finally, samples of multilayers of uranium and LiF were build up by putting 5.4 cm uranium on bottom followed by 5.4 cm LiF, 5.4 cm U and 5.4 cm LiF from bottom to top respectively as shown in figure (6.16 A). Interchanging LiF and uranium layers from the previous arrangement was also used as shown in figure (6.16 B).

6.7 Graphite Assemblies

The graphite was assembled as 62.2 cm cube, or slabs of different thickness. The assemblies were built from graphite blocks (density 1.718 gm cm^{-3}) having (8.9×8.9) cm^2 cross section area and with 62.2, 44.5, 27.9 and 8.9 cm lengths. The cube had a ($44.5 \times 44.5 \times 8.9$) cm^3 upper surface and a lower one of ($62.2 \times 44.5 \times 8.9$) cm^3 . This was a simple approximation to the sphere used for calculation purposes (figure 6.17 A). The graphite slabs of cross section area (62.2×44.5) cm^2 and with 8.9, 17.8 and 26.7 cm thickness were prepared as in Figure 6.17 B .

The graphite slabs 8.9 and 17.8 cm thicknesses were used with uranium and LiF assemblies to construct samples containing graphite slab on the bottom and uranium, LiF or a mixture of uranium and LiF on top with thickness up to 21.7 cm.

Figure (6.18 A, B and C) shows the diagrams of samples contained 8.9 cm graphite slab on bottom and 5.4, 8.2 and 10.9 cm uranium on top respectively .Figure (6.19 A, B and C) represents the samples contained 8.9 cm graphite slab with 5.4, 8.2 and 10.9 cm LiF on top.

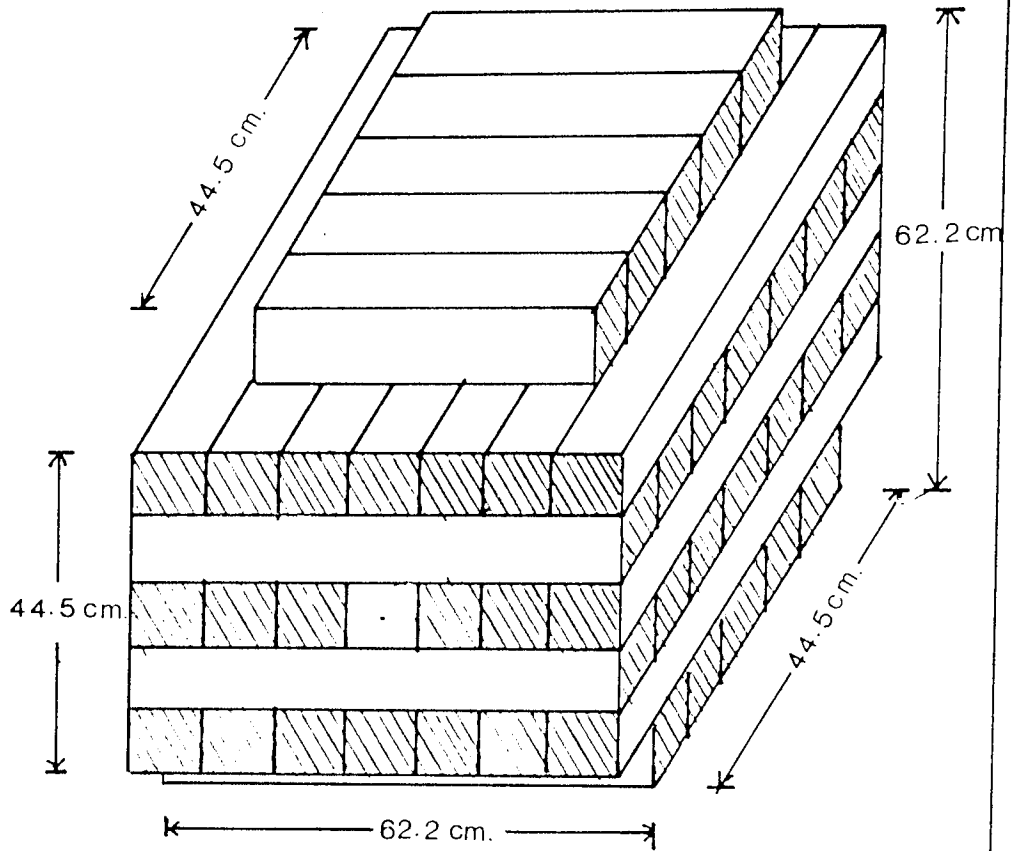


FIG. 6.17A THE GRAPHITE CUBE ASSEMBLY.

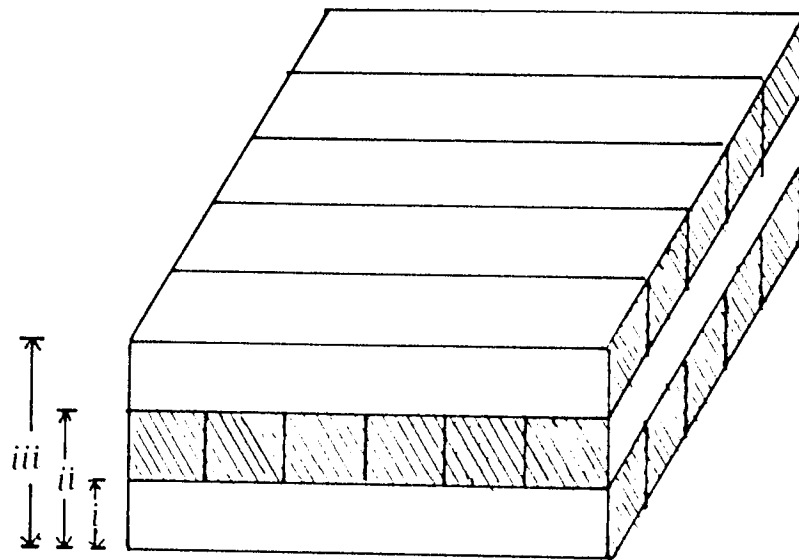


FIG. 6.17B THE GRAPHITE SLABS;
i - 8.9 cm. , *ii* - 17.8 cm. & *iii* - 26.7 cm.
THICK.

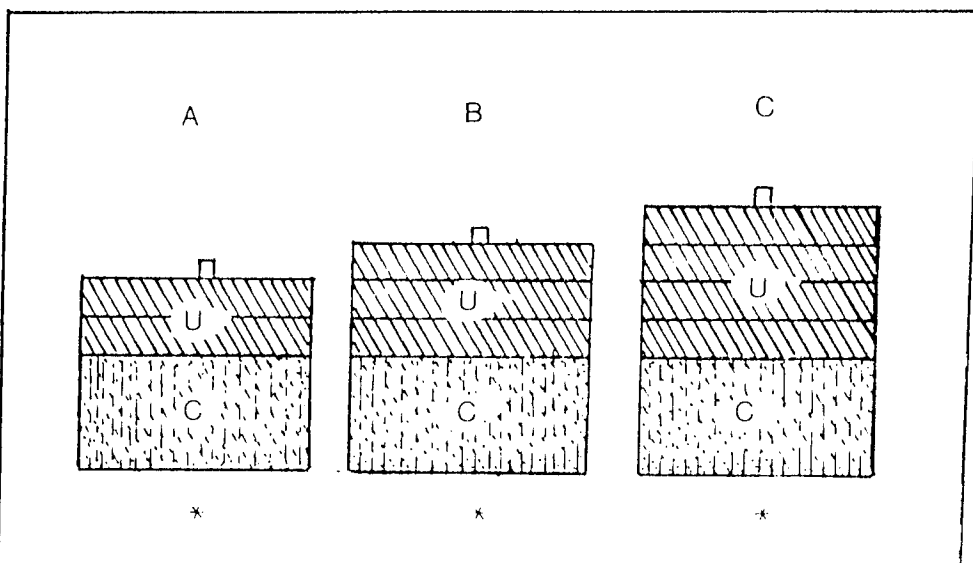


FIG. 6.18 SAMPLES CONTAINING 8.9 Cm GRAPHITE SLAB ON BOTTOM AND (A) 5.4, (B) 8.2 AND (C) 10.9 Cm URANIUM ON TOP.

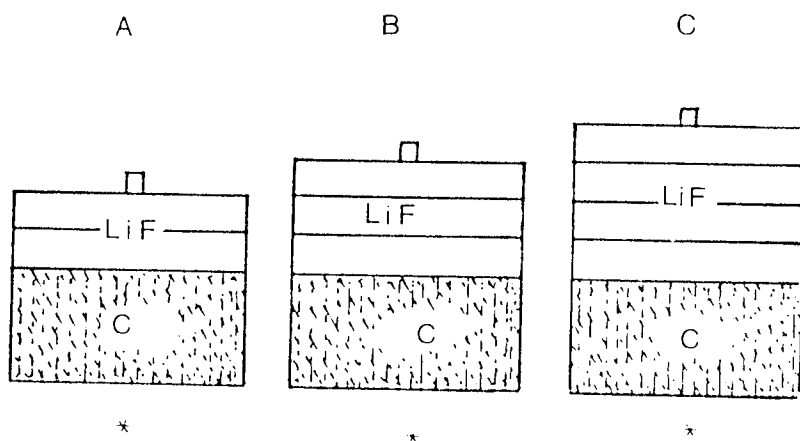


FIG. 6.19 SAMPLES CONTAINING 8.9 Cm GRAPHITE ON BOTTOM AND (A) 5.4 (B) 8.2 AND (C) 10.9 Cm LiF ON TOP.

Figure (6.21) represents the samples contained 17.8 cm graphite slab on bottom and 5.4, 8.2 and 10.9 cm thick uranium on top. Figure (6.22) shows the samples contained 17.8 cm graphite slab on bottom and 5.4, 8.2 and 10.9 cm thick LiF on top.

Also, 8.9 and 17.8 cm thickness of graphite slabs were used with the same manner with the homogenous media combinations of uranium and LiF (Section 6.6) with thickness up to 21.7 and 16.3 cm for graphite thicknesses 8.9 and 17.8 cm respectively. Figure (6.20 A to G) represents the combinations of 8.9 cm graphite slab with 5.4, 8.2, 10.9, 13.6, 16.3, 19 and 21.7 cm homogenous media. For 17.8 cm graphite slab, figure (6.23 A to E) shows the samples contained 5.4, 8.2, 10.9, 13.6 and 16.3 cm homogenous media on top.

6.8 Lead Assemblies

The lead material was available in the form of 5 cm thick interlocking blocks of (10.2 x 10.2) cm² cross sectional area with a density of 11.3 gm cm⁻³. In that case, the required thickness was obtained by putting these blocks horizontally on sheet of steel 1.3 cm thick, besides each other using the interlocking shape to build up 5 cm thickness and cross section area (61 x 61) cm². Also, 10 and 15 cm thicknesses with the same cross section area were built [Figure (6.24)].

The two layers configuration of lead and LiF were constructed by putting 5 cm thick lead followed by 5.4, 8.2 or 10.9 cm thickness LiF to build up thicknesses 10.4, 13.2 or 15.9 cm respectively. These samples

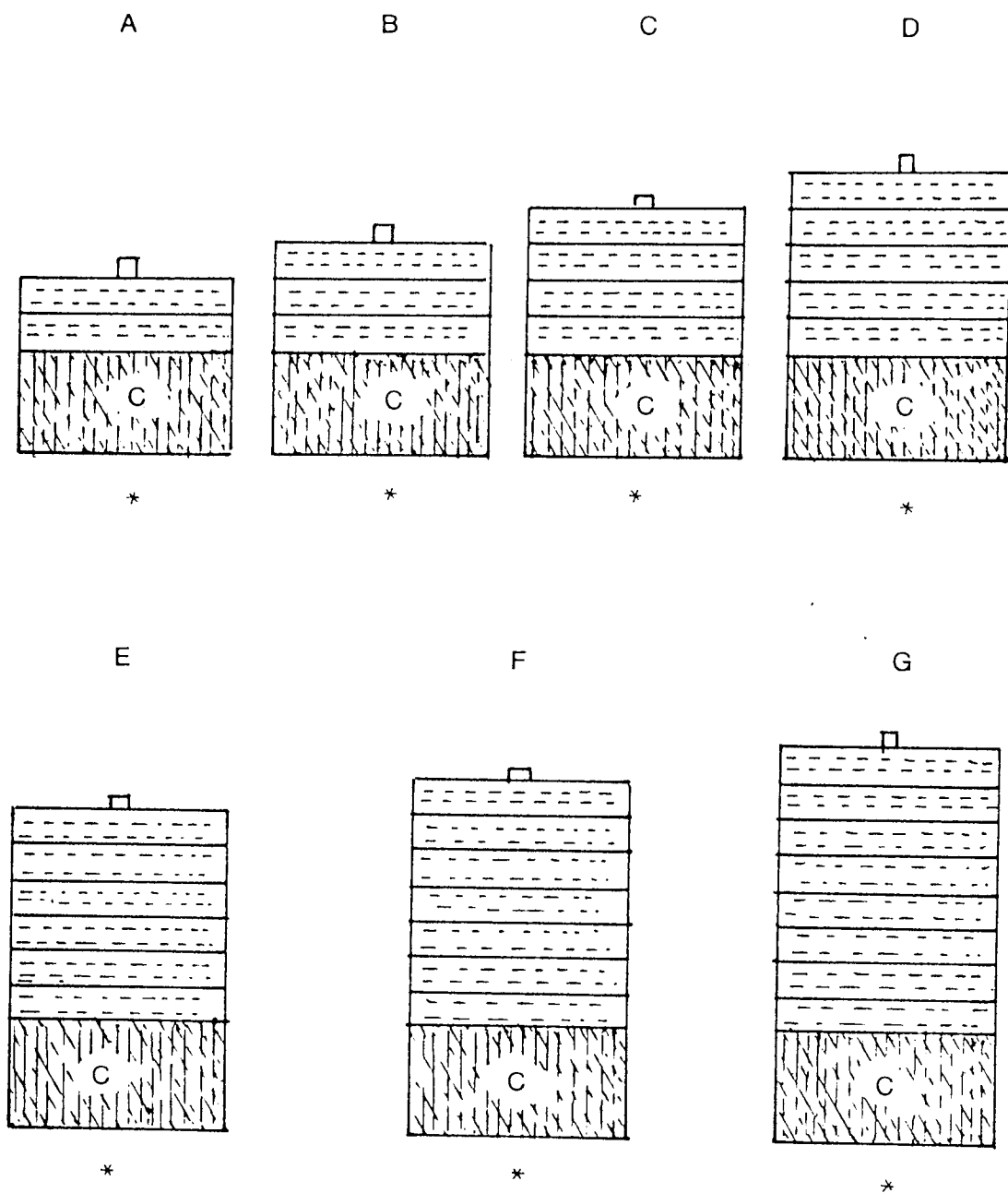


FIG. 6.20 SAMPLES CONTAINING 8.9 Cm GRAPHITE SLAB ON BOTTOM AND (A) 5.4 , (B) 8.2 , (C) 10.9 , (D) 13.6 , (E) 16.3 , (F) 19 AND (G) 21.7 Cm THICK OF URANIUM AND LiF MIXTURE .

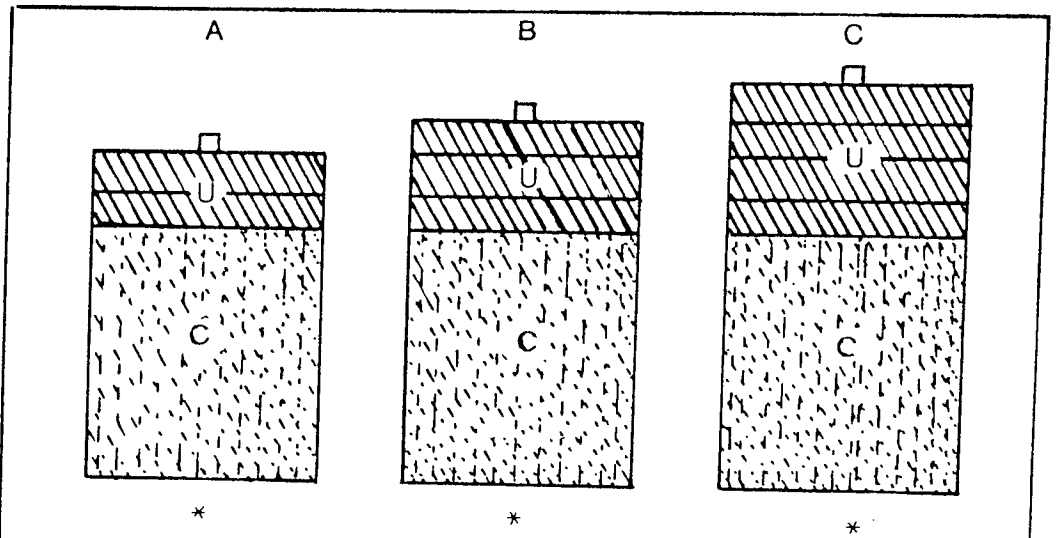


FIG. 6.21 SAMPLES CONTAINING 17.8 Cm GRAPHITE SLAB ON BOTTOM AND (A) 5.4, (B) 8.2 AND (C) 10.9 Cm. U ON TOP.

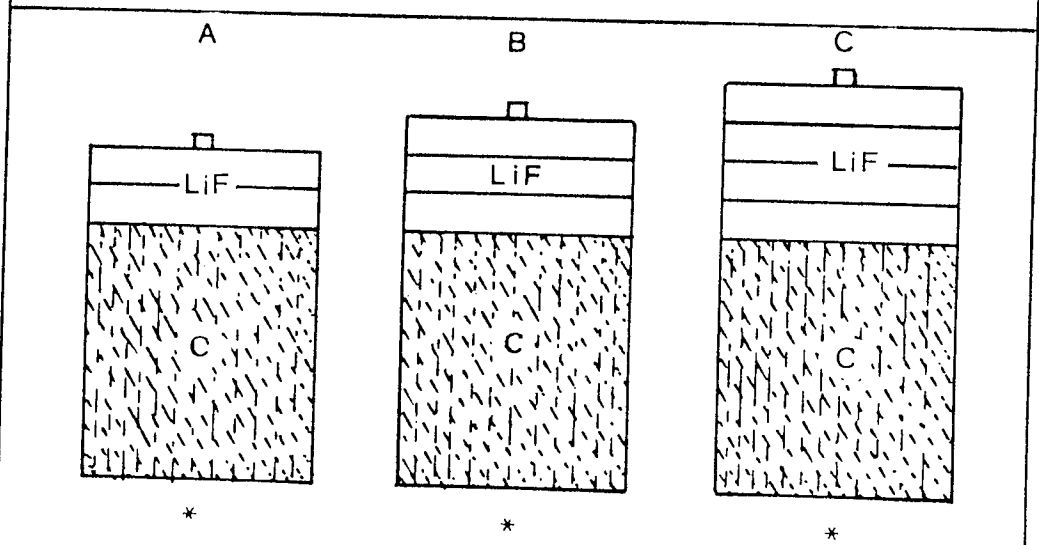


FIG. 6.22 SAMPLES CONTAINING 17.8 Cm. GRAPHITE SLAB ON BOTTOM AND (A) 5.4, (B) 8.2 AND (C) 10.9 Cm LiF ON TOP.

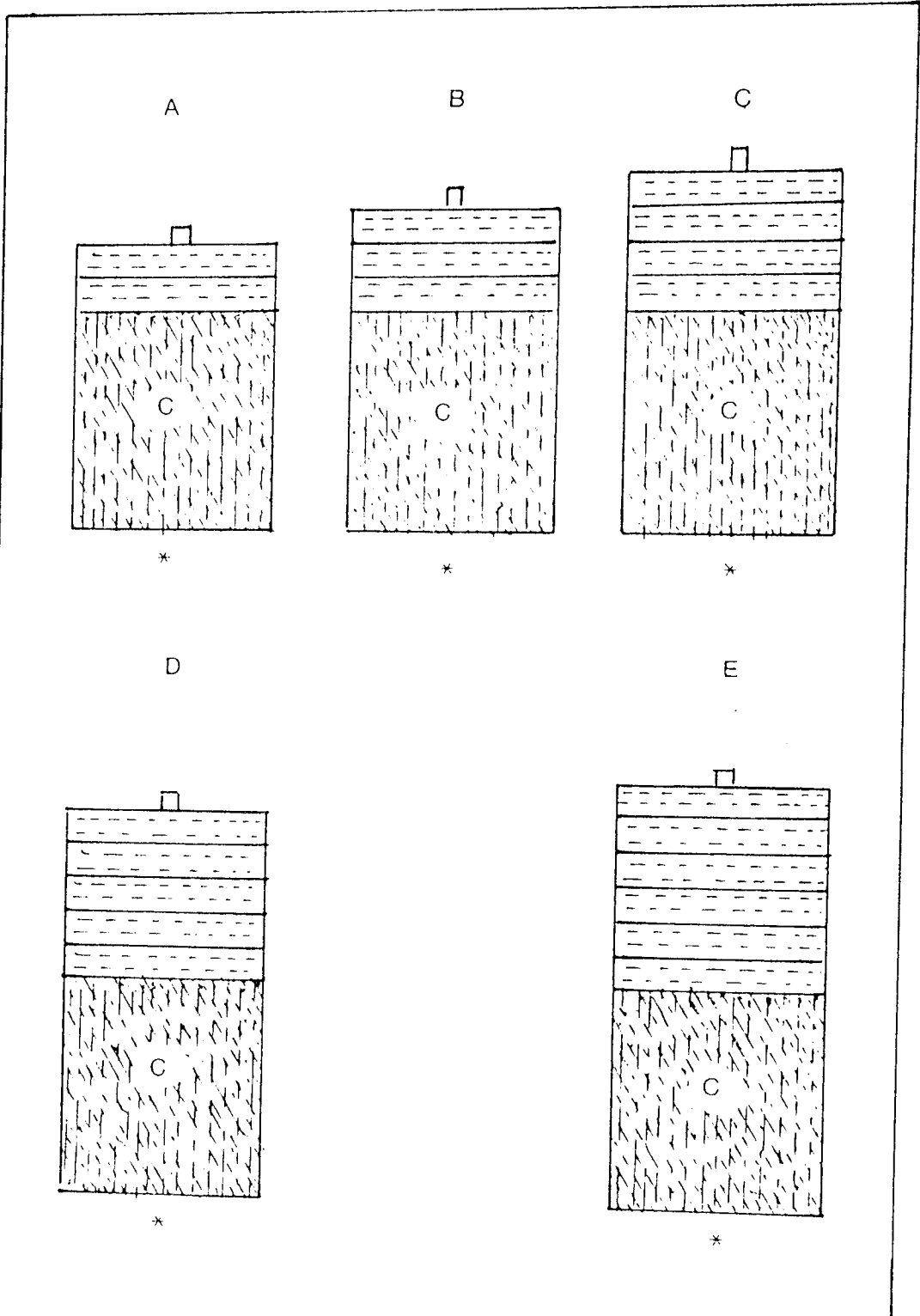


FIG. 6.23 SAMPLES CONTAINING 17.8 Cm GRAPHITE SLAB ON BOTTOM AND (A) 5.4, (B) 8.2, (C) 10.9, (D) 13.6 AND (E) 16.3 Cm THICK OF U AND LiF MIXTURE.

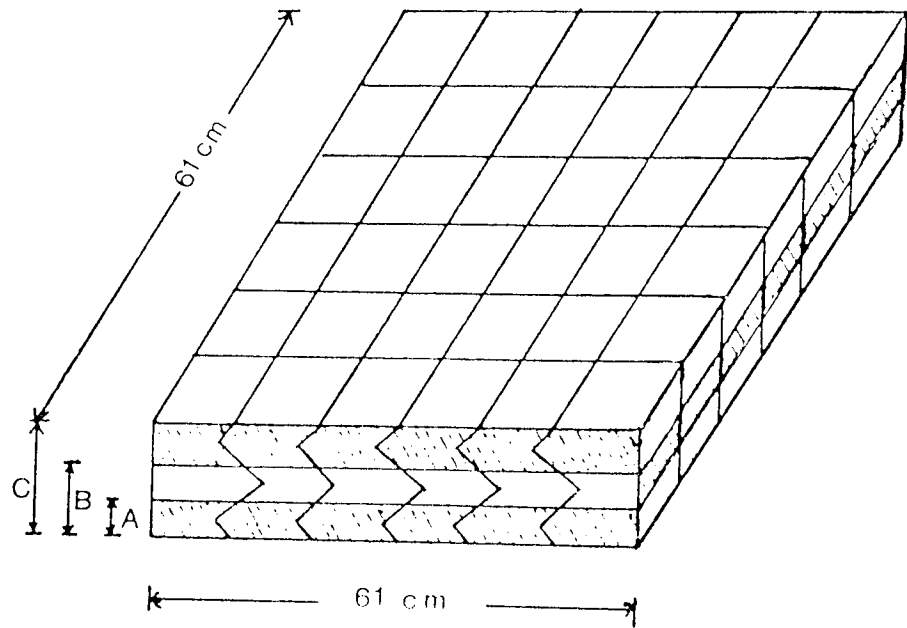


FIG. 6.24 THE LEAD SLABS ;
(A) 5 Cm , (B) 10 Cm AND (C) 15 Cm THICK.

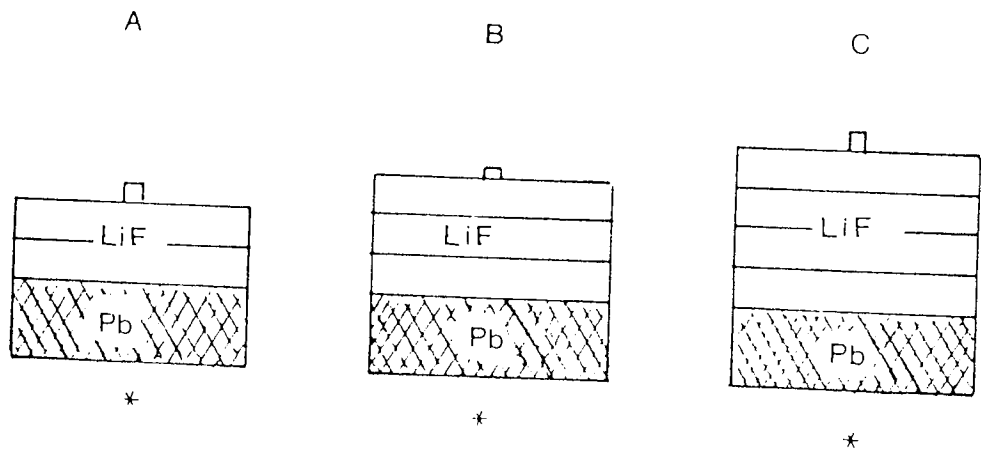
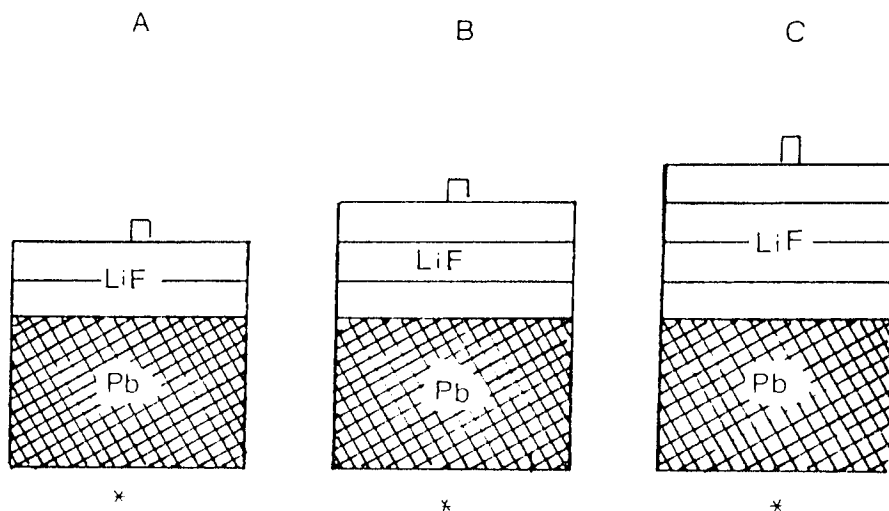


FIG. 6.25 SAMPLES CONTAINING 5 Cm LEAD SLAB ON
BOTTOM AND (A) 5.4 Cm , (B) 8.2 Cm AND
(C) 10.9 Cm LiF THICK ON TOP .

are shown in figure (6.25 A, B and C). This was repeated for lead thicknesses of 10 and 15 cm with the same LiF thickness mentioned before and samples with thicknesses up to 25.9 cm were obtained as shown in figures (6.26) and (6.27).

6.9 Steel Assembly

The steel assembly was built up by putting five sheets of steel 1.27 cm thick each to construct a sample 6.4 cm thick. The sheets used have a density 7.83 gm cm^{-3} .



e

FIG. 6.26 SAMPLES CONTAINING 10 Cm LEAD SLAB ON BOTTOM AND (A) 5.4 Cm , (B) 8.2 Cm AND (C) 10.9 Cm LiF THICK ON TOP .

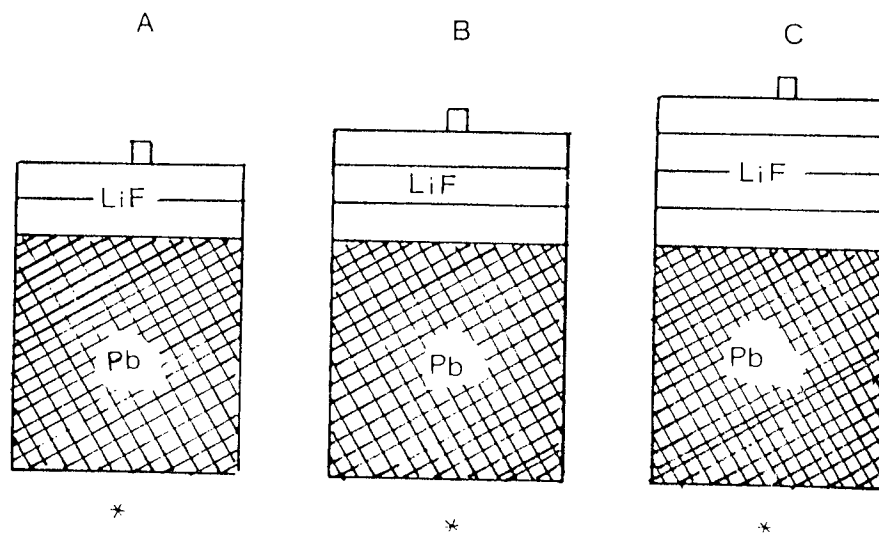


FIG. 6.27 SAMPLES CONTAINING 15 Cm LEAD SLAB ON BOTTOM AND (A) 5.4 Cm , (B) 8.2 Cm AND (C) 10.9 Cm LiF THICK ON TOP .

CHAPTER 7

RESULTS AND DISCUSSIONS

7.1 Introduction

The measured and calculated emitted neutron spectra from a graphite cube and the various slab assemblies described in chapter 6 are presented in this chapter with discussions.

All measurements have been made with NE - 213 liquid organic scintillator and using pulse shape discrimination system model 5010 manufactured by Link Systems (U.K.) to reject the gamma rays background. A computer programme NSPEC was used to analyse the experimental data by the differentiation unfolding method and to obtain neutron spectra as described in chapter 3 .

For the numerical calculations, the one - dimensional discrete ordinates transport code ANISN was used. The cross section data used was the ZZ - FEWG 1/31 - 1F cross section library. The numerical results obtained were smoothed with a Gaussian smoothing function (see section 5.4) using a computer programme SMOOTH , for comparison with the experimental results.

For some of the cases containing uranium, the ANISN calculations did not converge within the limits that were set (0.1 % in flux). Increasing the number of iterations did not improve the convergence and in some cases made it worse. An increase in the number of mesh points did not eliminate the effect. ANISN therefore does not seem to be always

reliable for thick natural uranium shields, but there may be an optimum number of iterations giving least error. Time has not permitted a detailed investigation of this effect.

All measured and calculated results were normalized for comparison purposes to a neutron flux of $1 \text{ neutron cm}^{-2}\text{s}^{-1}$ at the detector in the absence of any shield. The spectra were plotted as differential flux (neutron per cm^2 per sec per MeV) versus neutron energy in MeV. The neutron energy range used in this work is from 1.8 MeV upwards for all measured and calculated results, the lower energy limit being set by the neutron - gamma discrimination and the numerical method used for differentiating the pulse height spectrum.

7.2 Neutron Spectrum From Unshielded 14.1 MeV Source

The measured source spectrum emerging from the target assembly with no shielding present, is plotted in figure (7.1). The detector was placed 18 cm above the source.

From the figure; the 14.1 MeV peak was used to set the energy scale and the spectral peak around 12.5 MeV corresponds to the elastic backscattering of neutrons with the ordinary concrete walls and floor which were of necessity close to the source. The minimum energy due to elastic scattering of neutron with Si O_2 is around 11.6 MeV (10.98 MeV for ^{16}O and 12.22 MeV for ^{28}Si).

The effect of multiple elastic and inelastic backscattering of

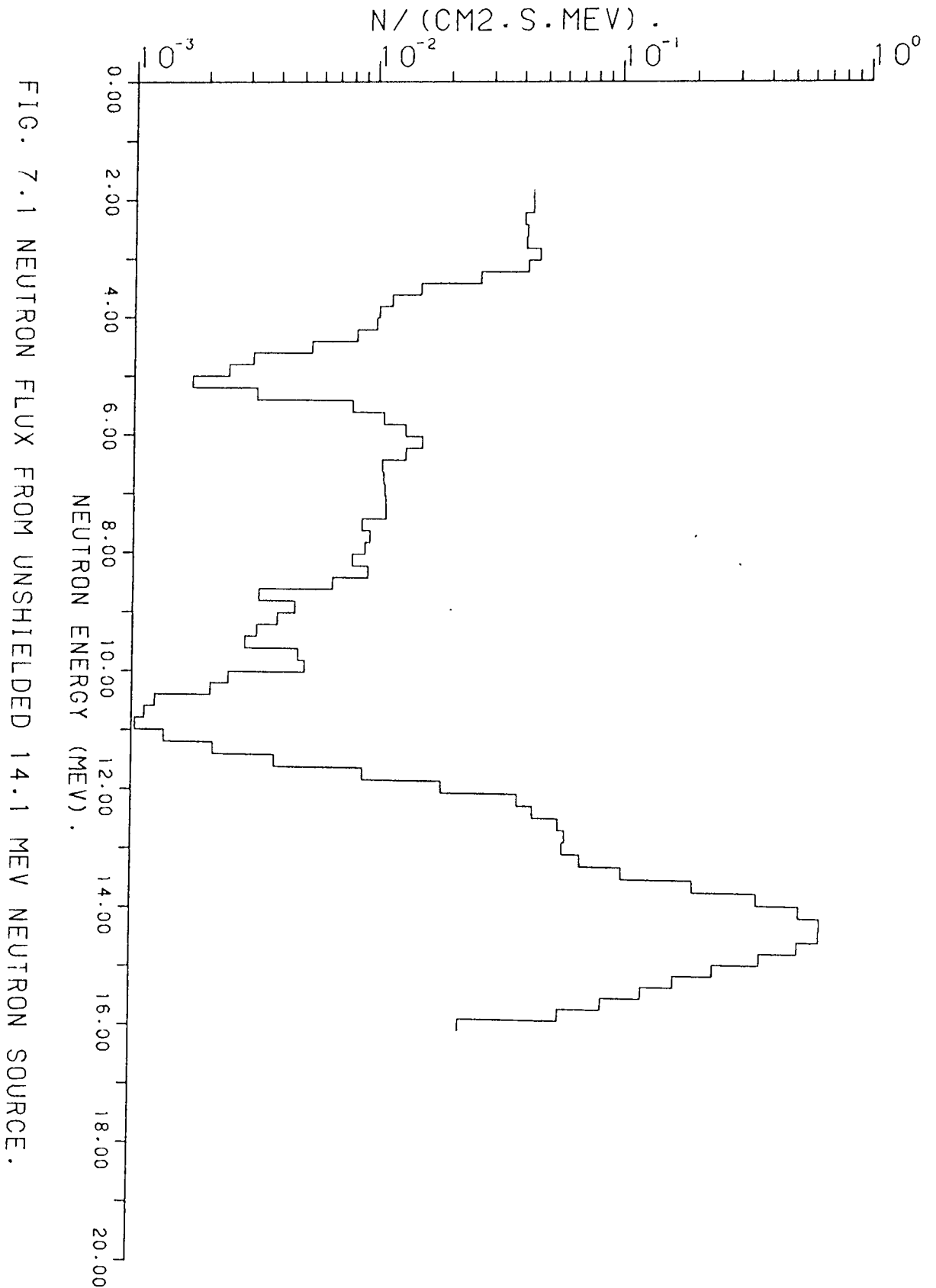


FIG. 7.1 NEUTRON FLUX FROM UNSHIELDED 14.1 MEV NEUTRON SOURCE.

neutrons with the concrete appears in the spectral region around 8 MeV and below.

7.3 Neutron Spectra For Uranium Slabs

Referring to diagrams shown in figure (6.5), measured and calculated neutron fluxes passing through uranium slabs of thicknesses 5.4, 8.2 and 10.9 cm are presented in figures (7.2), (7.3) and (7.4) respectively.

The figures show that ;

- 1- The theoretical spectrum in the 14 MeV region is wider than the experimental, although the same full width half maximum (FWHM) was used for smoothing.
- 2- The two " 14.1 MeV " peaks are not quite in the same position because the theoretical 14.1 MeV peak is a group from 13.8 to 14.2 MeV, i.e, $\bar{E} = 14$ MeV and $\Delta E = 0.4$ MeV which will add 0.4 MeV to the FWHM .
- 3- The next theoretical group is 13.8 to 12.8 MeV, this will also tend to add to the width of the smoothed curve on the low energy side. This will tend to mask the experimental bump in the range 12-13 MeV
- 4- Below 6 MeV, there is a discrepancy between calculated and measured flux probably due to streaming path through layers, figure (6.4 A). This effect decreases as the thickness increase, except for 8.2 cm thickness due to the calculation method errors as described in section 7.1 .

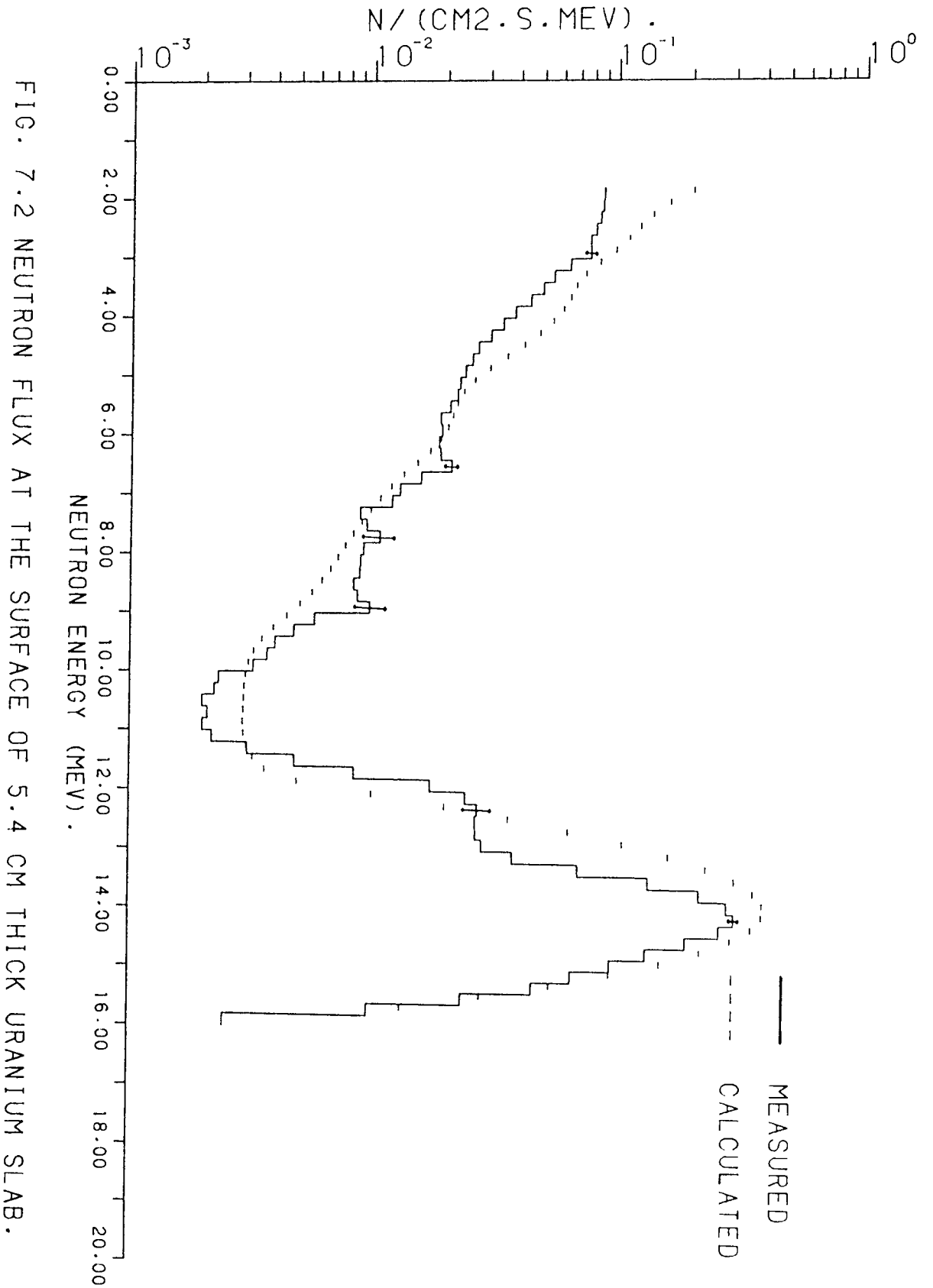


FIG. 7.2 NEUTRON FLUX AT THE SURFACE OF 5.4 CM THICK URANIUM SLAB.

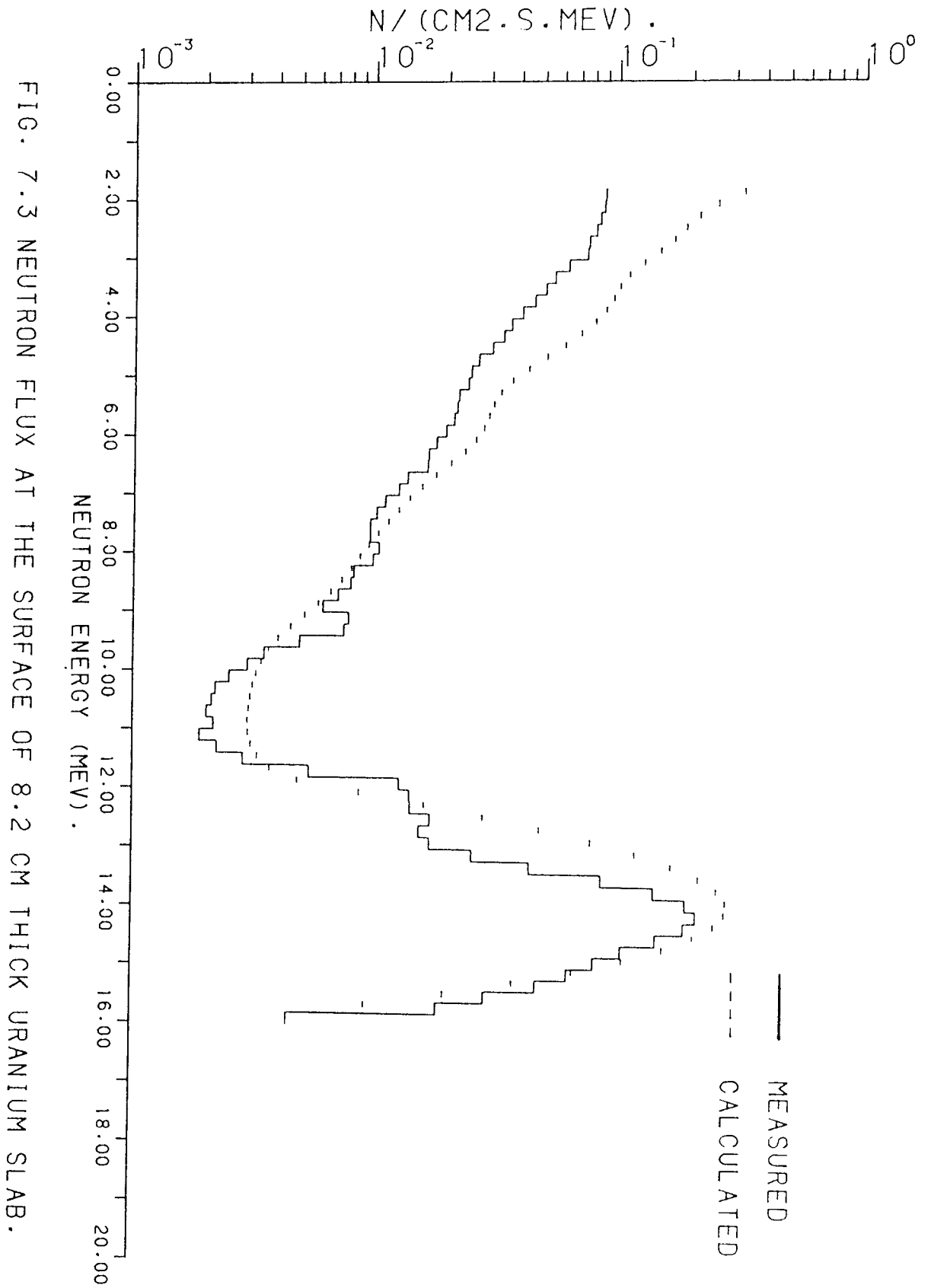


FIG. 7.3 NEUTRON FLUX AT THE SURFACE OF 8.2 CM THICK URANIUM SLAB.

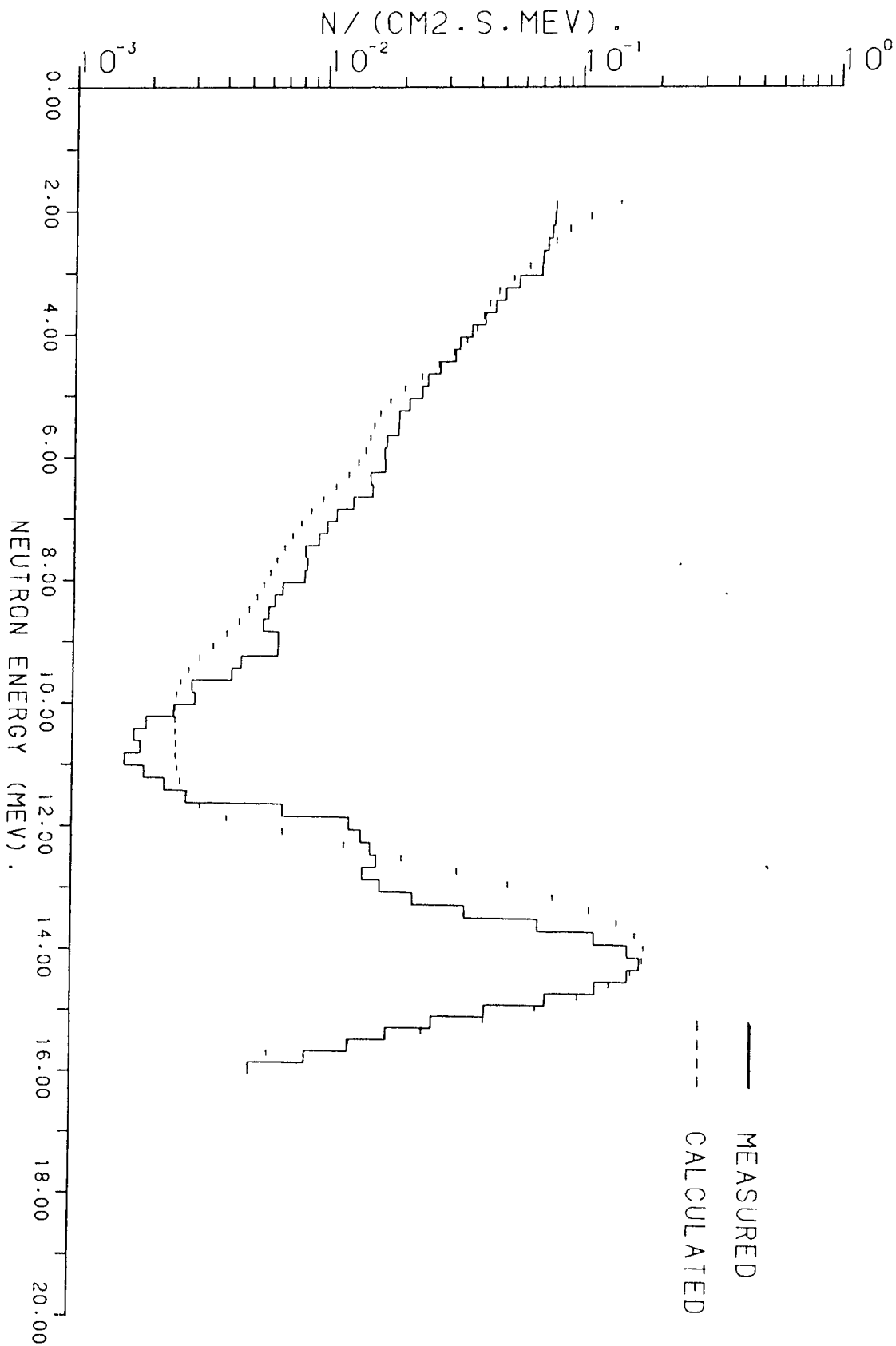


FIG. 7.4 NEUTRON FLUX AT THE SURFACE OF 10.9 CM THICK URANIUM SLAB.

As the thickness increases, the measured and calculated 14 MeV peak decreases through all spectra in which uranium was used as shielding material, but the lower energy part of the spectrum is more constant.

The isotopic composition of natural uranium is ⁽¹⁸⁰⁾; 0.0058 % ²³³U, 0.720 % ²³⁵U and 99.274 % ²³⁸U, therefore only ²³⁸U is of importance at high neutron energies. The (n,2n) reaction in U - 238, which has a broad (non resonance) cross section in the neutron energy range of about 7.7 to 12.5 MeV [figure (7.5)], will have the effect of increasing the flux in the low energy region below 1.8 MeV and so will not be observed. Also, the ²³⁸U(n,3n) reaction in the energy range starting at 11.41 MeV will also increase the flux at low neutron energy region of the spectra.

In comparison with spectra in air (without shield), it can be seen that below about 7 MeV, the flux is increased in uranium compared with air, but it is decreased above this energy. In addition to that, there is the fission threshold of uranium (1.35 MeV), so neutrons above this energy will produce fission neutrons up to about 10 MeV.

Elastic scattering cross section in U - 238 has its maximum value (4.78 barns) at 3.75 MeV, i.e, the maximum values of cross section are between 2.5 and 4.5 MeV.

Inelastic scattering in ²³⁸U starts from 0.045 MeV (10^{-4} barn) and increases as the neutron energy increase to the maximum value at 1.5 MeV (3.11 barns), then decreases to the constant value 0.4 barn at 13 MeV. Therefore, the inelastic scattering is the main reaction in addition to

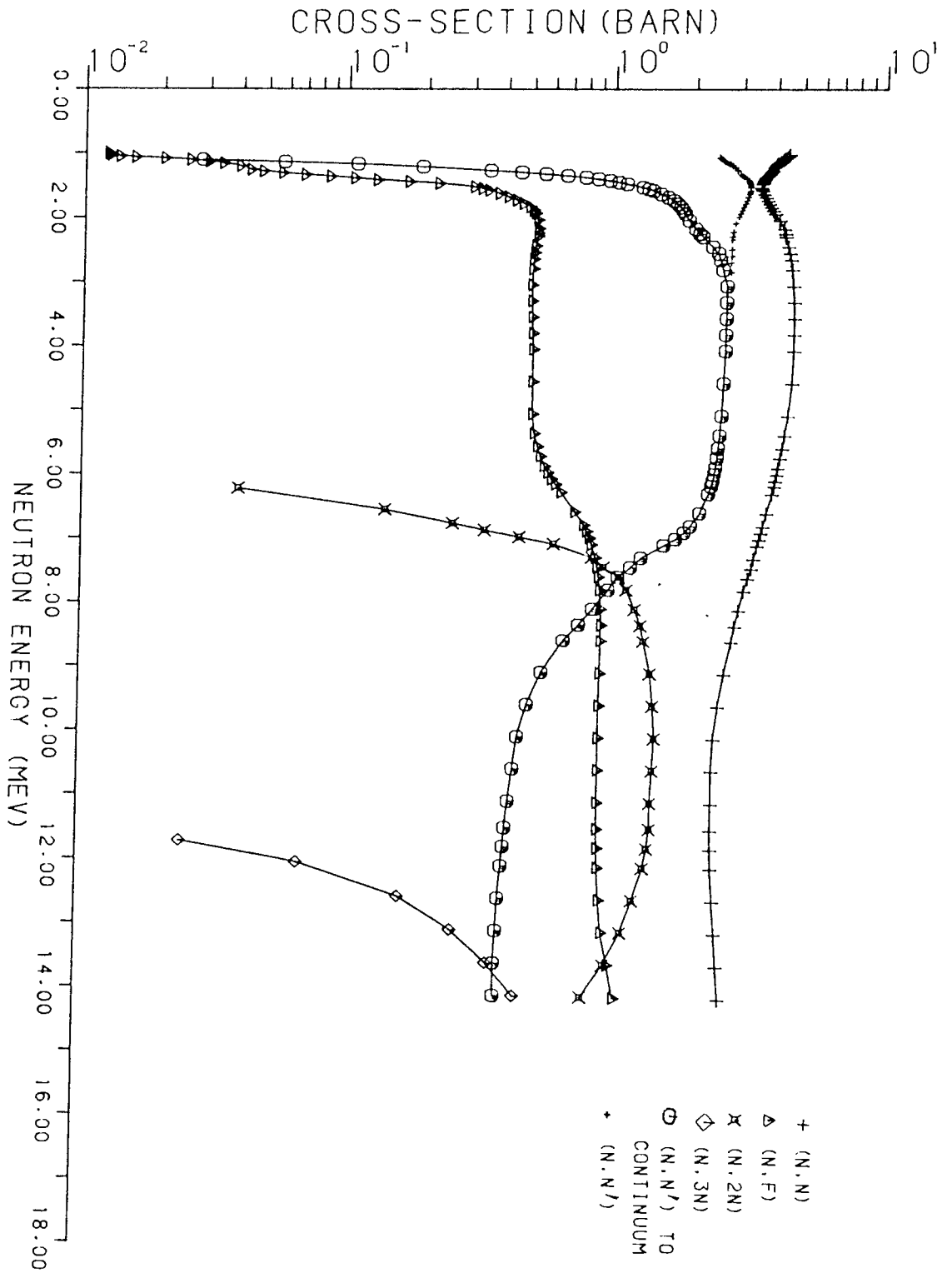


FIG. 7.5 (N,N), (N,F), (N,2N), (N,3N), (N, N') TO CONTINUUM AND (N,N') CROSS-SECTIONS OF U-238 .

(n,2n) and (n,3n) reactions in these cases, but elastic scattering will mainly affect the low energy range centred on 4 MeV.

For (n,n') to continuum, the inelastically scattered neutron energy is about 13 MeV and this appears in the experimental curve as a peak at about 12.5 MeV.

7.4 Neutron Spectra For LiF Slabs

Figures (7.6), (7.7) and (7.8) show measured and calculated neutron spectra emitted from 5.4, 8.2 and 10.9 cm thick LiF slabs [diagrams (6.6 A, B and C)].

Lithium fluoride consists of natural lithium (isotopic composition is 92.44 % ${}^7\text{Li}$ and 7.56 % ${}^6\text{Li}$) and fluorine ${}^{19}\text{F}$. The main reaction in ${}^7\text{Li}$ for 14.1 MeV neutrons is elastic scattering (0.98 barn compared with 0.48 barn for non - elastic) and is hidden in the 14 MeV transmission peak because the elastic scattering is strongly forward peaked. At 14 MeV region, as before with uranium, the calculated spectrum is wider than measured by about 0.3 MeV for the same reasons. The (n,2n) reaction in Li - 7 has a threshold at 8.3 MeV with a cross section at 14 MeV of 0.02 barn [figure (7.9)] which causes secondary neutrons in the energy region below 4 MeV. The (n,2n α) reaction with a 14 Mev cross section of 0.03 barn produces secondary neutrons below about 3 MeV. The (n,n') scattering of 14 MeV neutrons which excites the continuum of nuclear levels produces secondary neutrons from about 1 MeV to 12 MeV, but experimently very few neutrons in the energy range 10 - 12 MeV were observed. The peak around 8 MeV is attributed to the

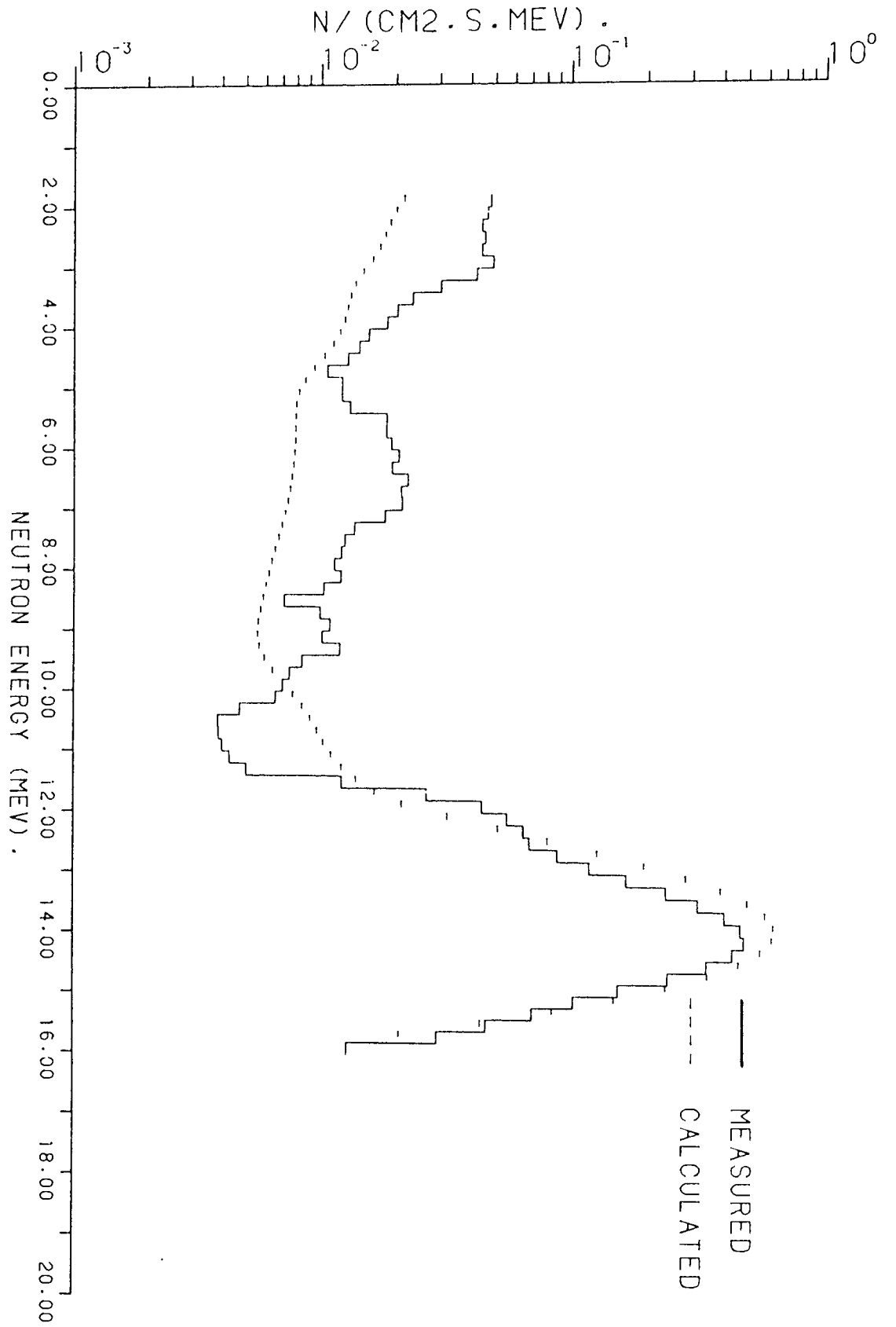


FIG. 7.6 NEUTRON FLUX AT THE SURFACE OF 5.4 CM THICK LIF SLAB.

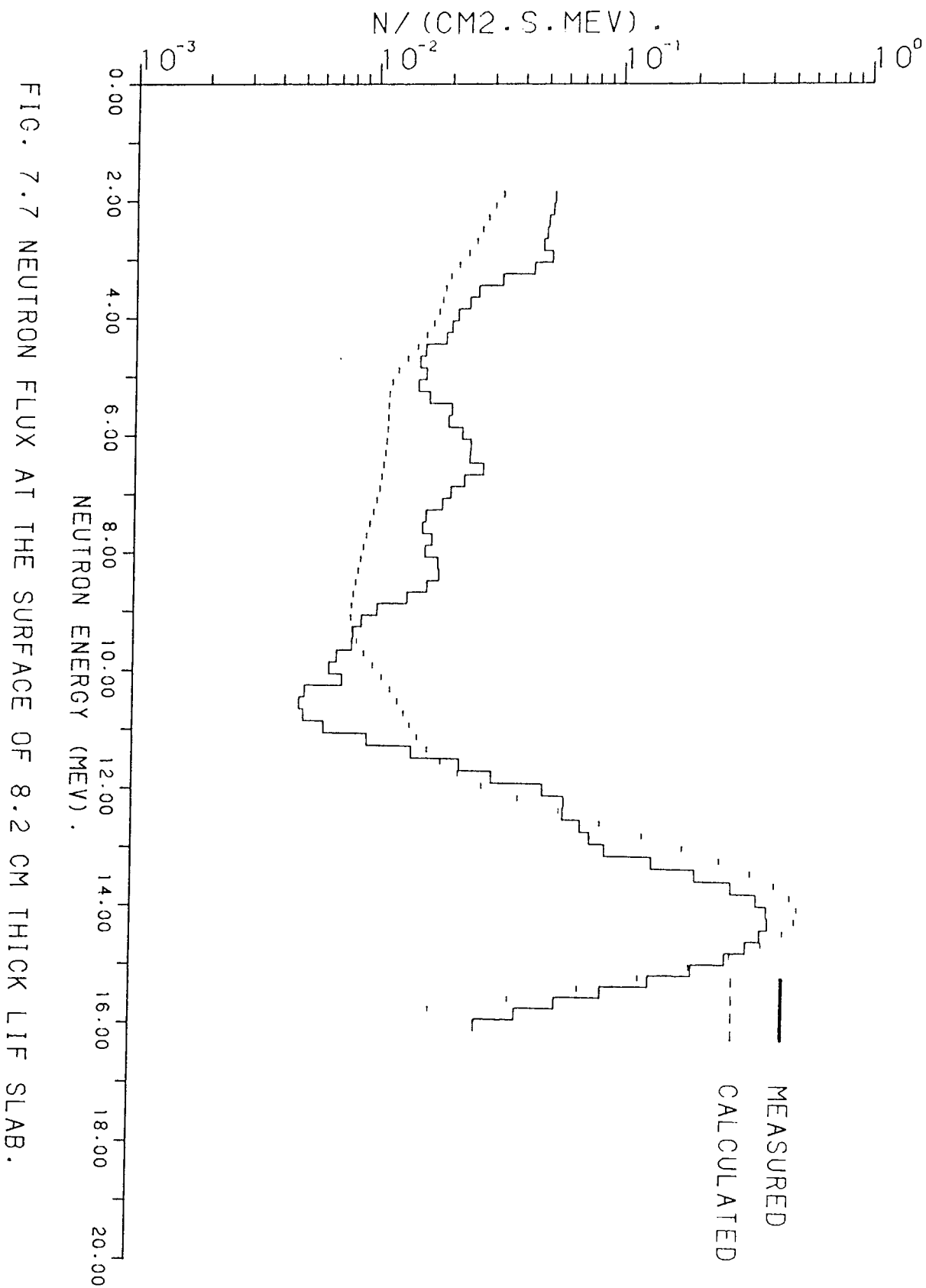


FIG. 7.7 NEUTRON FLUX AT THE SURFACE OF 8.2 CM THICK LIF SLAB.

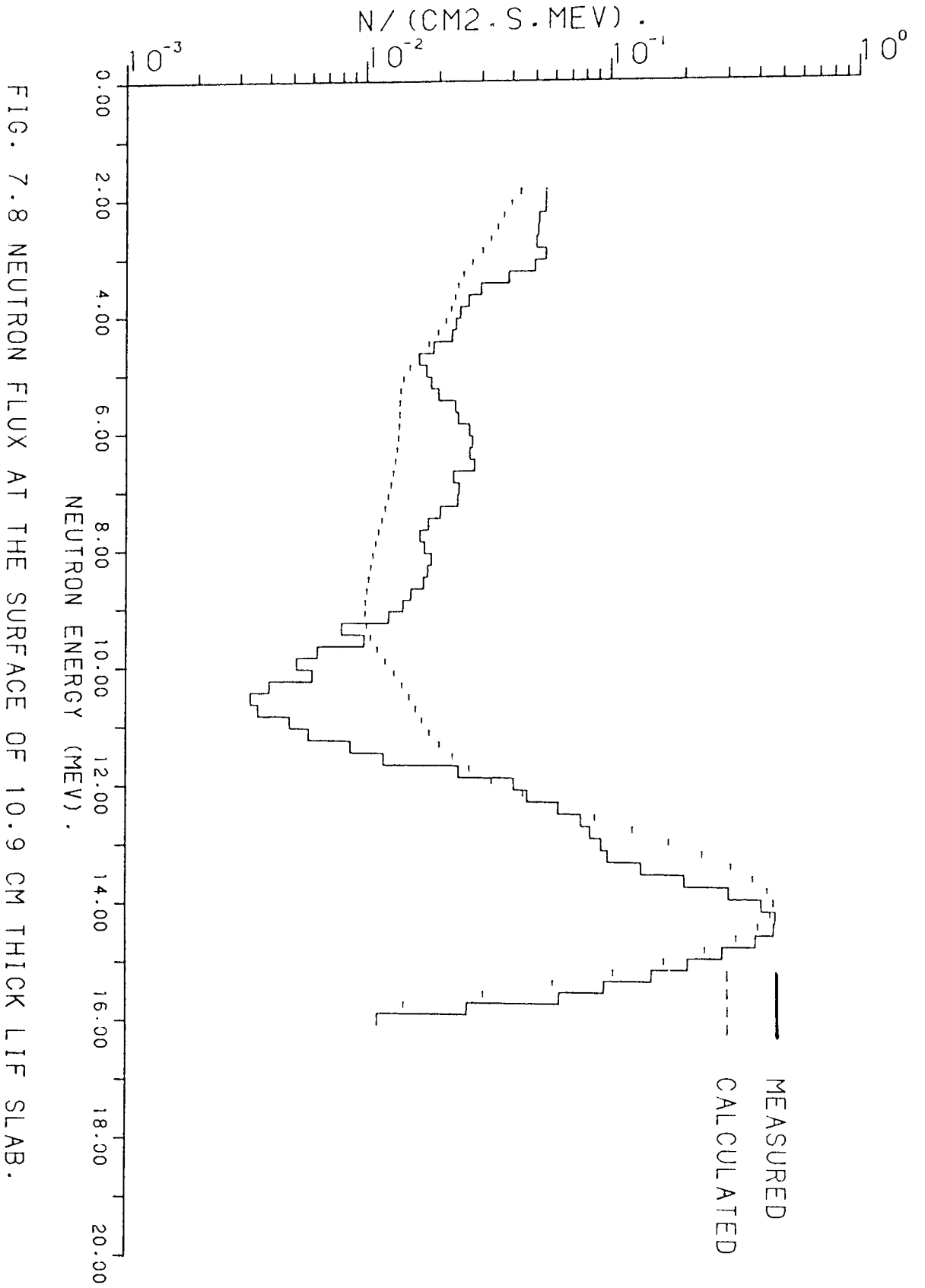


FIG. 7.8 NEUTRON FLUX AT THE SURFACE OF 10.9 CM THICK LIF SLAB.

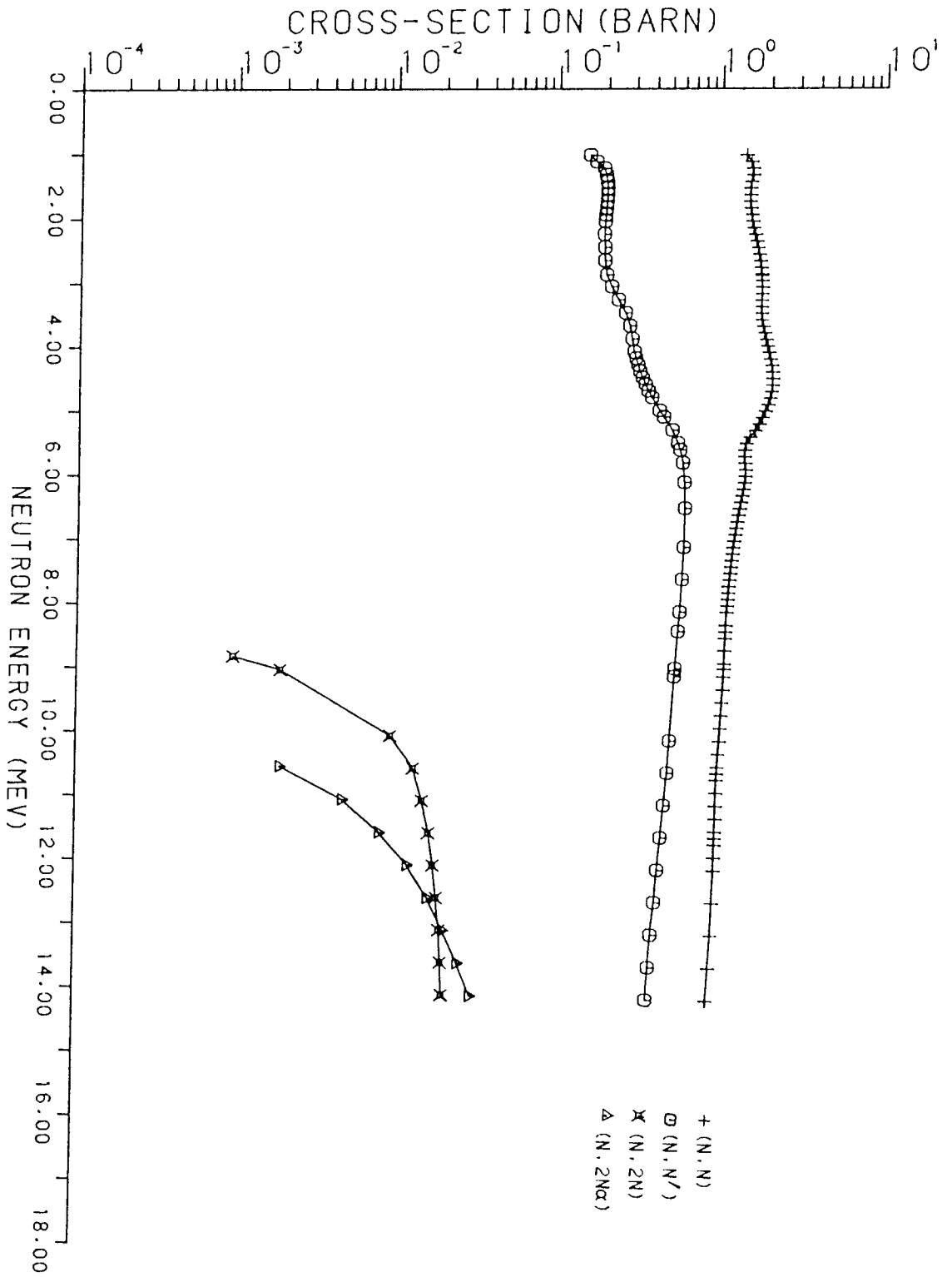


FIG. 7.9 (N,N), (N,N'), (N,2N) AND (N,2Nα) CROSS-SECTIONS OF LITHIUM-7.

secondary neutrons emitted by the inelastic scattering which results from the excitation of Li - 7 nucleus to the discrete energy level. The contribution of inelastic scattering is effective up to the second level for lithium - 7 ($Q_1 = - 0.478$ and $Q_2 = - 4.63$ MeV). For lithium - 6, the $(n,2n\alpha)$ reaction produces secondary neutrons with energies from 1.2 to 4.8 MeV. The elastic scattering of neutrons from the 14.1 MeV source is also not isotropic as in Li - 7 and the energy of most scattered neutrons is therefore close to 14 MeV source peak. The elastic cross section at 14 MeV is 0.88 barn compared with 0.55 barn for non - elastic cross section. The (n,n') in Li - 6 has a threshold at 1.716 MeV with a cross section 0.44 barn at 14 MeV neutron energy [figure (7.10)].

For fluorine, the $(n,2n)$ reaction has a threshold of 10.98 MeV with 0.05 barn at 14 MeV [figure (7.11)]. The secondary neutrons from this reaction have energies below about 3.5 MeV. The secondary neutrons emitted from $(n,n\alpha)$ reaction have energies below about 5 MeV. This reaction has a threshold of 5.13 MeV with 0.05 barn at 14 MeV. For (n,np) reaction with F - 19 , the threshold is 8.41 MeV with 0.01 barn at 14 MeV. The secondary neutrons have energies below 6 MeV.

In general, it was confirmed that the observed spectra in LiF was formed by a small number of collisions in the assembly, i.e, the first collision and its secondary neutrons distribution with respect to energy and scattering angles mainly contributed to the spectra.

There is relatively good agreement between the calculated and measured spectra in LiF slabs in the energy range above 11.5 MeV, except that the theoretical spectrum in the 14 MeV is wider than the experimental by about 0.3 MeV. It means that the effect of transverse

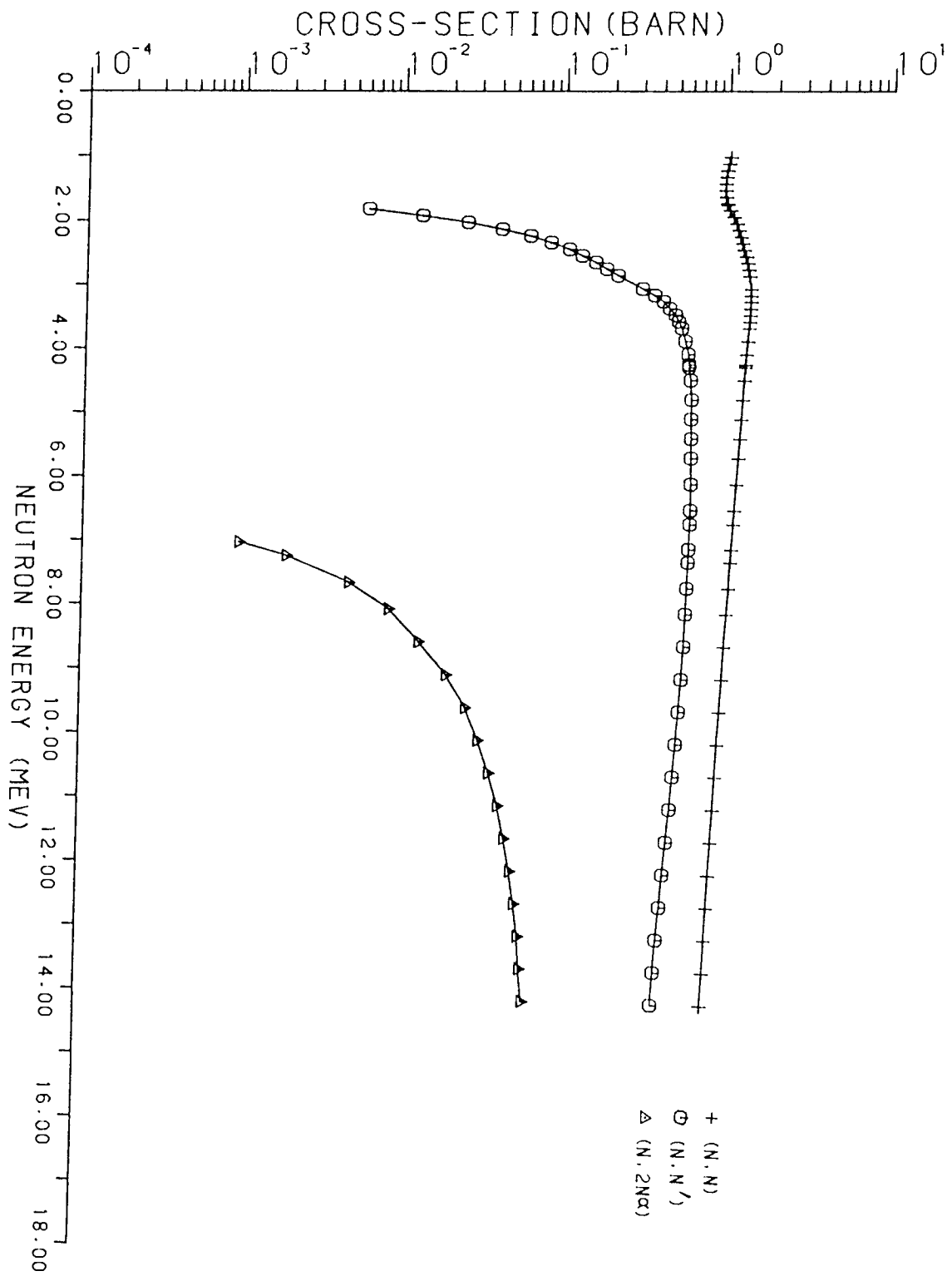


FIG. 7.10 (N,N), (N,N') AND (N,2Nα) CROSS-SECTIONS OF LITHIUM - 6.

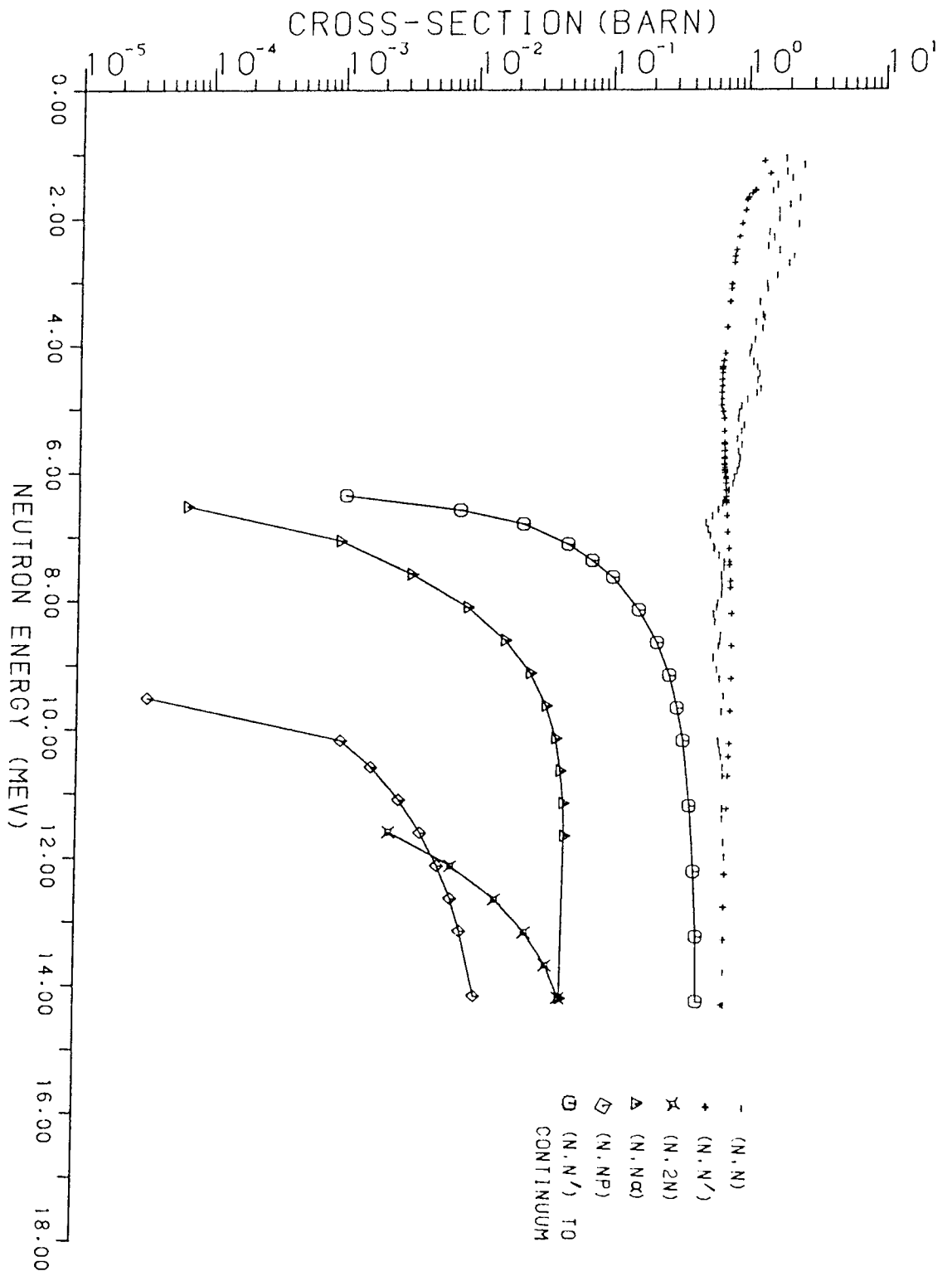


FIG. 7.11 (N,N), (N,N'), (N,2N), (N,Nα), (N,N') TO CONTINUUM AND (N,N') CROSS SECTIONS

leakage is small in the energy range, since secondary neutrons from the strongly forward elastic and first level inelastic scattering Q_1 (≈ 0.478 MeV) for the 14.1 MeV neutrons mainly contributed to the spectrum.

Large differences are observed in the low energy range because the effect of the background due to the floor and the walls surrounding the source which appear clearly in unshielded source spectra below 8 MeV [figure (7.1)]. The difference decreases with increase of the slab thickness, especially below about 5 MeV, because if the thickness increases, the streaming effect decreases, and the neutrons are more isotropic than ones emitted from the thin lithium slab due to multiple collisions. However, it is still necessary to include the full anisotropy of nonelastic scattering into the neutron transport collision, because the space-dependent formation of neutron spectra in a blanket assembly will be sensitive to the anisotropies of all kinds of scattering⁽¹⁸¹⁾, as can be seen from the dependence of leakage spectra upon slab thickness.

Figures (7.6 R), (7.7 R) and (7.8 R) show the new calculated spectra using the experimentally determined neutron source which includes neutrons scattered from the surroundings. The results are in good agreement between measured and calculated spectra in this case.

It was not felt necessary to perform the experimental source calculations with assemblies containing uranium since the neutron attenuation in uranium is large and so the lower energy part of the source spectrum will be strongly absorbed.

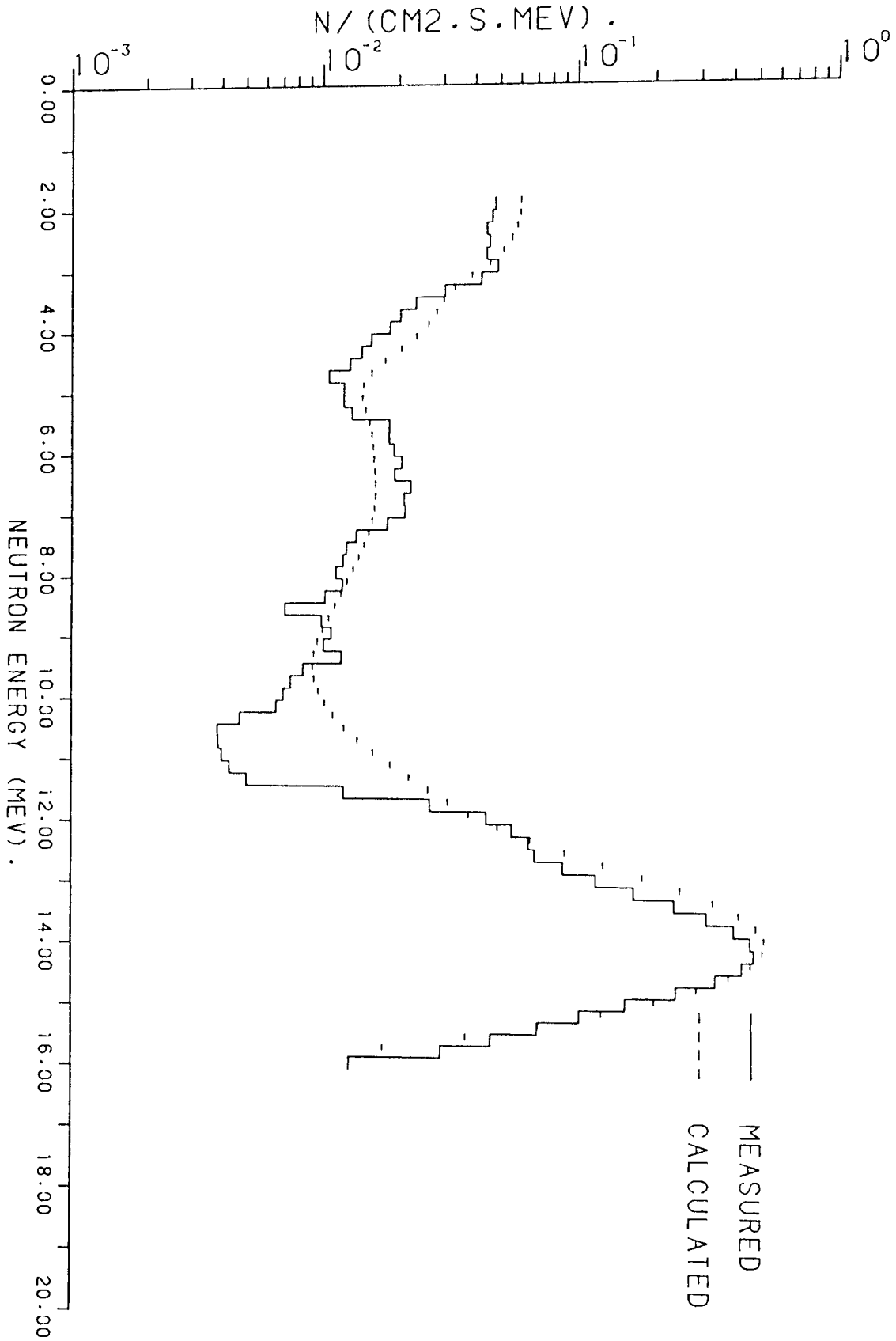


FIG. 7.6R NEUTRON FLUX AT THE SURFACE OF 5.4 CM THICK LIF SLAB
INCLUDING NEUTRONS SCATTERED FROM THE SURROUNDINGS.

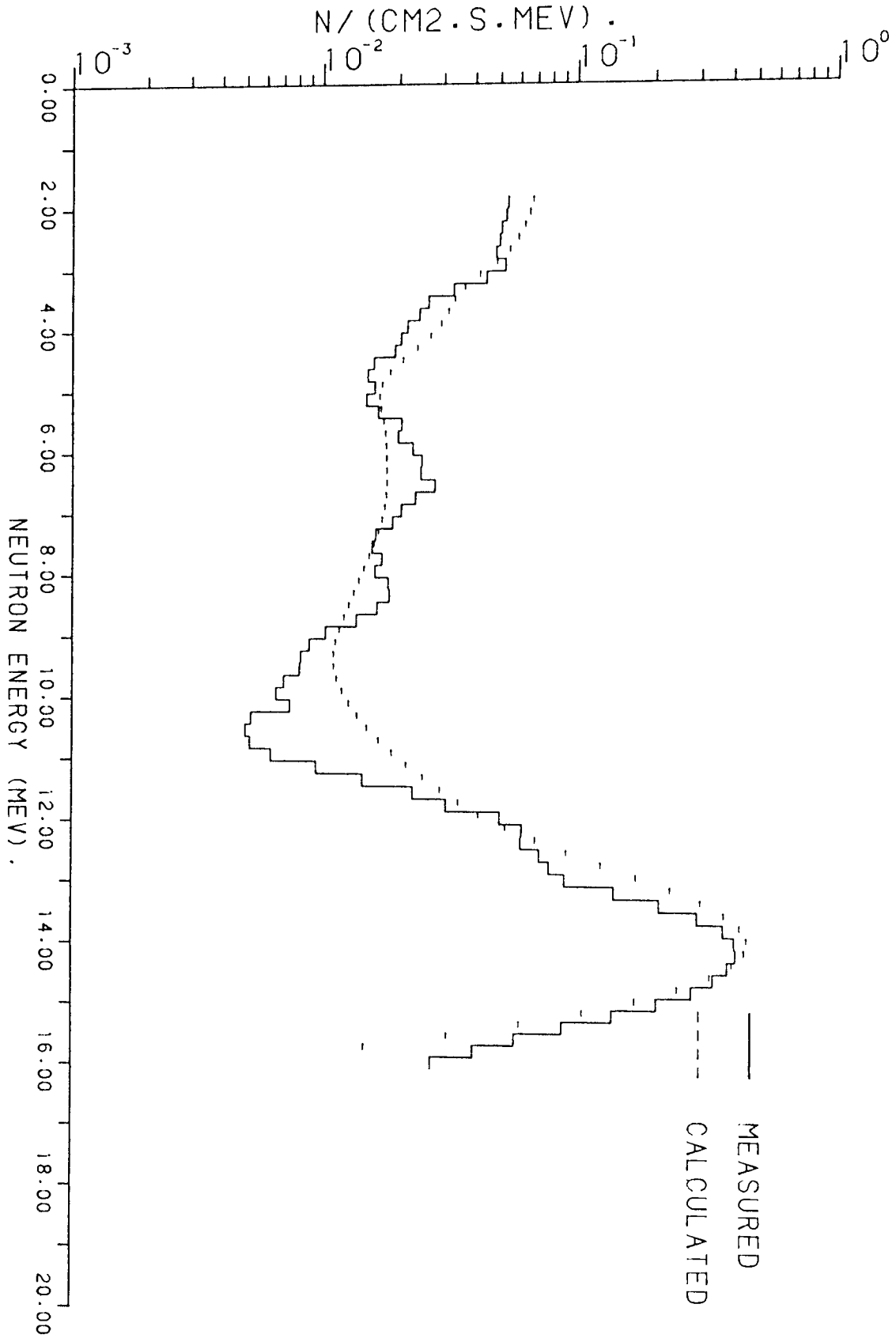


FIG. 7.7R NEUTRON FLUX AT THE SURFACE OF 8.2 CM THICK LiF SLAB
CALCULATED NEUTRON FLUX FROM THE NEUTRON SOURCE

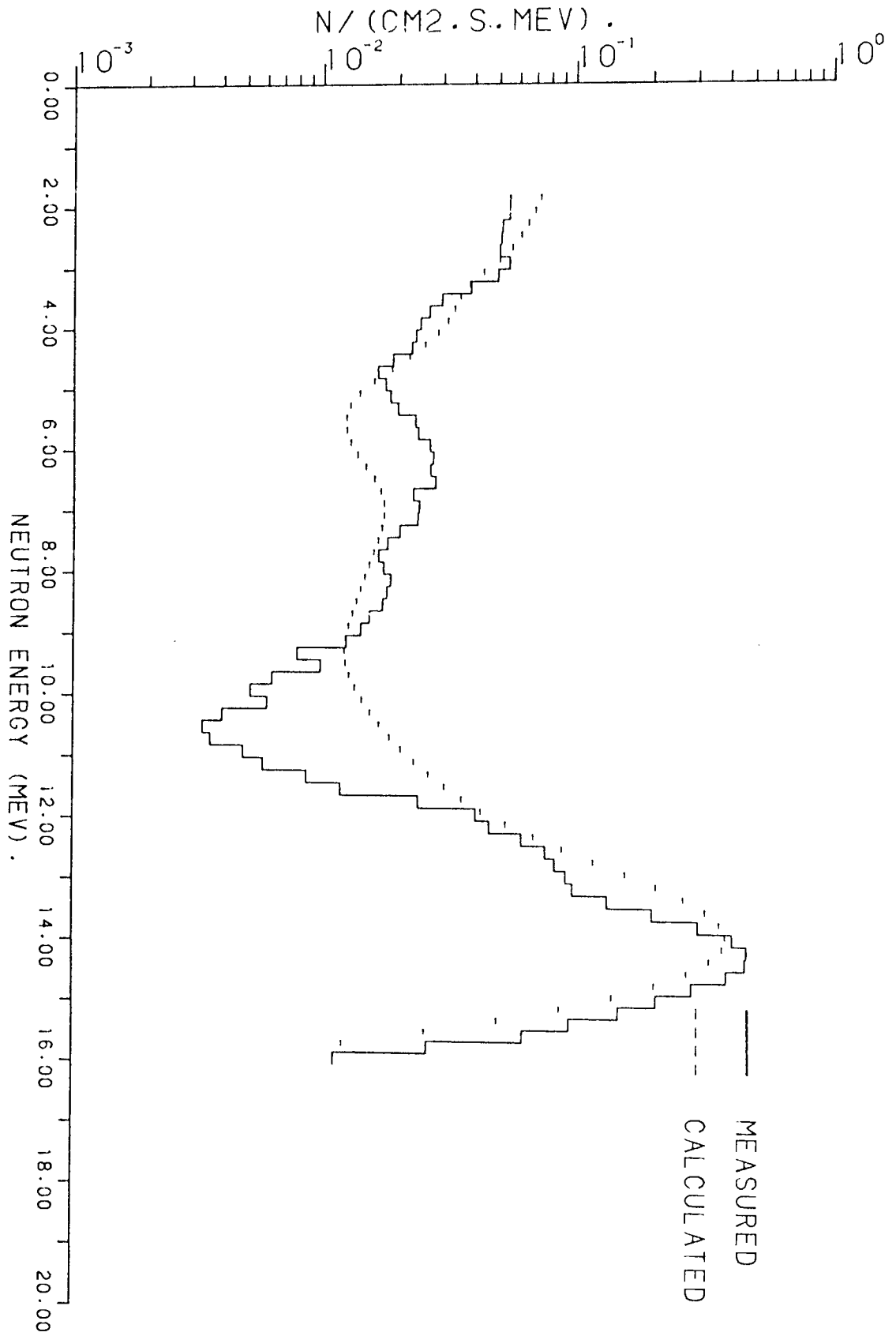


FIG. 7.8R NEUTRON FLUX AT THE SURFACE OF 10.9 CM THICK LiF SLAB

From the figures (7.2) to (7.8 R), it can be seen that, in the energy region below 6 MeV, the flux is higher in a uranium shield than a LiF in the same thickness. That is because, for lighter elements (LiF) elastic slowing down is important, whereas for heavy elements (uranium) the slowing down of the neutron by inelastic scattering is the main interaction which produces directly more low energy neutrons together with fission neutrons.

5 Neutron Spectra From A Mixture Of LiF And Uranium Slabs

Neutron fluxes at the surface of samples containing mixture of LiF and uranium bars (1 : 1) with 5.4, 8.2, 10.9, 13.6, 16.3, 19 and 21.7 cm thicknesses [diagrams A, B, C, D, E, F and G in figure (6.7)] are shown in figures (7.12), (7.13), (7.14), (7.15), (7.16), (7.17) and (7.18) respectively.

In general, the shape of spectrum does not change very much with thickness and measured spectra are in satisfactory agreement with those calculated for most thicknesses.

Comparing LiF and uranium slabs with same thickness as the mixture slabs, it was found that :

- For lithium fluoride slabs 5.4, 8.2 and 10.9 cm thick ;

Measured fluxes through mixture slabs below about 5 MeV are higher than in LiF slabs. This is because uranium causes an increase in flux in the low energy region due to fission as discussed in section 7.3.

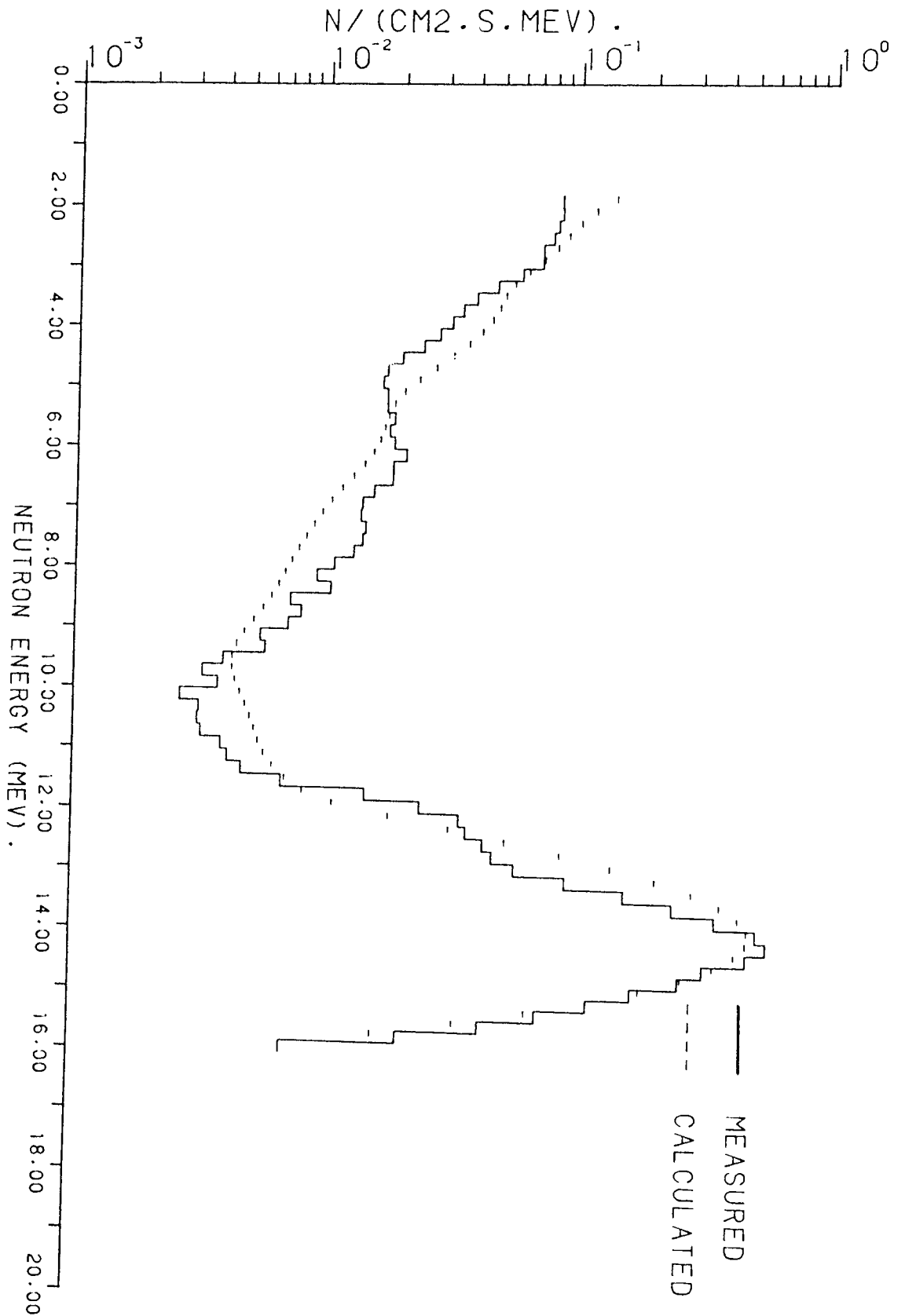


FIG. 7.12 NEUTRON FLUX AT THE SURFACE OF 5.4 CM THICK SLAB OF

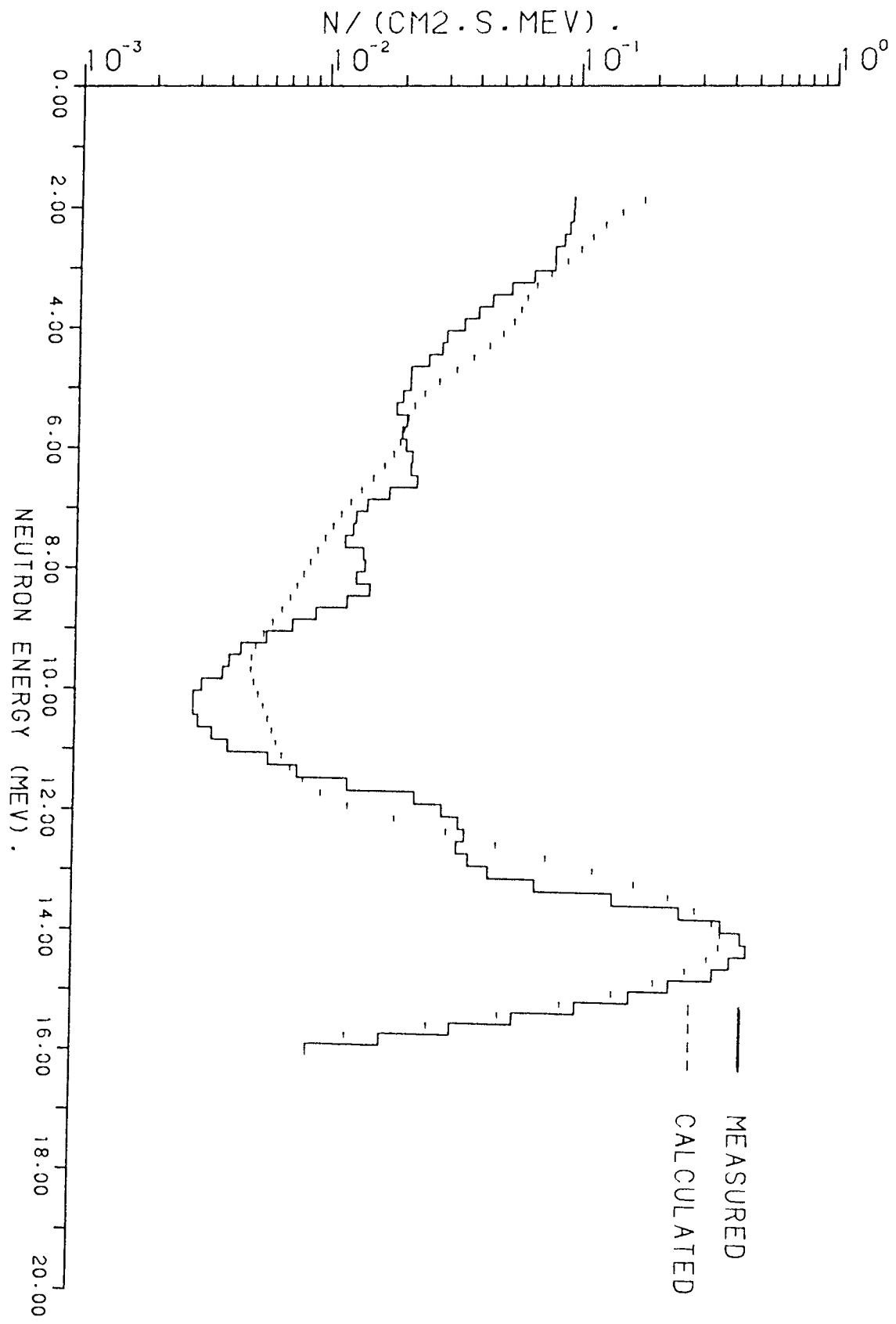


FIG. 7.13 NEUTRON FLUX AT THE SURFACE OF 8.2 CM THICK SLAB OF

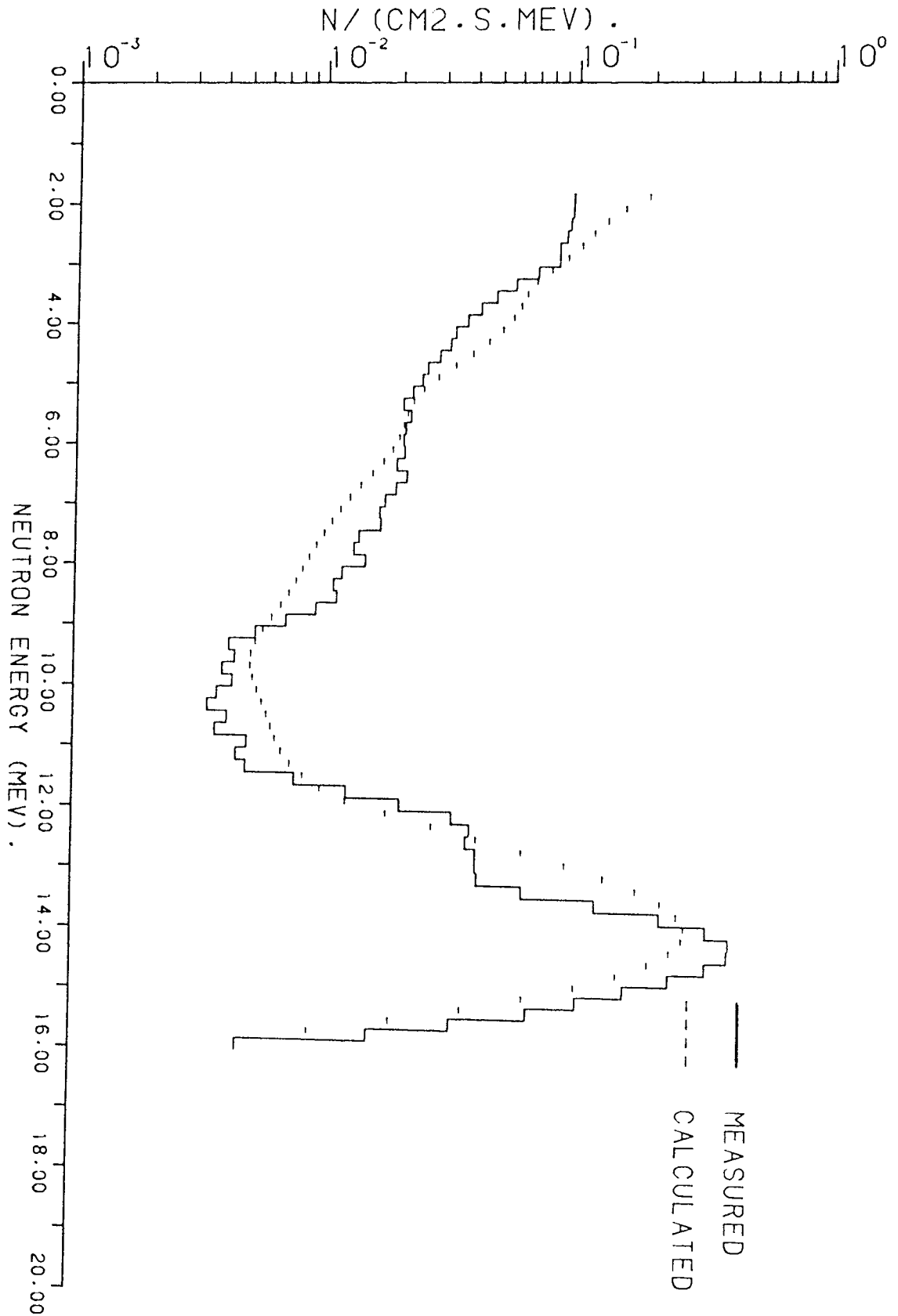


FIG. 7.14 NEUTRON FLUX AT THE SURFACE OF 10.9 CM THICK SLAB OF

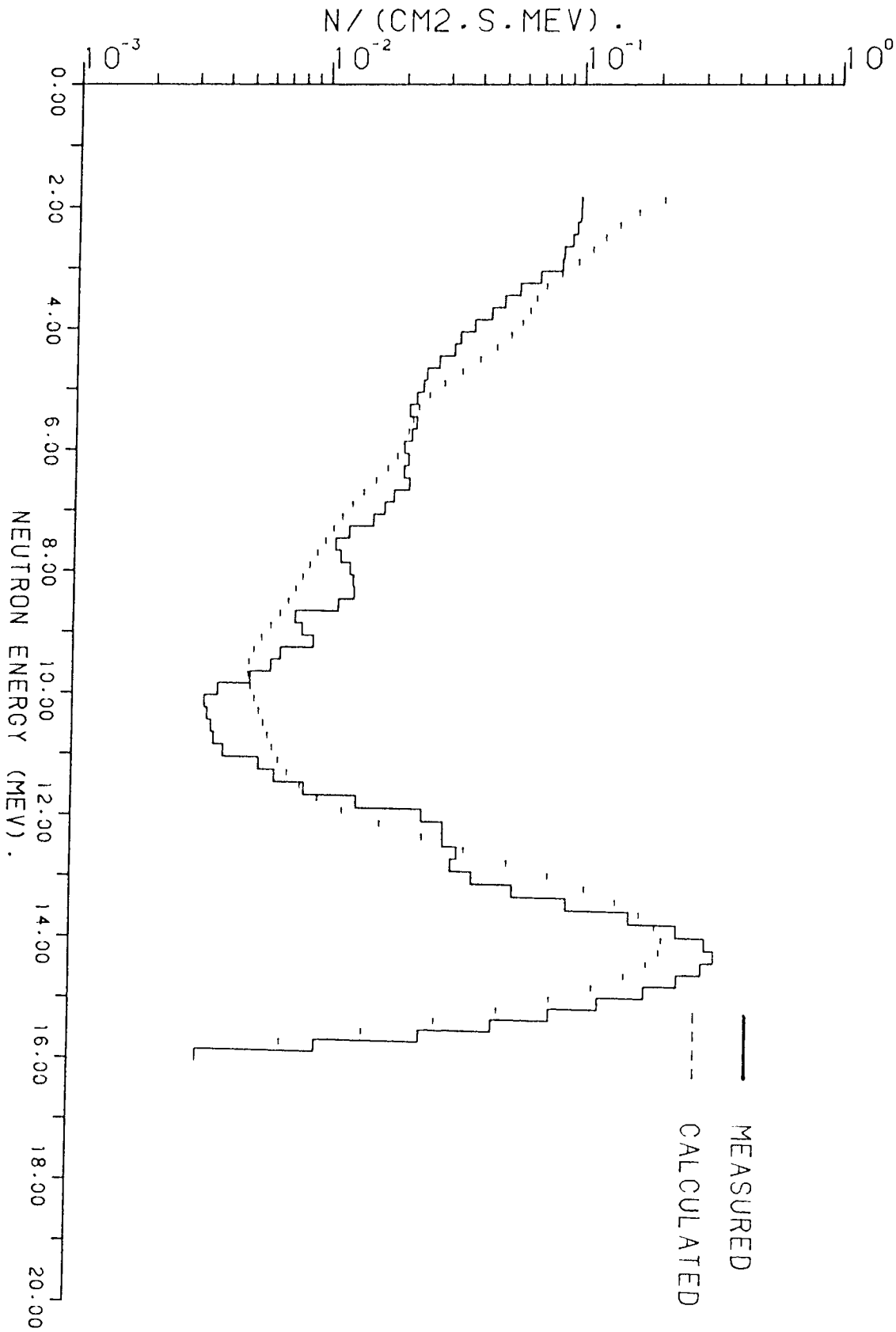


FIG. 7.15 NEUTRON FLUX AT THE SURFACE OF 13.6 CM THICK SLAB OF URANIUM AND LIF MIXTURE.

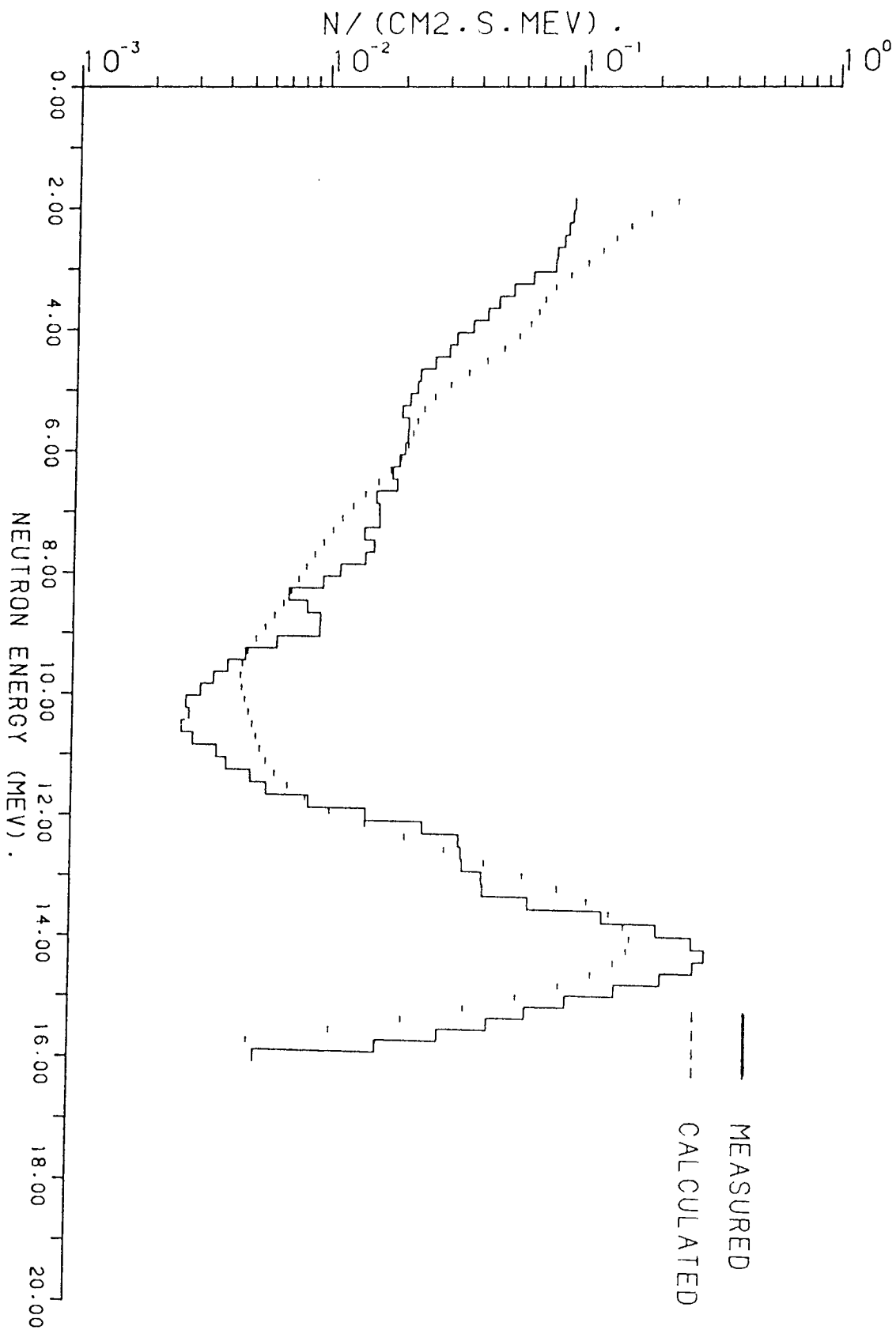


FIG. 7.16 NEUTRON FLUX AT THE SURFACE OF 16.3 CM THICK SLAB OF
DIPYANTHIM AND ITS ACTIVATION

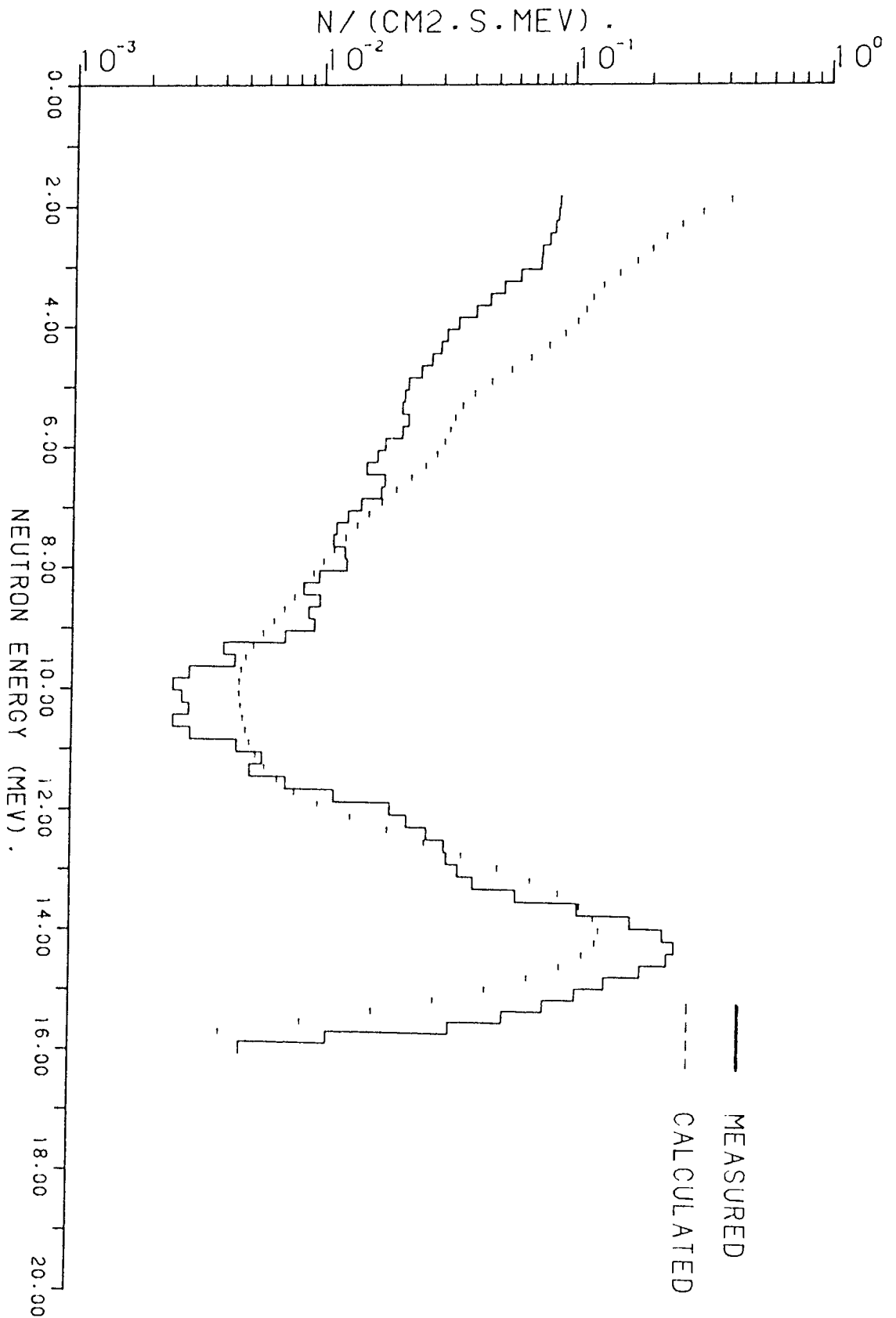


FIG. 7.17 NEUTRON FLUX AT THE SURFACE OF 19 CM THICK SLAB OF

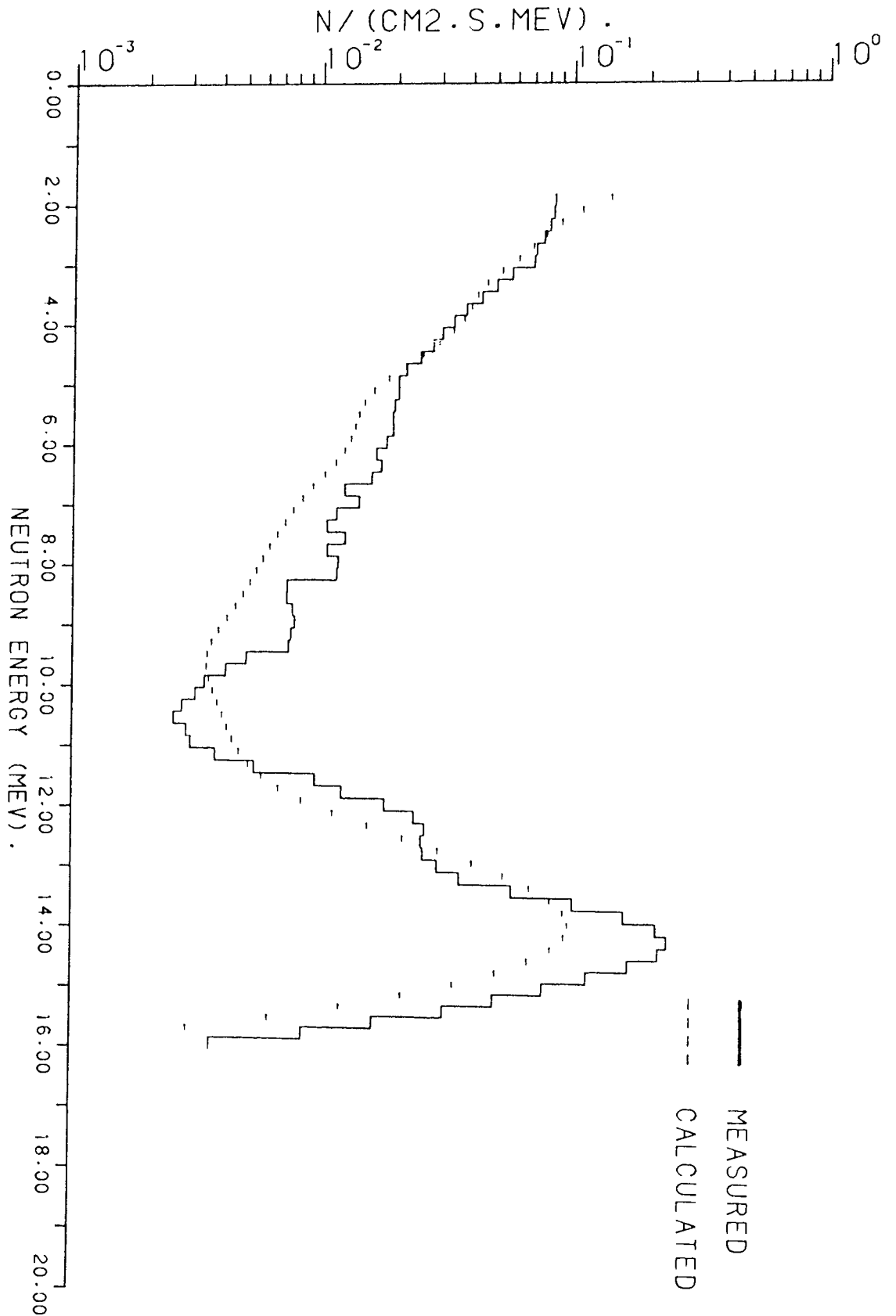


FIG. 7.18 NEUTRON FLUX AT THE SURFACE OF 21.7 CM THICK SLAB OF URANIUM AND ITS MYTHIC

2- Above about 5 MeV neutron energy, fluxes measured in LiF assemblies are slightly higher than in the mixtures. This due to the presence of uranium which due to its high density is an effective neutron absorber and uranium does not down scatter neutrons into this energy range.

- For uranium slabs 5.4, 8.2 and 10.9 cm thick ;

- Measured fluxes through mixture slabs 5.4 and 8.2 cm thick are somewhat lower than in uranium cases in the energy region 3 to 5.5 MeV. For 10.9 cm thick, measured fluxes in this range are nearly equal in both mixture and uranium. Above about 5.5 MeV, fluxes measured in mixture slabs are higher than fluxes in uranium slabs for all three thicknesses.

7.6 Neutron Spectra From Multilayer Assemblies Of U And LiF Slabs

Fast neutron fluxes at the surface of multilayer assemblies of uranium and LiF with different arrangements [diagrams (6.8 A) to (6.16 B)] have been measured and calculated and are represented in figures (7.19) to (7.44) .

7.6.1 Neutron Spectra At The Surface Of Samples Containing LiF On Top Of U

Measured and calculated fluxes from the samples presented in diagrams A, B and C in figures (6.8), (6.9) and (6.10), which contain 5.4, 8.2 and 10.9 cm LiF on top of 5.4, 8.2 and 10.9 cm uranium, are shown in figures (7.19) to (7.27) respectively.

Figures (7.19), (7.20) and (7.21) present fast neutron fluxes measured and calculated at the surface of 5.4, 8.2 and 10.9 cm LiF on top of 5.4 cm uranium [diagrams (6.8 A, B and C)].

The shape of the spectrum in these cases does not change very much with thickness. As the thickness increase the flux decreases. Generally, there is a good agreement between measured and calculated neutron fluxes for all thicknesses.

For the sample containing 8.2 cm uranium slab on bottom, measured and calculated neutron fluxes at the surface of 5.4, 8.2 and 10.9 cm LiF are shown in figures (7.22), (7.23) and (7.24) [diagrams A, B and C in figure (6.9)] respectively.

The shape of spectra in general changes slightly as the thickness increases and the flux decreases by a small value. There is a discrepancy between measured and calculated spectra below about 7 MeV. This discrepancy may be due to the error in the calculation due to incomplete convergence mentioned in section 7.1 for some cases containing uranium. The shape and values of these fluxes should be lower than the present values. Above about 7 MeV, there is a good agreement between calculated and measured spectra.

Calculated and measured fluxes at the surface of 5.4, 8.2 and 10.9 cm LiF on top of 10.9 cm uranium [diagrams (6.10 A, B and C)] are shown in figures (7.25), (7.26) and (7.27) respectively.

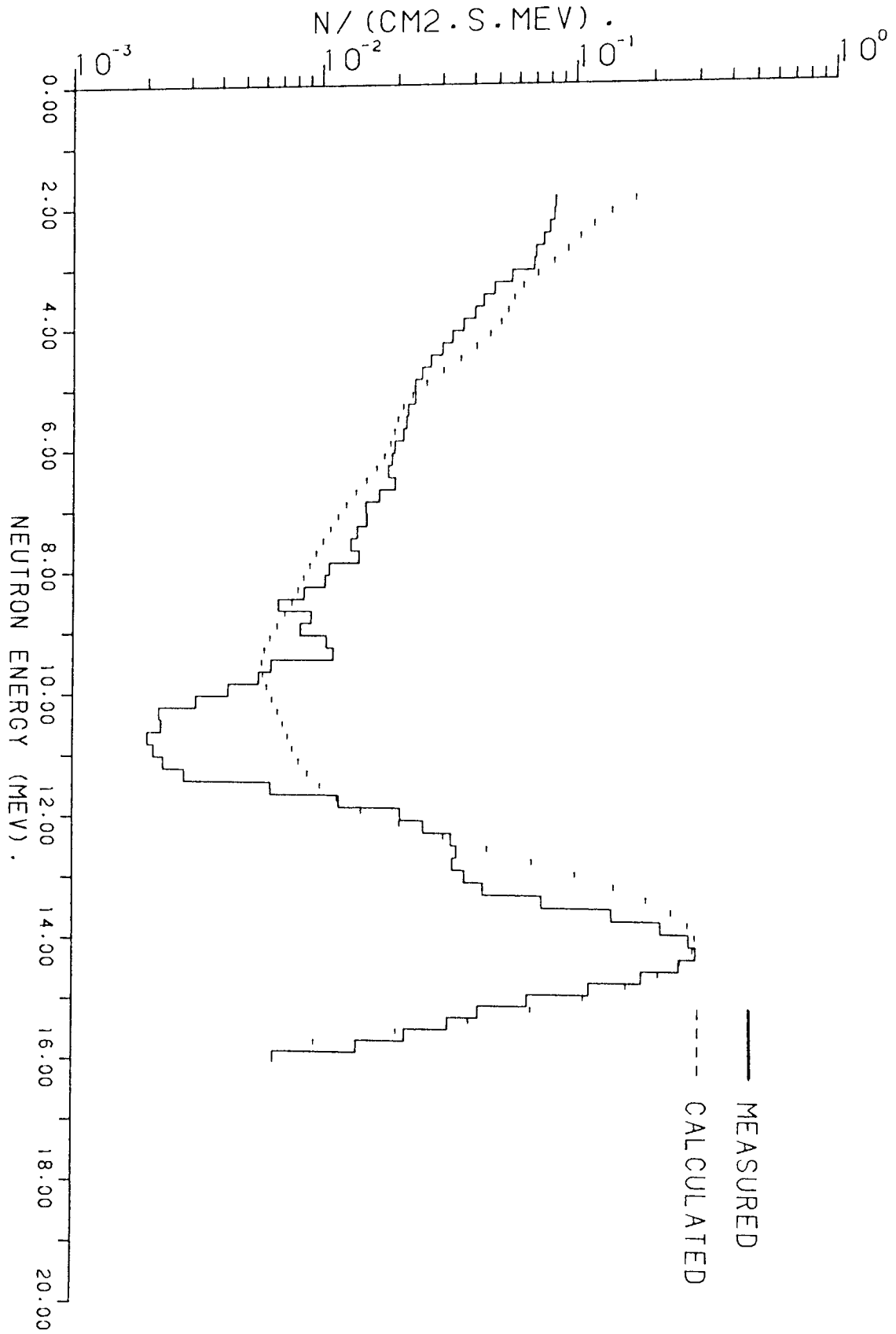


FIG. 7.19 NEUTRON FLUX AT THE SURFACE OF 5.4 CM URANIUM.
OF 5.4 CM URANIUM.

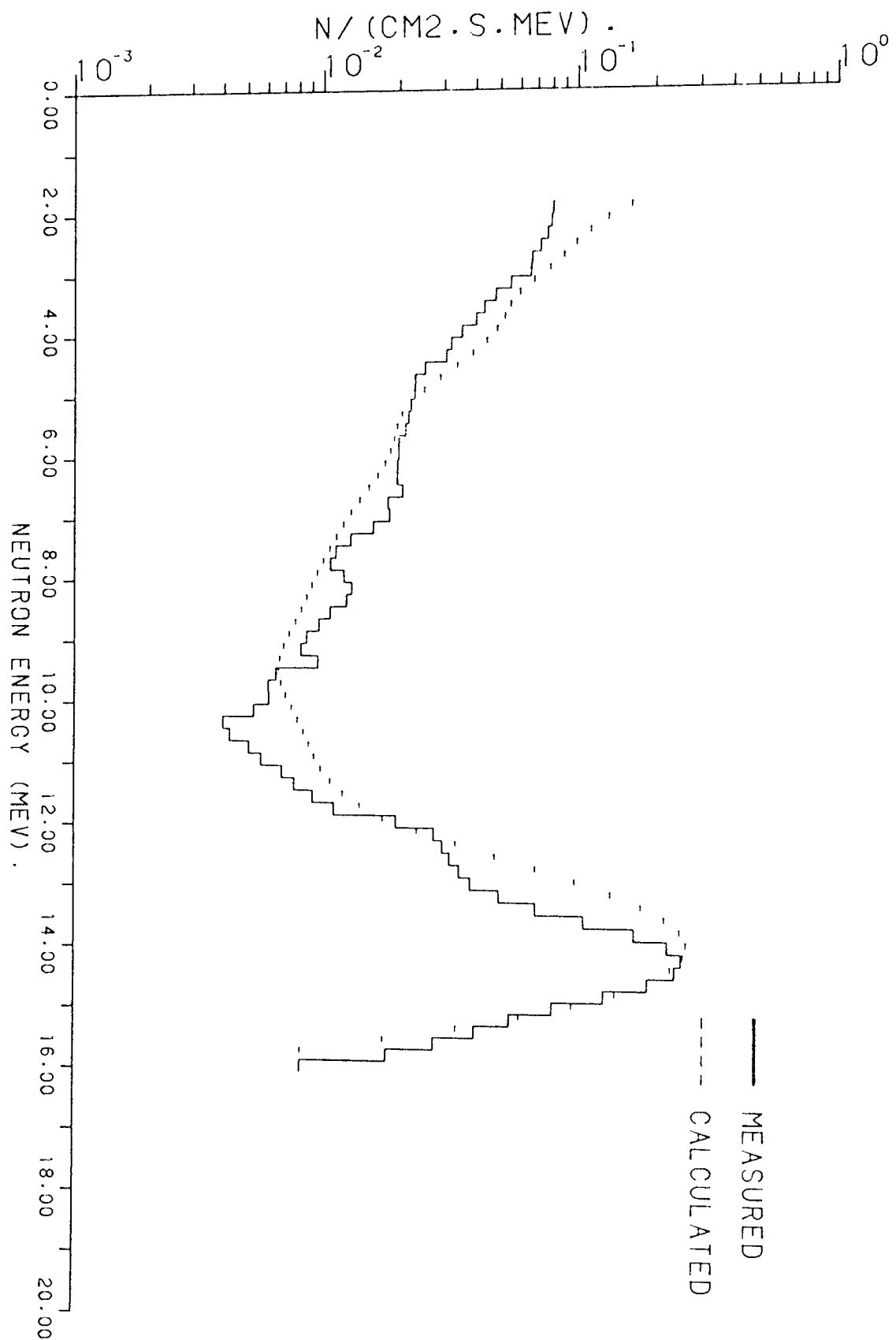


FIG. 7.20 NEUTRON FLUX AT THE SURFACE OF 8.2 CM LIF ON TOP OF 5.4 CM URANIUM.

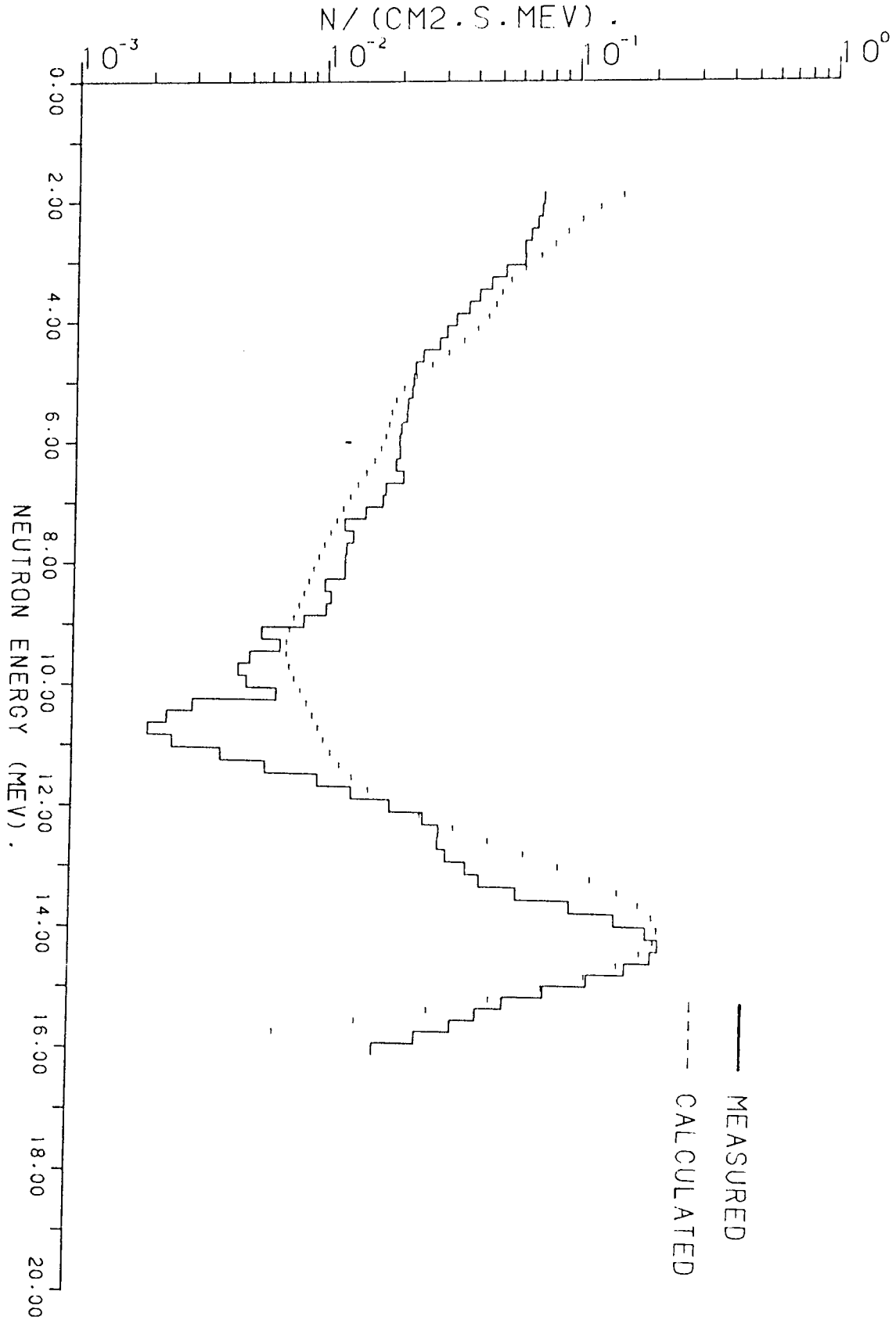


FIG. 7.21 NEUTRON FLUX AT THE SURFACE OF 10.9 CM LIF ON TOP OF 5.4 CM URANIUM.

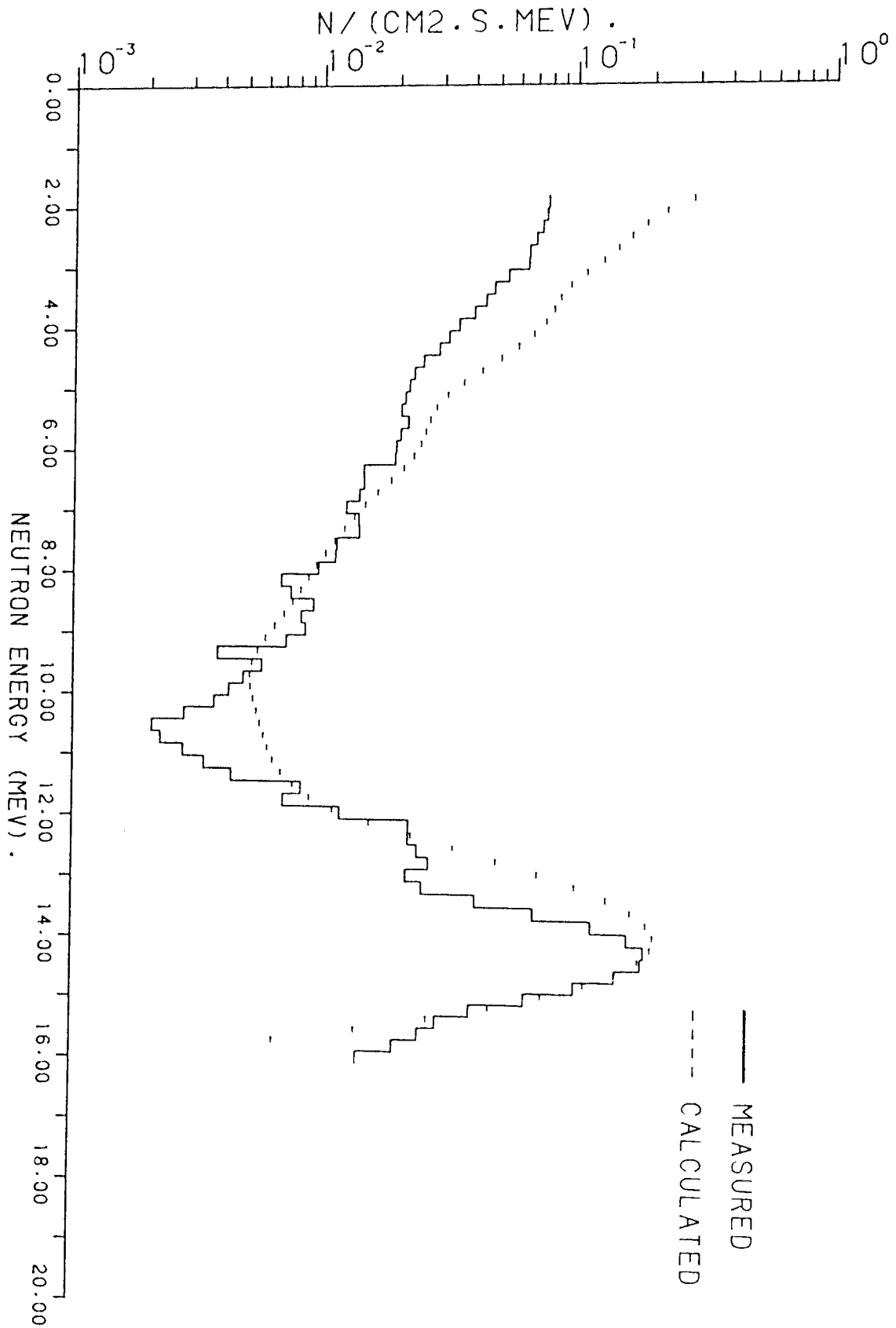


FIG. 7.22 NEUTRON FLUX AT THE SURFACE OF 5.4 CM LIF ON TOP OF 8.2 CM URANIUM.

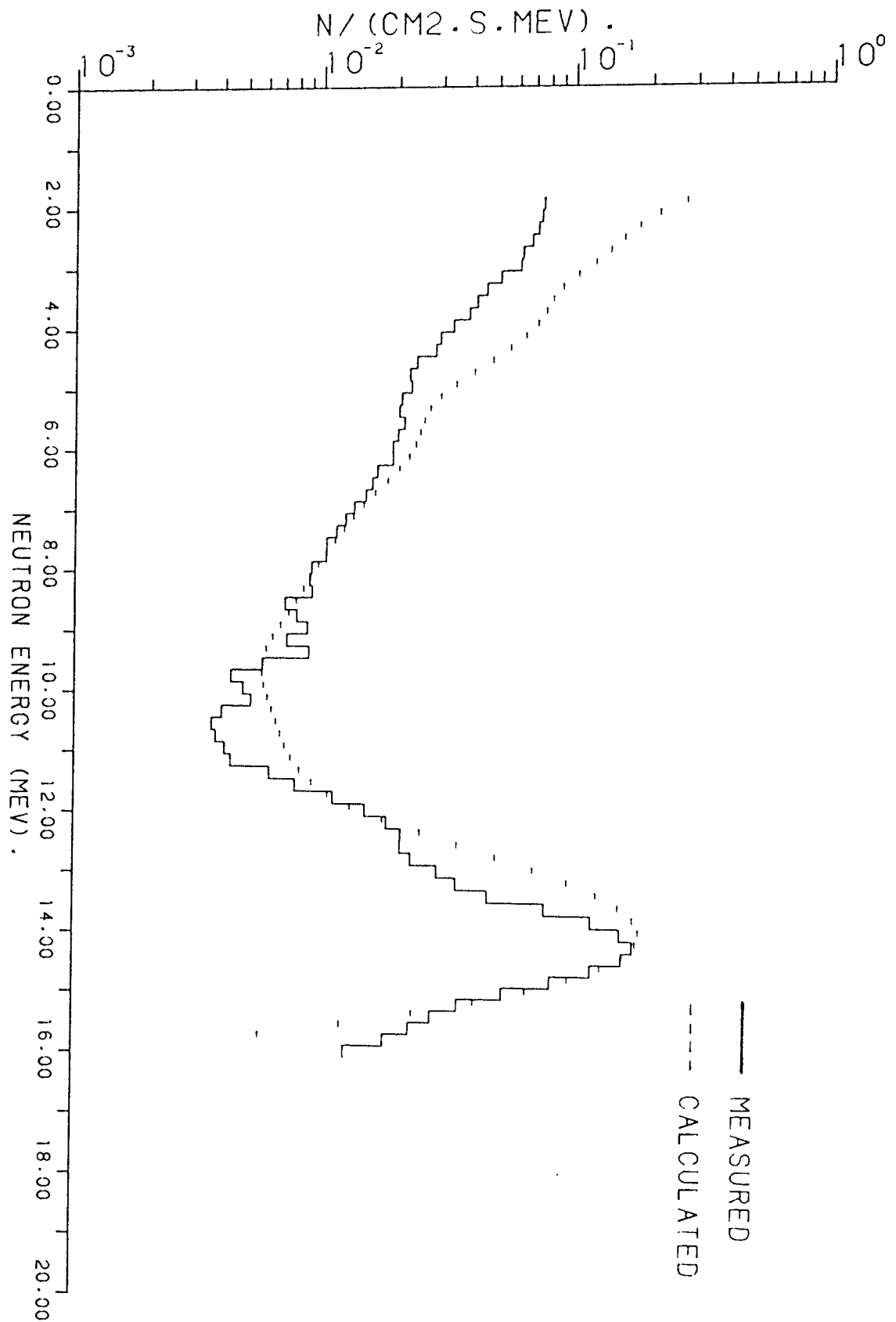


FIG. 7.23 NEUTRON FLUX AT THE SURFACE OF 8.2 CM LIF ON TOP OF 8.2 CM URANIUM.

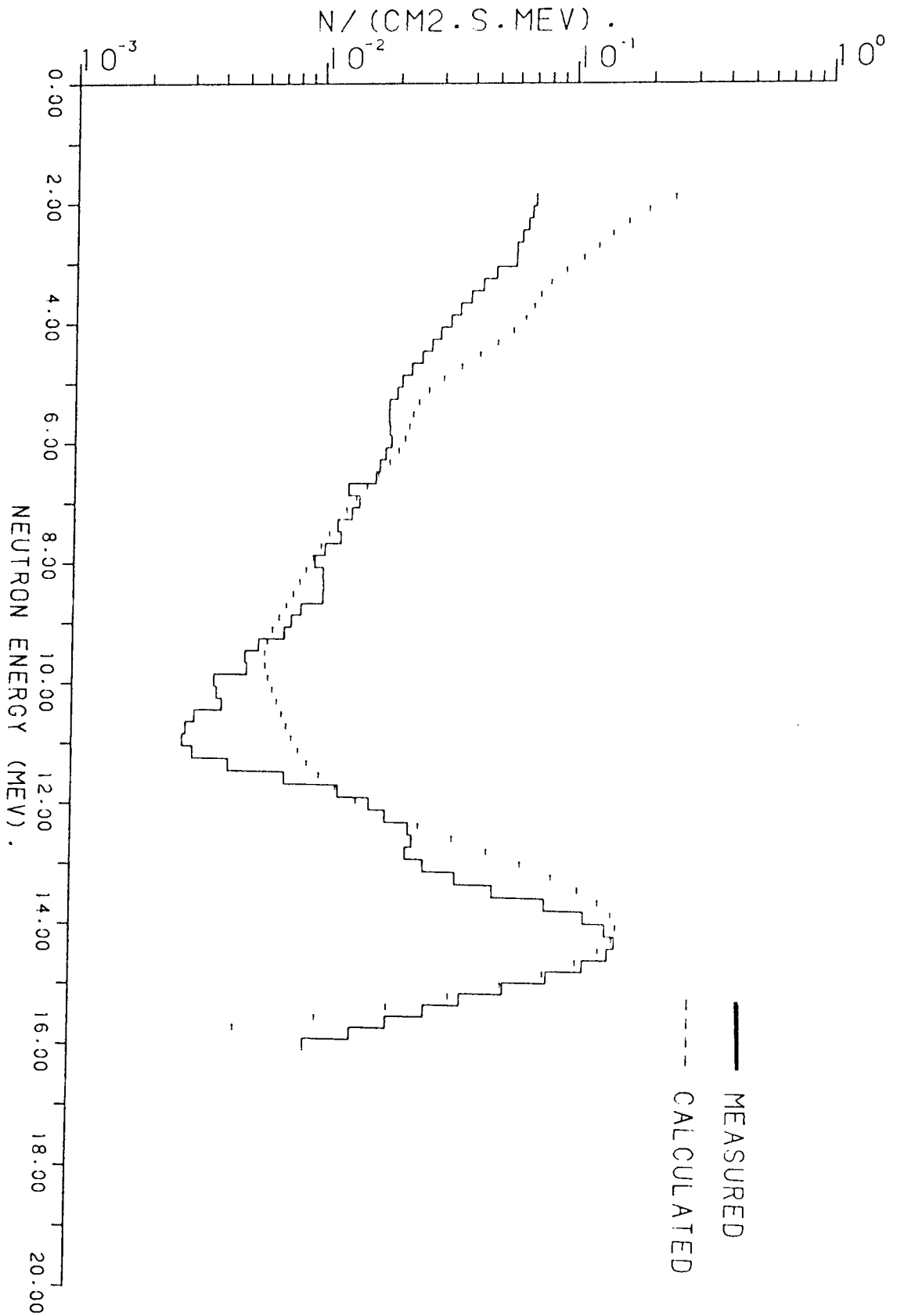


FIG. 7.24 NEUTRON FLUX AT THE SURFACE OF 10.9 CM LIF ON TOP OF 8.2 CM URANIUM.

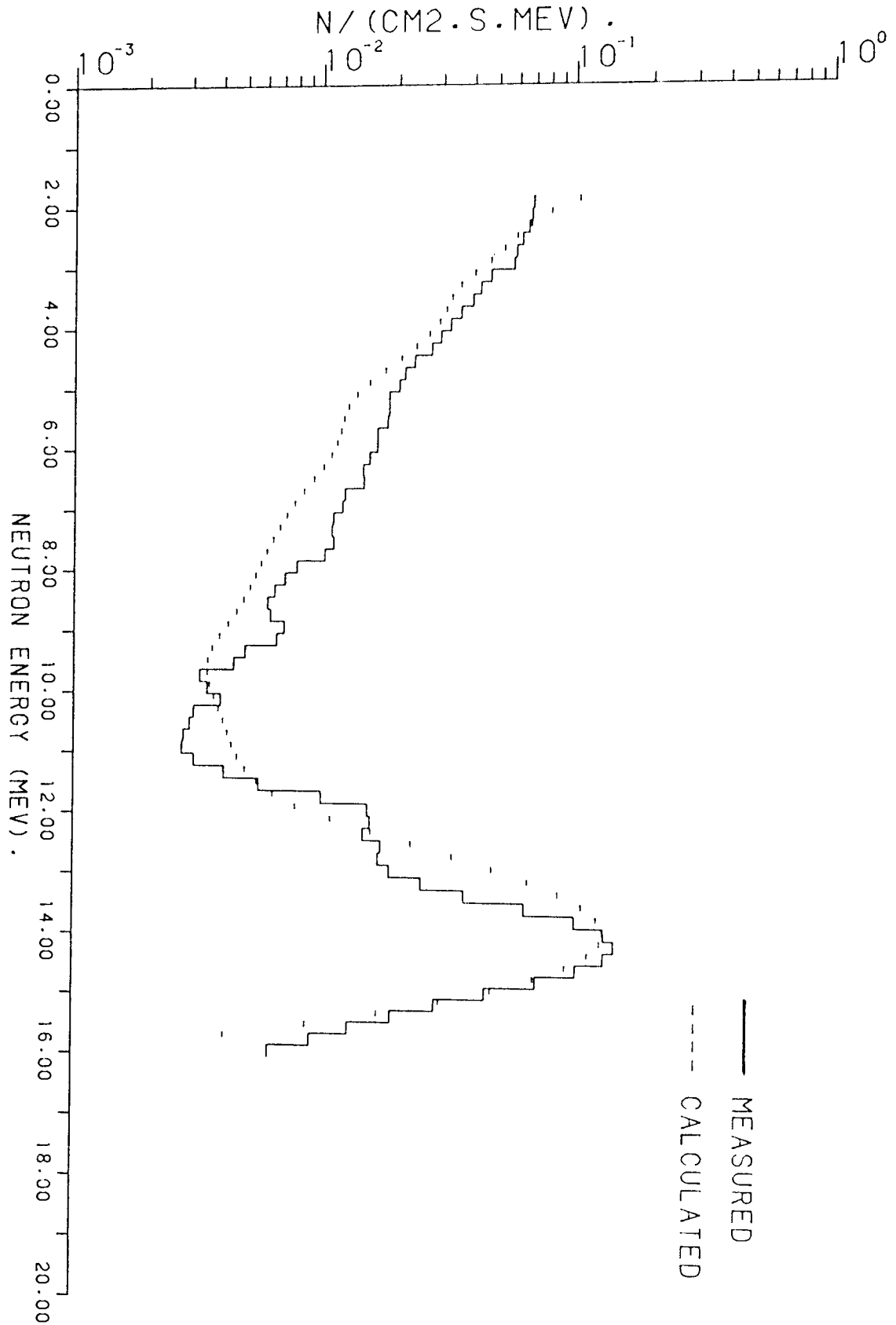


FIG. 7.25 NEUTRON FLUX AT THE SURFACE OF 5.4 CM LIF ON TOP OF 10.9 CM URANIUM.

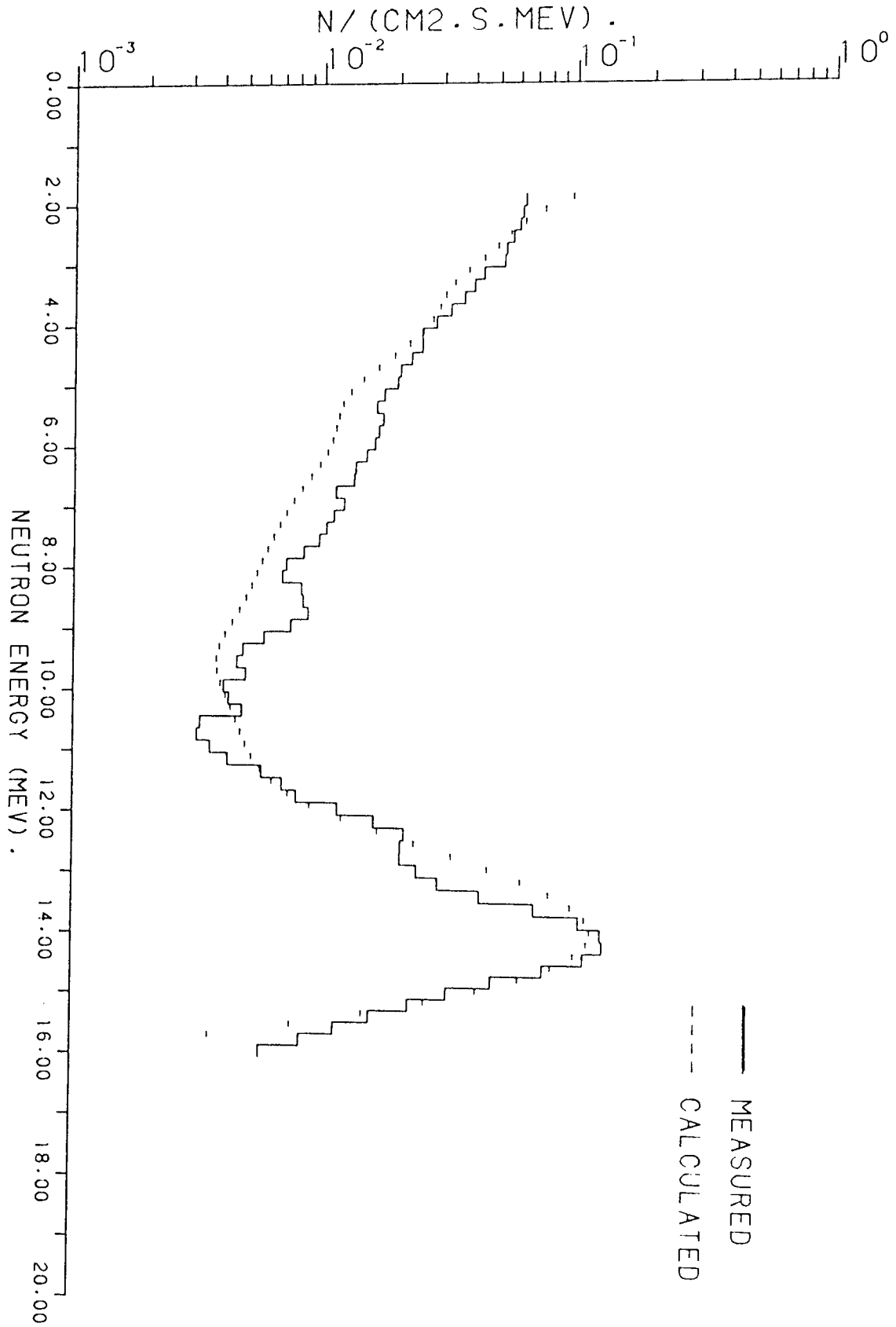


FIG. 7.26 NEUTRON FLUX AT THE SURFACE OF 8.2 CM LIF ON TOP
OF 10.9 CM URANIUM.

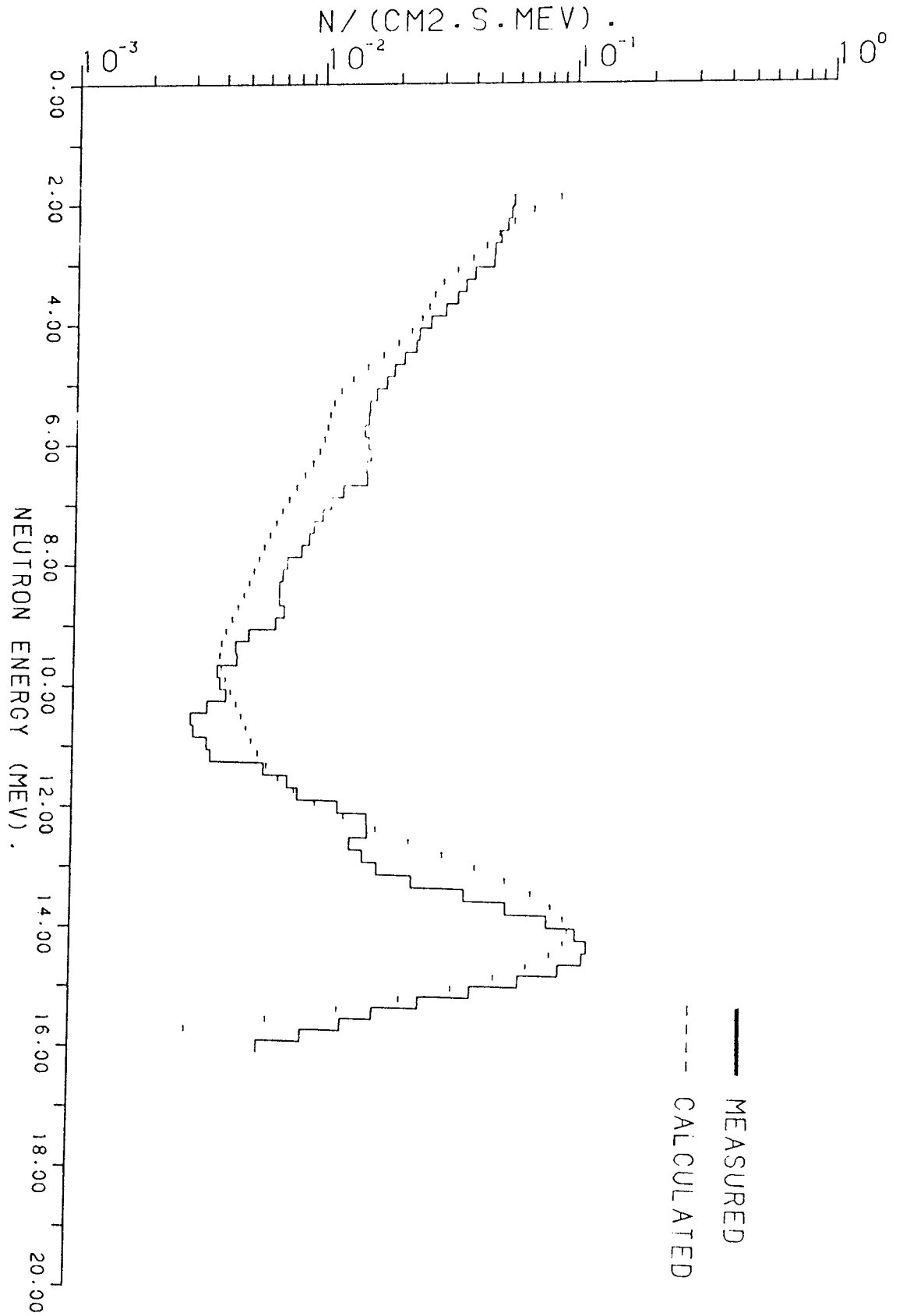


FIG. 7.27 NEUTRON FLUX AT THE SURFACE OF 10.9 CM LIF ON TOP

From the figures, measured fluxes between about 2.2 MeV and 9.5 MeV are higher than calculated fluxes. The flux increases in this region compared with the thinner uranium layer due to the secondary neutrons from uranium. As the thickness of LiF increases, the flux decreases for all the spectra as expected. There is a good agreement between measured and calculated neutrons around 14 MeV peak in all cases.

With all the previous cases it can be noticed that; the measured and calculated fluxes decrease as the thickness of uranium increases through all the spectra with the same thickness of LiF slabs, as is to be expected.

The measured and calculated fluxes from the assemblies containing only uranium [figures (7.2), (7.3) and (7.4)] are slightly higher than that from the cases containing LiF thicknesses on top of the similar thickness of uranium [figures (7.19) to (7.27)] below about 6 MeV and around the 14 MeV peak in all cases. This effect is expected but will not be pronounced due to the low density of LiF compared with uranium.

For comparison between the spectra from assemblies containing LiF slabs on top of uranium [figures (7.19), (7.23) and (7.27)] with those having the same thickness of mixture [figures (7.14), (7.16) and (7.18)], it was found that the flux over all the spectrum in mixtures is higher. This is may be due to a combination of inelastic and large energy loss elastic processes occurring together in the mixtures, whereas they follow in series in the twin slab assemblies.

7.6.2 Neutron Spectra At The Surface Of Samples Containing U On Top Of LiF

Figures (7.28), (7.29) and (7.30) show the measured and calculated fluxes at the surface of samples containing 5.4, 8.2 and 10.9 cm uranium on top of 5.4 cm LiF. These samples are as represented in diagrams A, B and C in figure (6.11).

In general, there is a good agreement between measured and calculated fluxes in these cases. There is a slight difference between measured and calculated fluxes below about 3 MeV. This difference decrease as thickness of uranium increase, and at 10.9 cm uranium case the measured and calculated fluxes are close to each other.

For 8.2 cm LiF thickness on the bottom and 5.4, 8.2 and 10.9 cm uranium thicknesses on top [diagrams (6.12 A, B and C)], figures (7.31), (7.32) and (7.33) show the measured and calculated fluxes in these cases

The spectral shape does not differ very much with the uranium thickness. The agreement between measured and calculated becomes closer with increase in uranium thickness (there is an apparent error in the calculation with 10.9 cm U possibly due to poor convergence).

Figures (7.34), (7.35) and (7.36) show measured and calculated neutron spectra from samples containing 5.4, 8.2 and 10.9 cm uranium on top of 10.9 cm LiF [diagrams (6.13 A, B and C)].

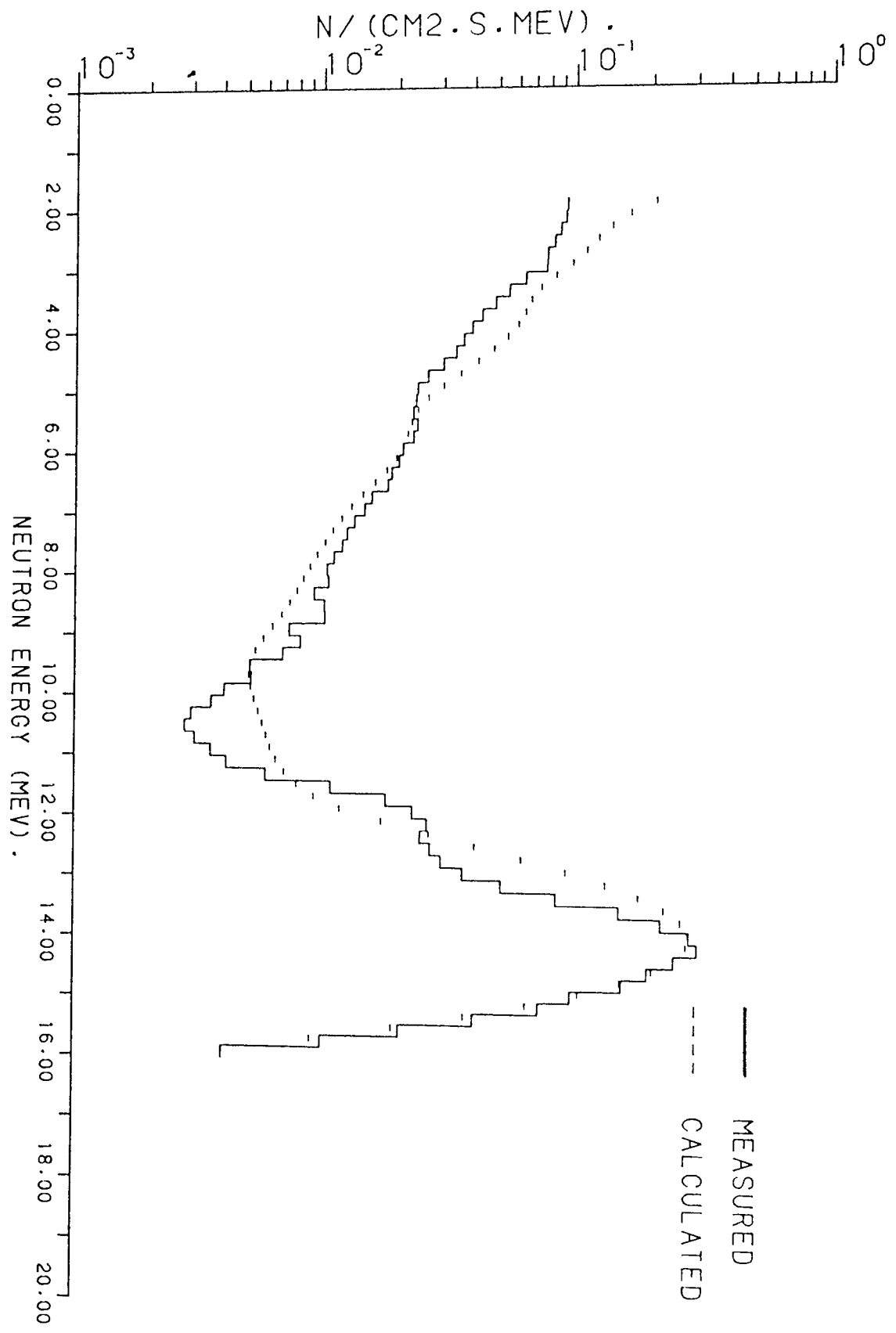


FIG. 7.28 NEUTRON FLUX AT THE SURFACE OF 5.4 CM URANIUM ON TOP OF 5.4 CM LIF.

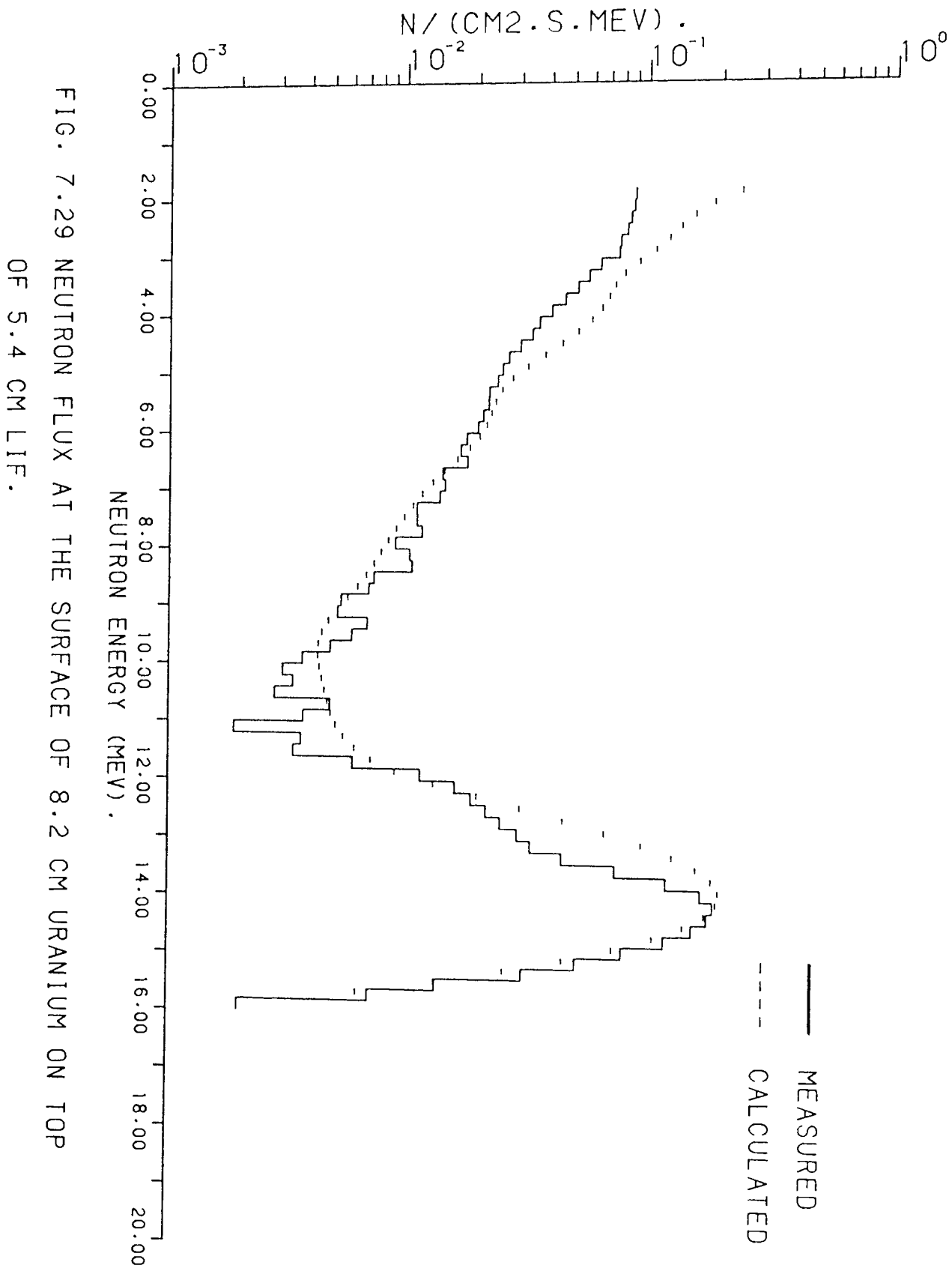


FIG. 7.29 NEUTRON FLUX AT THE SURFACE OF 8.2 CM URANIUM ON TOP OF 5.4 CM LIF.

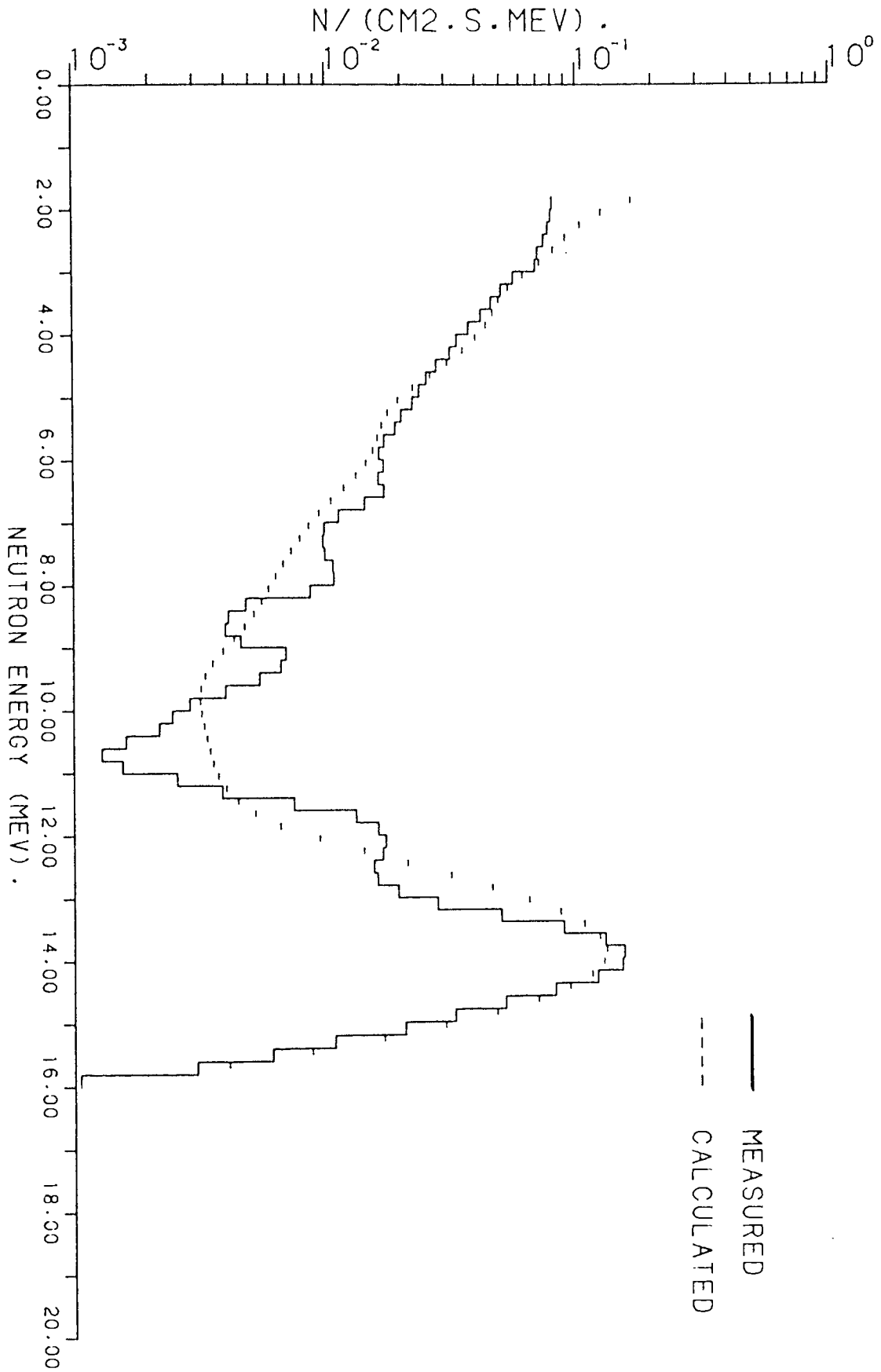


FIG. 7.30 NEUTRON FLUX AT THE SURFACE OF 10.9 CM URANIUM ON TOP OF 5.4 CM LIF.

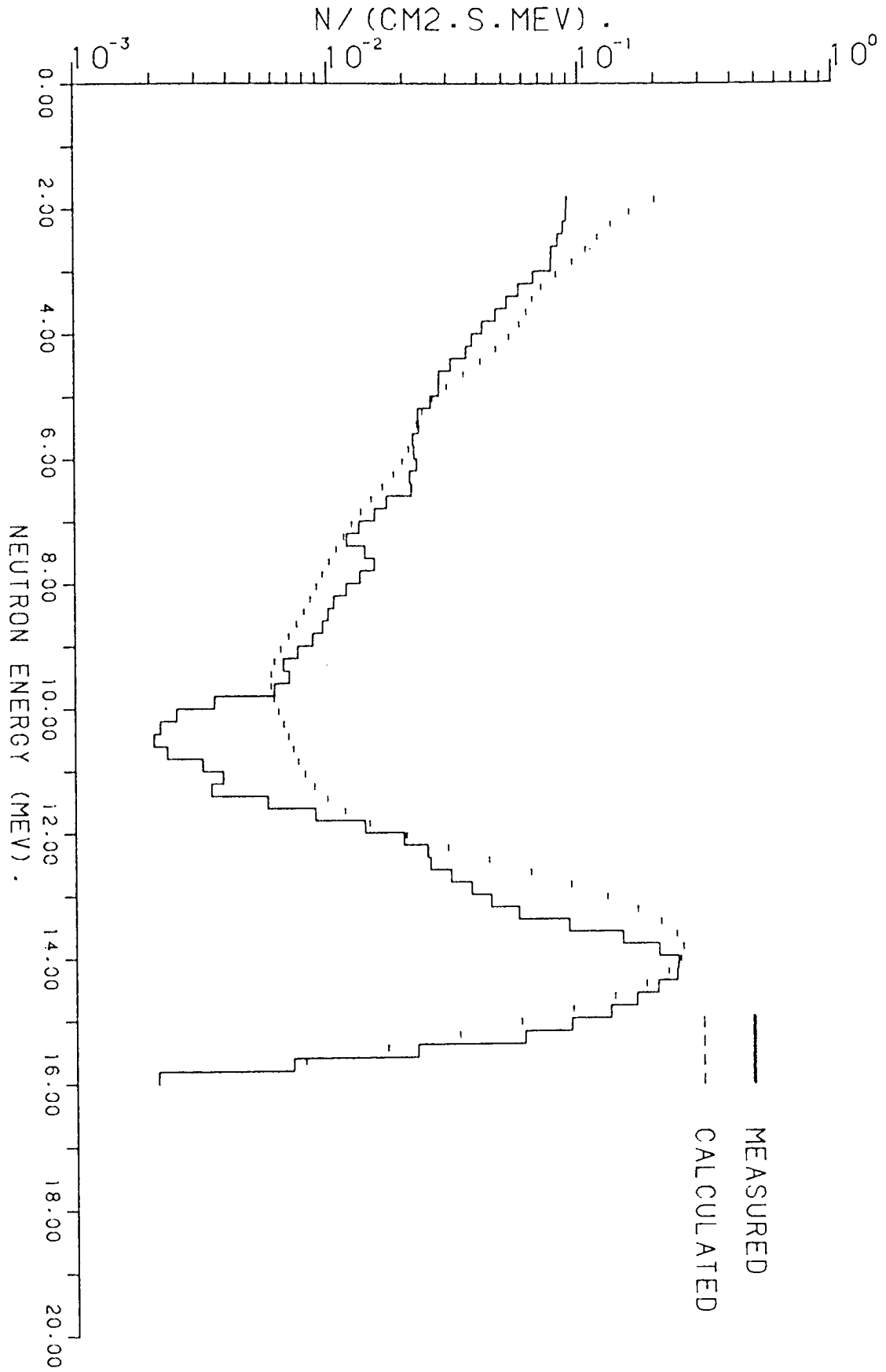


FIG. 7.31 NEUTRON FLUX AT THE SURFACE OF 5.4 CM URANIUM ON TOP OF 8.2 CM LIF.

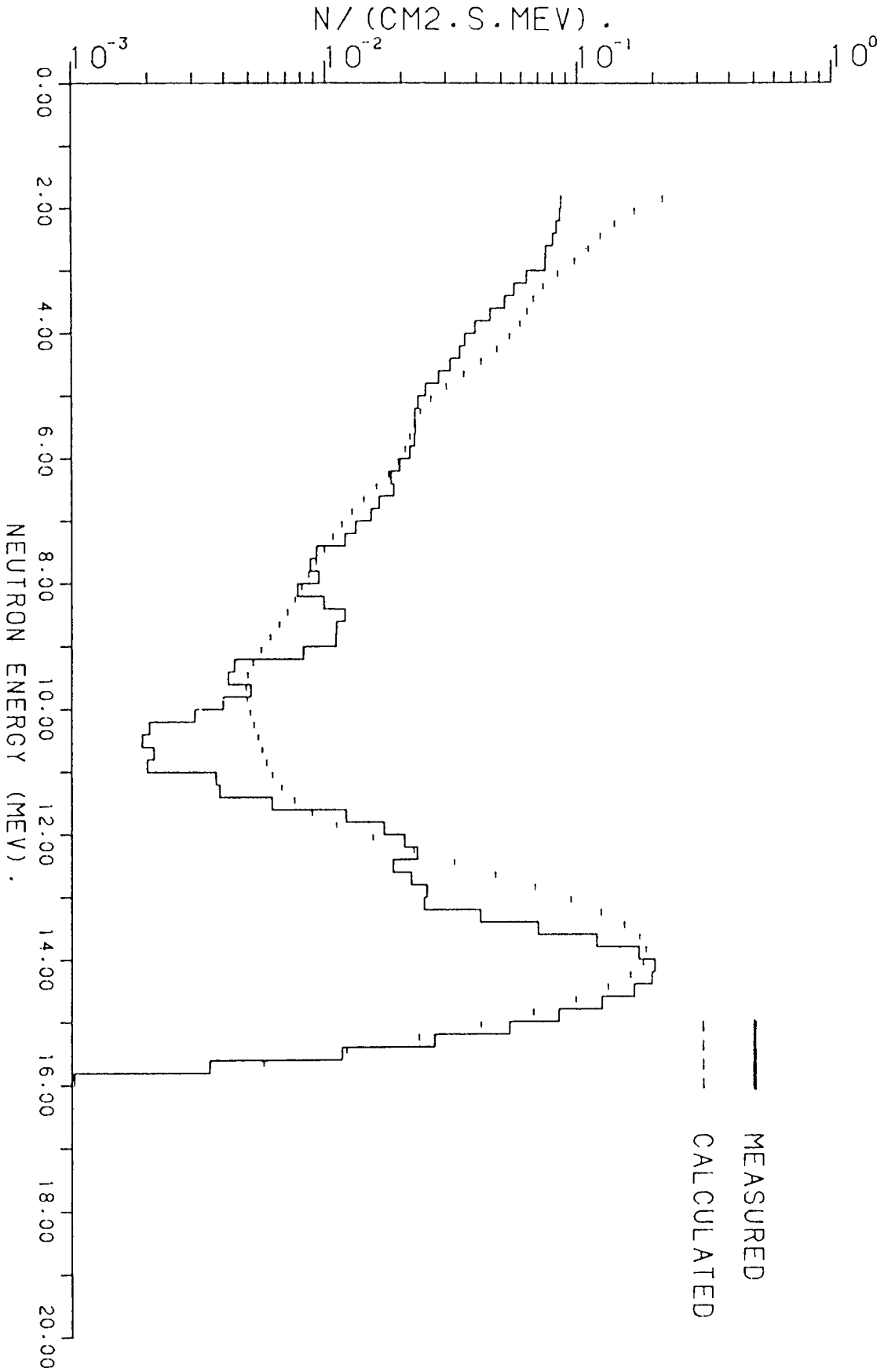


FIG. 7.32 NEUTRON FLUX AT THE SURFACE OF 8.2 CM URANIUM ON TOP OF 8.2 CM LIF.

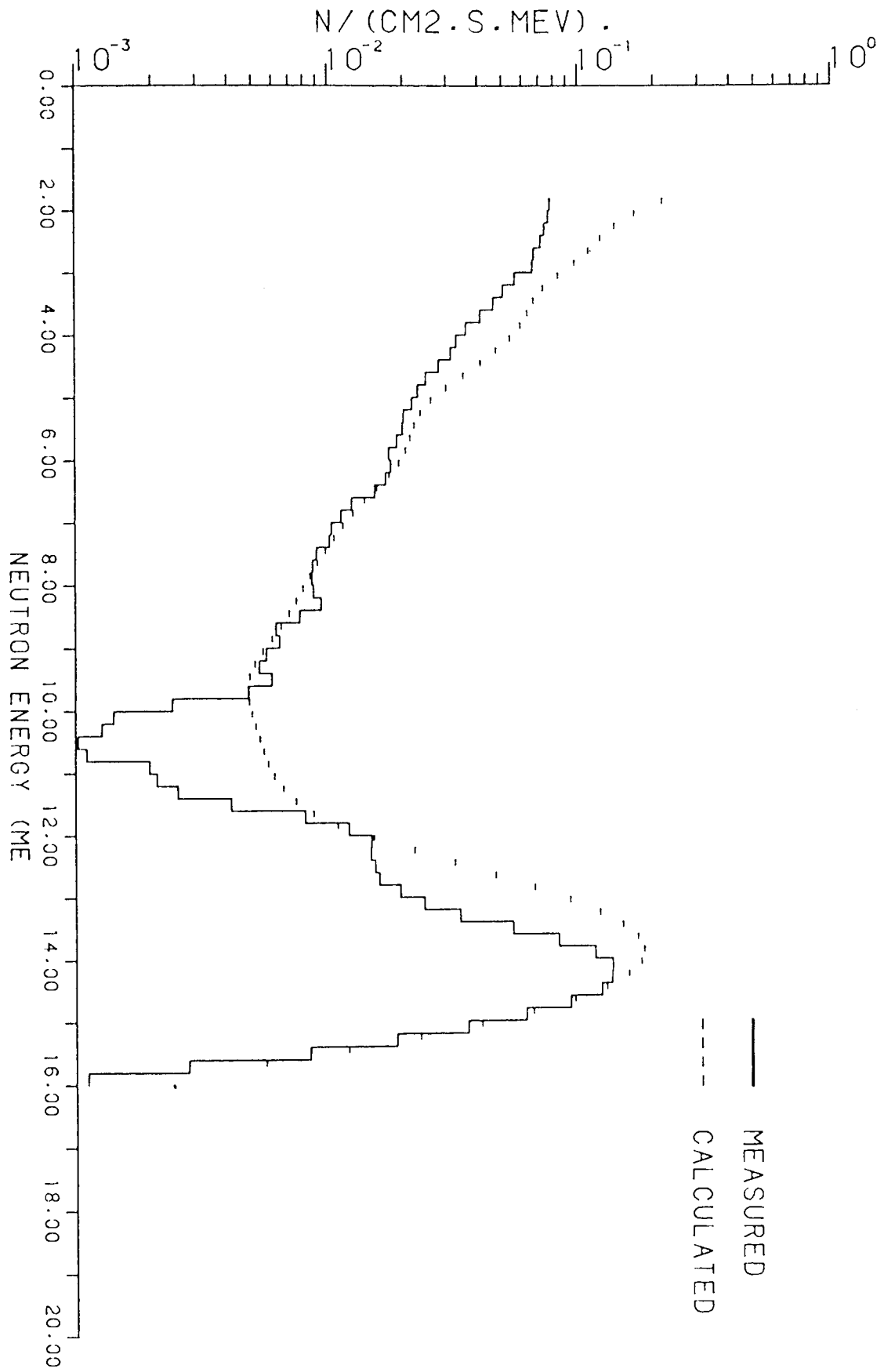


FIG. 7.33 NEUTRON FLUX AT THE SURFACE OF 10.9 CM URANIUM ON TOP OF 8.2 CM LIF.

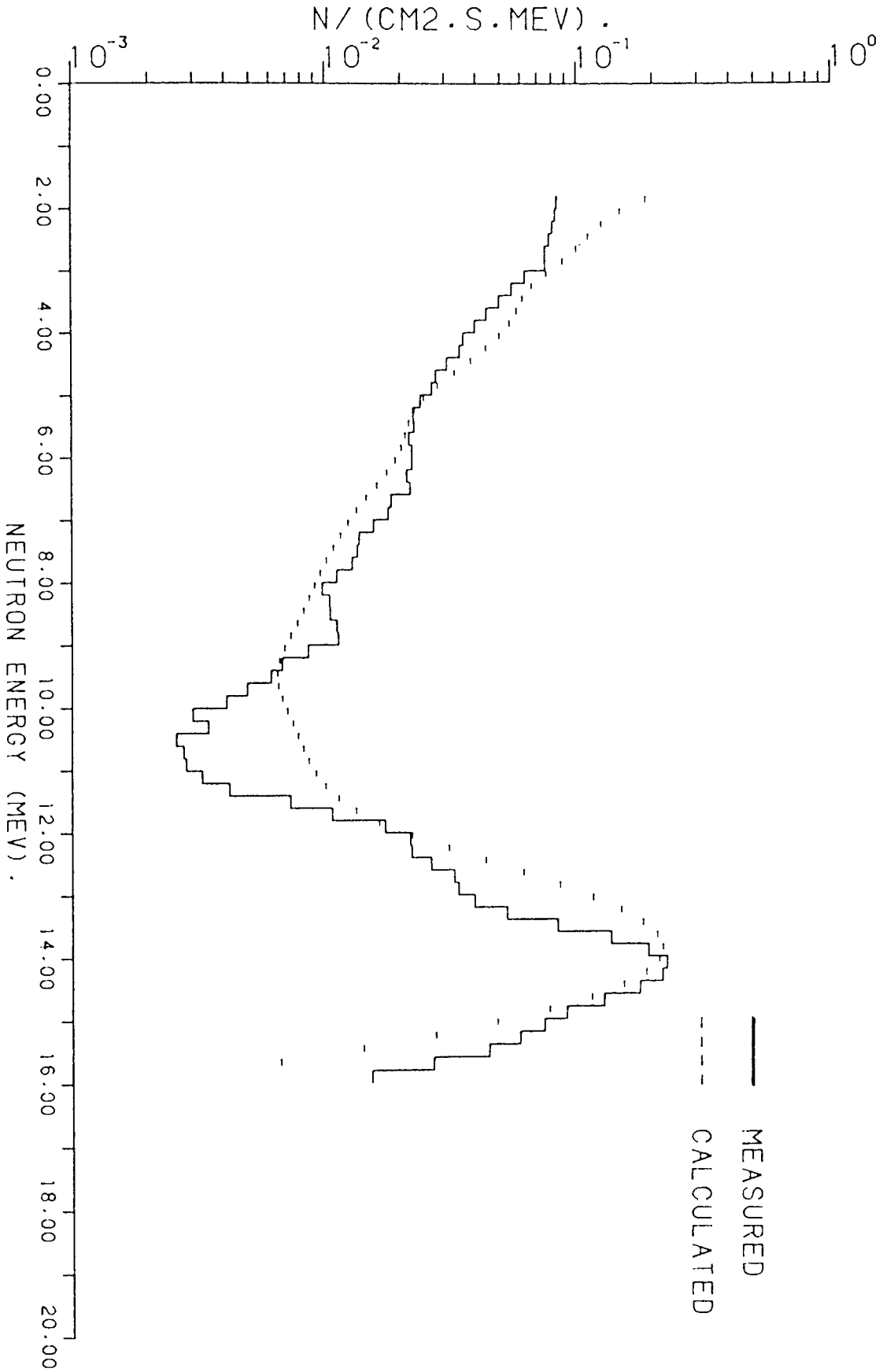


FIG. 7.34 NEUTRON FLUX AT THE SURFACE OF 5.4 CM URANIUM ON TOP OF 10.9 CM LIF.

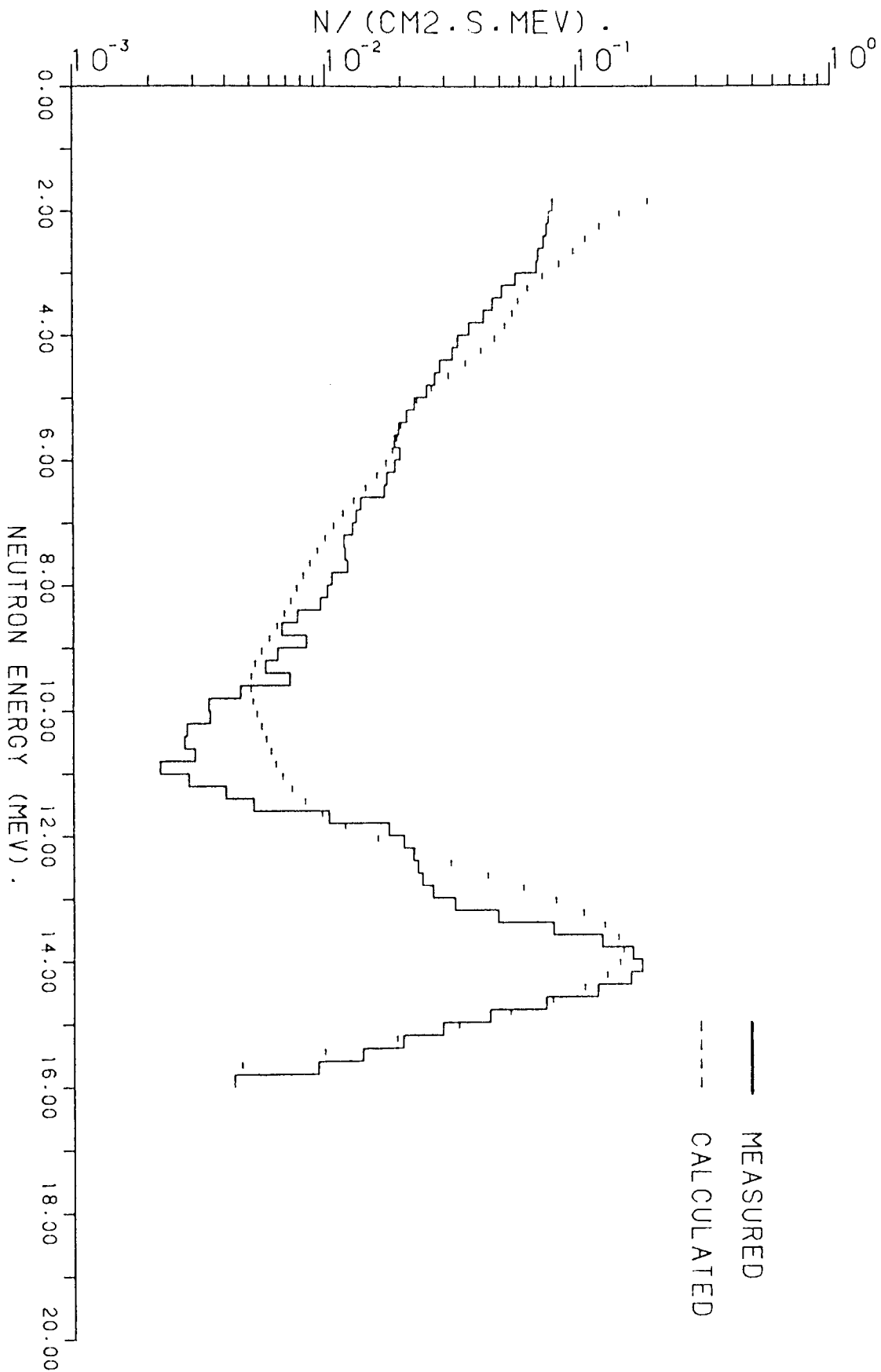


FIG. 7.35 NEUTRON FLUX AT THE SURFACE OF 8.2 CM URANIUM ON TOP OF 10.9 CM LIF.

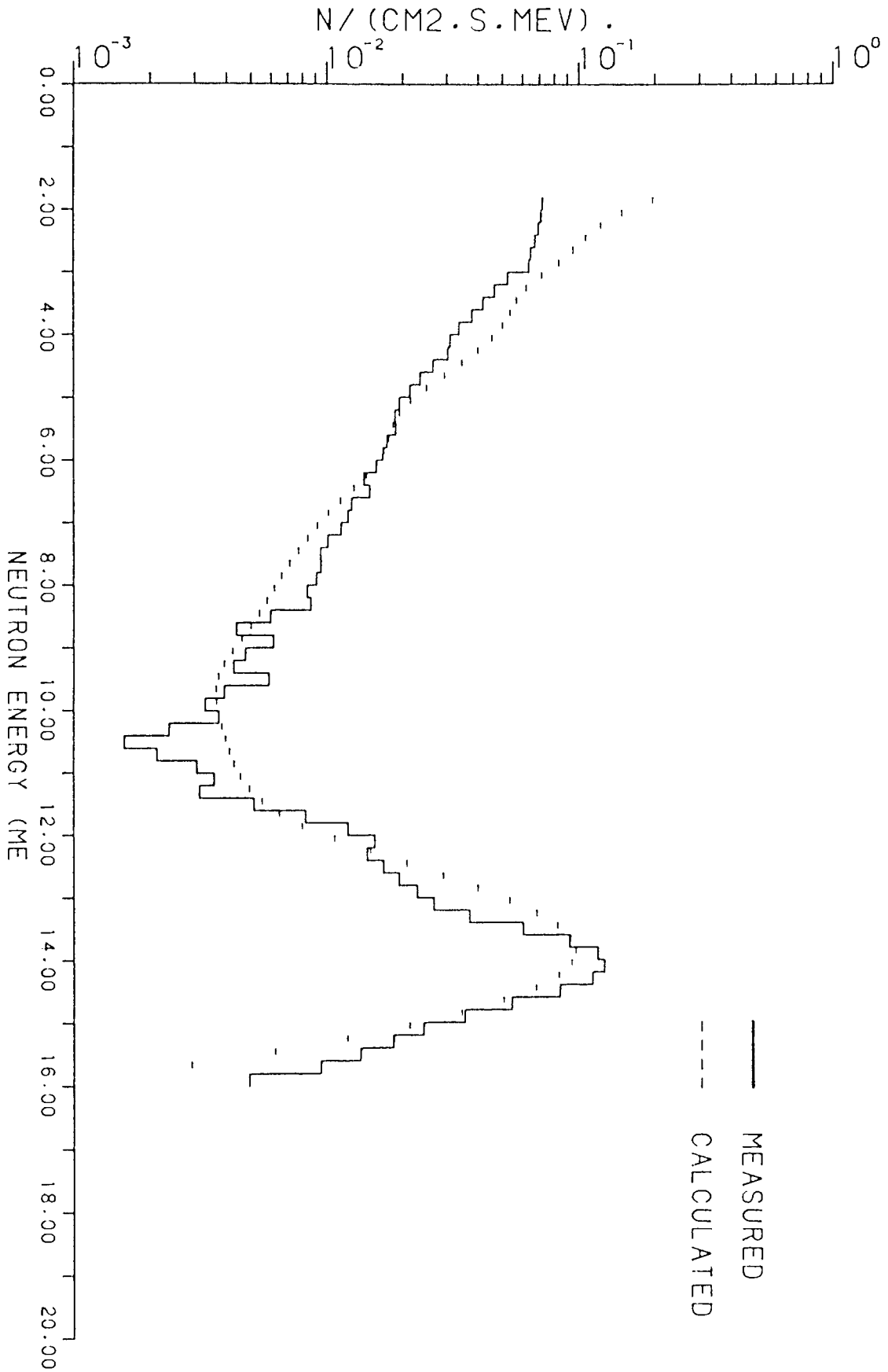


FIG. 7.36 NEUTRON FLUX AT THE SURFACE OF 10.9 CM URANIUM ON TOP OF 10.9 CM LIF.

There is good agreement between measured and calculated spectra, somewhat better than the previous cases.

From all the previous cases, the fluxes measured and calculated decrease as the thickness of LiF, uranium or both increase. Also, the shape of the spectra does not change much with LiF or U thickness.

In comparison between these cases [figures (7.28), (7.32) and (7.36)] and those which containing LiF on top of uranium [figures (7.19), (7.23) and (7.27)] it was found that, for all these cases there is very little difference between the experimental fluxes but rather more difference between the calculated fluxes, probably due to boundary conditions at the LiF / U interface at which there is a large density change.

7.6.3 Neutron Spectra At The Surface Of Samples Containing LiF Between Two Slabs Of Uranium

Figures (7.37), (7.38) and (7.39) show the neutron spectra measured and calculated from samples containing 5.4, 8.2 and 10.9 cm LiF between two slabs of uranium of 5.4 cm thickness each [diagrams (6.14 A, B and C) respectively]

From the figures;

- The fluxes calculated and measured decrease by a small amount as the thickness of LiF increases.

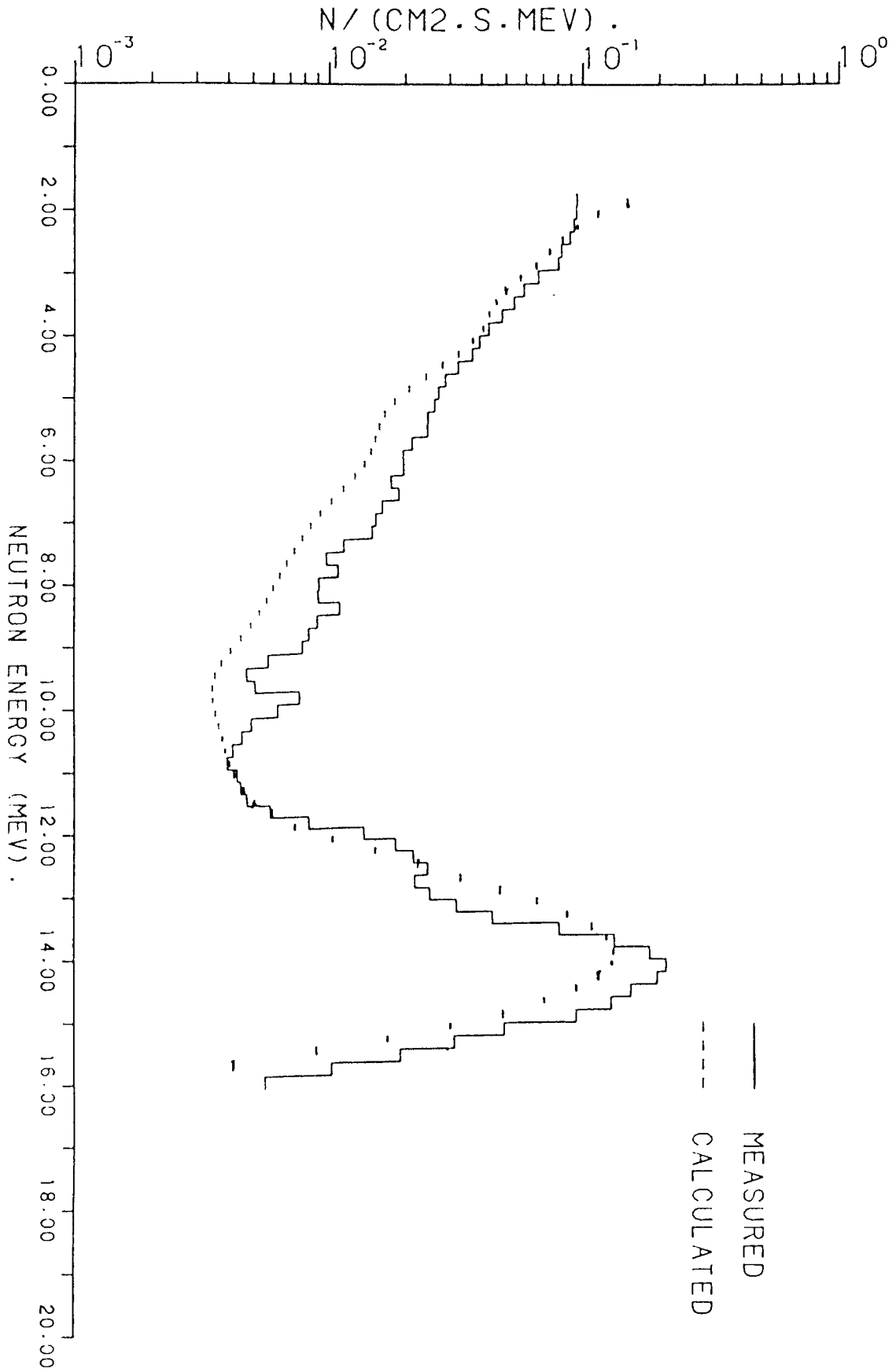


FIG. 7.37 NEUTRON FLUX AT THE SURFACE OF A SAMPLE CONTAINING 5.4CM LIF BETWEEN 2 SLABS OF 5.4CM U.

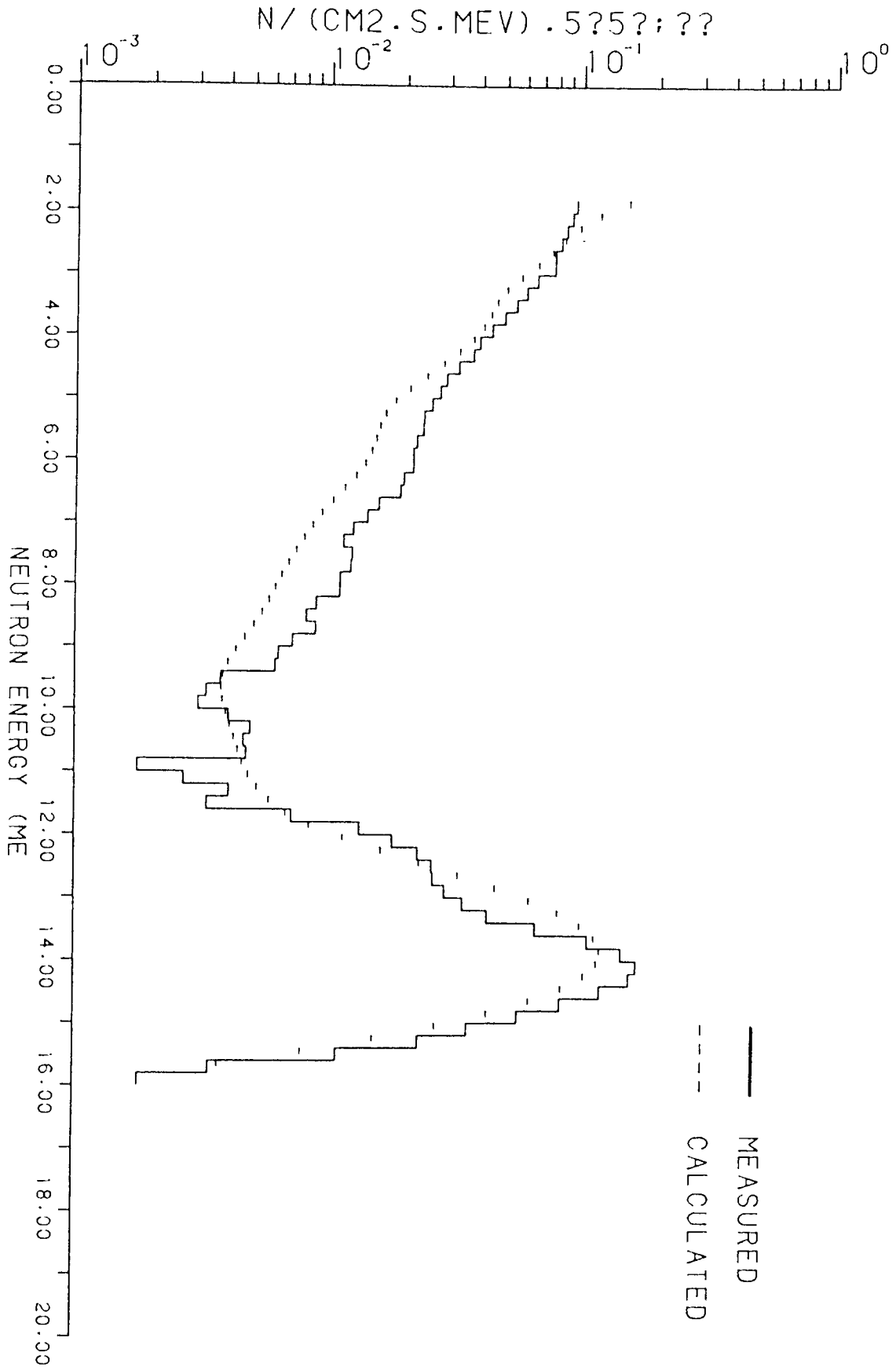


FIG. 7.38 NEUTRON FLUX AT THE SURFACE OF A SAMPLE CONTAINING 8.2CM LIF BETWEEN 2 SLABS OF 5.4CM U.

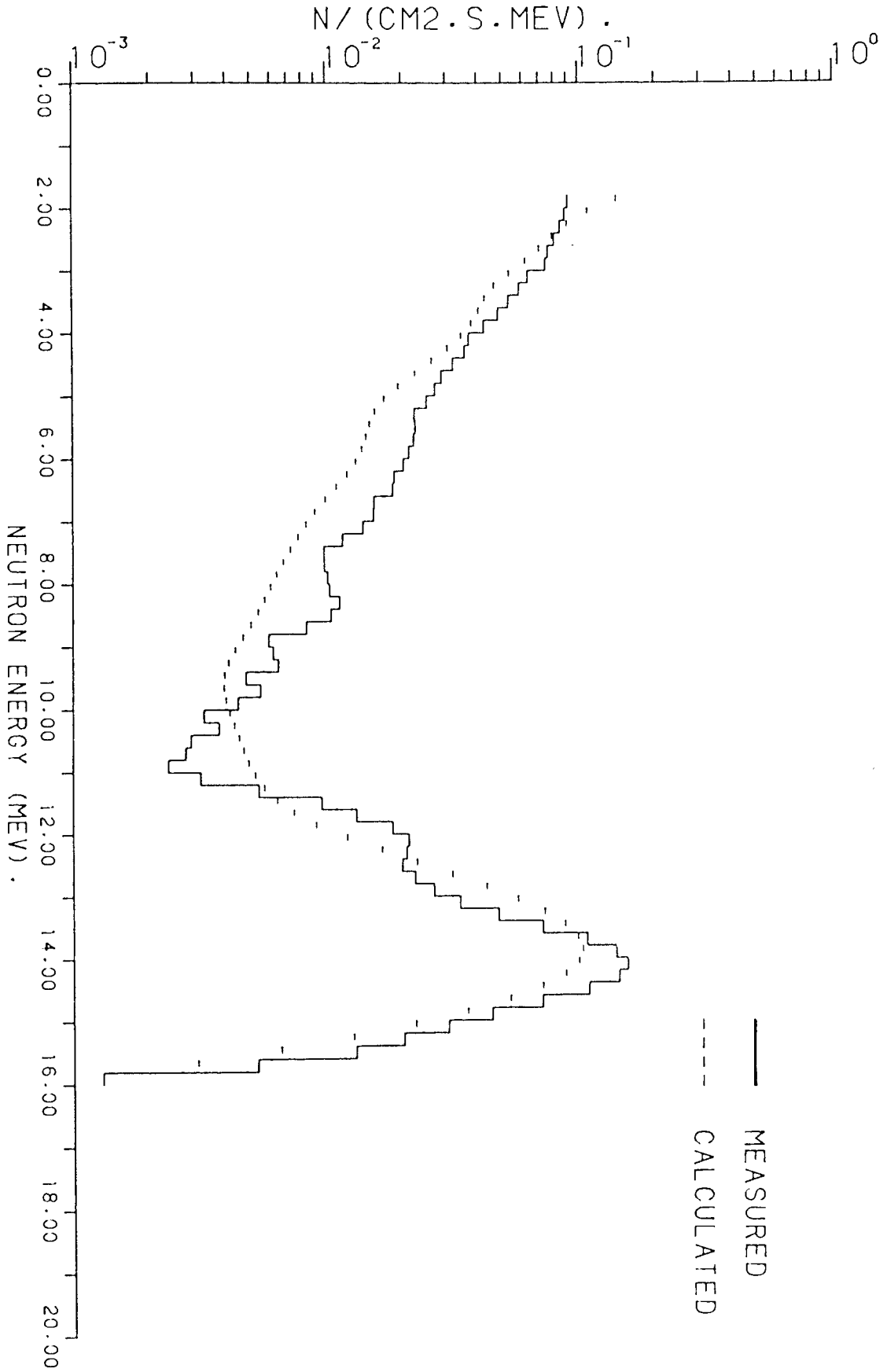


FIG. 7.39 NEUTRON FLUX AT THE SURFACE OF A SAMPLE CONTAINING 10.9CM LIF BETWEEN 2 SLABS OF 5.4CM U.

- The spectral shape is nearly the same over all the spectra.
- There is best agreement between measured and calculated fluxes at low and high energies.

In comparison between the flux from the previous samples [figures (7.37), (7.38) and (7.39)] with that containing LiF slabs on top of uranium [figures (7.25), (7.26) and (7.27)], it was found that the flux is slightly higher but that spectral shapes are generally similar.

7.6.4 Neutron Spectra At The Surface Of Samples Containing Uranium Between Two Slabs Of LiF

Fast neutron fluxes from the samples represented in figure (6.15) [diagrams A, B and C] are shown in figures (7.40), (7.41) and (7.42) respectively.

The figures show the spectra calculated below about 5 MeV is higher than measured. The difference decreases as the thickness of uranium increases. Above this energy the measured one is higher and extends to about 10 MeV. There is a good agreement between measured and calculated fluxes around the 14 MeV peak.

In comparing these cases [figures (7.40), (7.41) and (7.42)] and those mentioned in figures (7.21) and (7.34), (7.24) and (7.35), and (7.27) and (7.36) respectively since they contain similar amounts of material it will be seen that , there is very little difference between the equivalent cases. Therefore the order of the materials does not seem to be important at these thicknesses from the point of view of shielding.

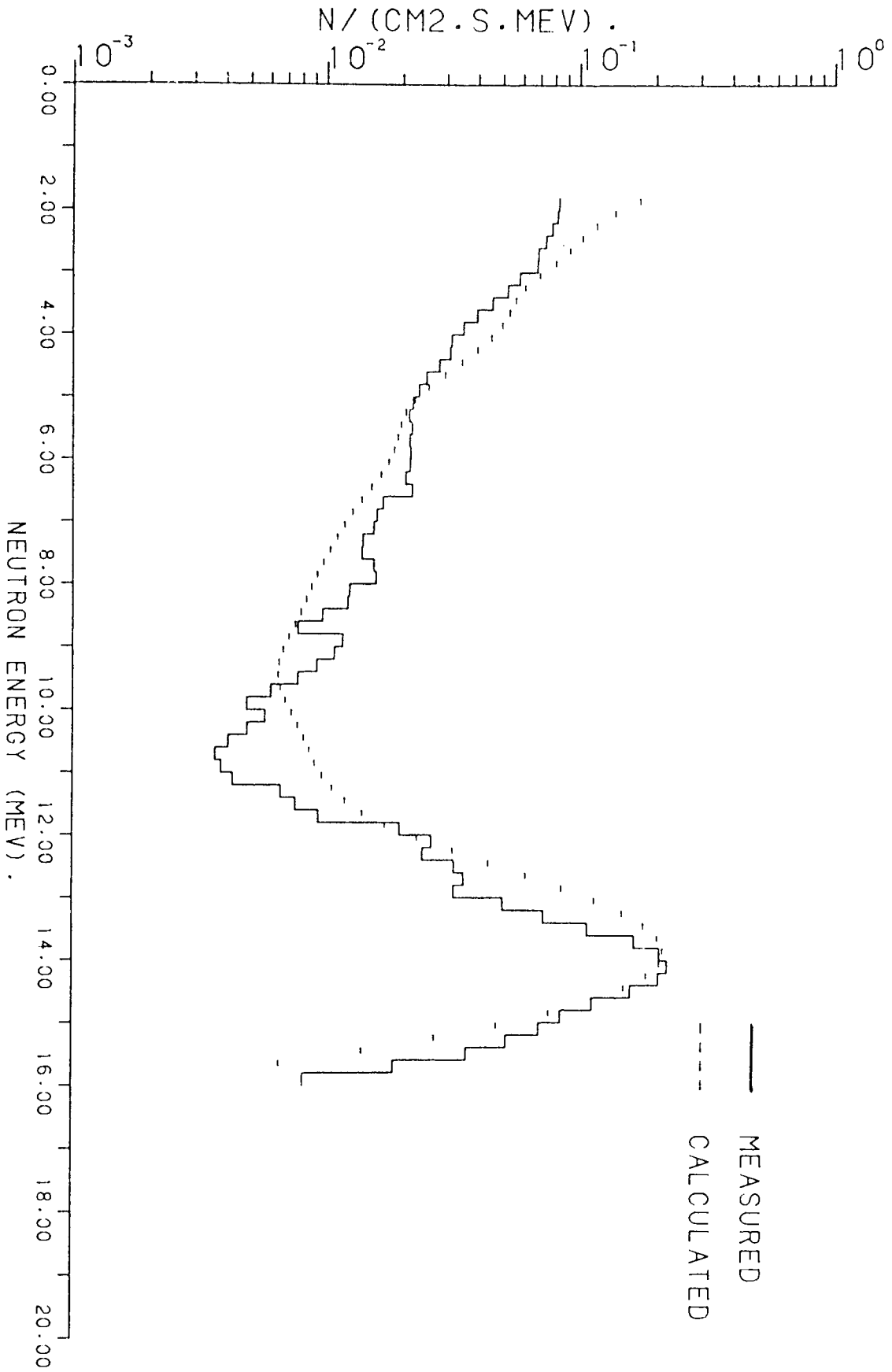


FIG. 7.40 NEUTRON FLUX AT THE SURFACE OF A SAMPLE CONTAINING 5.4CM U BETWEEN 2 SLABS OF 5.4CM LIF.

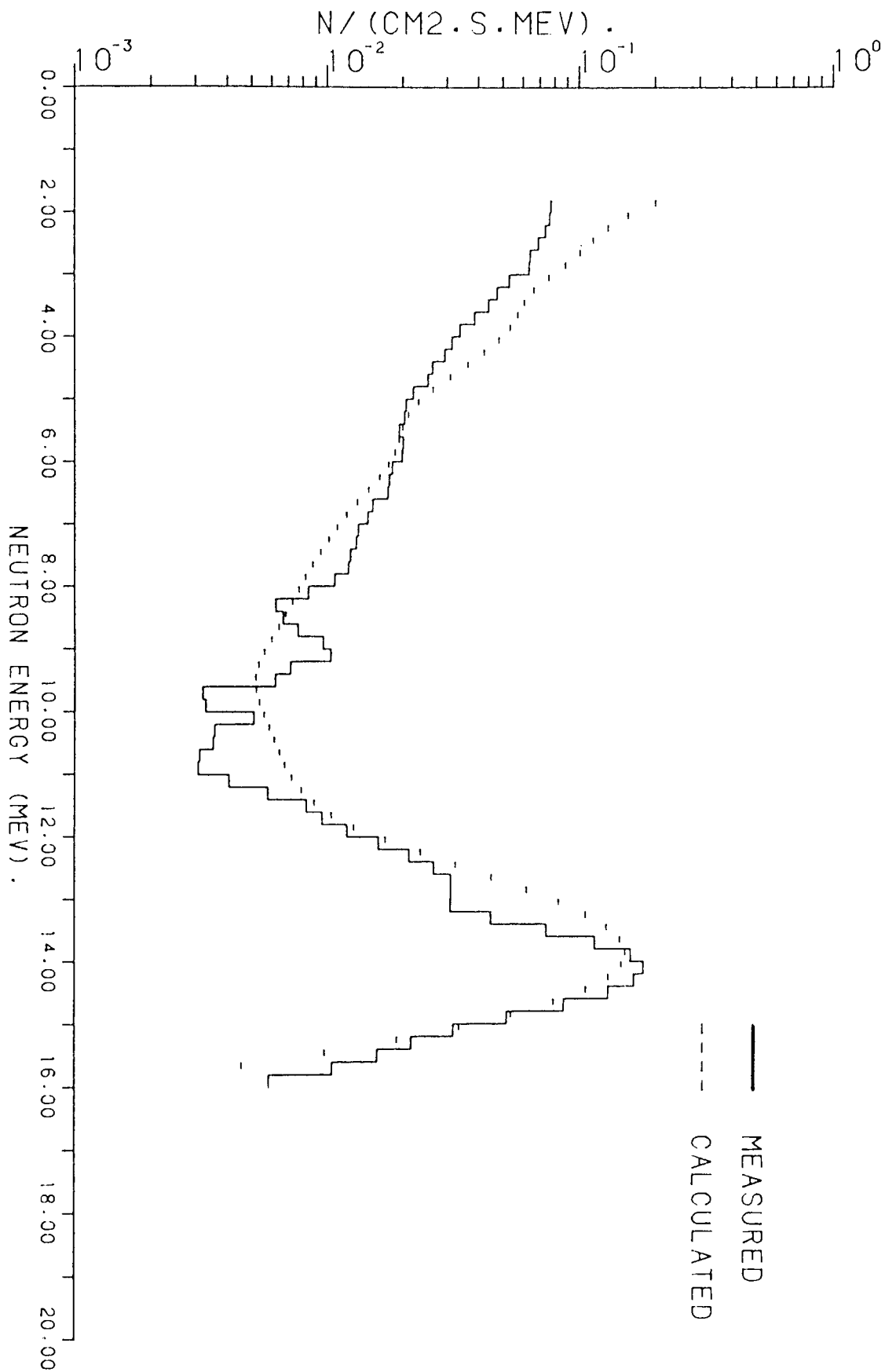


FIG. 7.41 NEUTRON FLUX AT THE SURFACE OF A SAMPLE CONTAINING 8.2CM U BETWEEN 2 SLABS OF 5.4CM LIF.

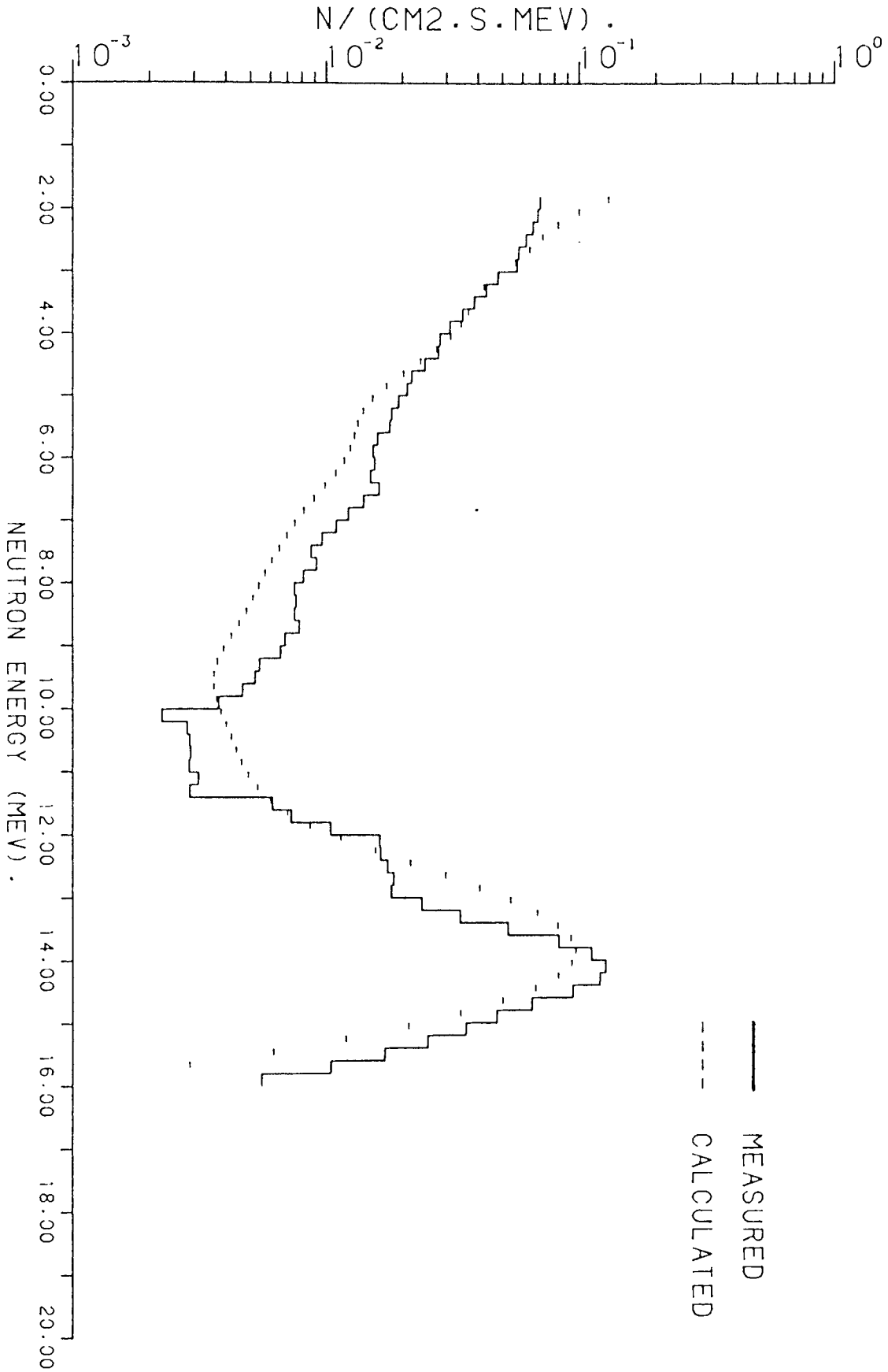


FIG. 7.42 NEUTRON FLUX AT THE SURFACE OF A SAMPLE CONTAINING 10.9CM U BETWEEN 2 SLABS OF 5.4CM LIF.

7.6.5 Neutron Spectra At The Surface Of Samples Containing Multilayers Of LiF And Uranium

Neutron fluxes measured and calculated from a sample containing from the top 5.4 cm LiF, 5.4 cm U, 5.4 cm LiF and 5.4 cm U [diagram 6.16 A] are represented in figure (7.43).

There is a good agreement between measured and calculated fluxes around the 14 MeV peak. Below about 10 MeV the difference between the two cases increases with the experimental flux higher than calculated. As the energy decreases the difference decreases too until the measured and calculated fluxes become close to each other at about 4 MeV.

For the sample containing (from the top) 5.4 cm U, 5.4 cm LiF, 5.4 cm U and 5.4 cm LiF [diagram 6.16 B] the calculated and measured fluxes are represented in figure (7.44).

The figure shows that, there is an apparent error in the calculation due to non - convergence as mentioned before (section 7.1). Therefore direct comparison between measured and calculated spectra can not be made especially at low energy region.

Figures (7.43) and (7.44) can be compared with figures (7.18), (7.27), (7.36), (7.39) and (7.42) which contain the same amounts of materials but arranged differently. With the exception of the calculated flux in figure (7.44) the agreement is good, apart from the mixture case figure (7.18) where the 14 MeV peak is higher. This may be due to streaming effects in the mixture.

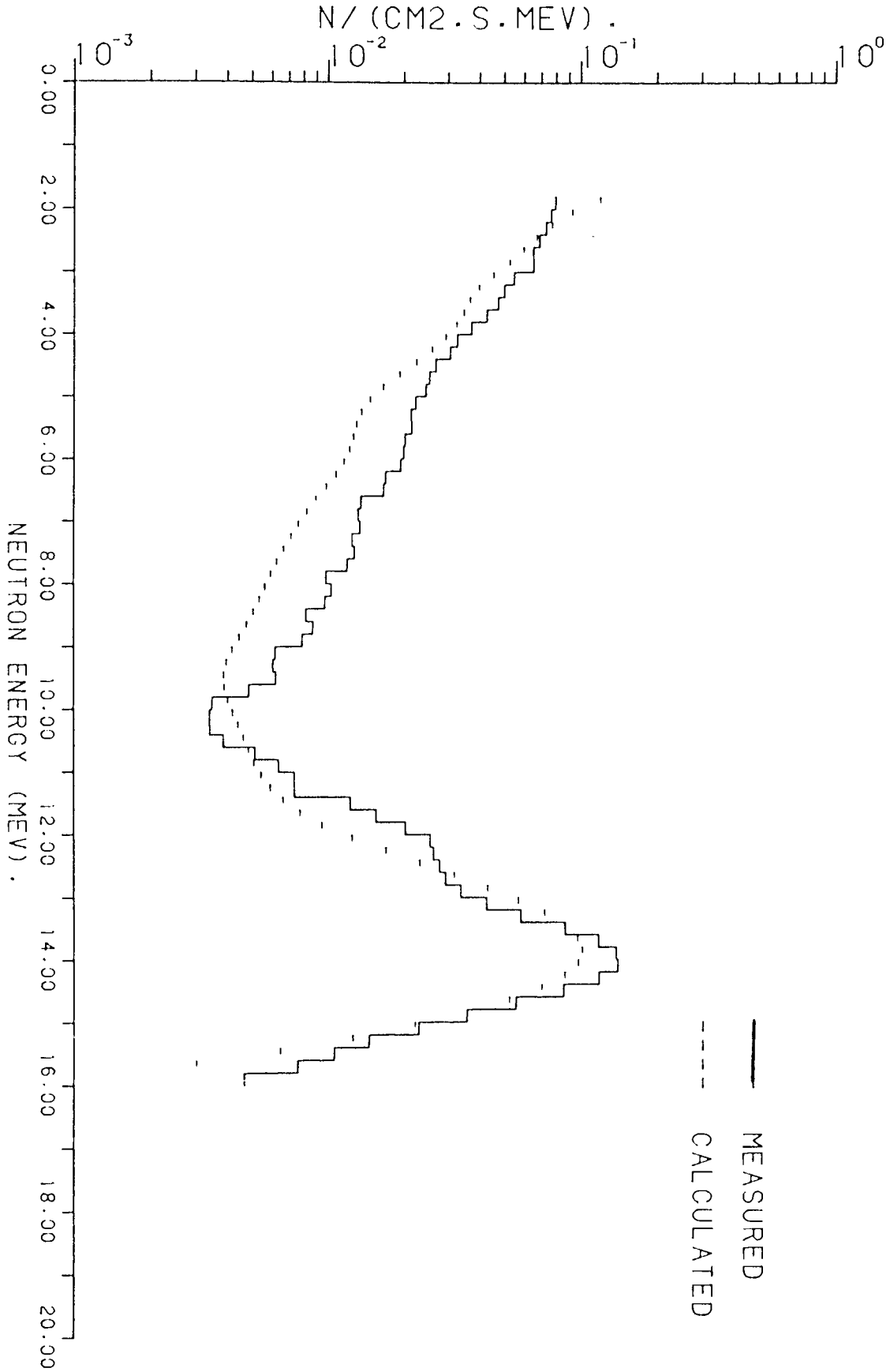


FIG. 7.43 NEUTRON FLUX AT THE SURFACE OF A SAMPLE CONTAINING FROM THE TOP 5.4CM LIF, 5.4CM U, 5.4CM LIF AND 5.4CM U.

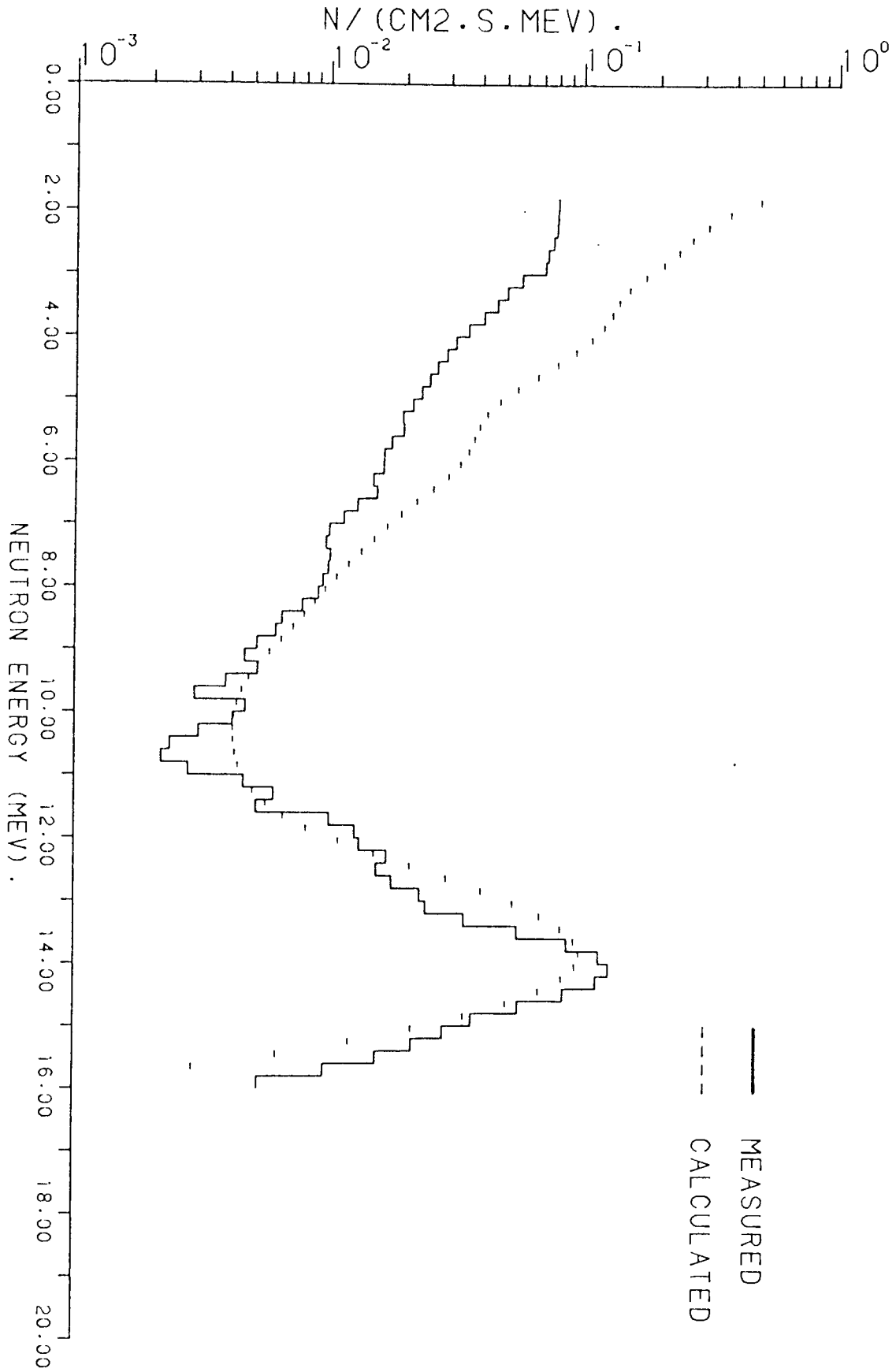


FIG. 7.44 NEUTRON FLUX AT THE SURFACE OF A SAMPLE CONTAINING FROM THE TOP 5.4CM U, 5.4CM LIF, 5.4CM U AND 5.4CM LIF.

7.7 Neutron Spectra From The Graphite Assemblies

The measured and calculated neutron spectra from the graphite assemblies which are represented in diagrams (6.17 A) to (6.23 E) are shown in figures (7.46) to (7.73) respectively.

7.7.1 Neutron Spectra From The Graphite Cube

The measured and calculated spectra from the graphite cube (62.2 cm) represented in diagram (6.17 A) are shown in figure (7.46).

Elastic scattering cross section in ^{12}C has its maximum value (3.11 barns) at 2.94 MeV. It decreases as the neutron energy increases and has many peaks throughout the spectral range as shown in figure (7.45). The effect of elastic scattering can be seen on the low energy side of the 14.1 MeV peak.

Inelastic scattering starts at 4.85 MeV (0.008 barn) and increases as the neutron energy increases with peaks at 6.34, 7.42, 7.82 and 8.11 MeV [figure (7.45)]. The spectral peak around 9 MeV corresponds to the inelastic scattering from 4.44 MeV level of ^{12}C . The peak around 6.5 MeV is due to the second (7.66 MeV) level.

The (n,n') to continuum threshold is 7.88 MeV and the cross section data has two peaks at 8 MeV (0.17 barn) and 9.92 MeV (0.2 barn)

The calculated flux is lower than the measured one over all the spectra. This probably is due to the spherical geometry used in the

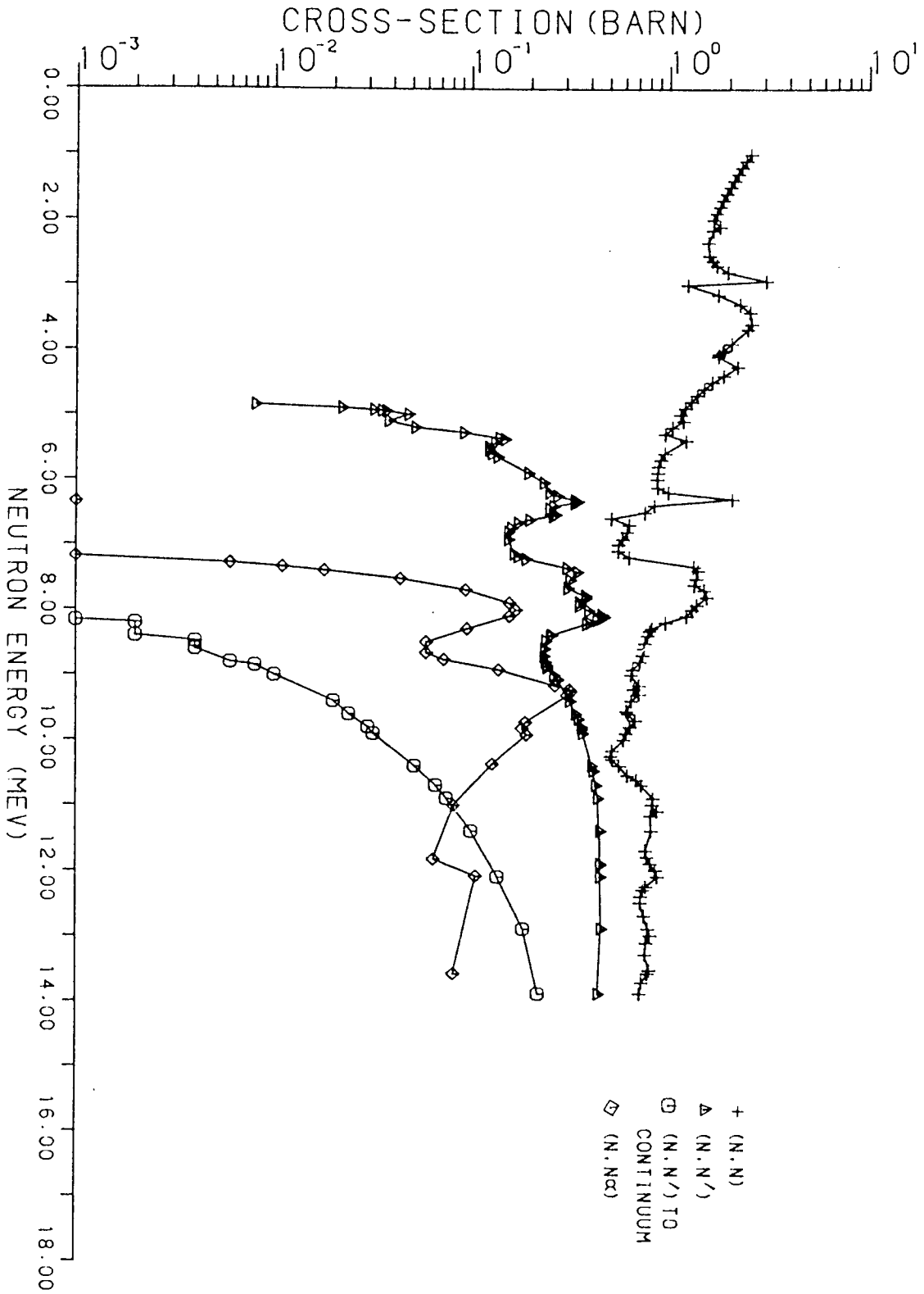


FIG. 7.45 (N,N), (N,N'), (N,N' α) AND (N,N') TO CONTINUUM CROSS-SECTIONS OF CARBON-12.

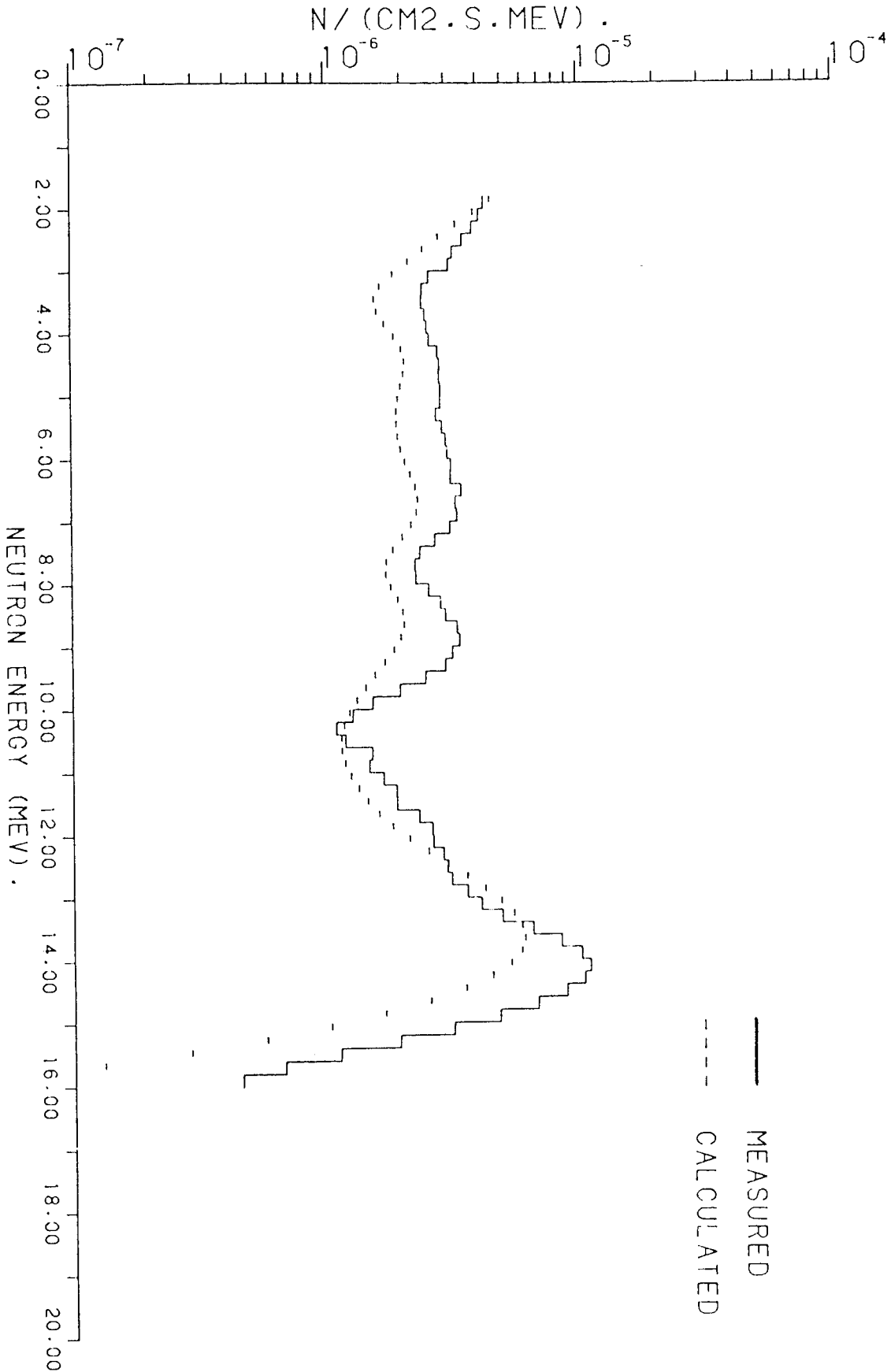


FIG. 7.46 NEUTRON FLUX AT THE SURFACE OF 62.2 CM GRAPHITE CUBE.

calculation, while the assembly was a cube with corners removed with a cubical central cavity to approximate a hollow sphere. The spectral shape of both are the same.

7.7.2 Neutron Spectra From The Graphite Slabs

The fast neutron spectra emitted from the graphite slabs with (62.2 x 44.5) cm² cross section area and thickness 8.9, 17.8 and 26.7 cm (diagram 6.17 B) are shown in figures (7.47), (7.48) and (7.49) respectively.

In these figures four peaks are observed in addition to the full energy peak from 14.1 MeV neutron source. These neutron spectra reflected the angular and energy distributions of secondary neutrons produced by the elastic and the inelastic scattering of 14.1 MeV neutrons.

The peak at about 12 MeV which appears as a bump on the low energy side of the 14 MeV peak is attributed to the calculation group (13.8 to 12.8 MeV), which tends to add to width of the smoothed curve on the low energy side (section 7.3). The other three peaks are attributed to the secondary neutrons emitted by the inelastic scattering which results from the excitation of ¹²C nucleus to the discrete energy levels, i.e, the peaks around about 9, 6 and 3 MeV are due to 4.44, 7.66 and 9.64 MeV levels respectively.

The secondary neutrons emitted from (n,n α) reaction have energies below about 6 MeV. This reaction has a threshold of 6.17 MeV with a

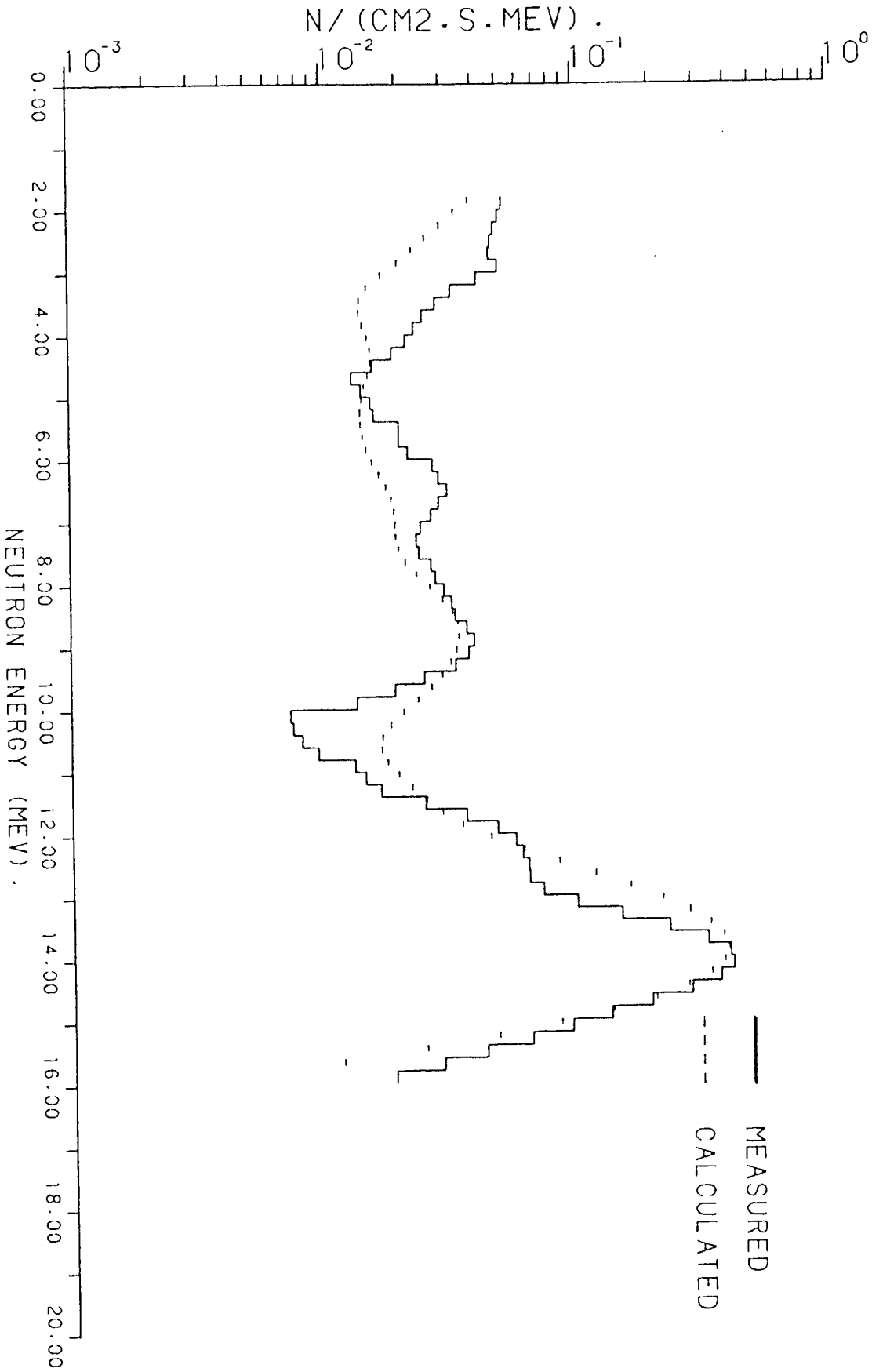


FIG. 7.47 NEUTRON FLUX AT THE SURFACE OF 8.9 CM THICK GRAPHITE SLAB.

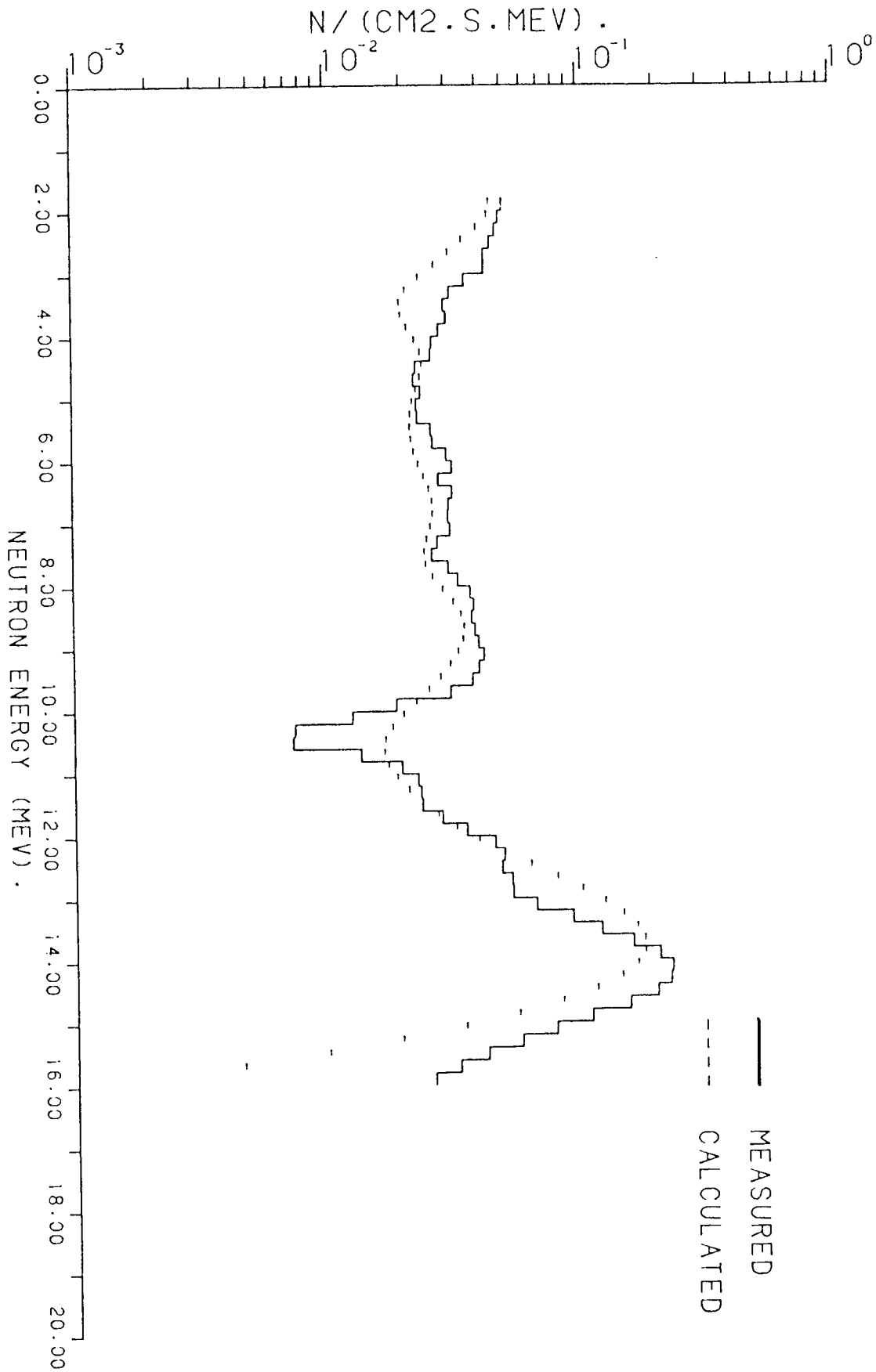


FIG. 7.48 NEUTRON FLUX AT THE SURFACE OF 17.8 CM THICK GRAPHITE SLAB.

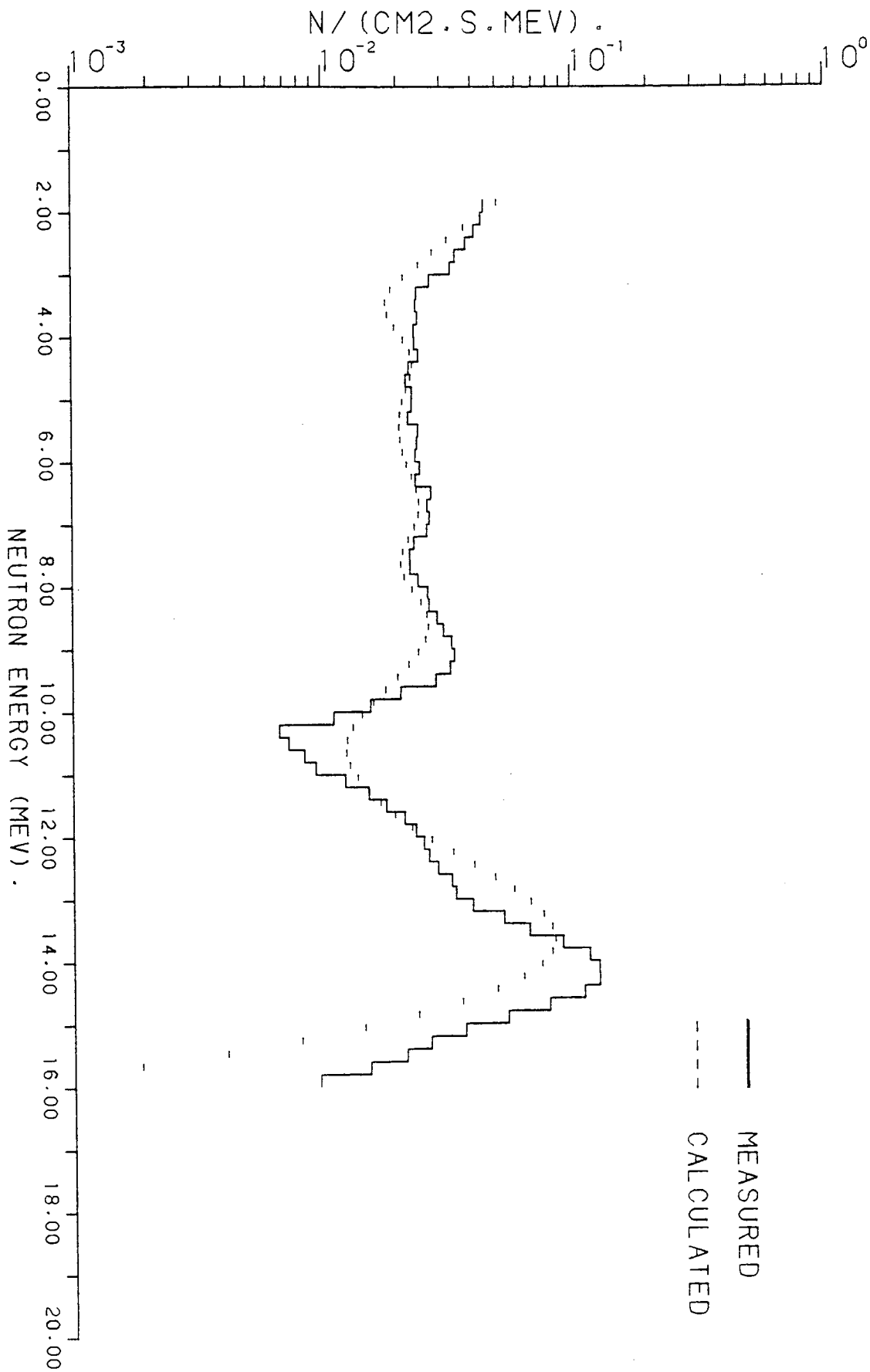


FIG. 7.49 NEUTRON FLUX AT THE SURFACE OF 26.7 CM THICK GRAPHITE SLAB.

cross section of 0.08 barn at 13.6 MeV and so will have a less marked effect on the spectrum than the (n,n') reaction.

With the thick slabs, the experimental neutron spectra agree fairly well with the calculated in the low and intermediate energy regions. A discrepancy between measured and calculated appears in thin slab in the low energy and intermediate ranges due to the small number of collisions in the assembly and also due to the effect of the background as discussed in section 7.3 .

By using the same method used before with LiF slabs which includes the experimentally determined scattered source neutrons into the source used for the neutron transport collisions, it can be see the correct spectra are calculated for 8.9, 17.8 and 26.7 cm thick graphite as in figure (7.47 R), (7.48 R) and (7.49 R) respectively. From these figures can be seen the better agreement between measured and calculated fluxes in the low energy range.

In comparison between 26.7 cm thick of graphite slabs [figure (7.49 R)] with that case of graphite cube [figure (7.45)], it was found that;

- Between about 4 MeV and 7.5 MeV, the fluxes from slab is lower than that from the cube. This is due to the secondary neutrons from inelastic and (n,n α) reaction, which are more in the cube case due to the larger volume of scatterer than slabs, especially in this energy region. Below and above this energy region, the difference between the two spectra is small .

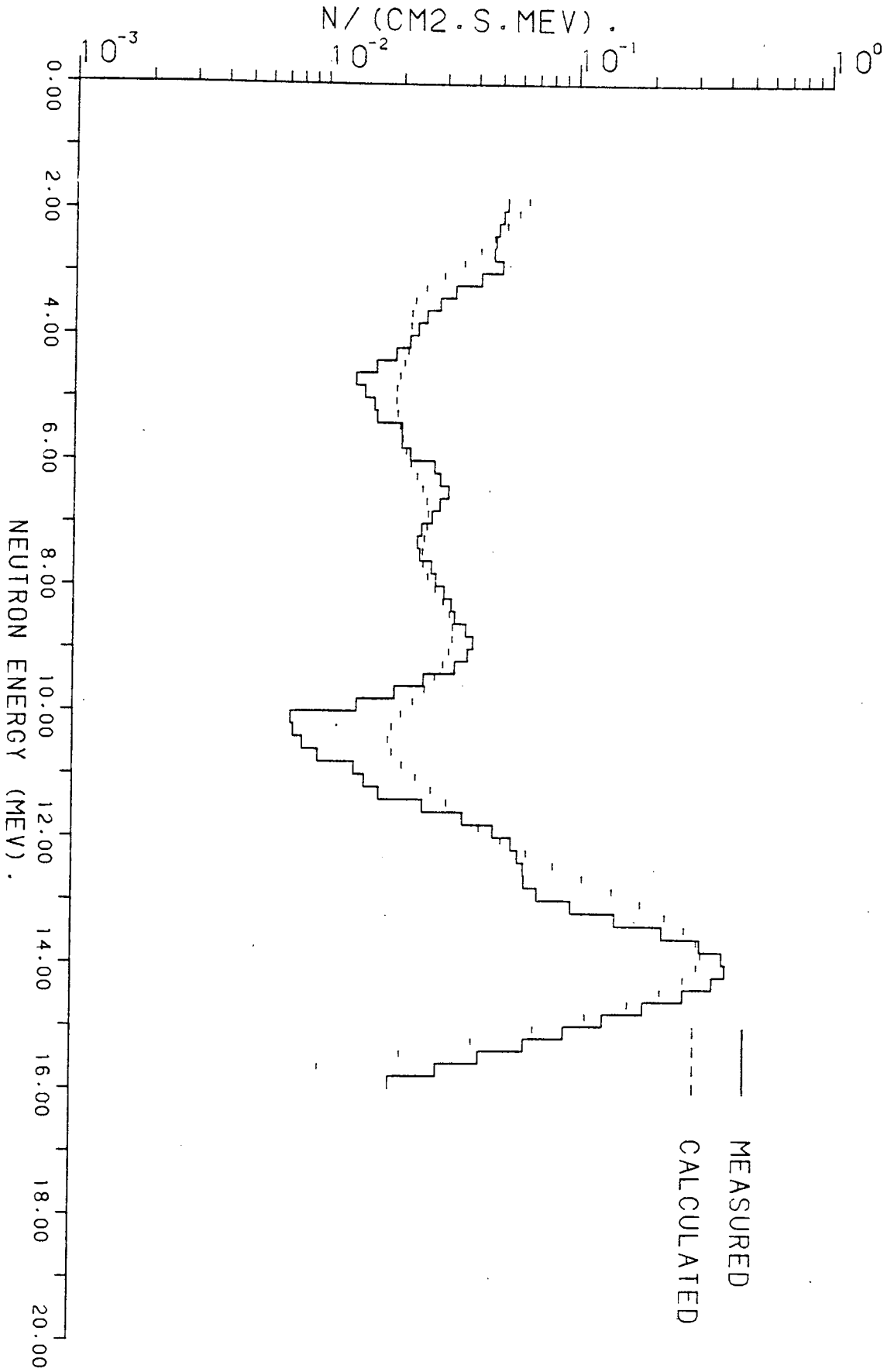


FIG. 7.47R NEUTRON FLUX AT THE SURFACE OF 8.9 CM THICK GRAPHITE SLAB INCLUDING NEUTRONS SCATTERED FROM THE SURROUNDINGS.

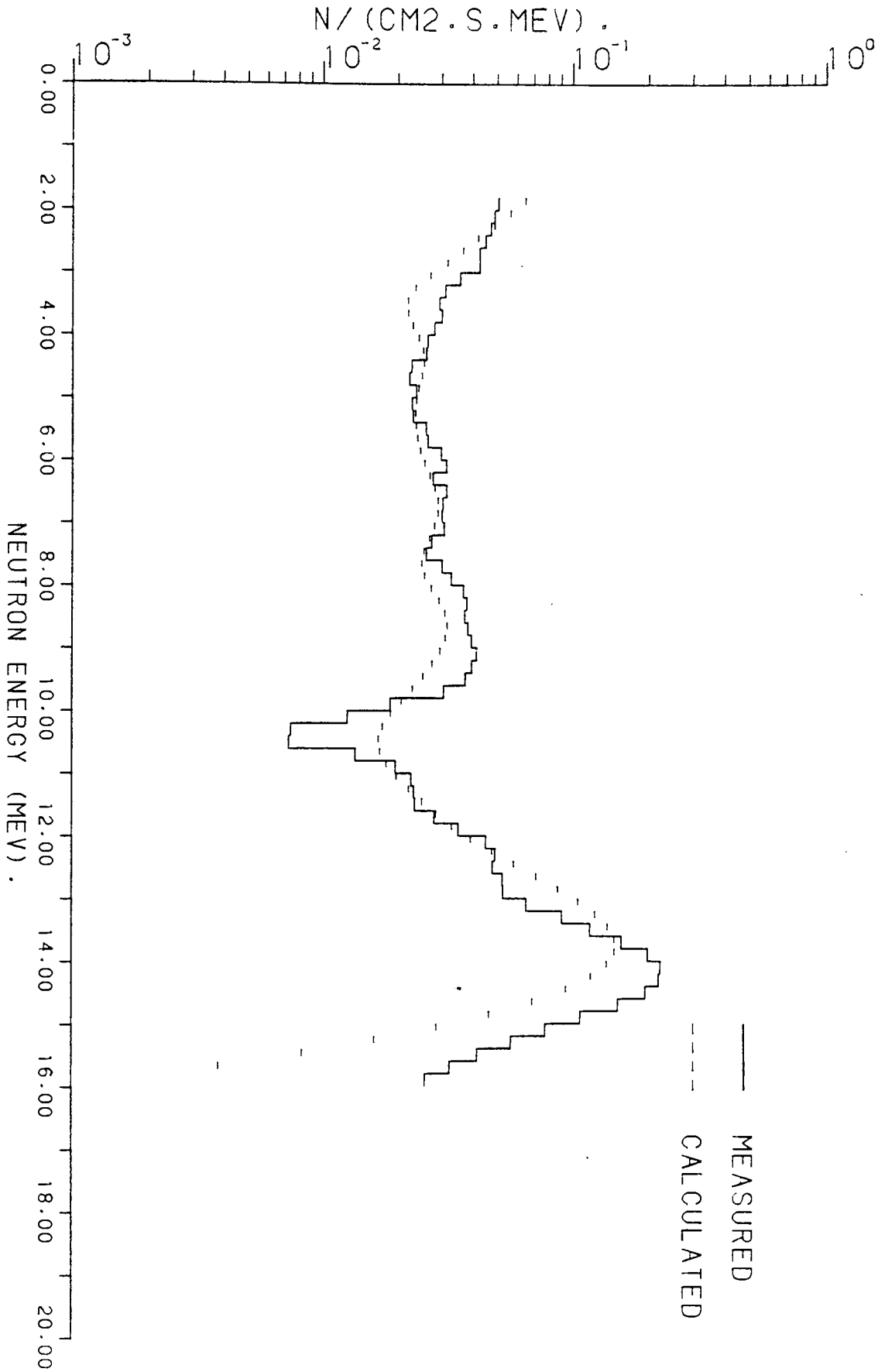


FIG. 7.48R NEUTRON FLUX AT THE SURFACE OF 17.8 CM THICK GRAPHITE SLAB INCLUDING NEUTRONS SCATTERED FROM THE SURROUNDINGS.

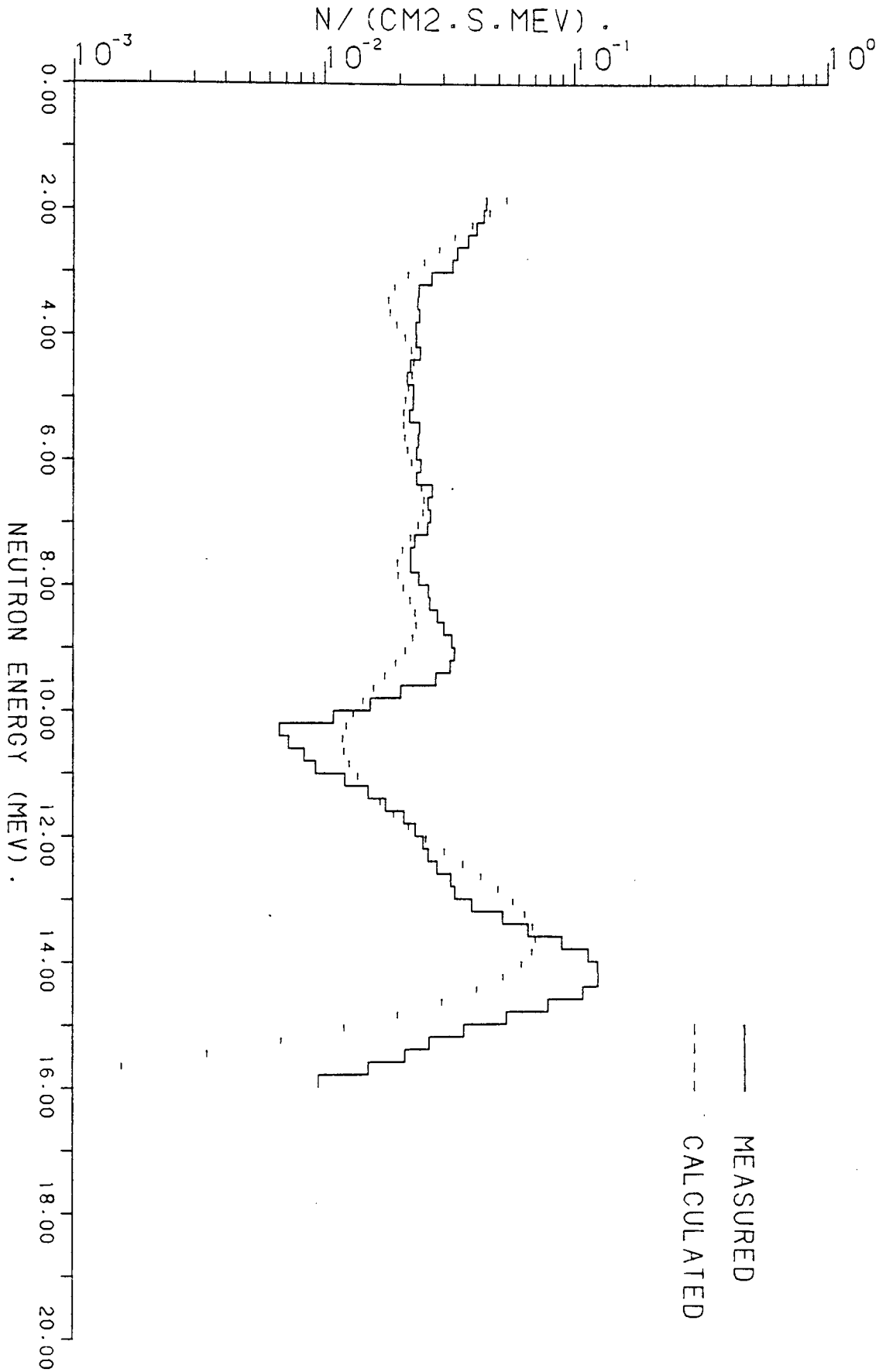


FIG. 7.49R NEUTRON FLUX AT THE SURFACE OF 26.7 CM THICK GRAPHITE SLAB INCLUDING NEUTRONS SCATTERED FROM THE SURROUNDINGS.

7.7.3 Neutron Spectra At The Surface Of Samples Containing Uranium On Top Of Graphite Slabs

Neutron fluxes measured and calculated at the surface of samples containing uranium on top of 8.9 and 17.8 cm graphite slabs [diagrams (6.18 A, B and C) and (6.21 A, B and C)] are shown in figures (7.50) to (7.55) respectively.

The fluxes, measured and calculated, decreases as the thickness of both uranium and graphite increase. The shape of the spectra does not change so much with thickness. The measured spectra are in satisfactory agreement with these calculated for most thicknesses.

Comparison between the spectra emitted from graphite slabs only [figures (7.47 R) and (7.48 R)] with that from containing uranium on top of the same thickness of graphite slabs [figures (7.50) to (7.55)] shows that;

- 1- Measured and calculated fluxes, below about 6 and 4 MeV in 8.9 cm and 17.8 cm graphite slabs respectively, are lower than those from samples containing uranium. As the thickness of graphite increases, this effect decreases which become evident in the 10.9 cm thick uranium on top of 17.8 cm graphite slab case. This is because uranium causes an increase in flux in the low energy region due to fission and as the thickness of graphite increases, the attenuation of these secondary neutrons by elastic scattering also increases.

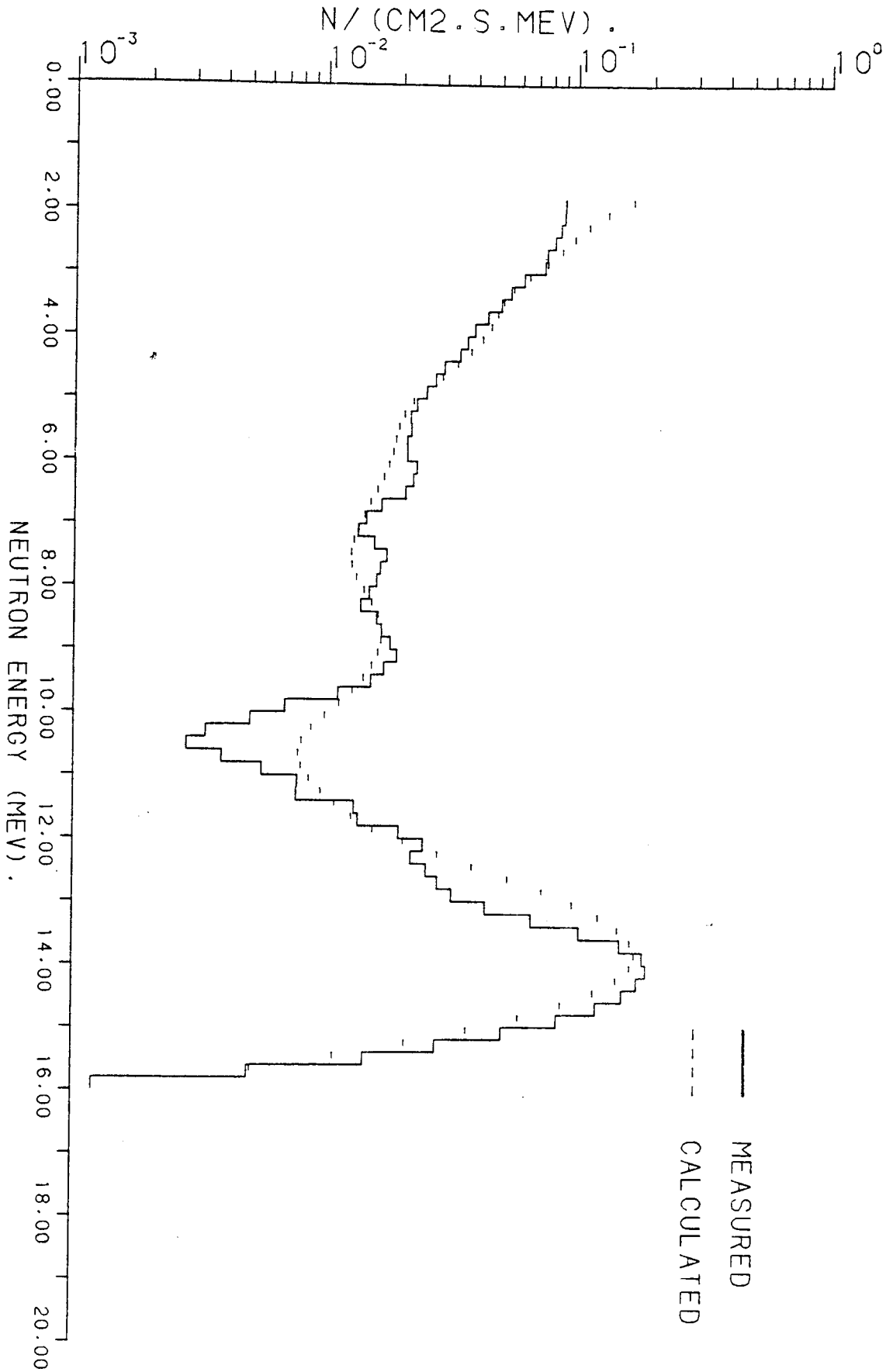


FIG. 7.50 NEUTRON FLUX AT THE SURFACE OF 5.4 CM URANIUM ON TOP OF 8.9 CM GRAPHITE.

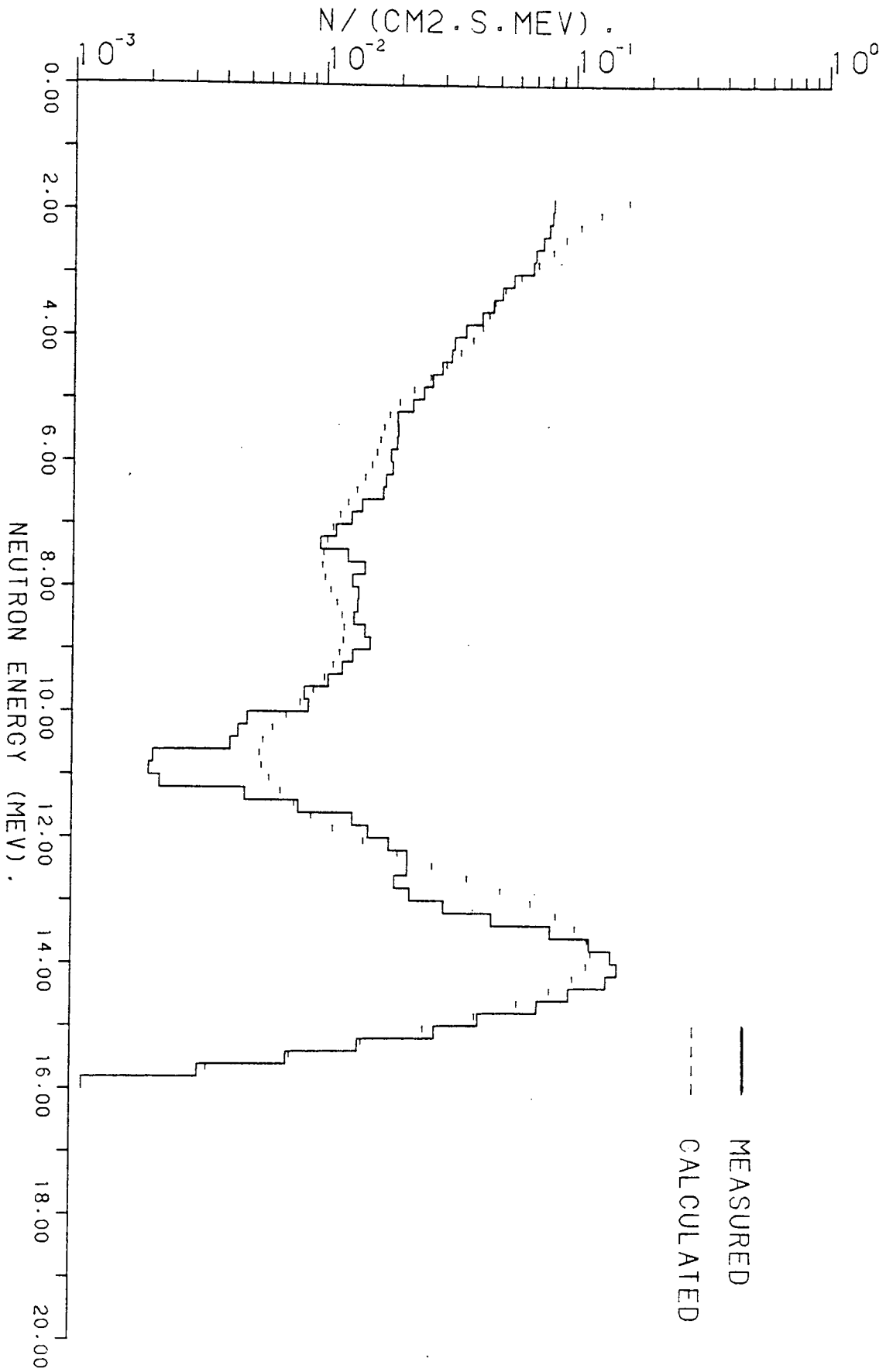


FIG. 7.51 NEUTRON FLUX AT THE SURFACE OF 8.2 CM URANIUM ON TOP OF 8.9 CM GRAPHITE.

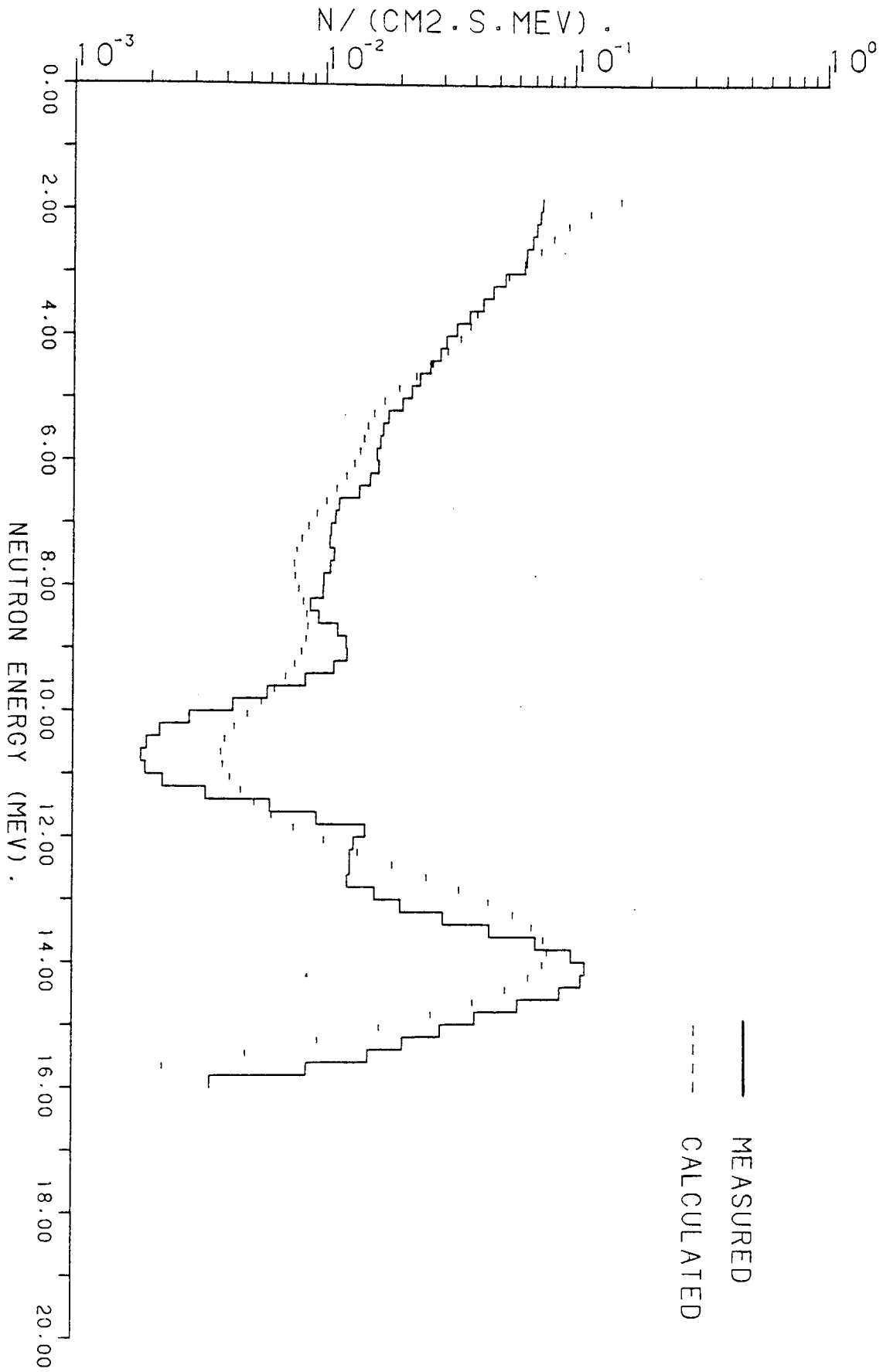


FIG. 7.52 NEUTRON FLUX AT THE SURFACE OF 10.9 CM URANIUM ON TOP OF 8.9 CM GRAPHITE.

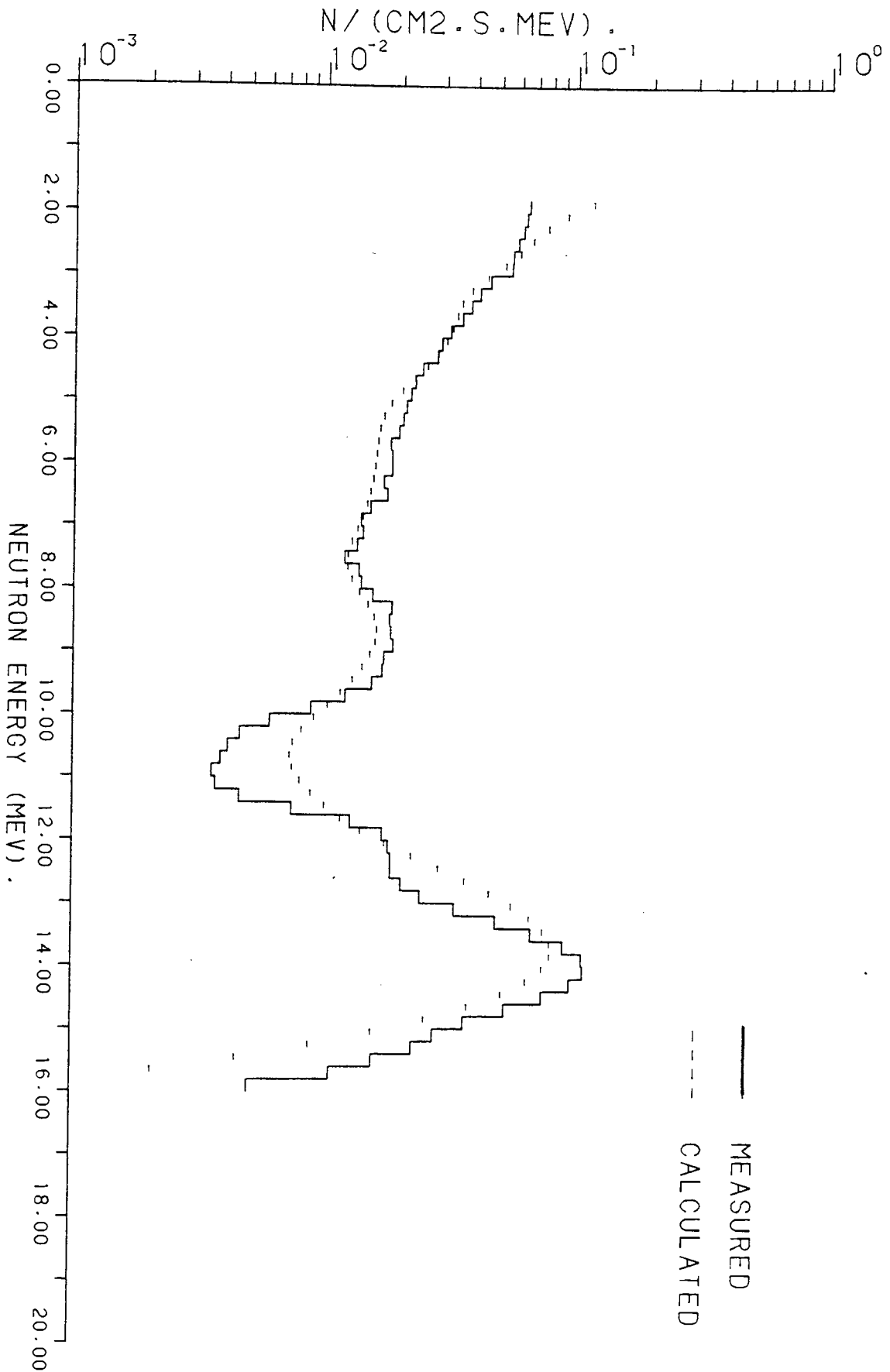


FIG. 7.53 NEUTRON FLUX AT THE SURFACE OF 5.4 CM URANIUM ON TOP OF 17.8 CM GRAPHITE.

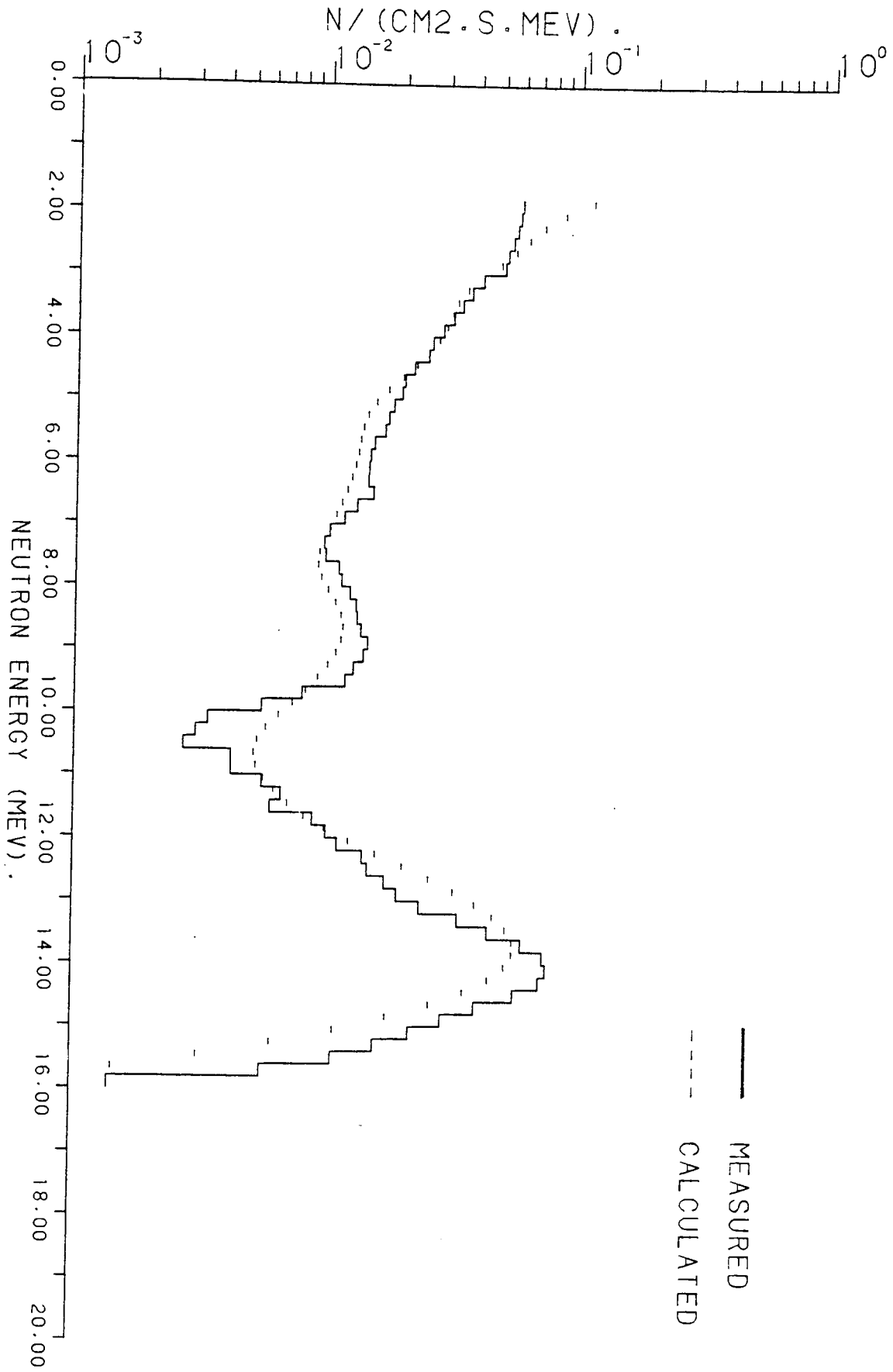


FIG. 7.54 NEUTRON FLUX AT THE SURFACE OF 8.2 CM URANIUM ON TOP OF 17.8 CM GRAPHITE.

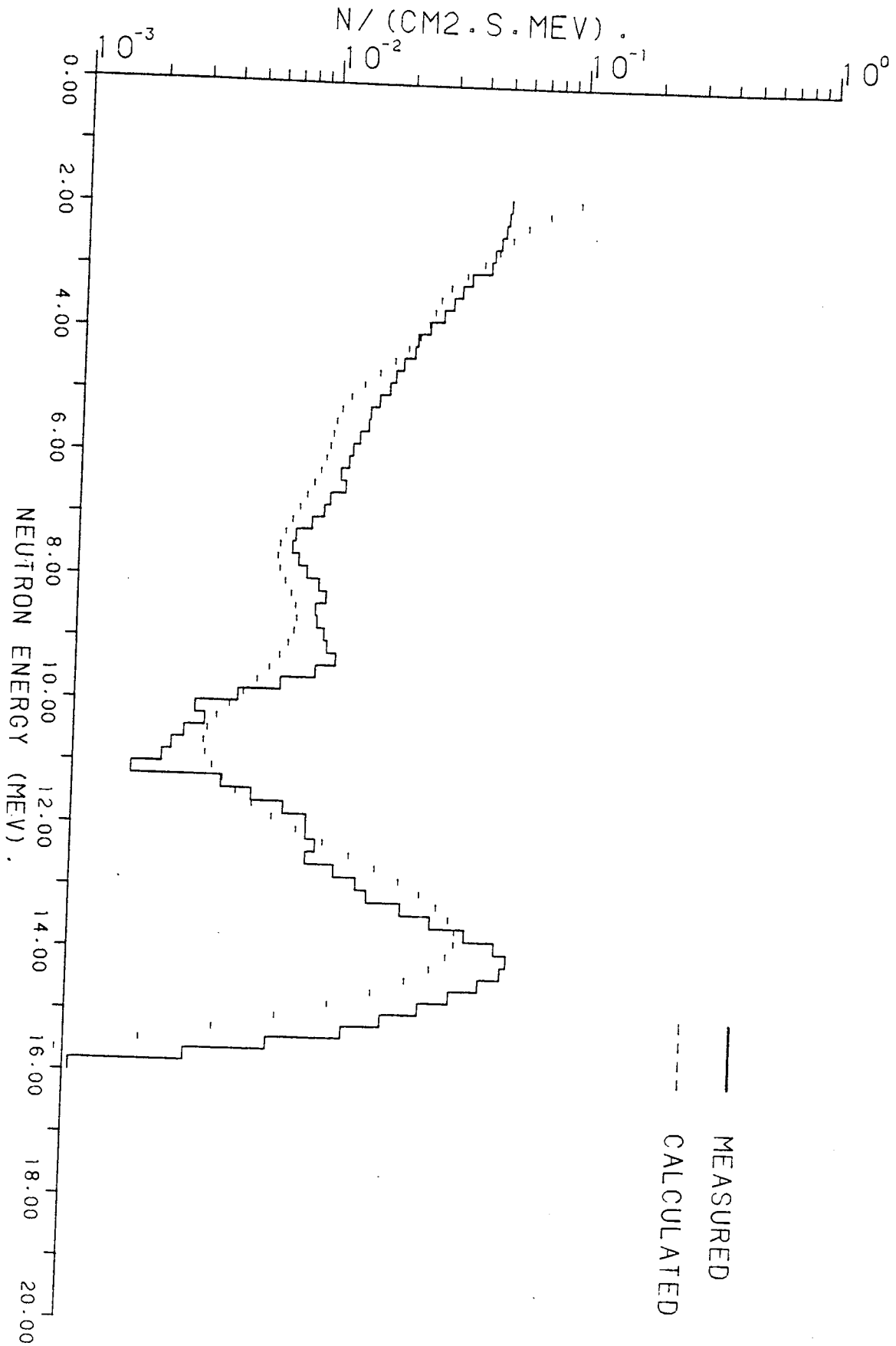


FIG. 7.55 NEUTRON FLUX AT THE SURFACE OF 10.9 CM URANIUM ON TOP OF 17.8 CM GRAPHITE.

2- Above these two energies (6 and 4 MeV), measured and calculated fluxes from graphite only are higher. This is due to the presence of uranium which due to its high density is a more effective neutron absorber in this energy range.

7.7.4 Neutron Spectra At The Surface Of Samples Containing LiF On Top Of Graphite Slabs

Figures (7.56) to (7.61) show measured and calculated fluxes emitted from 5.4, 8.2 and 10.9 cm LiF on top of 8.9 and 17.8 cm graphite slabs as represented in diagrams (6.19 A, B and C) and (6.22 A, B and C) respectively.

The flux and the shape of the spectra change slightly with LiF thickness. As the thickness of graphite increases from 8.9 to 17.8 cm with the same thickness of LiF, the flux decrease around the 14 MeV peak. Below this region, there is no significant difference between fluxes in both cases.

Comparison between the spectra from graphite slab only [figure (7.47 R) and (7.48 R)] with these containing LiF on top of the same thickness of graphite slab [figures (7.56) to (7.61)], show that below about 6 MeV (in 8.9 cm thick graphite) and 5 MeV (in 17.8 cm thick graphite) there is a slight difference in the flux. Above these two energies limit, the fluxes in the graphite slabs are slightly higher. It would also appear that the experimental spectrum should have been used for the thinner graphite layer combinations in the calculations.

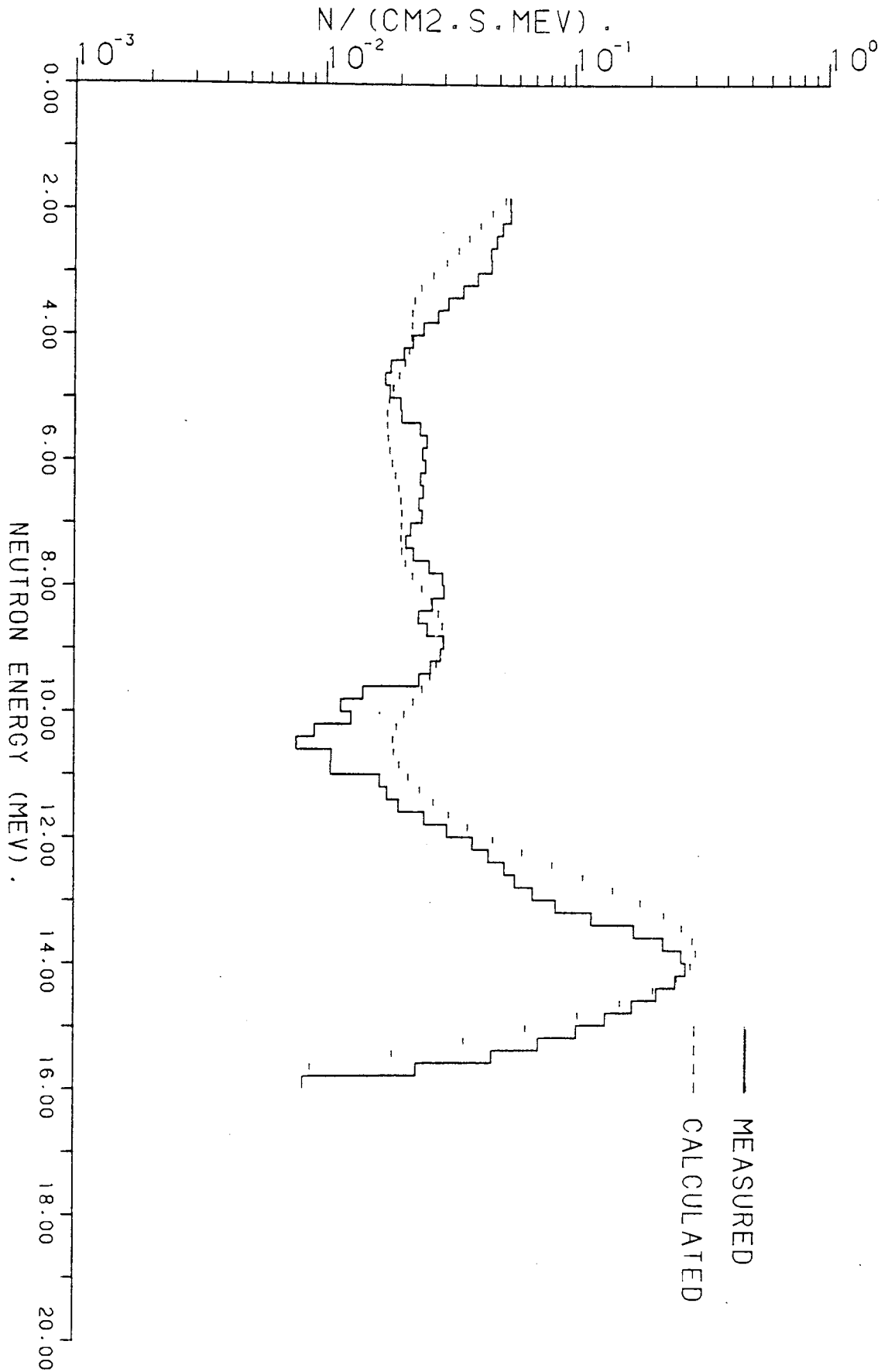


FIG. 7.56 NEUTRON FLUX AT THE SURFACE OF 5.4 CM LIF ON TOP
OF 8.9 CM GRAPHITE.

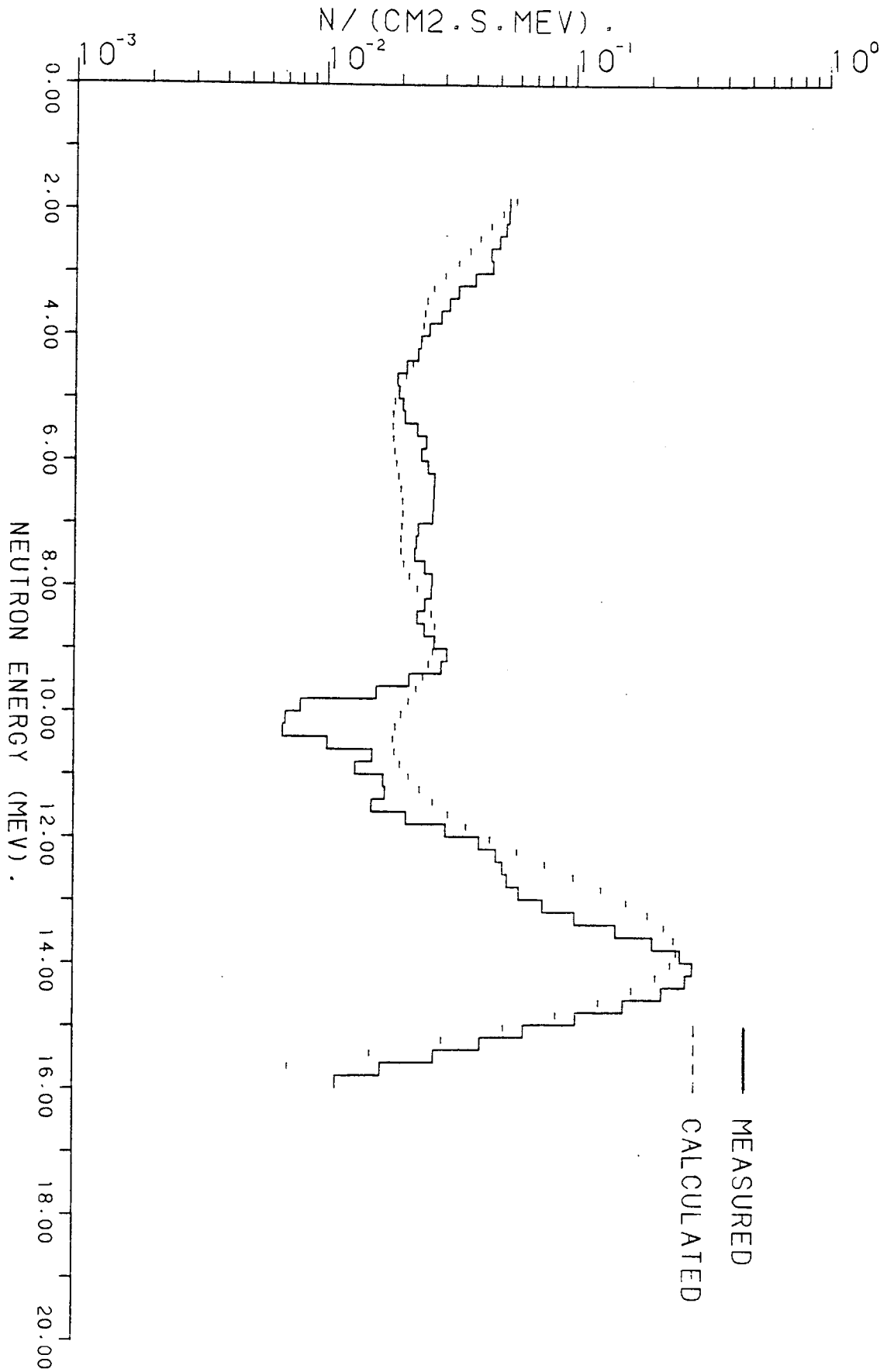


FIG. 7.57 NEUTRON FLUX AT THE SURFACE OF 8.2 CM LIF ON TOP OF 8.9 CM GRAPHITE.

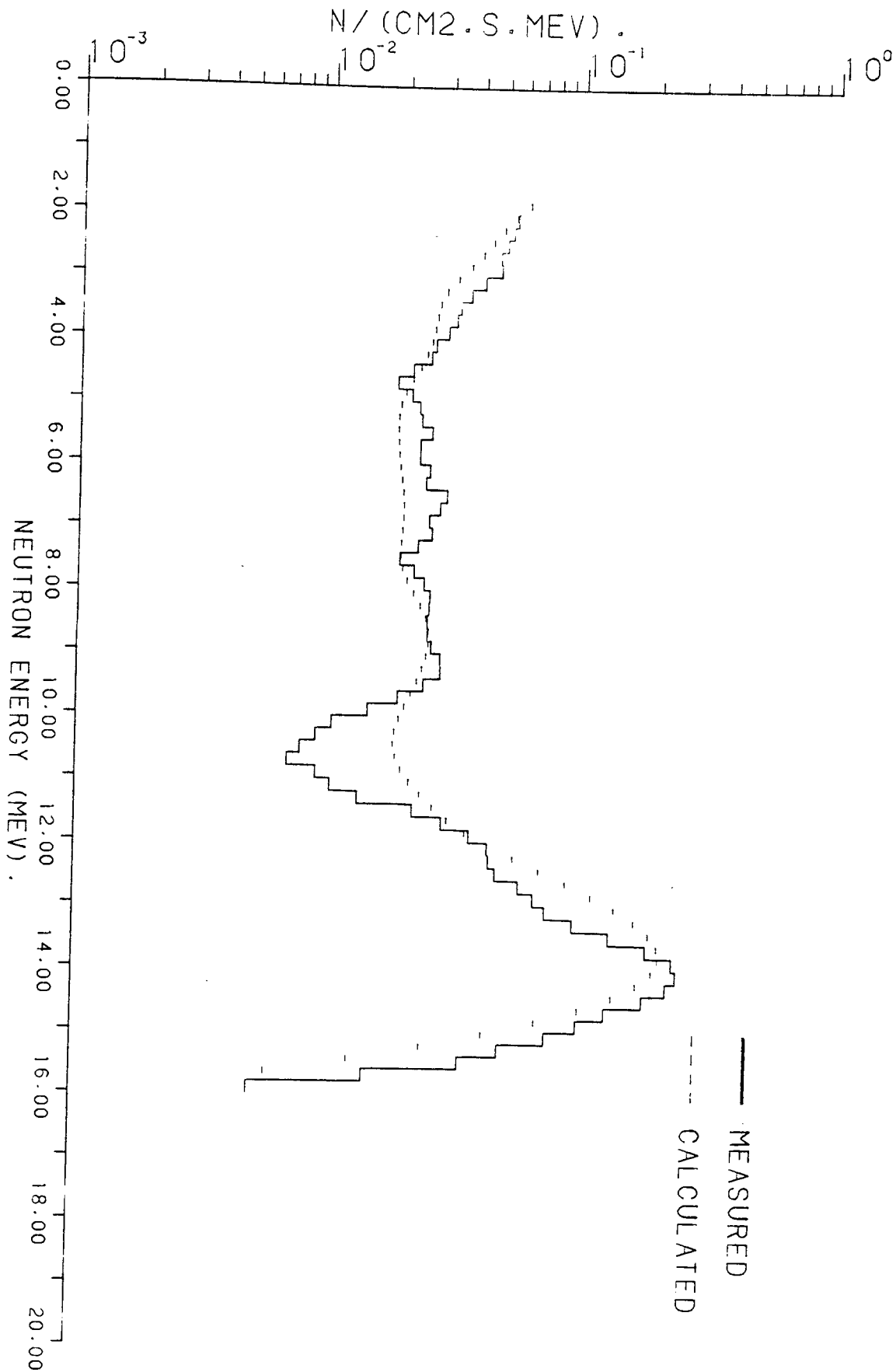


FIG. 7.58 NEUTRON FLUX AT THE SURFACE OF 10.9 CM LIF ON TOP OF 8.9 CM GRAPHITE.

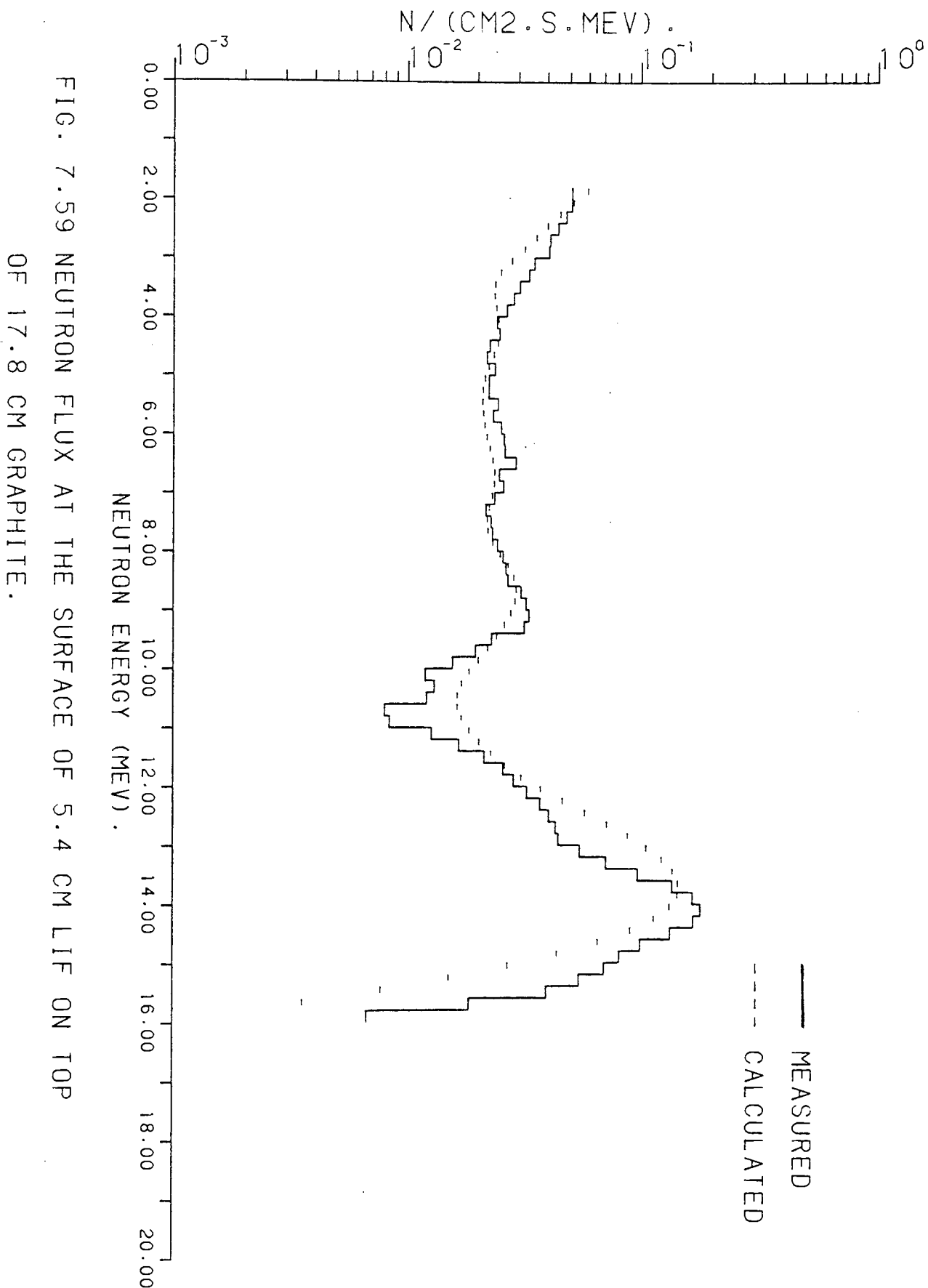


FIG. 7.59 NEUTRON FLUX AT THE SURFACE OF 5.4 CM LIF ON TOP OF 17.8 CM GRAPHITE.

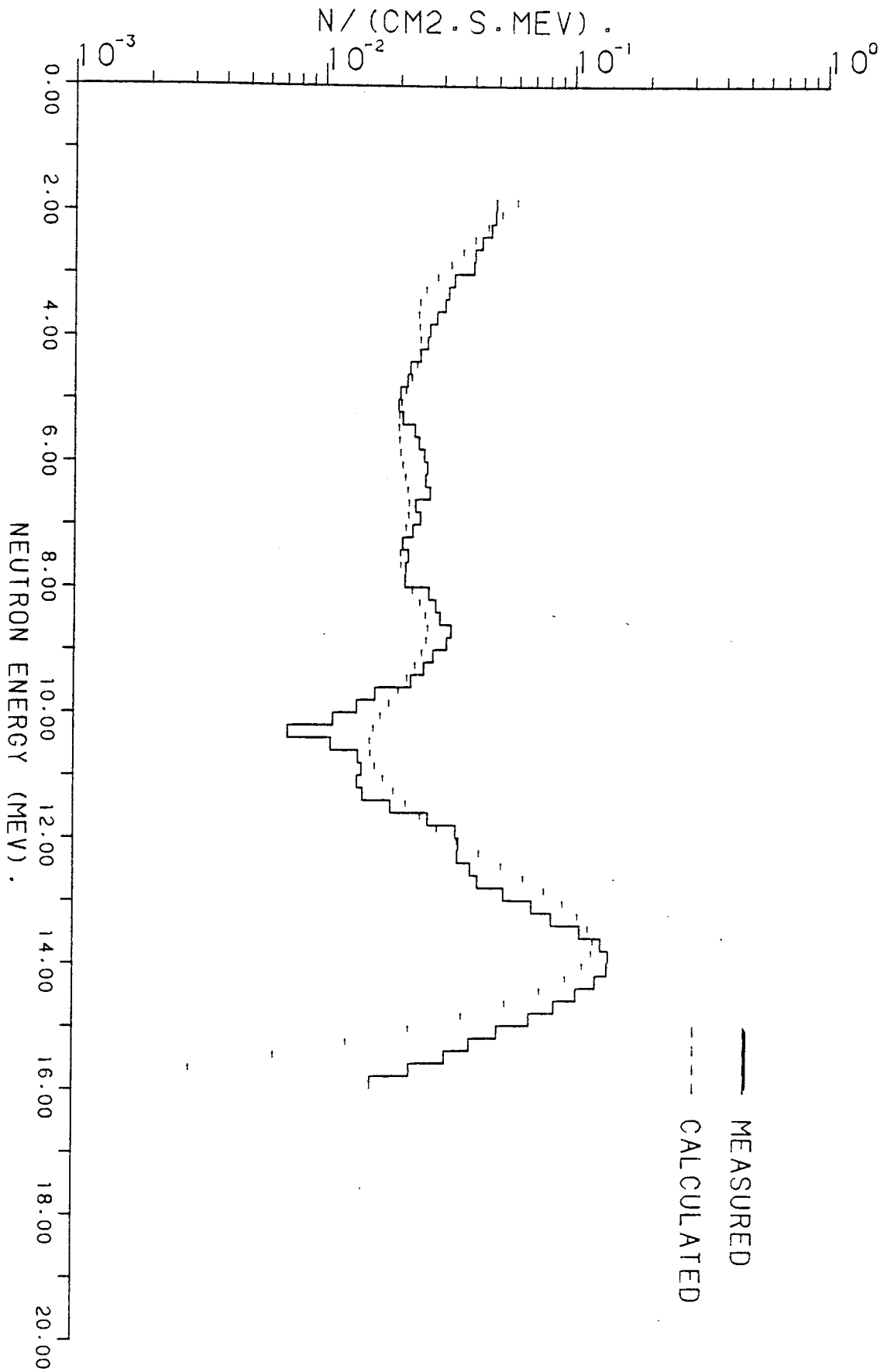


FIG. 7.60 NEUTRON FLUX AT THE SURFACE OF 8.2 CM LIF ON TOP OF 17.8 CM GRAPHITE.

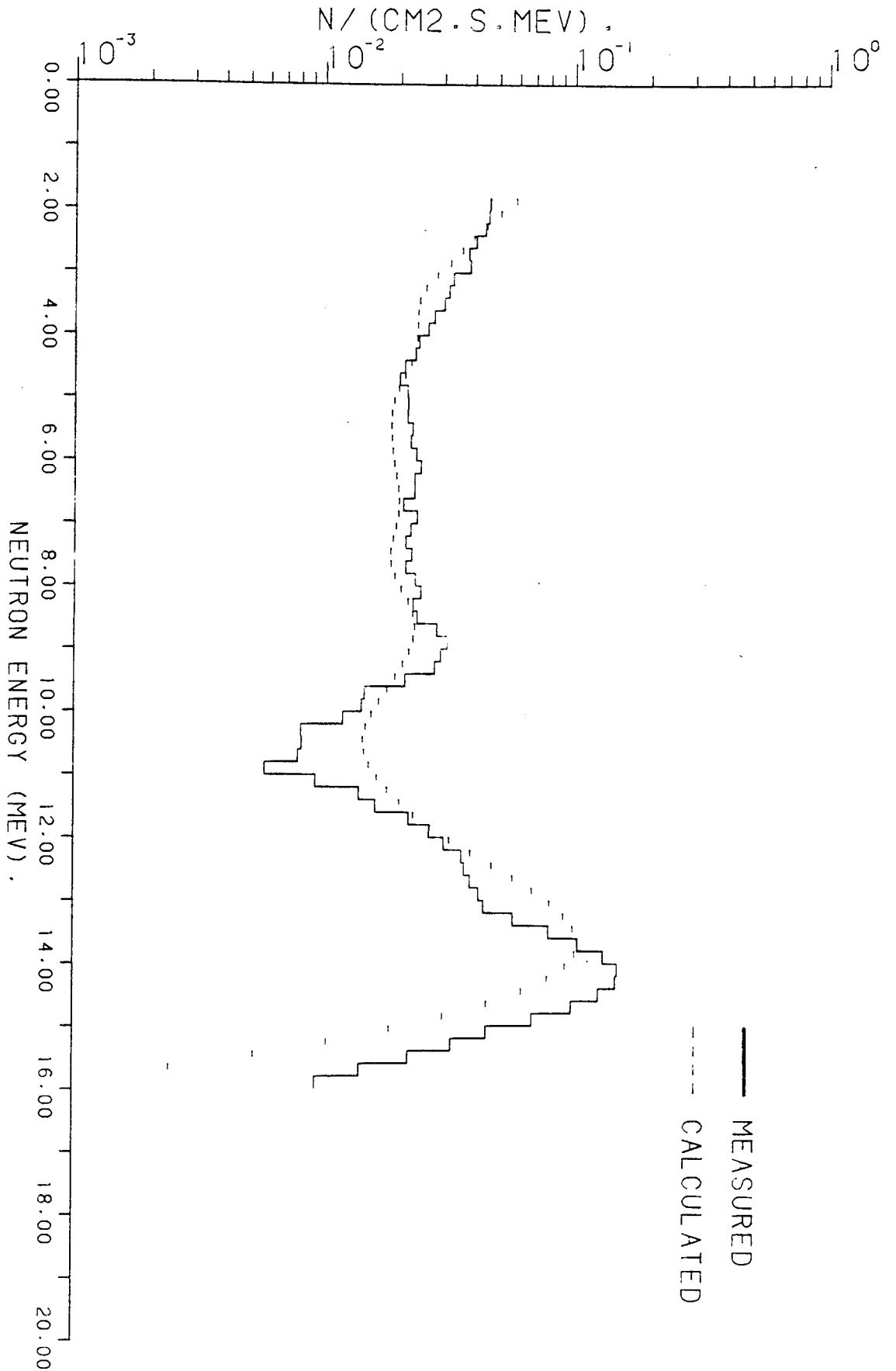


FIG. 7.61 NEUTRON FLUX AT THE SURFACE OF 10.9 CM LIF ON TOP OF 17.8 CM GRAPHITE.

7.7.5 Neutron Spectra At The Surface Of Samples Containing LiF and Uranium Mixture On Top Of Graphite Slabs

Measured and calculated fluxes emitted from 5.4, 8.2, 10.9, 13.6, 16.3, 19 and 21.7 cm thick LiF and uranium mixture on top of 8.9 cm graphite slab [diagrams (6.20 A) to (6.20 G)] are shown in figures (7.62) to (7.68) respectively. The measured and calculated fluxes from the samples containing mixture of LiF and uranium with 5.4, 8.2, 10.9, 13.6 and 16.3 cm thick on top of 17.8 cm graphite slab [diagrams (6.23 A) to (6.23 E)] are shown in figures (7.69) to (7.73) respectively.

The flux decreases as the thickness of the mixture increase in both cases (8.9 and 17.8 cm thick graphite). The attenuation of the neutrons becomes greater in the intermediate energy region especially with 17.8 cm graphite slab.

- 1- Comparing the spectra from the assemblies containing LiF and uranium mixture on top of 8.9 cm thick graphite [figures (7.62) to (7.68)] with those containing ;

(a)- 8.9 cm graphite [figure (7.47 R)]

Below about 6 MeV, the fluxes emitted from the mixture cases are higher than the flux from graphite assembly. Above this energy, the flux emitted from graphite assembly is higher than that emitted from mixture assemblies. As the thickness of mixture increase, this difference decreases. This effect is due to the fission neutrons emitted from the mixture which contains uranium.

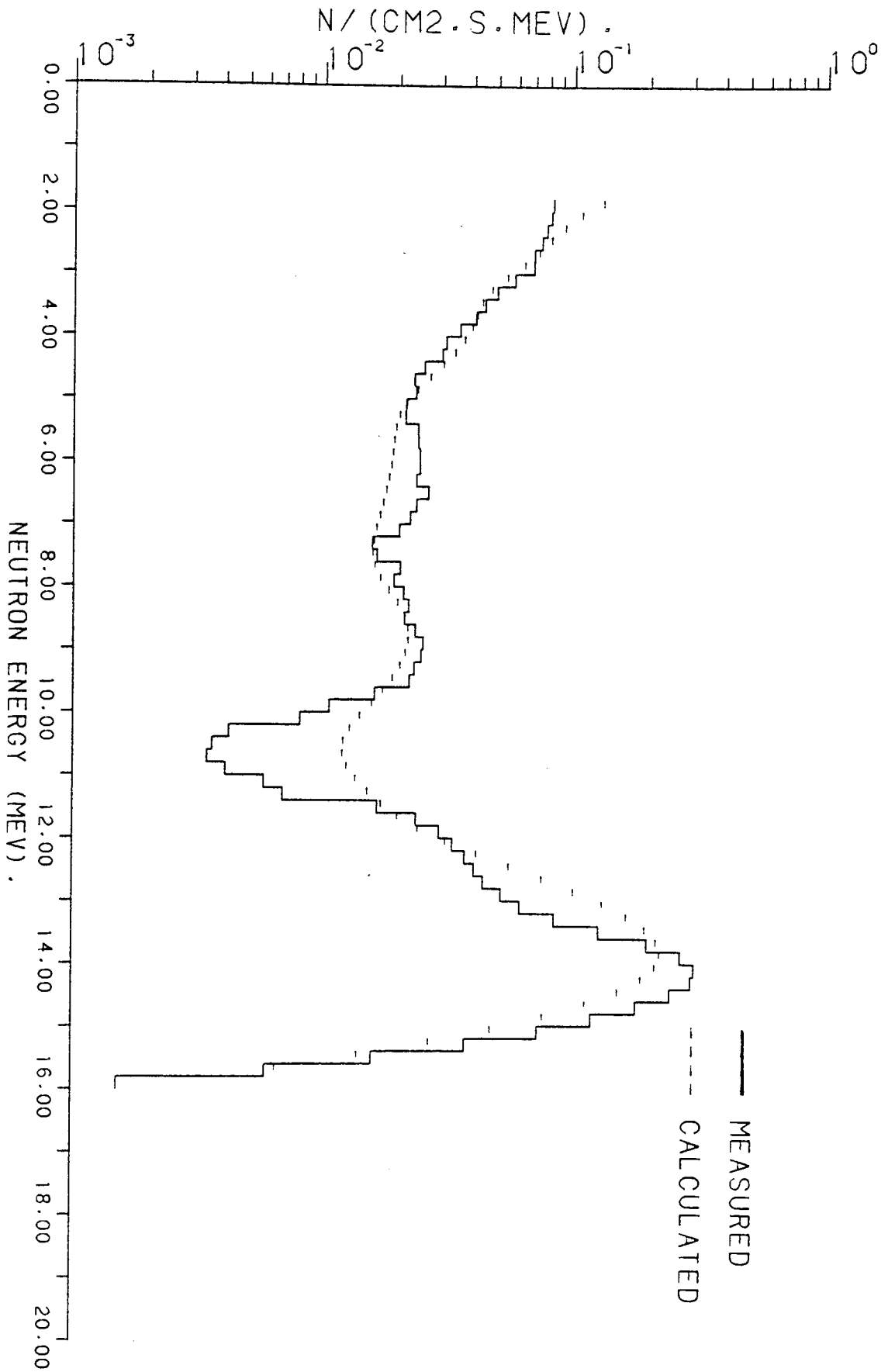


FIG. 7.62 NEUTRON FLUX AT THE SURFACE OF 5.4 CM LIF AND URANIUM MIXTURE ON TOP OF 8.9 CM GRAPHITE SLAB.

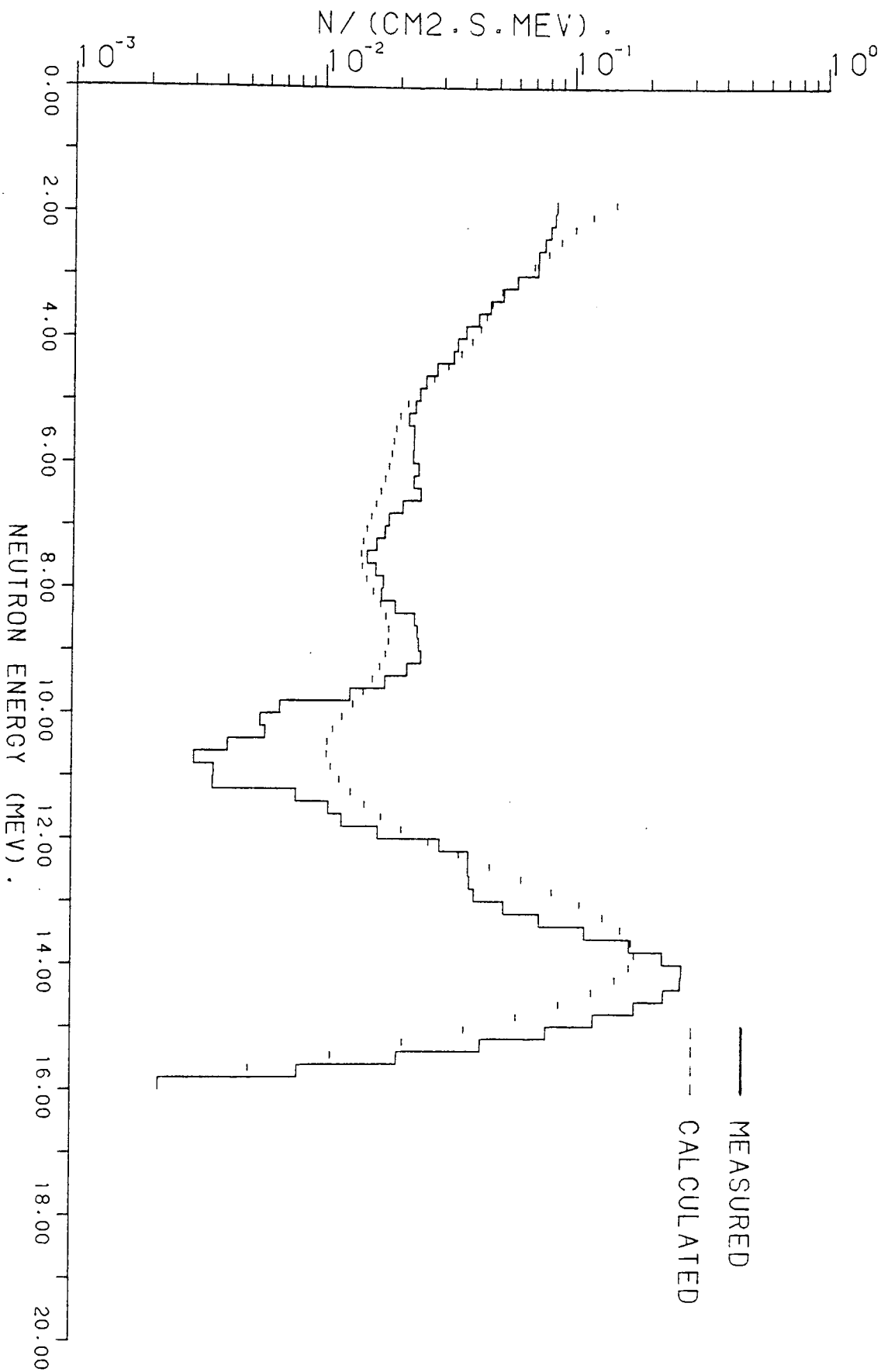


FIG. 7.63 NEUTRON FLUX AT THE SURFACE OF 8.2 CM LIF AND URANIUM MIXTURE ON TOP OF 8.9 CM GRAPHITE SLAB.

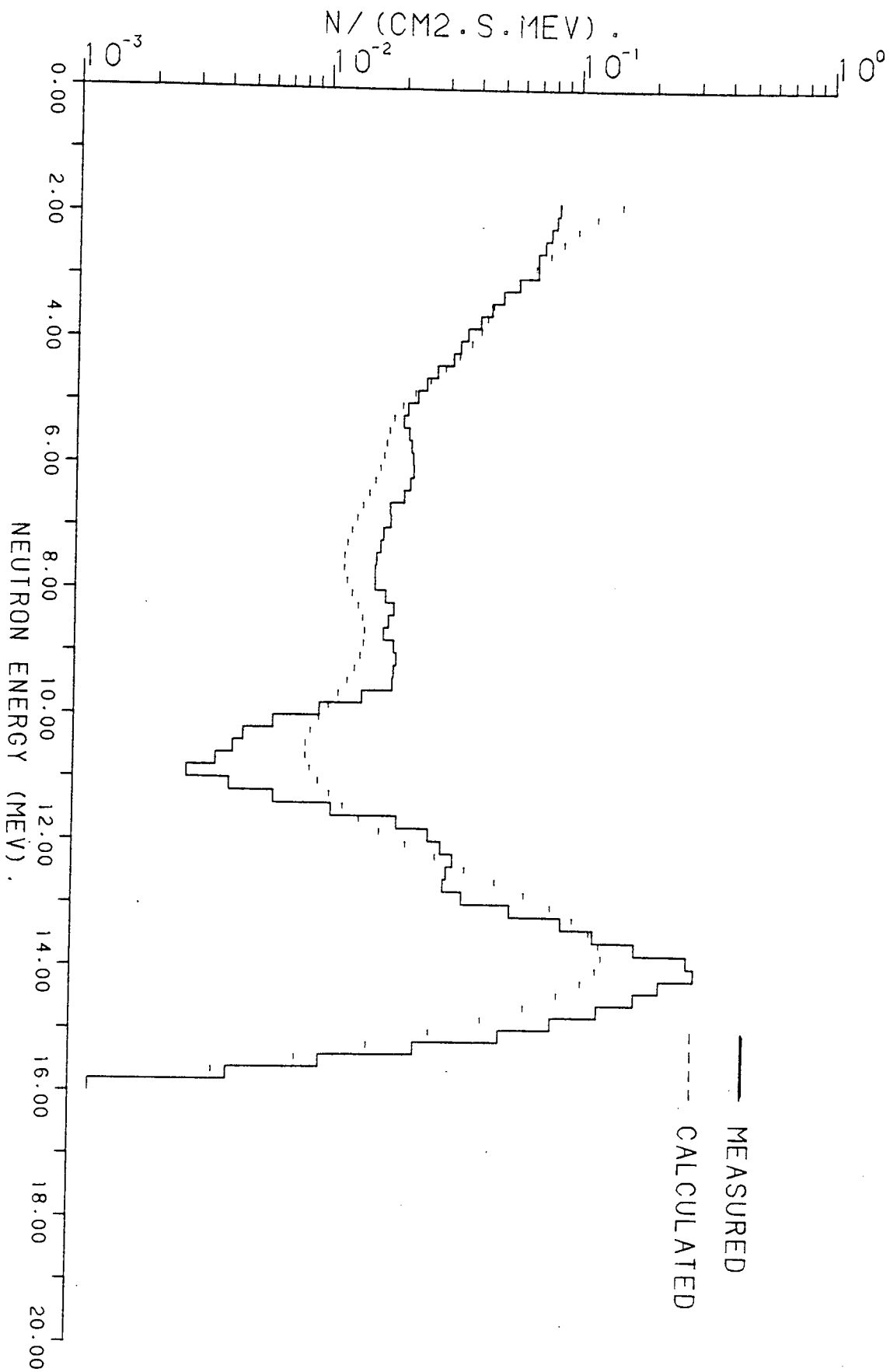


FIG. 7.64 NEUTRON FLUX AT THE SURFACE OF 10.9 CM LIF AND URANIUM MIXTURE ON TOP OF 8.9 CM GRAPHITE SLAB.

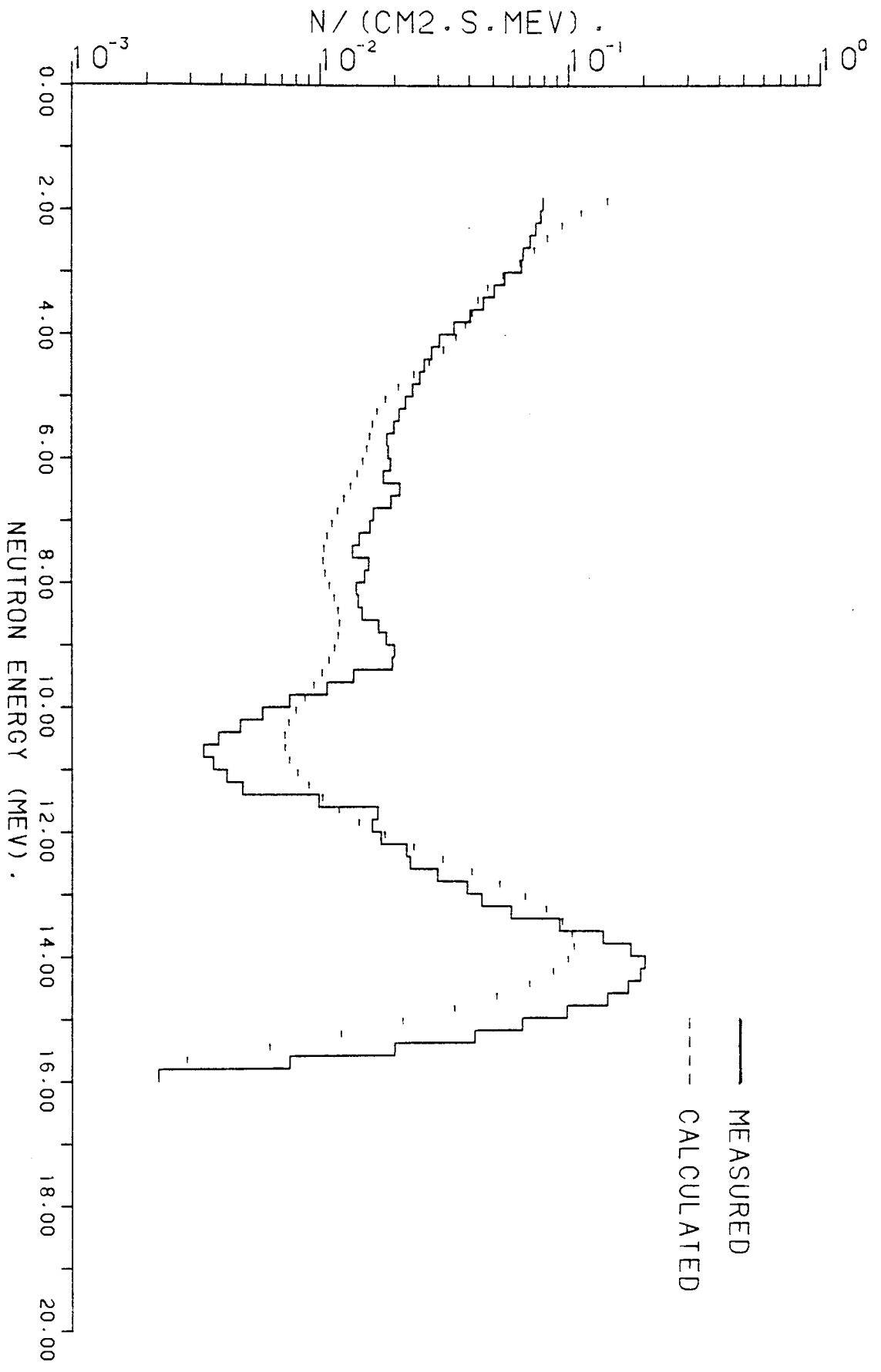


FIG. 7.65 NEUTRON FLUX AT THE SURFACE OF 13.6 CM LIF AND URANIUM MIXTURE ON TOP OF 8.9 CM GRAPHITE SLAB.

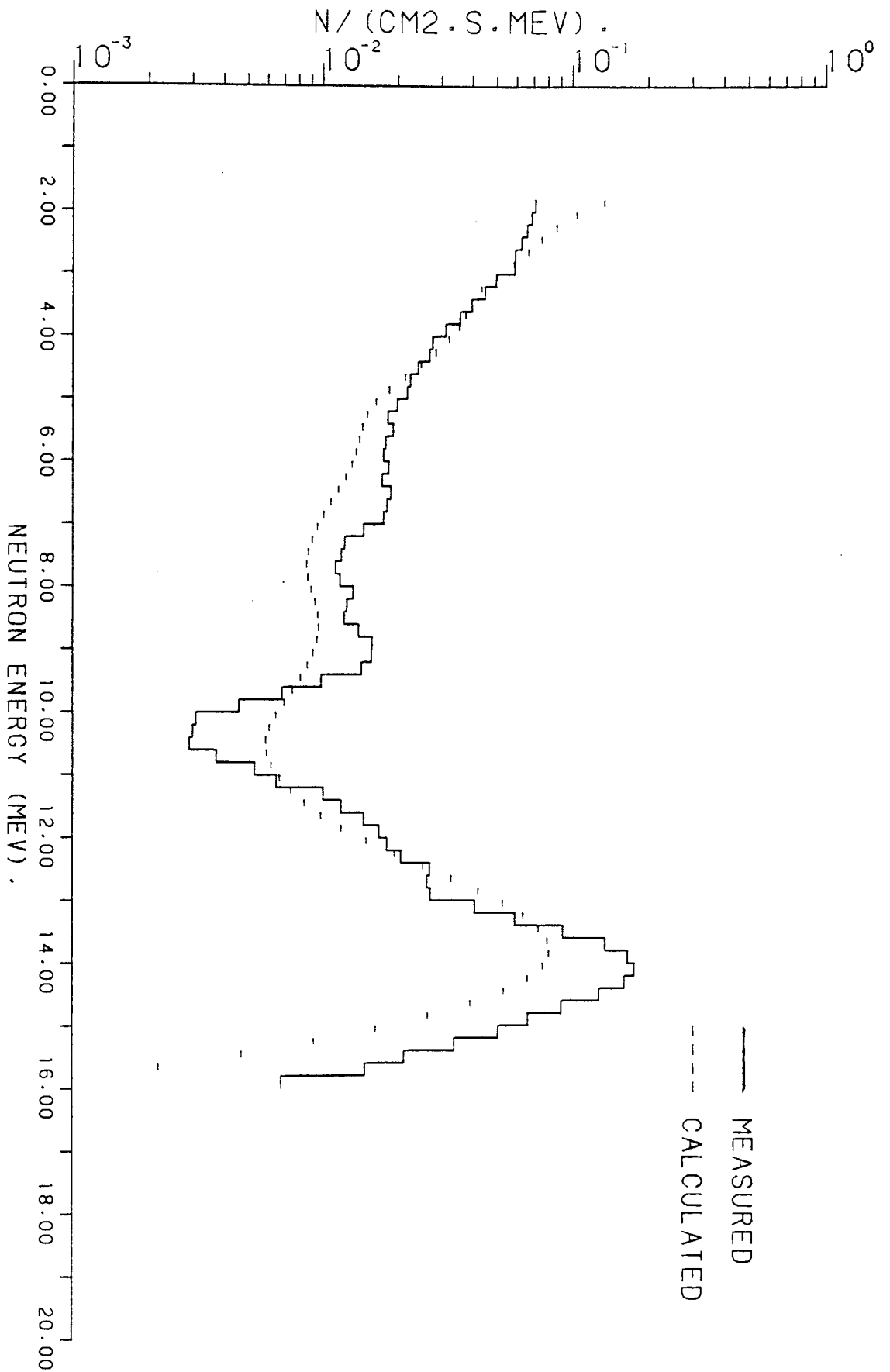


FIG. 7.66 NEUTRON FLUX AT THE SURFACE OF 16.3 CM LIF AND URANIUM MIXTURE ON TOP OF 8.9 CM GRAPHITE SLAB.

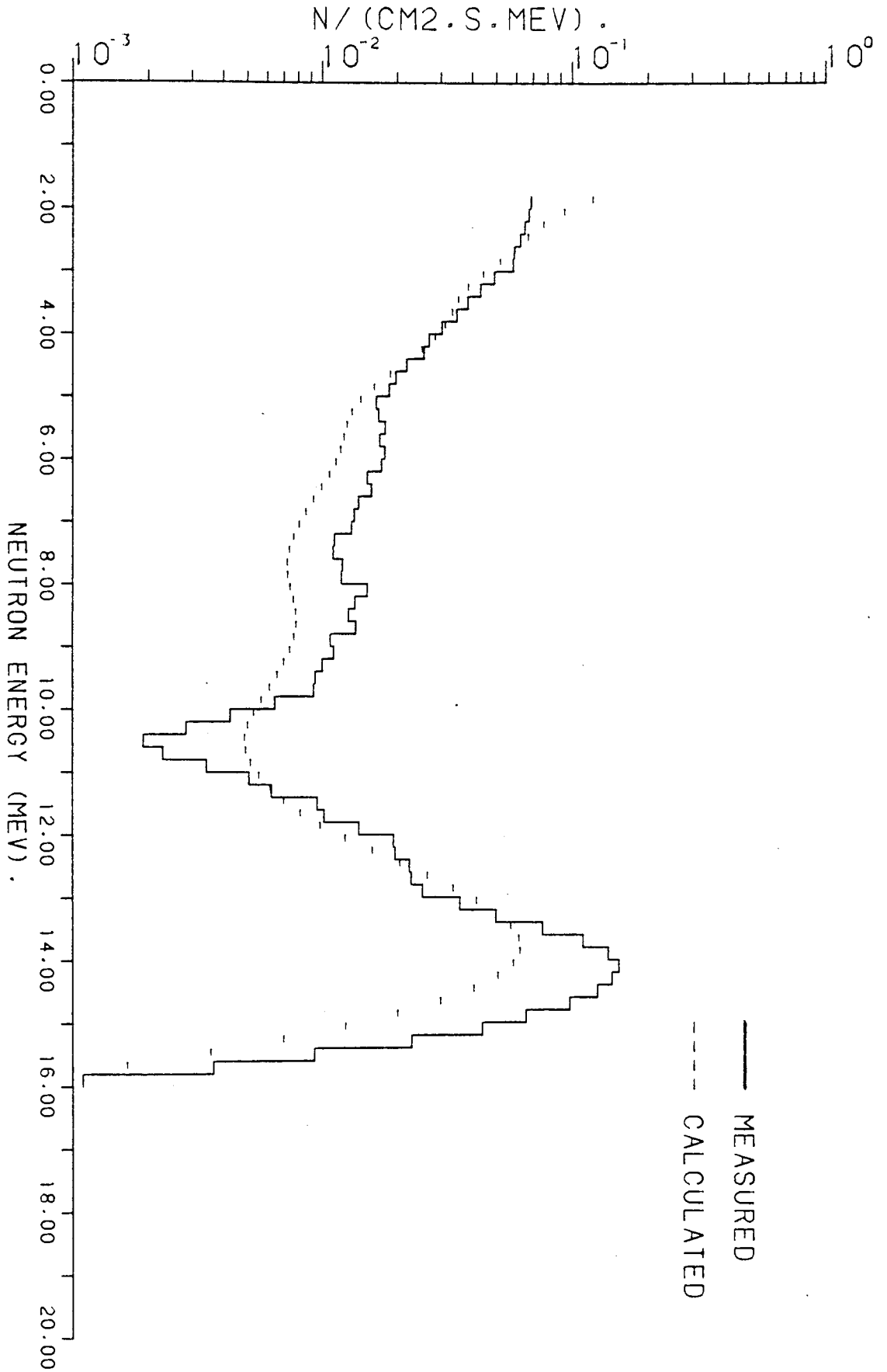


FIG. 7.67 NEUTRON FLUX AT THE SURFACE OF 19 CM LIF AND URANIUM MIXTURE ON TOP OF 8.9 CM GRAPHITE SLAB.

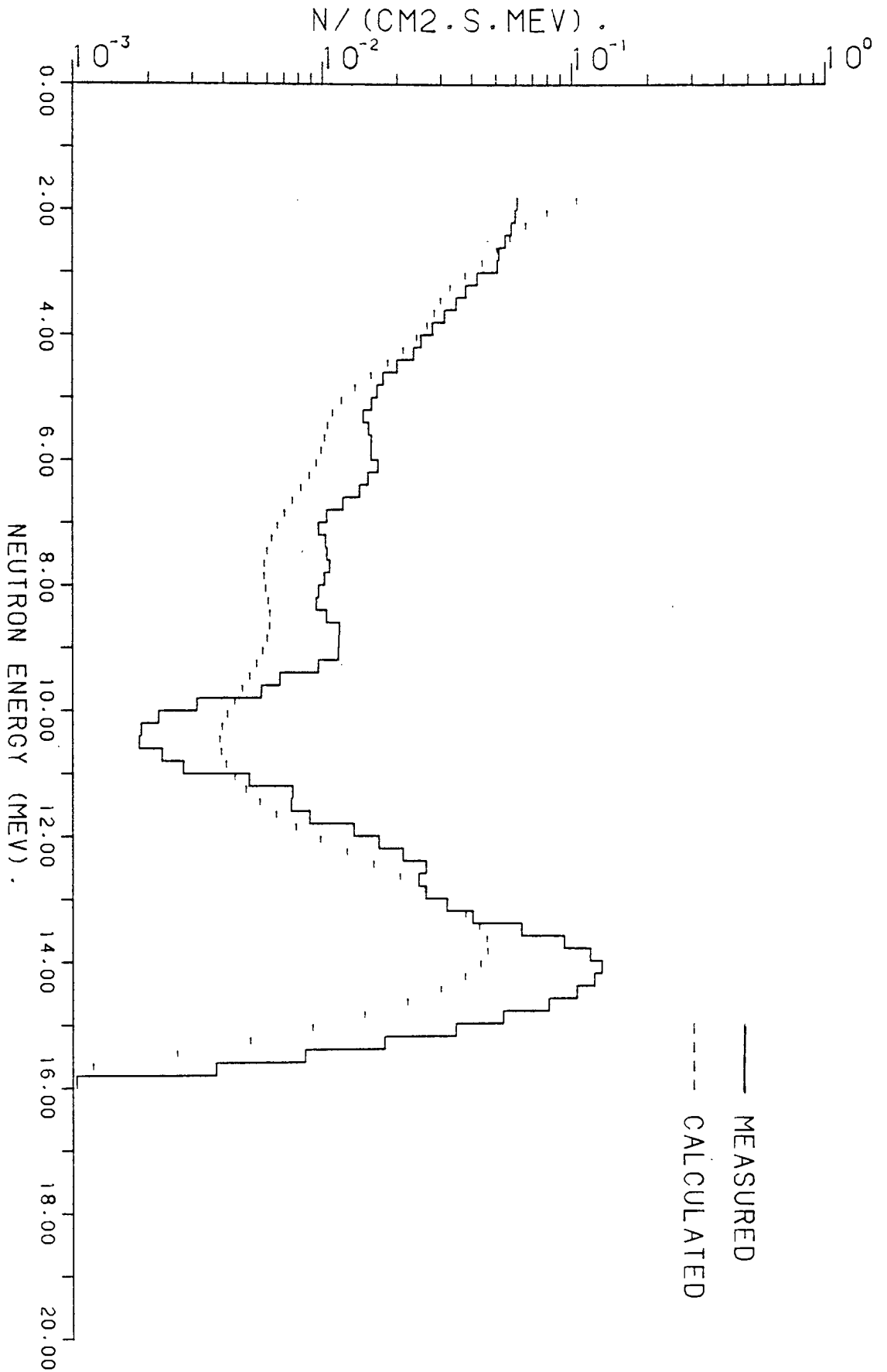


FIG. 7.68 NEUTRON FLUX AT THE SURFACE OF 21.7 CM LIF AND URANIUM MIXTURE ON TOP OF 8.9 CM GRAPHITE SLAB.

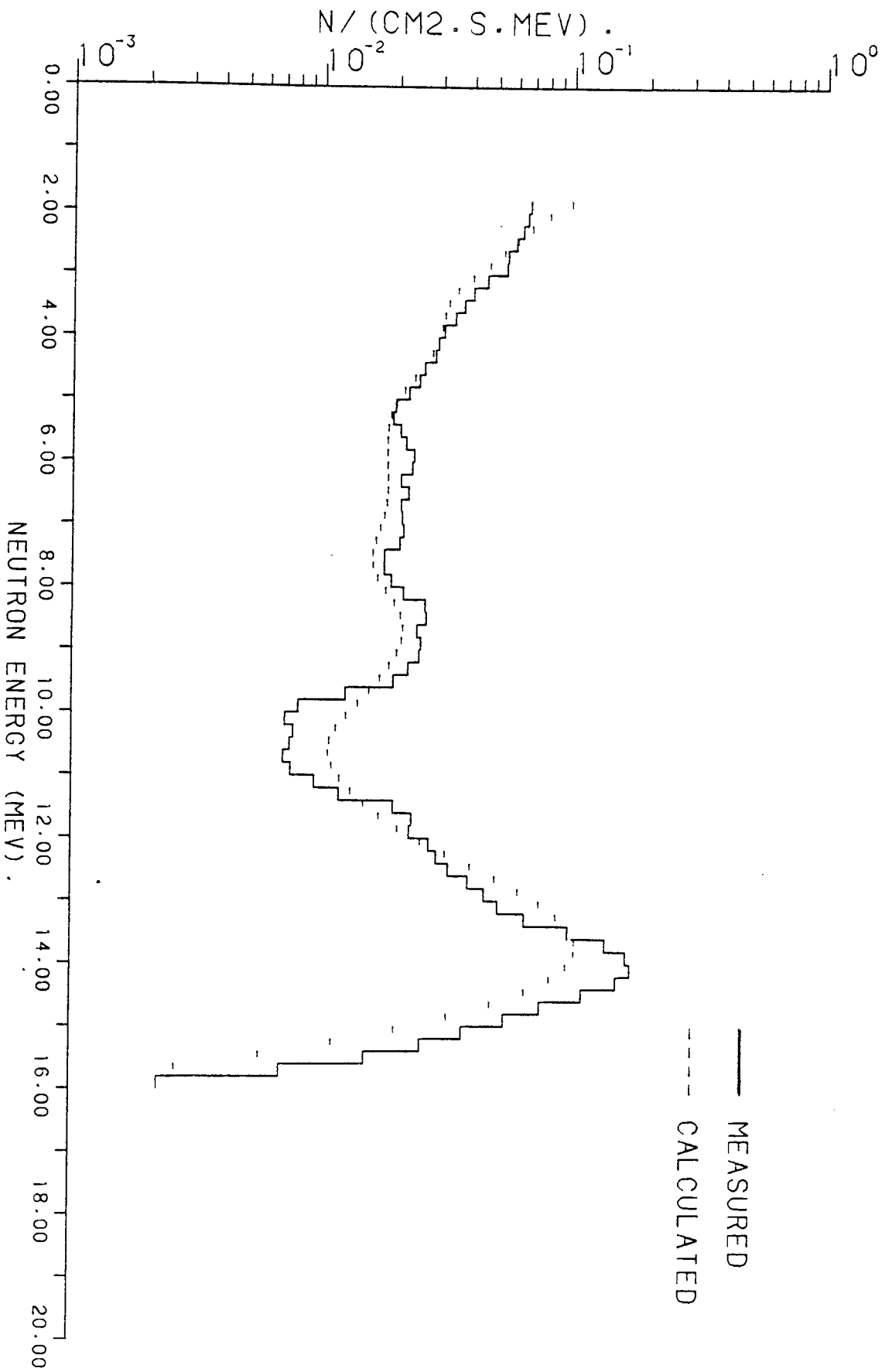


FIG. 7.69 NEUTRON FLUX AT THE SURFACE OF 5.4 CM LIF AND URANIUM MIXTURE ON TOP OF 17.8 CM GRAPHITE SLAB.

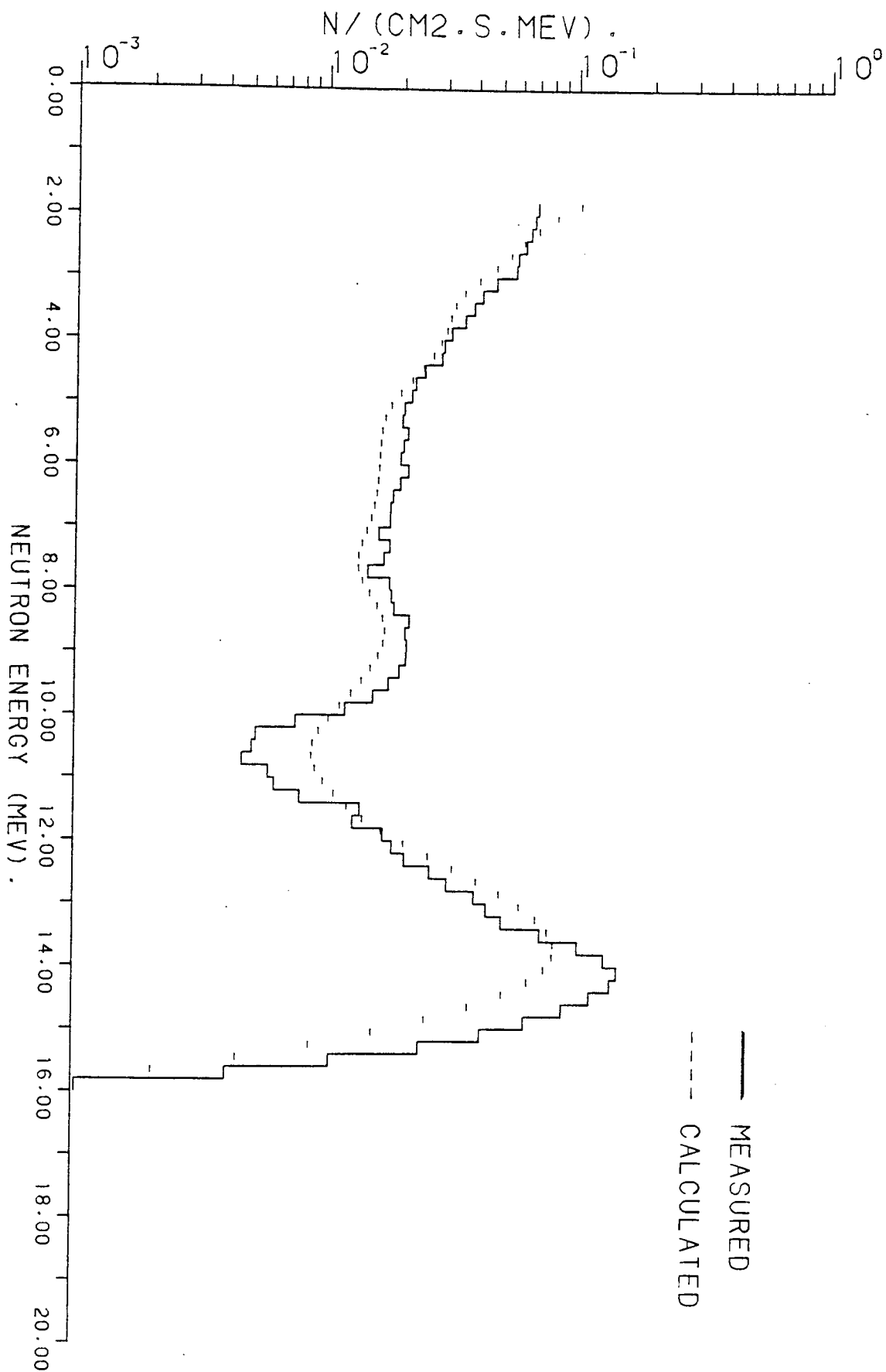


FIG. 7.70 NEUTRON FLUX AT THE SURFACE OF 8.2 CM LIF AND URANIUM MIXTURE ON TOP OF 17.8 CM GRAPHITE SLAB.

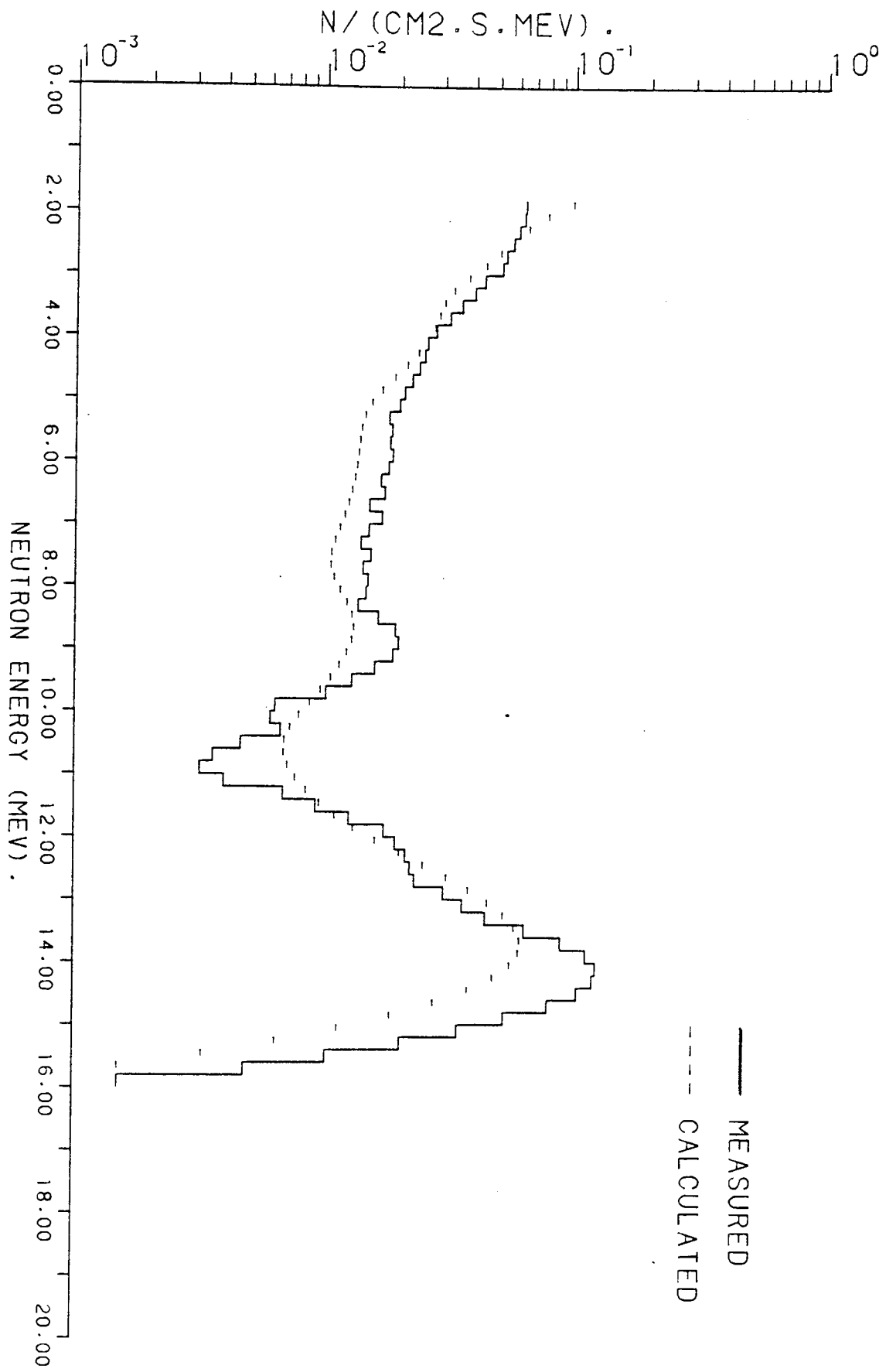


FIG. 7.71 NEUTRON FLUX AT THE SURFACE OF 10.9 CM LIF AND URANIUM MIXTURE ON TOP OF 17.8 CM GRAPHITE SLAB.

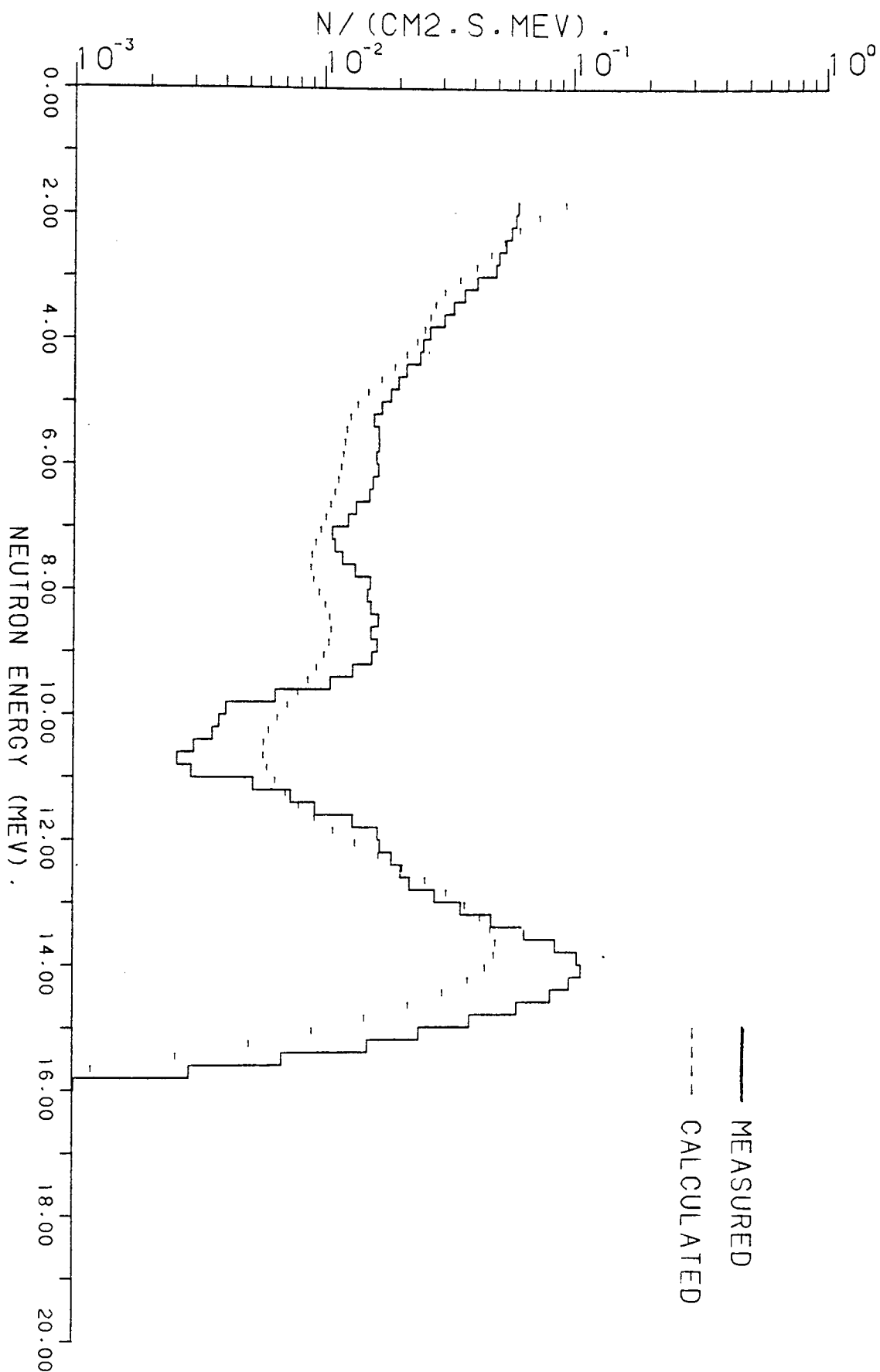


FIG 7.72 NEUTRON FLUX AT THE SURFACE OF 13.6 CM LIF AND URANIUM MIXTURE ON TOP OF 17.8 CM GRAPHITE SLAB.

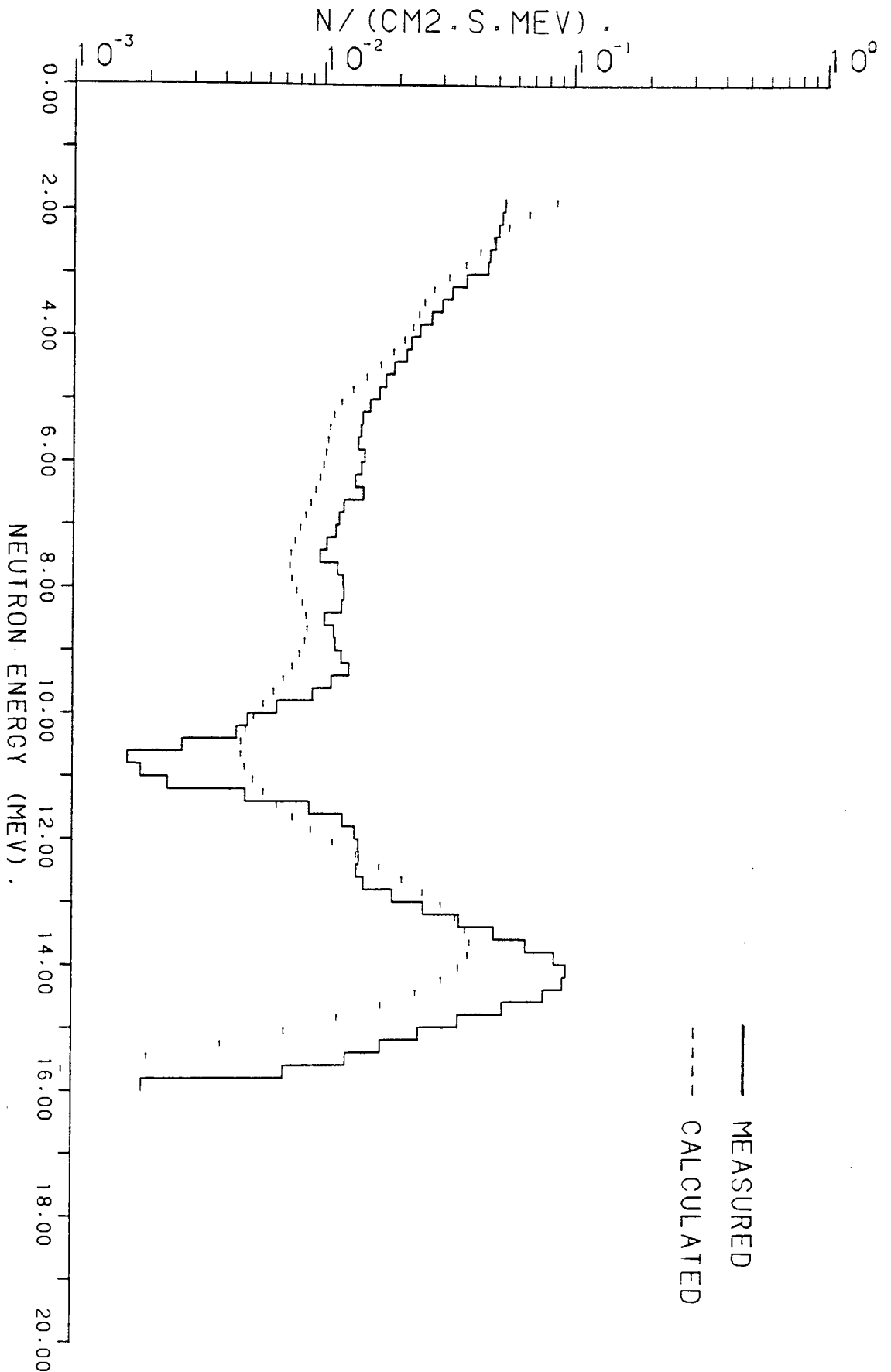


FIG. 7.73 NEUTRON FLUX AT THE SURFACE OF 16.3 CM LIF AND URANIUM MIXTURE ON TOP OF 17.8 CM GRAPHITE SLAB.

(b) The same thickness of uranium on top of 8.9 cm graphite [figures (7.50), (7.51) and (7.52)]

Below about 5 MeV, the fluxes emitted from the mixture cases are slightly lower than that from uranium cases. As the thickness of mixture (or uranium on top of 8.9 cm thick graphite) increases, the difference decreases and the fluxes become nearly the same at 10.9 cm thick. This effect is due to LiF found in mixture slabs which act as an attenuator for secondary neutrons while uranium increases these neutrons. Above this energy (about 5 MeV) the fluxes from mixture cases are higher due to the light density of LiF in mixture.

(c) The same thickness of LiF on top of 8.9 cm graphite [figures (7.56), (7.57) And (7.58)]

There is a big difference below about 5.5 MeV between the fluxes from these two cases. The fluxes from mixture are higher than that from LiF cases. Above about 5.5 MeV, the fluxes from the mixture become lower than those emitted from LiF cases. As the neutron energy increases, the difference decreases to become slight around the 14.1 MeV peak. This effect comes from LiF which has a small number of collisions with neutrons compared with mixture due to its low density.

2- Comparing the fluxes emitted from the assemblies containing LiF and uranium mixture on top of 17.8 cm thick graphite [figures (7.69) to (7.73)] with those containing ;

(a)- 17.8 cm graphite [figure (7.48 R)]

Below about 5 MeV, the fluxes from mixture cases are higher than that from graphite only due to fission . Above this energy the flux from the graphite assembly is higher than that from mixture cases especially in the intermediate region, since the main effect is the extra shielding due to the uranium in the mixture.

(b)- The same thickness of uranium on top of 17.8 cm graphite [figures (7.53), (7.54) and (7.55)]

The fluxes over all the spectra emitted from mixture cases are higher than those emitted from uranium cases. The difference between them is very small below about 5 MeV. This is due to the lower density of the LiF / U mixture compared with uranium.

(c)- The same thickness of LiF on top of 17.8 cm graphite [figure (7.59), (7.60) and (7.61)]

Below about 5 MeV, fluxes emitted from mixture on graphite slab (17.8 cm thick) are higher than that emitted from LiF on the same thickness of graphite slab again due to fission . Above this energy the fluxes are lower in the mixture case. This effect due to the presence of uranium in mixture.

7.8 Neutron Spectra From The Lead Assemblies

The measured and calculated neutron spectra from the lead slabs and

LiF on top of lead slabs which are represented in diagrams (6.24 A) to (6.27 C) are shown in figures (7.75) to (7.86) respectively.

7.8.1 Neutron Spectra From The Lead Slabs

The calculated and measured neutron spectra from lead slabs [61 X 61] cm² cross sectional area and 5, 10 and 15 cm thicknesses [diagram (6.24)] are shown in figures (7.75), (7.76) and (7.77) respectively. These slabs are supported upon a steel plate 1.3 cm thick.

The spectral shape does not change very much with the lead thickness. The fluxes decrease as the thickness of lead increases. The spectra can be divided into three parts;

- 1- The high energy peak near the source energy which comes from the elastic and inelastic scattering. The elastic cross section is high and increases as the neutron energy increases to a maximum value (7.24 barns) at 3.31 MeV. Above this energy it decreases as the neutrons energy increases to become 2.9 barns at 14 MeV as shown in figure (7.74).
- 2- The intermediate region, caused mainly by inelastic scattering which has a broad (non resonance) cross section of about 2.5 barns in the neutron energy range of about 4.4 to 8 MeV. The (n,n') to continuum reaction has threshold of 4.42 MeV. It starts with 0.01 barn and increases as the neutron energy increases to a maximum value (1.83 barns) at 8 MeV. Above this energy, the cross section value decreases as the neutron energy decreases to become 0.22 barn at 14 MeV.

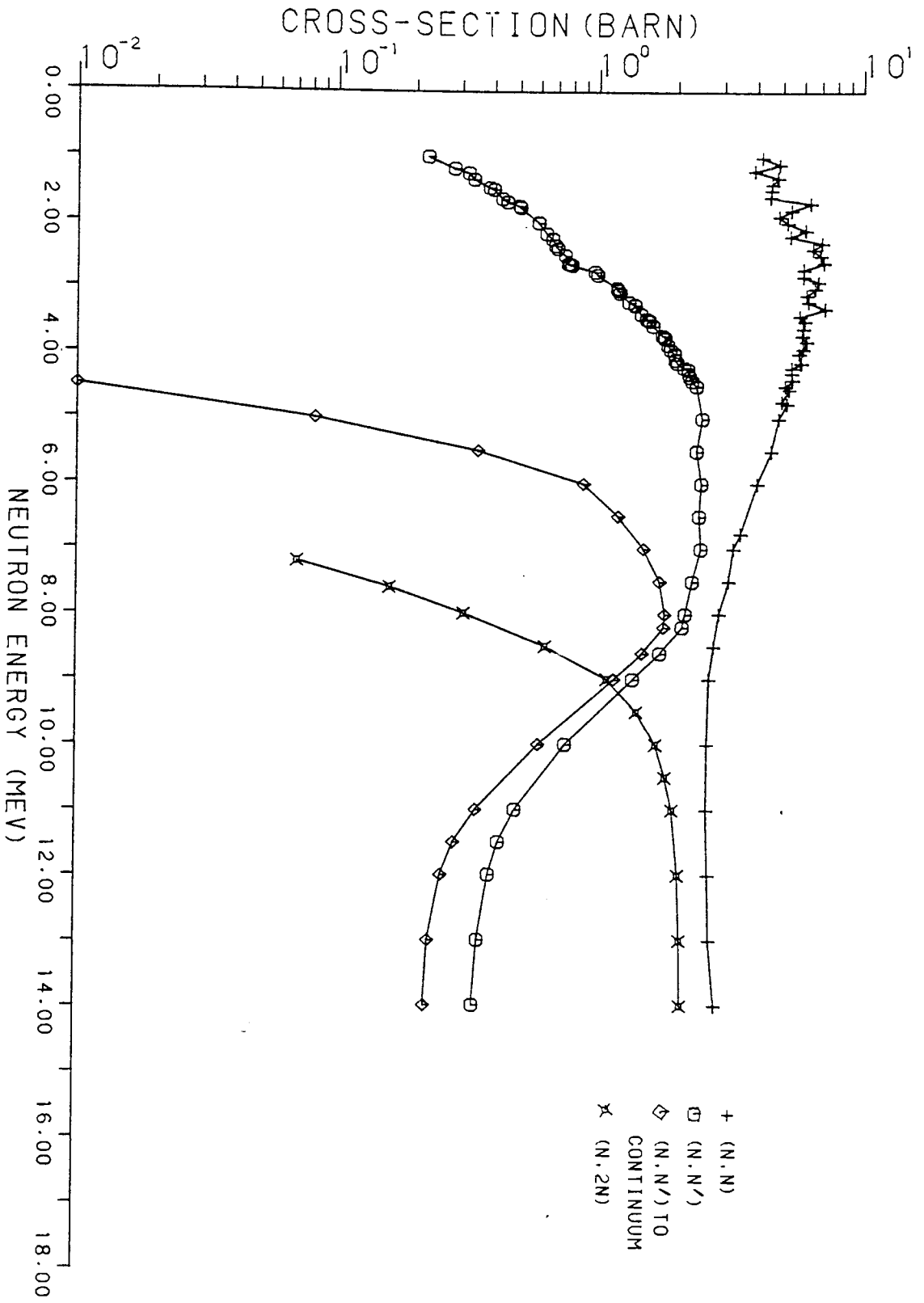


FIG. 7.74 (N,N), (N,N'), (N,2N) AND (N,N') TO CONTINUUM CROSS-SECTIONS OF LEAD-82.

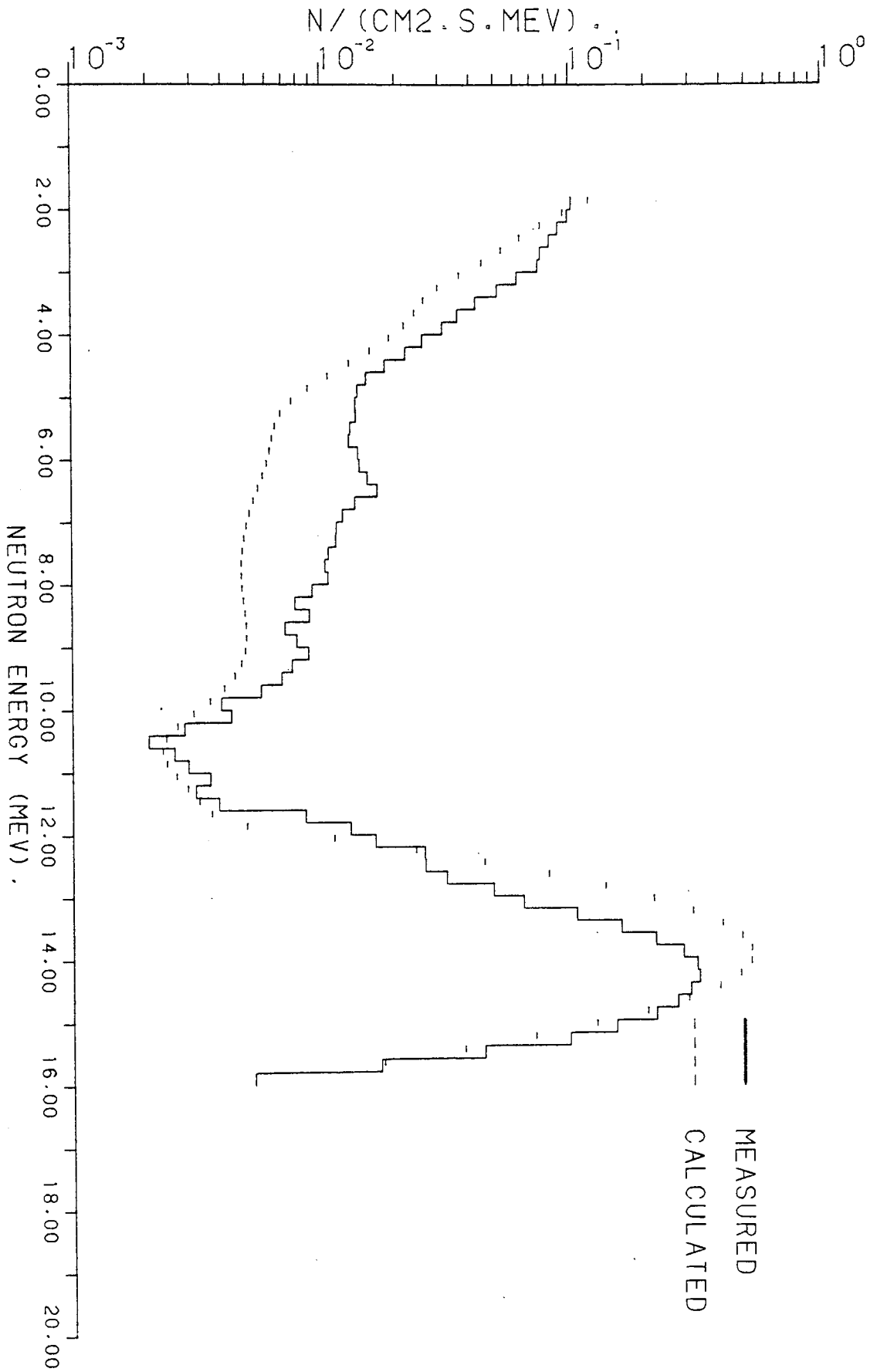


FIG 7.75 NEUTRON FLUX AT THE SURFACE OF 5 CM THICK LEAD SLAB.

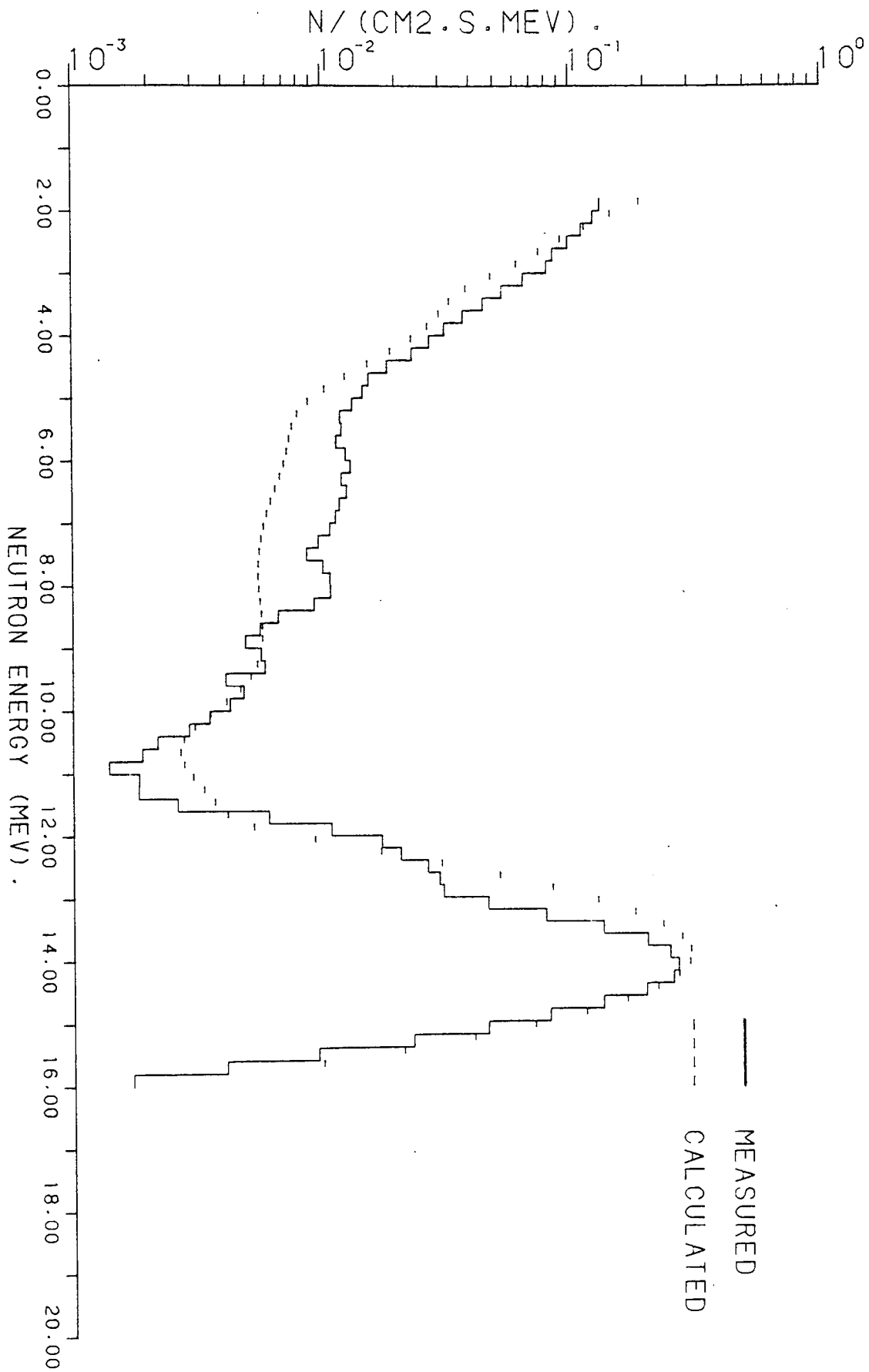


FIG. 7.76 NEUTRON FLUX AT THE SURFACE OF 10 CM THICK LEAD SLAB.

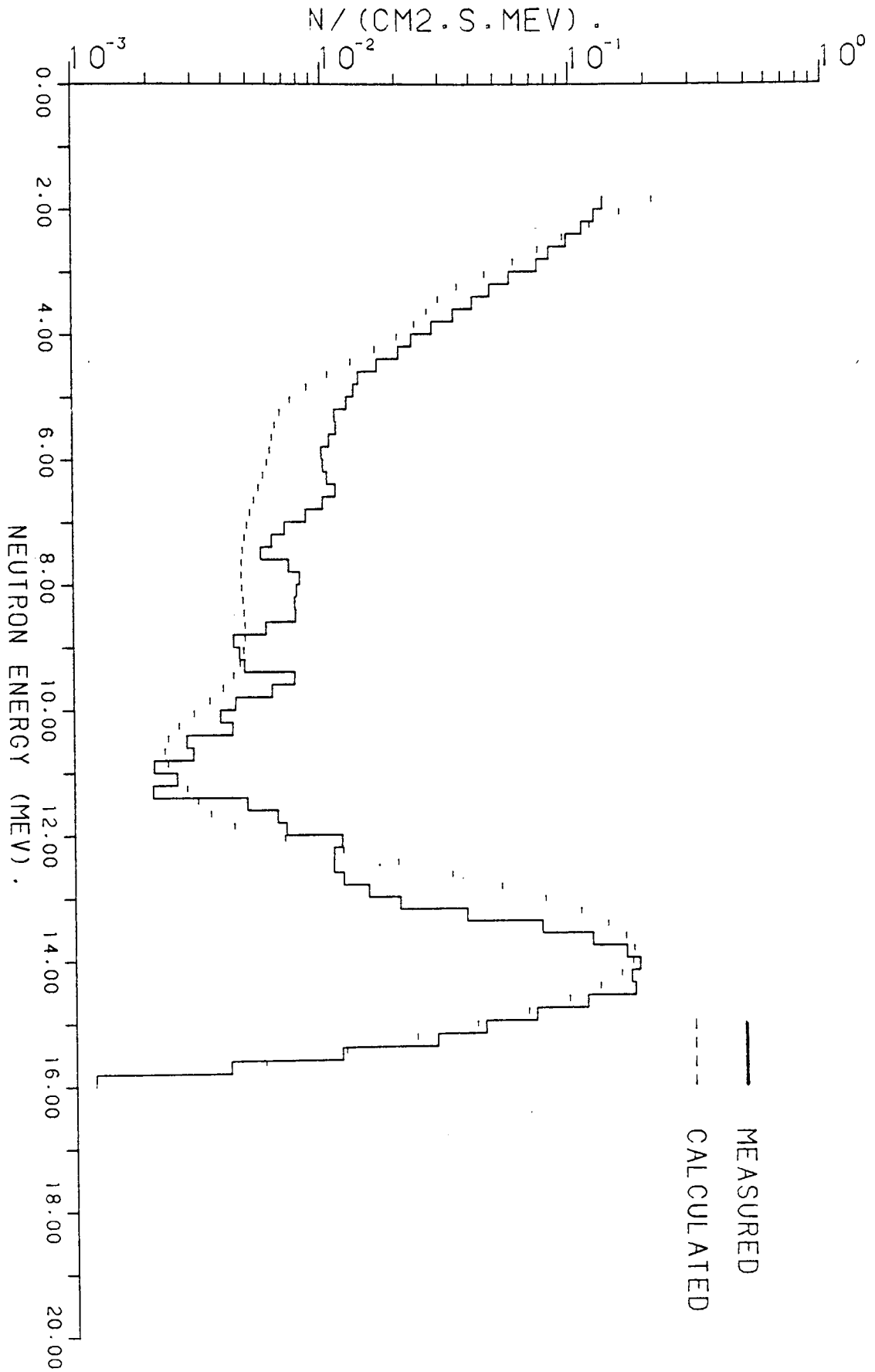


FIG. 7.77 NEUTRON FLUX AT THE SURFACE OF 15 CM THICK LEAD SLAB.

- 3- The low energy tail, mainly due to (n,2n) reaction. this reaction has a threshold at 6.765 MeV with a cross section at 14 MeV of 2.16 barns.

There is an apparant discrepancy between measured and calculated spectra in thin slabs in the low and in the intermediate regions. Measured flux is larger than the calculated one in these two energy regions due to the effect of the secondary neutron sources which were not included in the calculations.

Figures (7.75 R), (7.76 R) and (7.77 R) show the calculated spectra using the experimentally determined secondary neutron sources. There is much better agreement between measured and calculated spectra in this case.

7.8.2 Neutron Spectra At The Surface Of Samples Containing LiF On Top Of Lead Slabs

Measured and calculated neutron fluxes from the samples presented in figures (6.25), (6.26) and (6.27) which contain 5.4, 8.2 and 10.9 cm LiF on top of 5, 10 and 15 cm lead, are shown in figures (7.78) to (7.86) respectively.

From these figures, the general shape of the spectra does not change very much with thickness. As the thickness of LiF increase, with a certain lead thickness, the flux slightly decrease in the low energy tail and around the 14.1 MeV peak. In the intermediate region, there is no significant difference observed especially in thick lead slabs.

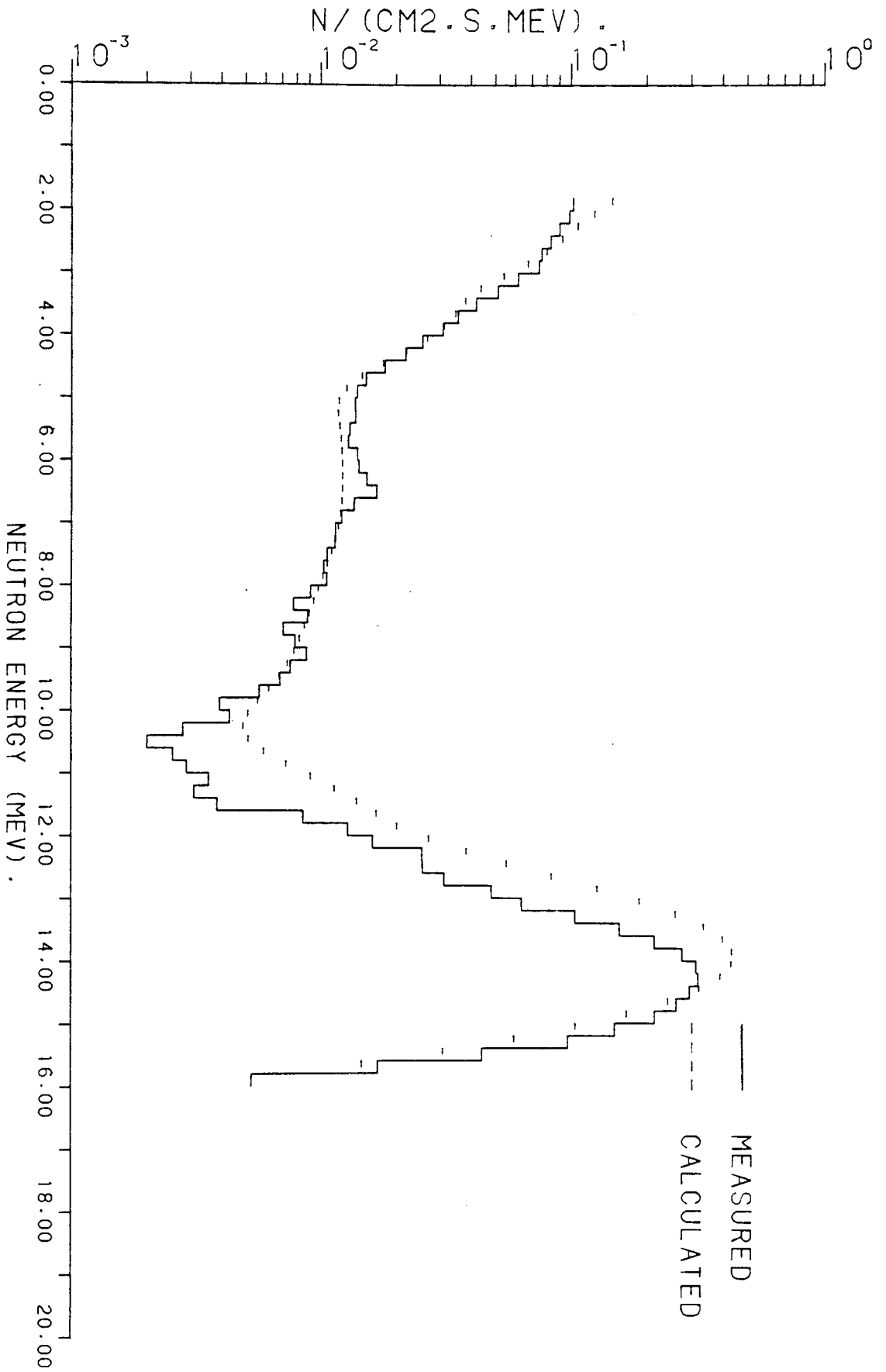


FIG. 7.75R NEUTRON FLUX AT THE SURFACE OF 5 CM THICK LEAD SLAB INCLUDING NEUTRONS SCATTERED FROM THE SURROUNDINGS.

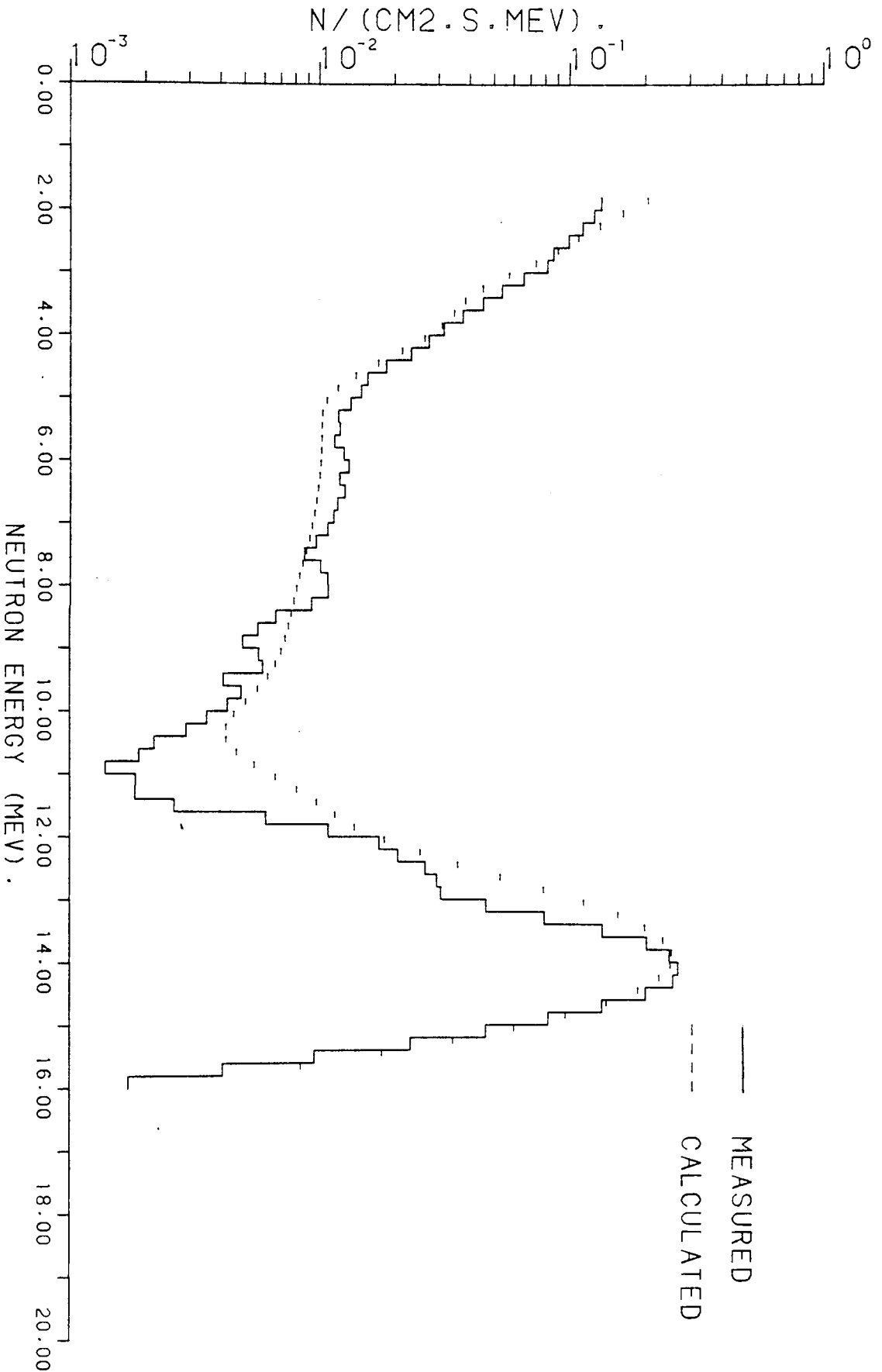


FIG. 7.76R NEUTRON FLUX AT THE SURFACE OF 10 CM THICK LEAD SLAB INCLUDING NEUTRONS SCATTERED FROM THE SURROUNDINGS.

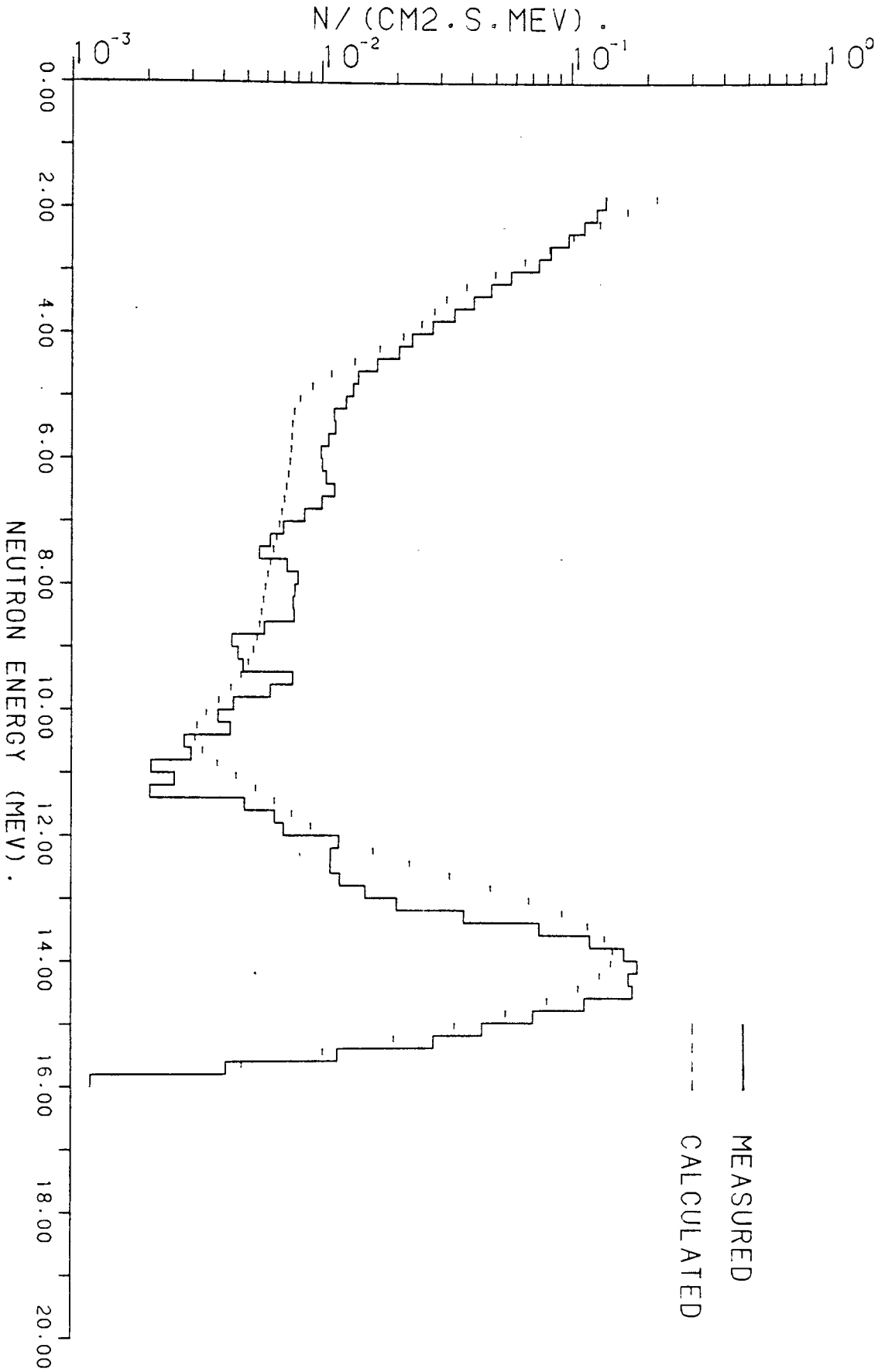


FIG. 7.77R NEUTRON FLUX AT THE SURFACE OF 15 CM THICK LEAD SLAB INCLUDING NEUTRONS SCATTERED FROM THE SURROUNDINGS.

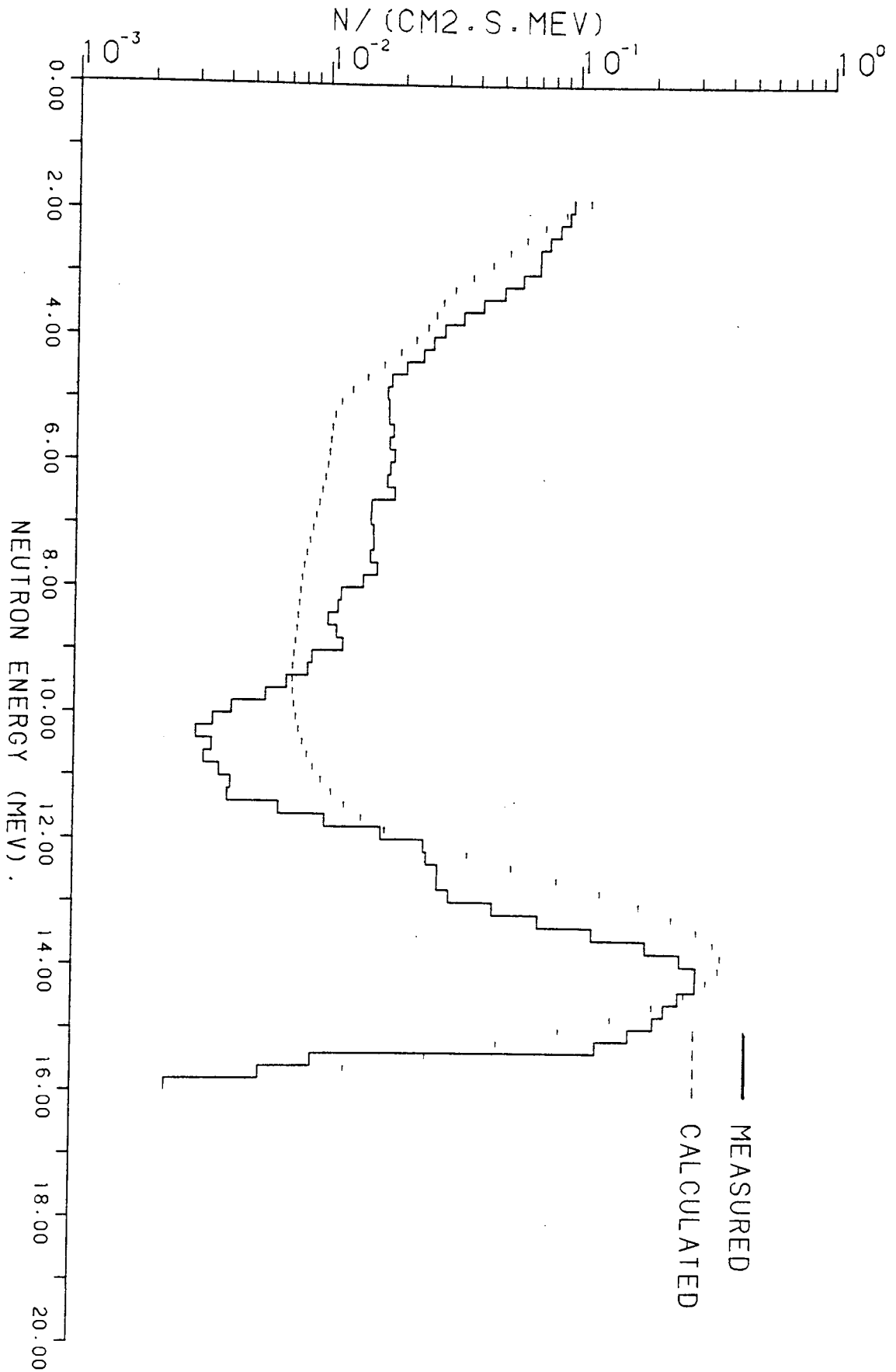


FIG. 7.78 NEUTRON FLUX AT THE SURFACE OF 5.4 CM LIF ON TOP OF 5 CM LEAD.

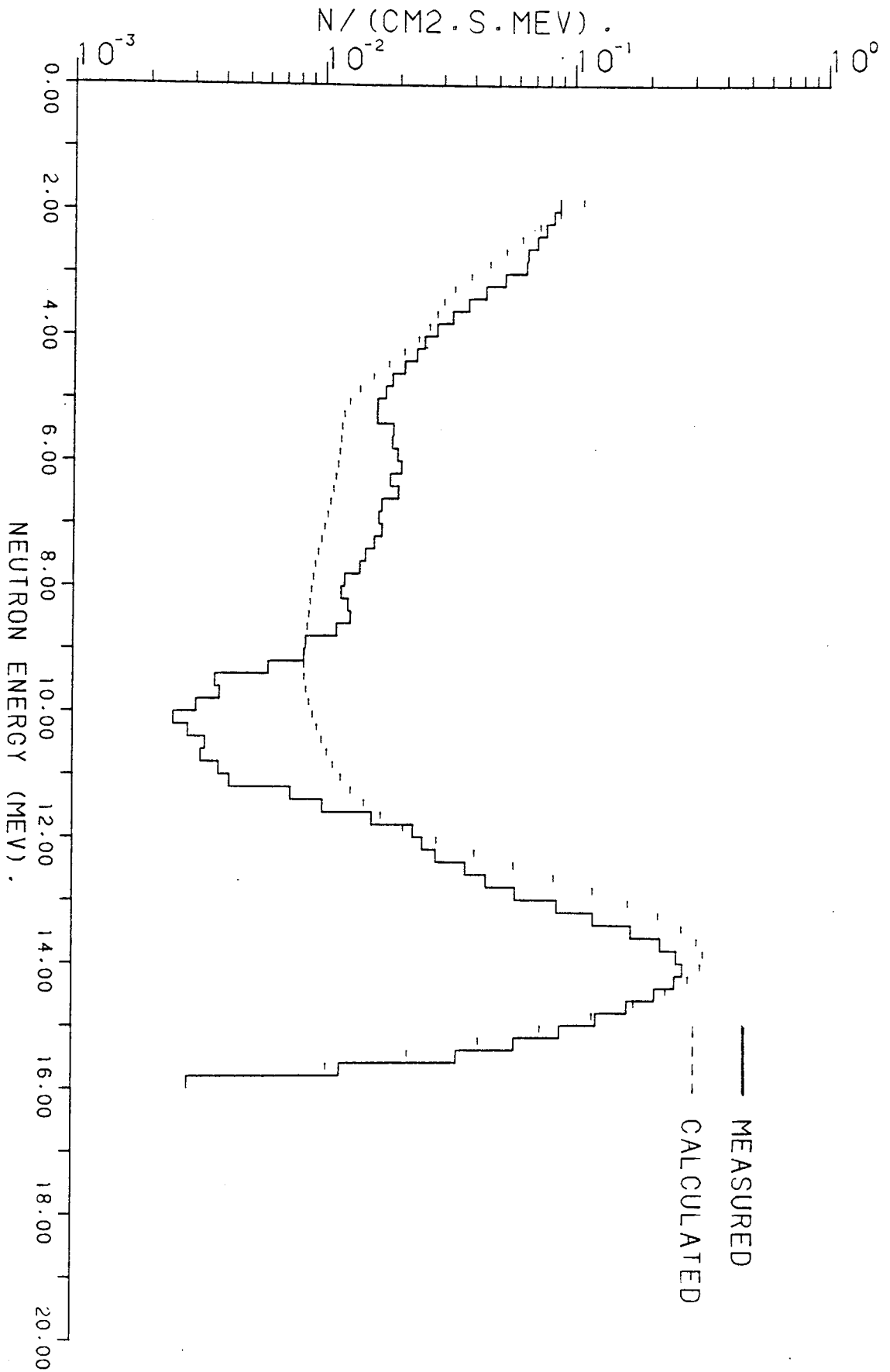


FIG. 7.79 NEUTRON FLUX AT THE SURFACE OF 8.2 CM LIF ON TOP OF 5 CM LEAD.

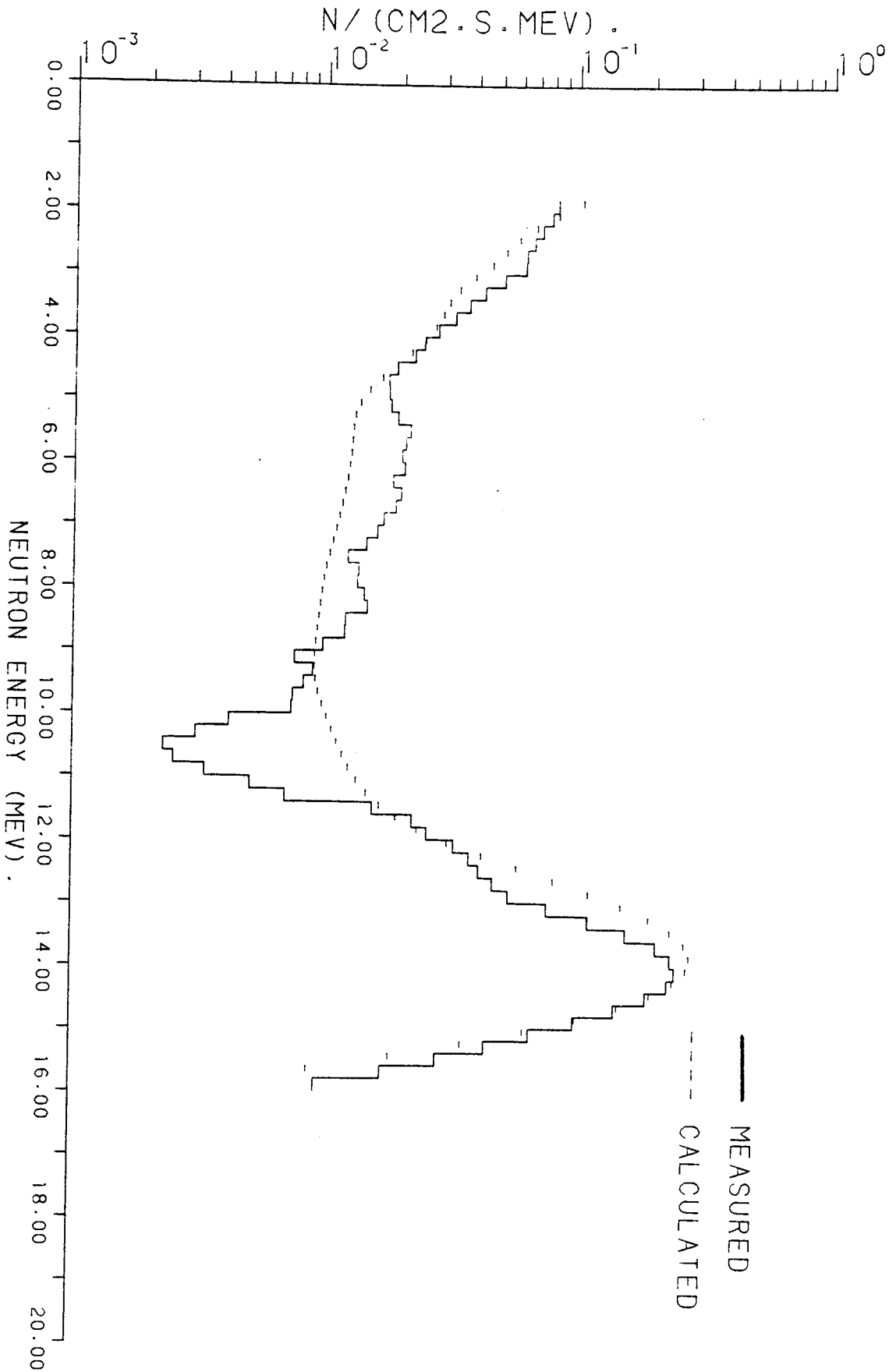


FIG. 7.80 NEUTRON FLUX AT THE SURFACE OF 10.9 CM LIF ON TOP OF 5 CM LEAD.

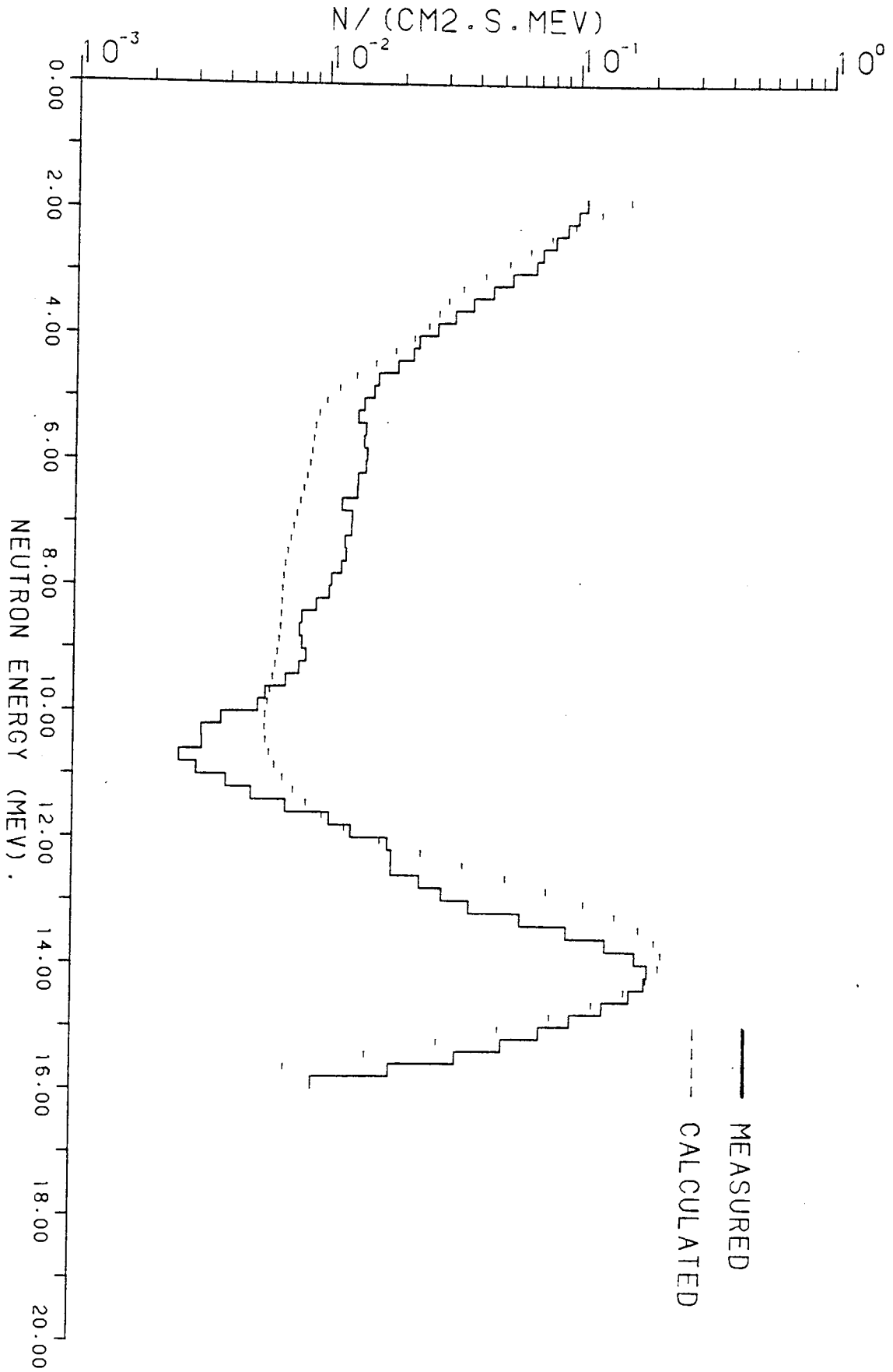


FIG. 7.81 NEUTRON FLUX AT THE SURFACE OF 5.4 CM LIF ON TOP OF 10 CM LEAD.

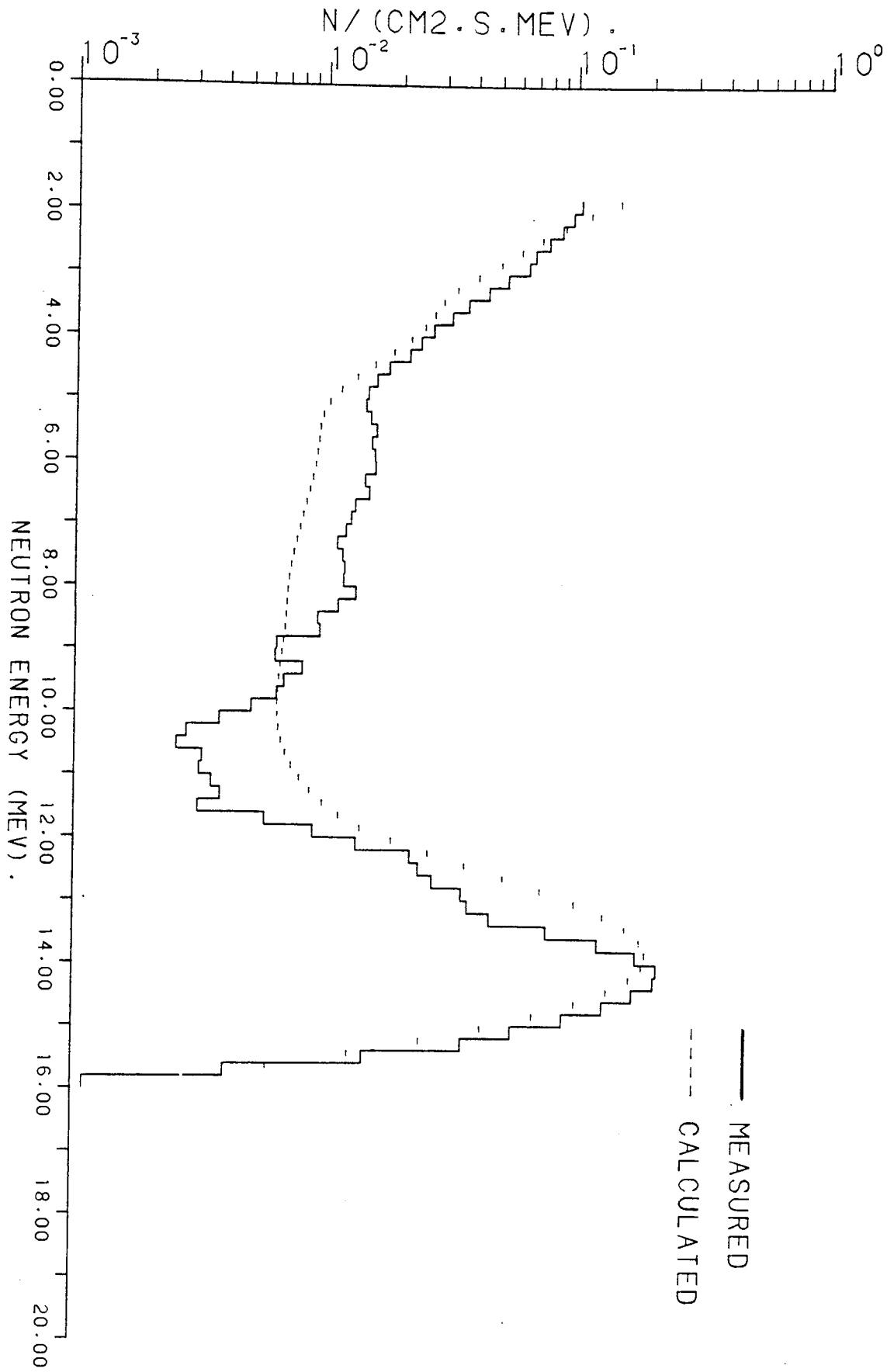


FIG. 7.82 NEUTRON FLUX AT THE SURFACE OF 8.2 CM LIF ON TOP OF 10 CM LEAD.

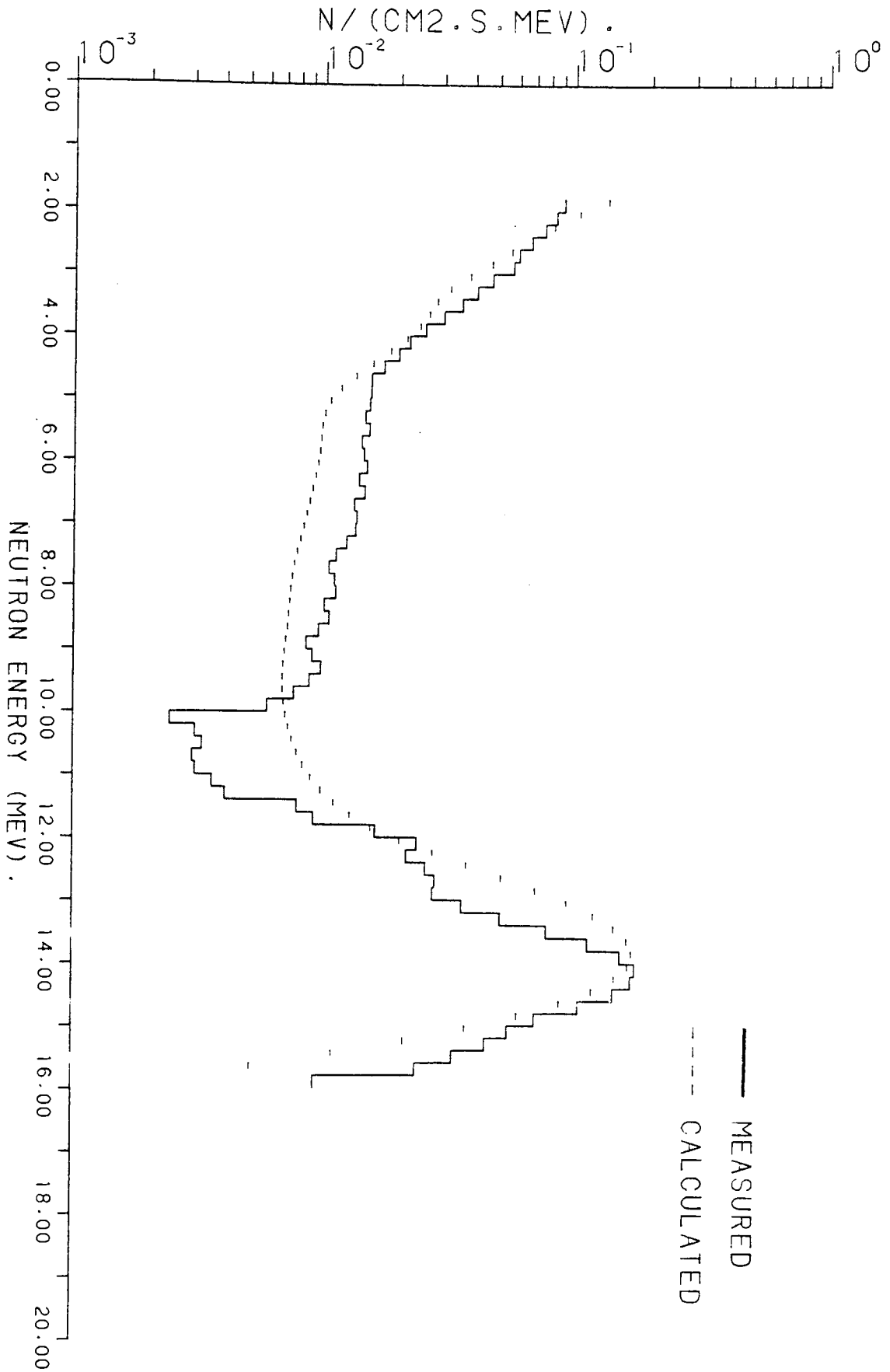


FIG. 7.83 NEUTRON FLUX AT THE SURFACE OF 10.9 CM LIF ON TOP OF 10 CM LEAD.

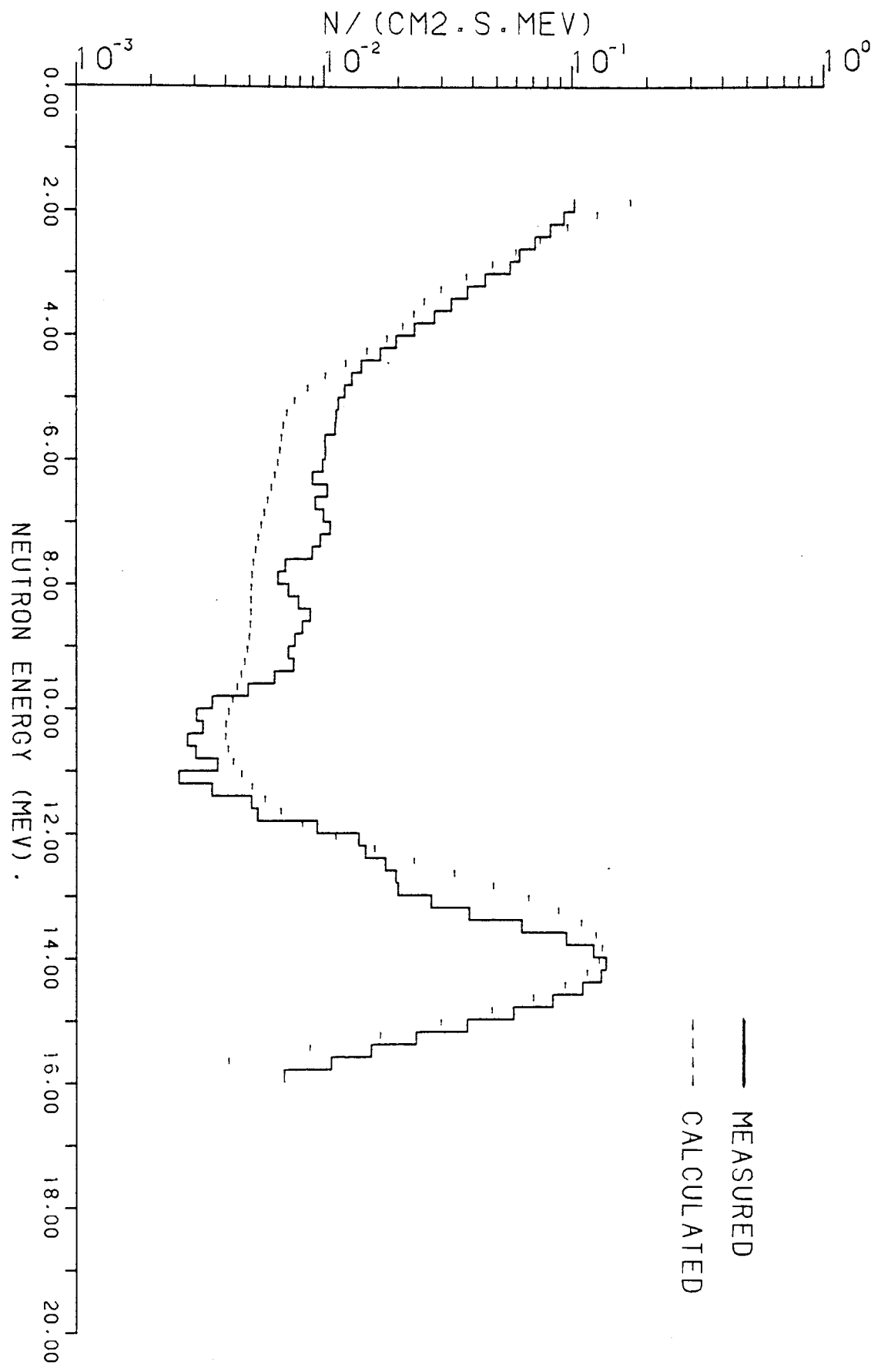


FIG. 7.84 NEUTRON FLUX AT THE SURFACE OF 5.4 CM LIF ON TOP OF 15 CM LEAD.

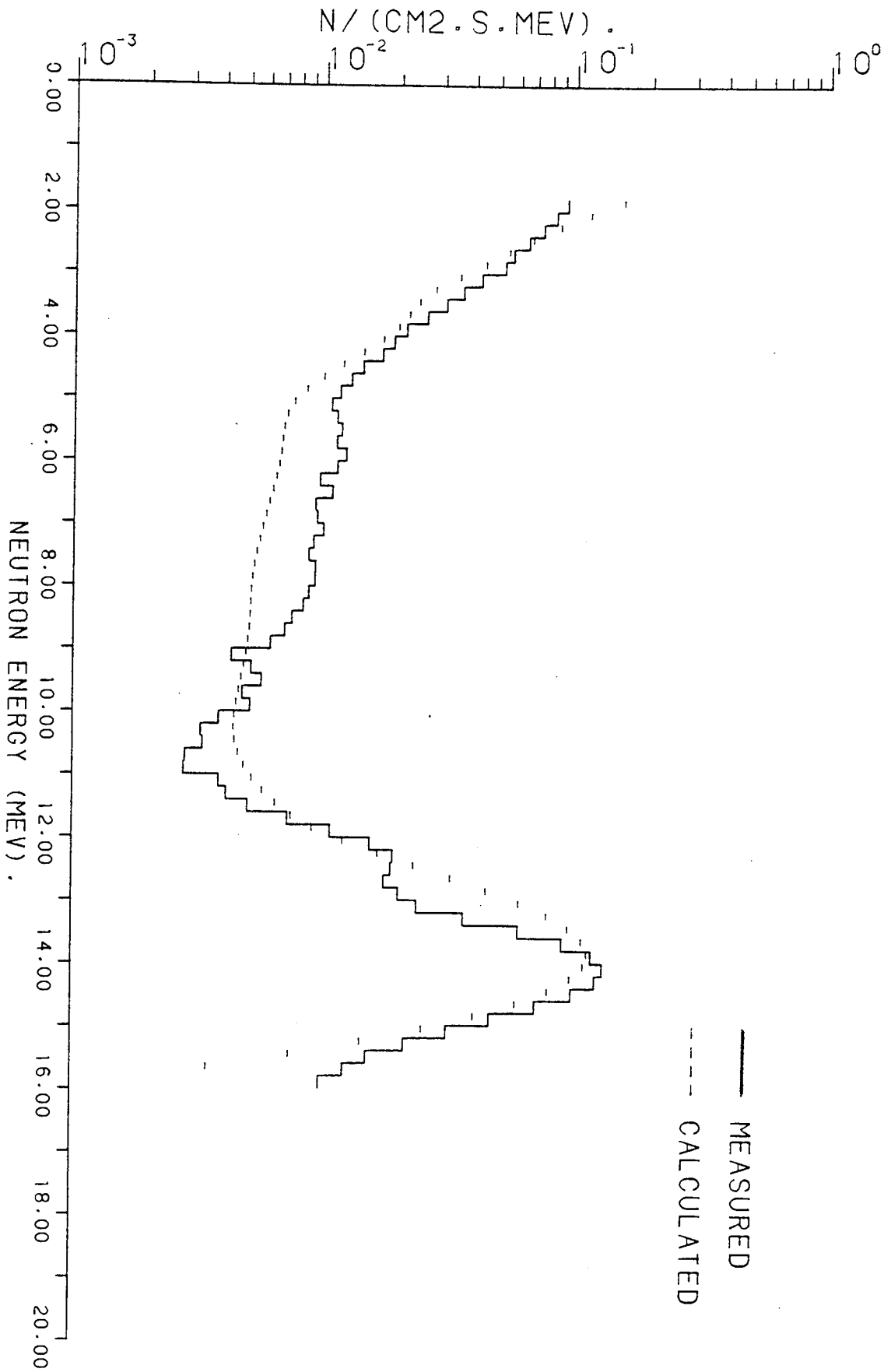


FIG. 7.85 NEUTRON FLUX AT THE SURFACE OF 8.2 CM LIF ON TOP OF 15 CM LEAD.

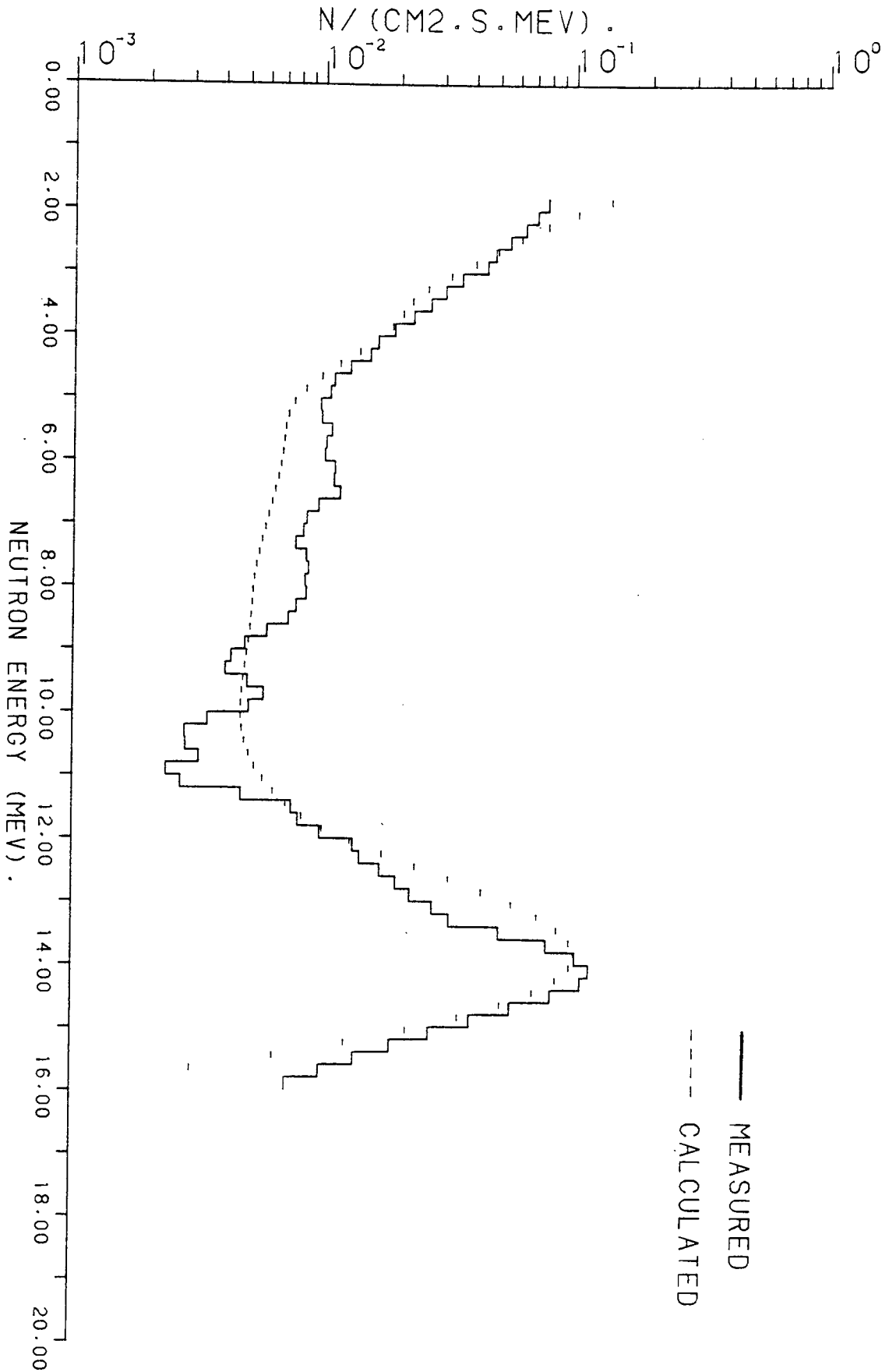


FIG. 7.86 NEUTRON FLUX AT THE SURFACE OF 10.9 CM LIF ON TOP OF 15 CM LEAD.

As the thickness of lead increase, with the same thickness of LiF, i.e , 5.4, 8.2 and 10.9 cm , the flux decreases especially in the intermediate and high energy regions.

In comparison between the cases containing lead only with that containing LiF on top of the same thickness of lead, it was found that;

- In the low energy region and around the 14.1 MeV neutron peak, the flux from lead slabs only is higher. The difference increases as the thickness of lead increase.
- In the intermediate region, the flux in lead assemblies is higher than that containing LiF. The difference decreases as the thickness of lead increases and becomes negligible with thick slabs.

As for lead slabs the effect of degraded source neutrons from the surroundings can be seen. These source neutrons from surroundings can be seen. These calculation were not repeated using the true source due to lack of time.

7.9 Neutron Spectrum From The Steel Slab

Figure (7.87) shows the calculated and measured neutron spectra for steel slab (6.4 cm thick).

There is agreement between measured and calculated neutron fluxes around the 14 MeV peak. In the low and intermediate region there is a

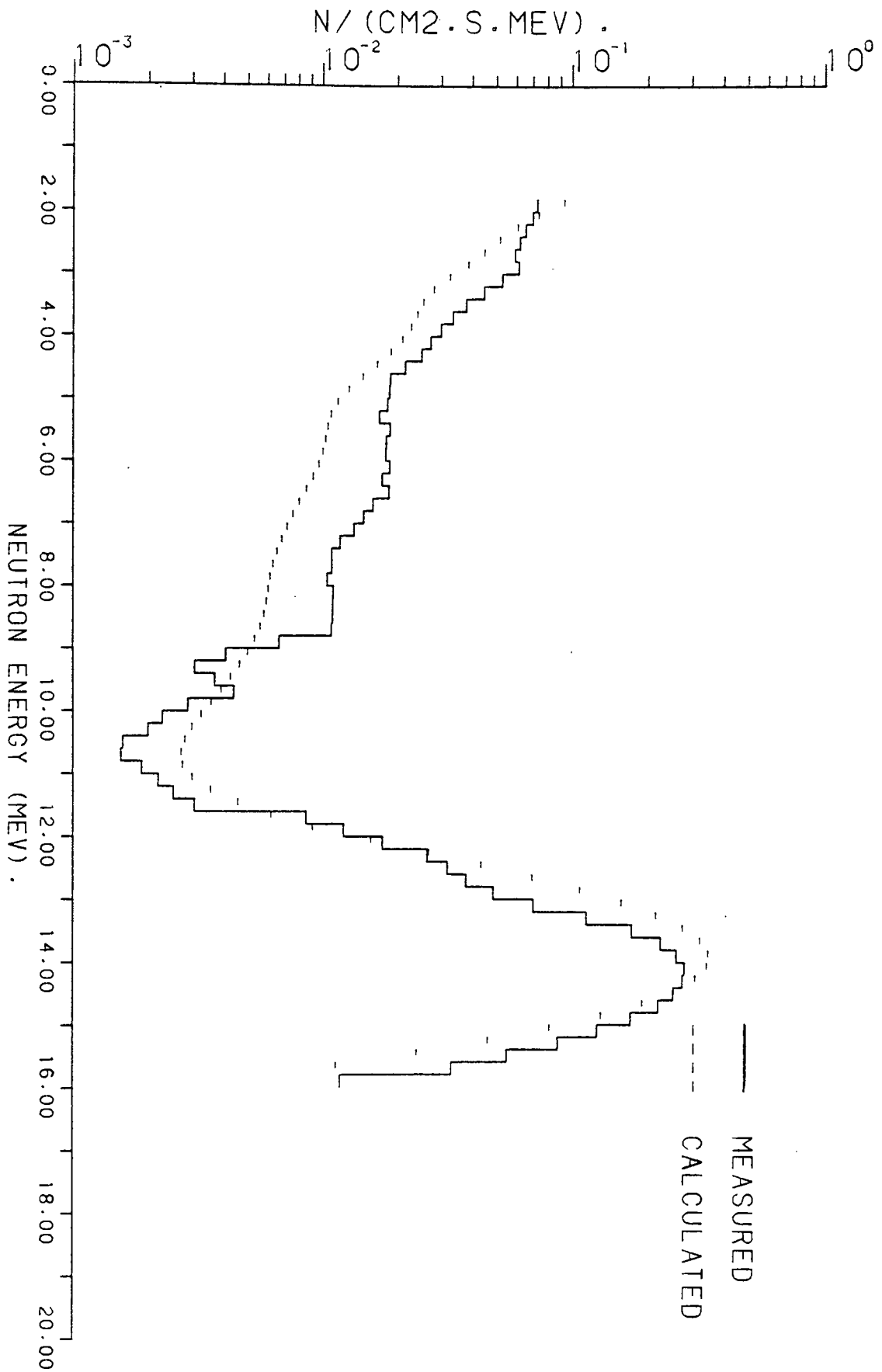


FIG. 7.87 NEUTRON FLUX AT THE SURFACE OF 6.4 CM THICK STEEL SLAB.

discrepancy between measured and calculated spectra due to the secondary neutron sources as mentioned before. Figure (7.87 R) shows the corrected spectra after including the secondary neutron sources. In this case There is a good agreement between measured and calculated spectra.

Elastic scattering cross section in ^{56}Fe has a maximum values between about 1 and 2 MeV. The slight peak in the neutron distribution that appears in this region (about 2.8 MeV) is probably due to this effect. Inelastic scattering starts from 1.0 MeV (1.16 barns) and increases as the neutron energy increases to the maximum values [figure (7.88)]. Therefore the inelastic scattering is the main reaction in addition to (n,2n) reaction which has a threshold of 11.4 MeV. This reaction also causes an increase of secondary neutrons in the intermediate and low regions.

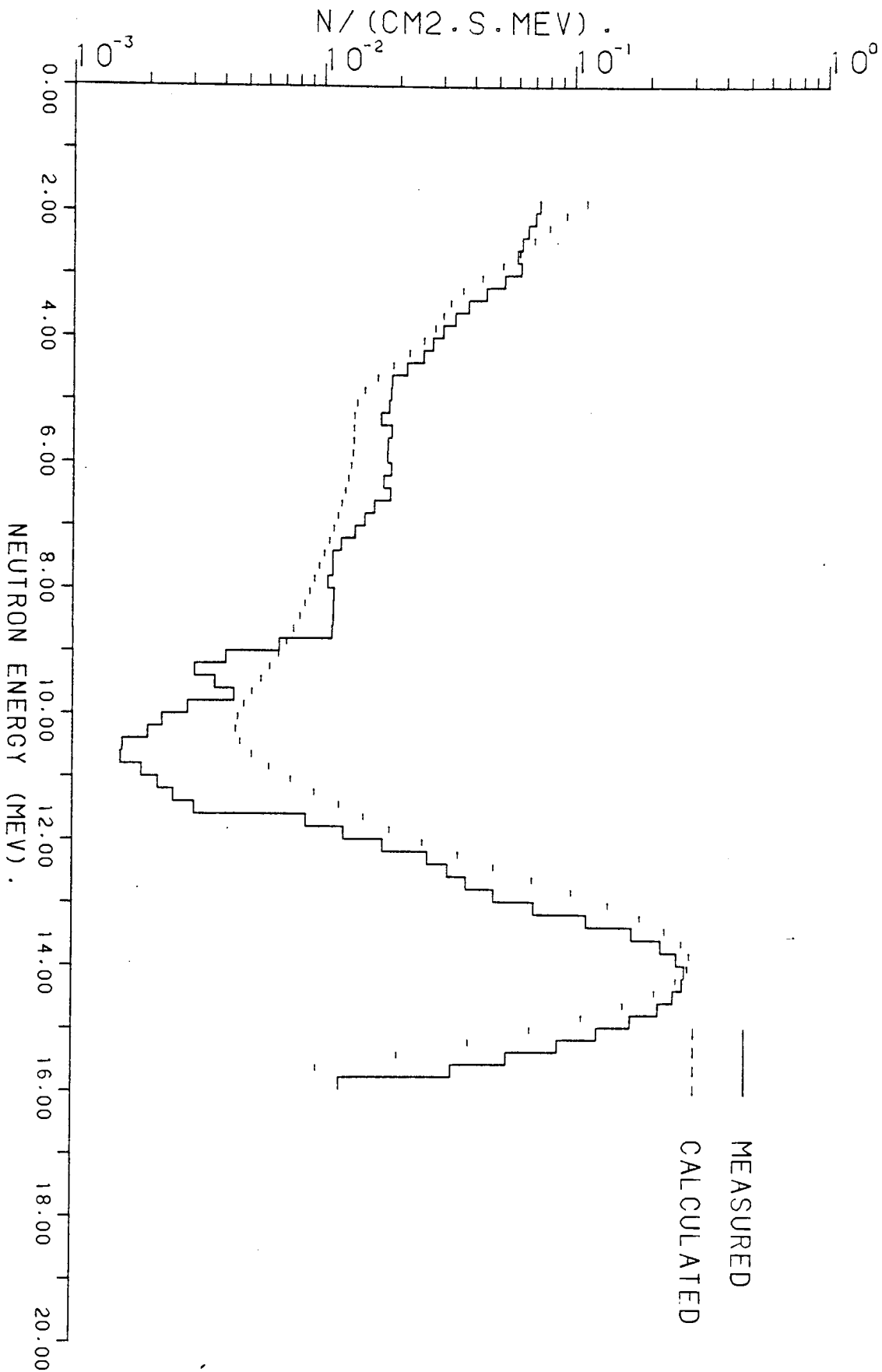


FIG. 7.87R NEUTRON FLUX AT THE SURFACE OF 6.4 CM THICK STEEL SLAB INCLUDING NEUTRONS SCATTERED FROM THE SURROUNDINGS.

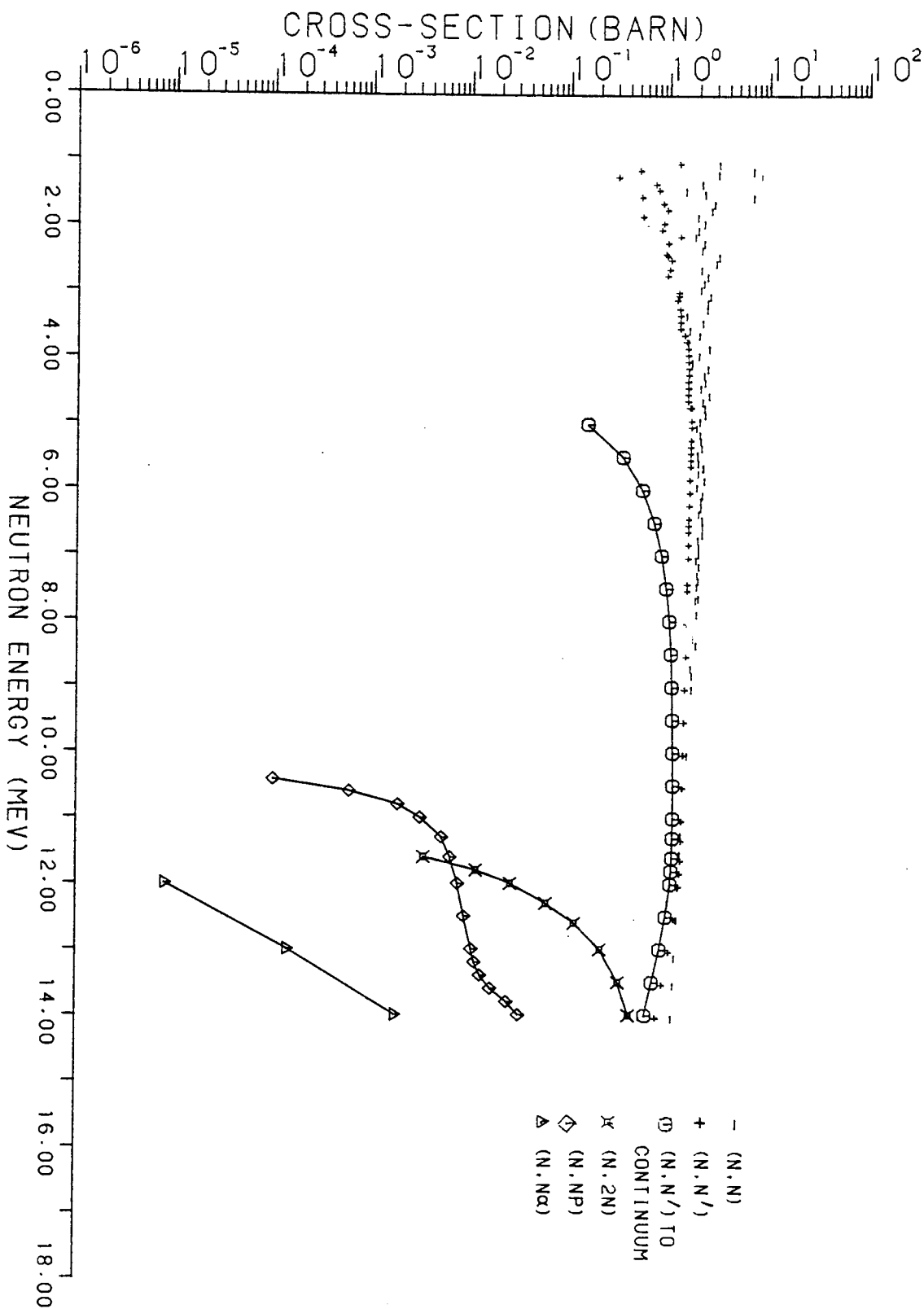


FIG. 7.88

(N,N), (N,N'), (N,2N), (N,NP), (N,N') TO CONTINUUM AND

(N,Nα) CROSS-SECTIONS OF FE-56.

CHAPTER 8

CONCLUSIONS

8.1 Introduction

The objective of the work described in this thesis were to set out an experimental and theoretical study of the energy distribution of neutron emerging from shields exposed to a source of 14.1 MeV neutrons. Shielding materials were chosen that could be of possible interest to the fusion reactor programme for use in breeding blankets. This enabled checks to be made on the validity of a combination of a calculation method and a data set. For calculation purpose the ANISN one dimensional transport theory code was chosen and the data set used was one that become readily available as the work started, the ZZ - FEWG 1/ 31 - 1F set that was originally produced for calculating shielding for use against nuclear weapons. The materials covered by the data, in P_3 expansion, included the relevant ones needed for calculations in the experimental shields and part of the objective was to see if this data set could be used satisfactory for thin shields.

A part from graphite, for which there was sufficient to construct a shield that could be represented as a sphere for calculation purposes, the experimental assemblies were finite slabs with a point source of neutrons below them.

8.2 Neutron Detection

A scintillation counter using a 40 mm x 40 mm cylinder of the liquid scintillator NE - 213 was used in this work. Gamma ray events occurring in this scintillator can be rejected using pulse shape discrimination. Initial attempts to use the zero crossing method of pulse shape discrimination were not satisfactory at lower neutron energies, possibly due to poor performance by the shaping amplifier used. Better discrimination was achieved using the charge comparison method with a commercial unit.

Facilities were not available for measuring and calculating a family of monoenergetic response functions, so the differentiation method of extracting the neutron spectrum from the pulse height spectrum had to be used. Despite its limitations, this method appeared to give satisfactory results.

Normalization of experimental data was carried out by using the associated alpha particle emitted in the D - T reaction to determine total neutron output. The alpha particle was detected at 90° to the beam direction by means of a silicon surface barrier detector, which is effectively insensitive to gamma radiation.

8.3 Calculation Methods And Cross Section Set

The ZZ - FEWG 1/ 31 - 1F cross section set was tested with this work. It is a coupled neutron - gamma cross section set with 37 neutron

groups from 19.6 MeV to effectively zero neutron energy and 21 gamma ray groups from 14 MeV to 10 KeV. Angular distribution of scattering events is represented by the P_3 approximation. This data set was seemingly originally intended for calculation of shielding from the radiations from nuclear weapons but contains a wide variety of elements, making it suitable for both shielding and fusion blanket studies. The elements provided in the cross section set provided by the NEA data bank are :

H - 1, H - 3, Li - 6, Li - 7, Be, B - 10, B - 11, C - 12, N, O, F, Na, Mg, Al, Si, Cl, K, Ca, V, Cr, Mn, Fe, Ni, Cu, Mo, Ta - 181, W - 182, W - 183, W - 184, W - 186, Pb, U - 235, U - 238, Pu - 239, Pu - 240, Ar, Ti, Gd, P, S and Ba.

Only a limited selection of these was used but it would be possible to study typical concrete mixes as well as pure materials and simple mixtures. The major components tested were; Li - 6, Li - 7, C - 12, F, Fe, Pb and natural uranium and aluminium was also present in smaller proportions as a capping material.

Calculation methods used the discrete ordinates transport code ANISN and the cross section data was directly in suitable form for input to this code. In order to perform the calculations a version of ANISN suitable for a CDC - 7600 computer was obtained (also from the NEA data bank) and this was implemented on the UMRCC CDC - 7600. No measurements of gamma radiation were made, and the neutron source energy used experimentally was 14.1 MeV, so an additional programme was written to extract the data from groups 4 to 24 inclusive when no fissile material was present (14.2 MeV to 52.5 KeV) and groups 4 to 37 inclusive (14.2

MeV to 10^{-5} eV) when uranium was included, so that all fission sources were taken into account.

Since ANISN is a one - dimensional code the slab assemblies were not correctly modelled using the slab geometry option. This is because it assumes an infinite slab in two dimensions with a uniform source distribution in these two directions, quite unlike the finite slab with a point source centrally beneath it. Buckling corrections were not possible since this required the transport cross section instead of the total cross section in the P_0 cross sections of the data set.

The most satisfactory solution was to treat the slab as a hollow sphere of thickness equal to the slab thickness and with the radius of the inner cavity equal to the source to slab distance. In addition, the inner boundary condition is set for no reflection to simulate the leakage from the underneath (source side) of the slab (A true sphere would use a reflection boundary condition at this surface which would be equivalent to a uniform flux within the cavity). Provided that the detector is placed over the slab directly above the source position, then the computed and measured leakage fluxes should be very similar as is indicated in general by the results obtained. The point neutron source is represented by a radially outward directed shell source at the inner boundary of the spherical cavity.

Certain difficulties were noticed with ANISN. Firstly, it proved impossible to retain the nuclear data for successive calculations of different dimensions, even when a fault in the main calling subroutine

was corrected, so complete data sets had to be produced for every individual case. Secondly, and perhaps more seriously, a source option calculation when fissile material in the form of natural uranium was present failed to converge properly, and when the permitted number of iterations increased there were continued fluctuations with no evidence of approaching convergence. This effect varied with the different slab thicknesses and mixtures used, but generally enabled reasonable agreement to be obtained between theory and experiment.

Measured fluxes with no shield present showed that neutrons reflected from the concrete floor and surrounding shielding material contributed a significant lower energy degraded neutron flux. For low density shields such as LiF or thin shields some of this degraded spectrum would reach the detector. If the 14 MeV neutron source was replaced in the calculations by the measured neutron spectrum for no shield, including both the 14 MeV and degraded neutrons, then much better agreement between theory and experiment was found. For strongly attenuating shields this recalculation did not prove necessary since the lower energy neutrons are more strongly absorbed than the 14 MeV neutrons.

Trials were made to determine the minimum number of angular ranges necessary for a satisfactory calculational results. S_4 , S_8 and S_{16} calculations were tried with graphite and no significant difference in the leakage flux could be found between S_8 and S_{16} . As a consequence the S_8 approximation was used for the remainder of the calculations since the computing time was shorter than for S_{16} .

8.4 Calculations And Experiments Compared

Provided that the measured input spectrum was used with low attenuation shields, as mentioned in the previous section, there was general agreement between measured and calculated spectra for the range of materials studied. With some of the assemblies containing uranium there was somewhat worse agreement at lower neutron energies, but this was thought to be due to the unexplained lack of convergence in the calculations rather than possible defects in the cross section set. In general it can be concluded that ANISN calculations using the P_3 cross section set ZZ - FEWG 1/ 31 - 1F and S_0 angular approximation, together with the representation of the slab assemblies by a hollow sphere with no reflection at the internal boundary were adequate to model the experimental data and hence it appears that the cross section set is satisfactory and for the materials tested needs no modification in the range 14 MeV to 2 MeV.

It was also noticed that, the geometrical make - up of the shield had little effect on the emergent flux for combination shields of the same thickness and same average composition, for example U + LiF shields with an average composition of 50 % by volume of each component. This was investigated as a " homogeneous " mixture (alternate tubes of each), two layers and four alternate layers with either the U nearest the source or the LiF nearest the source. Apart from a possible slight streaming effect on the 14 Mev neutrons for the " homogeneous " mixture the measured and calculated fluxes looked very similar. This gives confidence that despite highly anisotropic scattering of neutrons at high energies that ANISN handles sudden changes between light and dense

materials in a satisfactory manner.

8.5 Further Work And Improvements

The first improvement that could be made is to use a three - dimensional calculation method. A Monte - Carlo code, such as MORSE, would enable more realistic modelling of the experimental assemblies at the expense of very much longer calculation times for each case. It should prove possible to use the same data set with MORSE as with ANISN. Time and availability of a suitable computer have prevented this approach being followed so far.

Lower scatter conditions for the experimental work are highly desirable to reduce the degraded neutron spectrum that is present with the 14 MeV source neutrons. This is much more difficult to achieve in the available laboratory space due to both the presence of shielding for other experimental assemblies and the limited height of about 1.46 meter between the beam line and the floor.

Certain improvements could be made to the neutron detection system. Noise in the system limits the lowest energy for which discrimination is possible. Two methods could be tried. Firstly use a photomultiplier with lower noise than the 56AVP used here (e.g. RCA8850) and secondly, modify the dynode chain by removing the zener diodes and replacing them with resistors and also using a dual power supply to maintain fixed voltages over the early focusing stages and varying the gain by having a variable voltage over part of the dynode chain. By these means, it should be possible to decrease the lowest resolvable neutron energy,

although there are limits because of the much larger dynamic range of pulse sizes compared with the energy range. For the energy range 14.1 to 2 MeV the proton pulse height range is 15.14 : 1 and for the range 14.1 to 1 MeV the proton pulse height range is 42.8 : 1.

Finally, it would be interesting to compare the matrix method with the differentiation method for extracting the neutron spectrum from the pulse height spectrum. This involves further computing to use the Ø5S Monte - Carlo code to calculate the response functions at closely spaced energies for the particular scintillator that is used. Although a copy of the programme has recently been obtained it appears to be very difficult to implement on readily available computers since it contains IBM machine code subroutines.

A further extension of the work would be to measure the gamma ray spectrum, since the data set enables gamma ray spectra as well as neutron spectra to be calculated.

8.6 Conclusions

The measurements indicate that the data set is satisfactory, and with the aid of ANISN it would therefore be possible to carry out a study on fusion reactor blankets, using cylindrical geometry and including a series of concentric cylindrical shells to represent the torus wall, possible neutron converter and breeder regions, and reflector and shielding regions. From the calculated fluxes it would then be possible to calculate tritium breeding and heat production in each region due to neutron and gamma ray interactions.

APPENDICES

APPENDIX (1)

```
PROGRAM NSPEC
DIMENSION CC(700),PTAB(82),PSI(79),OP(228),NC(575)
CHARACTER INF*80,I0*4,ICH*4
DO 1 I=513,700
CC(I)=1.0
1 CONTINUE
DATA I0/' 0'/
READ(3,*)(PTAB(I),I=1,82)
READ(3,*)(PSI(I),I=4,79)
READ(1,*)NDATA
DO 999 KK=1,NDATA
JK=KK+3
READ(1,'(A80)') INF
WRITE(2,'('' ''',A80)') INF
READ(1,*)EEC,EEZ
WRITE(2,600)EEC,EEZ
600 FORMAT(' EEC=',F8.4,' EEZ=',F8.4)
READ(1,*)TOTN
998 READ(JK,'(A4)') ICH
IF(ICH.NE.I0) GO TO 998
READ(JK,*)(NC(I),I=1,575)
J=-1
DO 210 I=1,505,8
DO 200 K=1,8
L=I+K-1
M=I+K+J
CC(L)=NC(M)
200 CONTINUE
J=J+1
210 CONTINUE
E=-0.2
PM1=0.0
PM2=0.0
PM3=0.0
N1=1
N2=1
DO 5 N=1,228
5 OP(N)=0.0
DO 10 J=1,81
C1=(PTAB(J)+EEZ)/EEC+1.0
C2=(PTAB(J+1)+EEZ)/EEC+1.0
IF(C1)10,10,15
15 IF(C2-700)20,20,25
20 L1=C1
L2=C2+1.0
F1=C1-L1
F2=L2-C2
L1=L1+1
SUM=0.0
DO 40 I=L1,L2
40 SUM=SUM+CC(I)
```

```
SUM=SUM-F1*CC(L1)-F2*CC(L2)
GO TO (45,50,55,60),N1
45 PP1=SUM
   N1=2
   GO TO 10
50 PP2=SUM
   N1=3
   GO TO 10
55 N1=4
   GO TO 65
60 PM3=PM2
   PM2=PM1
   PM1=PP1
   PP1=PP2
   PP2=PP3
65 PP3=SUM
   GO TO (70,70,70,75),N2
70 N2=N2+1
   GO TO 10
75 SPEC=(PM3+PM2-PP2-PP3)*3.125*PSI(J-2)
   SPEC=SPEC/TOTN
   UNC=((PM3+PM2+PP2+PP3)**0.5)*3.125*PSI(J-2)
   UNC=UNC/TOTN
   NE=3*J-17
   OP(NE)=E
   OP(NE+1)=SPEC
   OP(NE+2)=UNC
10 E=E+0.2
25 WRITE(2,300)
300 FORMAT(' E MEV FLUX/MEV UNC/MEV      E MEV FLUX/MEV UNC/M
2EV      E MEV FLUX/MEV UNC/MEV      E MEV FLUX/MEV UNC/MEV')
WRITE(2,400)(OP(N),N=1,228)
400 FORMAT(' ',4(F6.2,2E11.4,2X))
WRITE(14,500)(OP(N),N=2,227,3)
500 FORMAT(' ',6E12.4)
999 CONTINUE
STOP
END
FINISH
```

APPENDIX (2)

```
PROGRAM SMOOTH
REAL FA(17),C(141),F(161),FS(80),EB(81),G(-20:20)
INTEGER EN(0:17)
DATA (EN(I),I=0,17)/142,138,128,122,111,100,90,82,74,64,50,47,
+41,30,24,23,18,11/
READ(1,*) FA
DO 10 I=1,17
  NU=EN(I-1)-1
  DO 10 J=EN(I),NU
    C(J)=FA(I)*10.0/(EN(I-1)-EN(I))
10 CONTINUE
DO 20 I=1,161
  F(I)=0.0
20 CONTINUE
DO 50 I=11,141
  E=I*0.1+0.05
  S=0.171*SQRT(E)
  NMAX=INT(30.0*S+0.5)
  Z=0.005/(S*S)
  DO 30 J=0,NMAX
    G(J)=C(I)*0.00665/S*(EXP(-(J-0.5)**2*Z)+4*EXP(-J*J*Z)+EXP(-(J+0.5)
+**2*Z))
    G(-J)=G(J)
30 CONTINUE
  NMIN=-NMAX
  DO 40 J=NMIN,NMAX
    F(I+J)=F(I+J)+G(J)
40 CONTINUE
50 CONTINUE
DO 60 I=9,80
  FS(I)=(F(2*I)+F(2*I+1))*0.5
  EB(I)=I*0.2
60 CONTINUE
EB(81)=16.2
WRITE(2,'(1X,5(''ENERGY-MEV FLUX/MEV ''))')
WRITE(2,'(5(1X,2F5.1,E11.4,1X))')(EB(I),EB(I+1),FS(I),I=9,80)
WRITE(3,'('' ''',6E13.5)')(FS(I),I=9,80)
STOP
END
FINISH
****
```

APPENDIX (3)

```

PROGRAM ANXSEC
REAL X(3538),XX(4,3538),DN(20)
INTEGER IN(6),NUM(6),NE(6),NID(20)
CHARACTER *1 RCH,SA,SM,SP,ZC,R(6),SN(6),SX(6),CN(0:9),ZB*10,
+BLANK*12,W(6)*12,XM(2000)*10,CID*3,NCH*3
DATA RCH,SA,SM,SP,ZC,(CN(I),I=0,9),ZB,BLANK/'R','8','-','+','7',
+'0','1','2','3','4','5','6','7','8','9','0',
+
READ(1,*) NG1,NG2
NG=NG2-N61+1
WRITE(2,('(OF FIRST GROUP=',I2,', ' LAST GROUP=',I2,', ' GROUPS=',
+I2)') NG1,NG2,NG
NSTOP=NG2+61
NM=NG*(NG+3)
DO 10 I=1,4

DO 10 J=1,NM
YX(I,J)=0.0
10 CONTINUE
READ(1,*) NMAT
READ(1,*)(NID(I),DN(I),I=1,NMAT)
WRITE(2,('(O MATERIAL NUMBER DENSITY'))')
DO 20 NN=1,NMAT
DO 35 K=1,4
N=NID(NN)
N1=N/100
N=N-N1*100
N2=N/10
N3=N-N2*10
IF(N1.EQ.0) THEN
CID(1:1)=BLANK
ELSE
CID(1:1)=CN(N1)
END IF
IF(N1.EQ.0.AND.N2.EQ.0) THEN
CID(2:2)=BLANK
ELSE
CID(2:2)=CN(N2)
END IF
CID(3:3)=CN(N3)
25 READ(3,('(OX,I2,9X,A3)') N61,NCH
IF(N61.NE.61) GO TO 25
IF(NCH.NE.CID) GO TO 25
WRITE(2,('(O ',8X,A3,7X,F8.6)') NCH,DN(NN)
J=0
40 IF(J.LT.NSTOP) THEN
READ(3,1000)(IN(I),R(I),SN(I),NUM(I),SX(I),NE(I),I=1,6),(W(I),I=1,
+6)
1000 FORMAT(6(I2,2A1,I5,A1,I2),T1,6A12)
DO 50 I=1,6
IF(W(I).NE.BLANK) THEN
IF(SN(I).EQ.SA)LL=1
IF(SN(I).EQ.SM)LL=-1
IF(SX(I).EQ.SA)MM=1
IF(SX(I).EQ.SM)MM=-1
ME=MM*NE(I)
Y=LL*NUM(I)
Z=Y*10.0**ME
IF(R(I).EQ.RCH) THEN
DO 55 M=1,IN(I)
J=J+1
X(J)=Z
55 CONTINUE
ELSE
J=J+1
X(J)=Z
END IF
END IF
50 CONTINUE
GO TO 40
END IF
N1=(NG1-1)*61+1
N2=N1+3
J=0
DO 70 I=1,NG
DO 80 L=N1,N2
J=J+1
XX(K,J)=XX(K,J)+X(L)*DN(NN)
80 CONTINUE
J=J+(NG+3)
N1=N1+61

```

```
      N2=N2+62
70  CONTINUE
      MID(NN)=MID(NN)+1
35  CONTINUE
20  CONTINUE
      DO 100 I=1,4
      L=1
      N=1
130 IF (XX(I,L).NE.0.0) GO TO 160
      NZ=1
140 IF ((L+1).GT.NM) GO TO 150
      IF (XX(I,L+1).NE.0.0) GO TO 150
      NZ=NZ+1
      L=L+1
      GO TO 140
150 IF (NZ.EQ.1) THEN
      XM(M)=ZB
      ELSE
      IF (NZ.GT.9) THEN
      K1=NZ/10
      K2=NZ-K1*10
      XM(M)(1:1)=CN(K1)
      XM(M)(2:2)=CN(K2)
      XM(M)(3:3)=ZC
      XM(M)(4:4)=BLANK
      ELSE
      XM(M)(1:1)=CN(NZ)
      XM(M)(2:2)=ZC
      XM(M)(3:3)=BLANK
      END IF
      END IF
      GO TO 170
160 CONTINUE
      IF (XX(I,L).LT.0.0) THEN
      XM(M)(1:1)=SM
      XX(I,L)=-XX(I,L)
      ELSE
      XM(M)(1:1)=BLANK
      END IF
      Z=ALOG10(XX(I,L))
      N=INT(Z)
      IF (Z.LT.0.0) THEN
      XM(M)(7:7)=SM
      NN=5-N
      ELSE
      NN=4-N
      IF (NN.GT.0) THEN
      XM(M)(7:7)=SM
      ELSE
      XM(M)(7:7)=SP
      END IF
      END IF
      X=INT(XX(I,L)*(10.0**NN))
      K1=K/10000
      K=K-K1*10000
      K2=K/1000
      K=K-K2*1000
      K3=K/100
      K=K-K3*100
      K4=K/10
      K5=K-K4*10
      XM(M)(2:2)=CN(K1)
      XM(M)(3:3)=CN(K2)
      XM(M)(4:4)=CN(K3)
      XM(M)(5:5)=CN(K4)

      XM(M)(6:6)=CN(K5)
      IF (NN.LT.0) THEN
      NN=-NN
      END IF
      IF (NN.GT.9) THEN
      K1=NN/10
      K2=NN-K1*10
      XM(M)(8:8)=CN(K1)
      XM(M)(9:9)=CN(K2)
      ELSE
```

```
        XM(M)(8:8)=CN(NN)
        XM(M)(9:9)=BLANK
      END IF
      XM(M)(10:10)=BLANK
170  L=L+1
      M=M+1
      IF(L.LE.NM) GO TO 130
      JMAX=M-1
      WRITE(4, '(** ',7A10)')(XM(J),J=1,JMAX)
100  CONTINUE
      STOP
      END
```

FINISH

REFERENCES

- 1- L. Spitzer et al.,
"Problems of the Stellarator as a Useful Power Source",
YNO - 6047, U.S. Atomic Energy Commission, (1954).
- 2- R.F. Post,
"Some Aspects of the Economics of Fusion Reactors",
UCRL - 6077, Lawrence Livermore Laboratory, (1960).
- 3- A.J. Impink, Jr.,
"Neutron Economy in Fusion Reactor Blanket Assemblies",
Technical Report No. 434, Massachusetts Institute of Technology,
(1965).
- 4- W.G. Homeyer,
"Thermal and Chemical Aspects of the Thermonuclear Blanket
Problem" Technical Report No. 435, Massachusetts Institute of
Technology, (1965).
- 5- L.N. Lontal,
"Study of a Thermonuclear Reactor Blanket with Fissile Nuclides",
Technical Report No. 436, Massachusetts Institute of Technology,
(1965).
- 6- F.L. Ribe et al.,
"Feasibility Study of a Pulsed Thermonuclear Reactor",
LA - 3294 - MS, Los Alamos Scientific Laboratory, (1965).

- 7- R.G. Mills,
"Some Engineering Problems of Thermonuclear Reactors",
MAIT - 548, Princeton University, (1967).
- 8- R. Carruthers et al.,
"The Economic Generation of Power from Thermonuclear Fusion",
CLM - R85, Culham Laboratory, Abingdon, England, (1967).
- 9- D.J. Rose,
Nucl. Fusion, 9 (1969) 183.
- 10- D. Steiner,
Nucl. Sci. Eng., 58 (1975) 107.
- 11- B.R. Leonard,
"A compendium of 14 MeV Neutron Source Experiments",
Brookhoren National Laboratory, ERDA - 76 - 117 - 1, p. 66,
U.S. Energy Research and Development Administration, (1976).
- 12- H. Bachmann et al,
Nucl. Sci. Eng., 67 (1978) 74.
- 13- R.T. Santoro et al.,
Nucl. Sci. Eng., 70 (1979) 225.
- 14- H. Nakashima et al.,
J. Nucl. Sci. Technol., 18 [1] (1981) 46.
- 15- H. Iida et al.,
J. Nucl. Sci. Technol., 18 [4] (1981) 309.

- 16- K. Sako et al.,
J. Nucl. Sci. Technol., 19 [6] (1982) 491.
- 17- "Plasma Physics and Controlled Nuclear Fusion Research - 1982",
Ninth Conference Proceedings Boltimor, 1 - 8 September 1982 ;
Volumes I, II and III , International Atomic Energy Agency ;
Vienna, (1983).
- 18- F. Ahmed et al.,
Nucl. Sci. Eng., 86 (1984) 219.
- 19- "An Engineering Design Study of a Reference Theta - Pinch Reactor
(RTPR) ", LA - 5336 or ANL - 8019, A Joint Report by Argonne
National Laboratory and Los Alamos Scintific Laboratory, (1974).
- 20- R.W. Boom, et al.,
"pulsed Power Supply for The University of Wisconsin Tokamak
Reactor", FDM89, The University of Wisconsin, (1974)..
- 21- K. Sako et al.,
"Conceptual Design of a Gas Cooled Tokamak Reactor",
JAERI - M 5502, Japan Atomic Energy Research Institute, (1973).
- 22- G.L. Kulcinski and R.W. Conn,
"The Conceptual Design of a Tokamak Fusion Power Reactor, UMWAK-
I", Proc. 1 st. Topl. Mtg. Technology of Controlled Nuclear
Fusion, San Diego, CONF - 740402, Vol. I, p. 38, U.S. Atomic
Energy Commission and the American Nuclear Socitey, (1974).

- 23- R.G. Mills,
"A Fusion Power Plant",
MATT 1050 , Princeton University, (1974).
- 24- R.W. Werner et al.,
"Progress Report No. 2 on the Design Considerations for a Low
Power Experimental Mirror Fusion Reactor", UCRL - 74054 - 2,
Lawrence Livermore Laboratory, (1974).
- 25- R.W. Moir,
"Conceptual Design Considerations for D - T Mirror Reactors with
and without a Fission Blanket", UCRL - 75596, Lawrence Livermore
Laboratory, (1974).
- 26- F.T. Finch et al.,
"Laser Fusion Power Plant Systems Analysis",
CONF - 740402, Vol. I, p. 142, U.S. Atomic Energy Commission and
American Nuclear Society, (1974).
- 27- T. Frank et al.,
"A Laser Fusion Reactor Concept Utilizing Magnetic Fields for
Cavity Wall Protection", CONF - 740402, Vol. I, p. 83, U.S. Atomic
Energy Commission and American Nuclear Society, (1974).
- 28- J. Williams et al.,
"A Conceptual Laser Controlled Thermonuclear Reactor Power Plant",
CONF - 740402, Vol. I, p. 70, U.S. Atomic Energy Commission and
American Nuclear Society, (1974).

- 29- R.F. Post,
"Mirror Systems: Fuel Cycles, Loss Reduction and Energy Recovery
in Nuclear Fusion Reactors", CONF - 690901 - 7, U.S. Atomic Energy
Commission, (1969).
- 30- P.J. Persiani et al.,
"Some Comments on the Power - Balance Parameters Q and ϵ as
Measures of Performance for Fusion Power Reactors",
ANL - 7932, Argonne National Laboratory, (1972).
- 31- M. Nozawa and D. Steiner,
"An Assessment of the Power Balance in Fusion Reactors",
ORNL - TM - 4421, Oak Ridge National Laboratory, (1974).
- 32- D. Steiner,
Nucl. Appl. Technol., 9 (1970) 83.
- 33- W.F. Vogelsang,
Nucl. Technol., 15 (1972) 470.
- 34- R.G. Hichkman,
"Tritium in Fusion Power Reactor Blankets",
UCRL - 74633, Lawrence Livermore Laboratory, (1973).
- 35- M.A. Hoffman and G.A. Carlson,
"Calculation Techniques for Estimating the Pressure Losses
for Conducting Fluid Flows in Magnetic Fields", UCRL - 51010,
Lawrence Livermore Laboratory, (1971).

- 36- R.W. Werner,
"Materials Problems in Steady State Fusion Reactors with Direct Conversion", UCRL - 75336, Lawrence Livermore Laboratory, (1974).
- 37- R.W. Moir and C.E. Taylor,
"Magnets for Open - Ended Fusion Reactors",
UCRL - 74326 Lawrence Livermore Laboratory, (1972).
- 38- M.S. Lubell et al.,
"Engineering Design Studies on the Superconducting Magnet System of a Tokamak Fusion Reactor", LAEA - CN - 28/ k - 10,
International Atomic Energy Agency Mtg. Plasma Physics and Controlled Thermonuclear Research, Madison, Wisconsin, (1971).
- 39- J. File,
"Proposed Superconducting Coils for the Princeton Fusion Reactor",
MATT - 1042, Princeton University, (1974).
- 40- J. File et al.,
"Large Super Conducting magnet Designs for Fusion Reactors",
MATT - 848, Princeton University, (1971).
- 41- D. Duchs et al.,
"Surface Effects in Controlled Fusion",
p. 102, North - Holland Publishing Company, Amsterdam, (1974).
- 42- F.W. Wiffen and E.E. Bloom,
"Effects of High Helium Content on Stainless Steel Swelling",
ORNL - TM - 4541, Oak Ridge National laboratory, (1974).

- 43- S. Cantor and W.R. Grimes,
Nucl. Technol. 22 (1974) 120.
- 44- W.F. Vogelsang et al.,
Trans. Am. Nucl. Soc., 17 (1973) 138.
- 45- M.A. Abdou and C.W. Maynard,
"Neutronics and Photonics Study of Fusion Reactor Blankets",
CONF - 740402, Vol. II, P. 87, U.S. Atomic Energy Commission and
American Nuclear Society, (1974).
- 46- C.R. Hopkins,
"Fusion Reactor Applications of Silicon Carbide and Carbon",
CONF - 740402, Vol. II, P. 437, U.S. Atomic Energy Commission and
American Nuclear Society, (1974).
- 47- W.G. Price, Jr.,
"Blanket Neutronic Studies for a Fusion Power Reactor",
Proc. 5 th. Symp. Engineering Problems of Fusion Research,
Princeton University, (1973).
- 48- G.M. McCracken and S. Blow,
"The Shielding of Superconducting Magnets in a Fusion Reactor",
CLM - R 120, Culham Laboratory, Abingdon, England, (1972).
- 49- T.A. Gabriel et al.,
"Shielding Design Calculations for ORMAK - F/ BX",
ORNL - TM - 4619, Oak Ridge National Laboratory, (1974).

- 50- C.Y. Fu et al.,
"The Status of Neutron - Induced Nuclear Data for Controlled
Thermonuclear Research Applications : Critical Reviews of Current
Evaluations", USNDC - CTR - 1, p. 55, U.S. Nuclear Data Committee,
(1974).
- 51- D. Steiner and M. Tobias,
Nucl. Fusion, 14 (1974) 153 .
- 52- R.G. Alsmiller et al.,
"Comparison of the Cross - Section Sensitivity of the Tritium
Breeding Ratio in Various Fusion - Reactor Blankets",
ORNL - 4696, Oak Ridge National Laboratory, (1975) .
- 53- W.G. Price, Jr.
Trans. Am. Nucl. Soc., 17 (1973) 35 .
- 54- J.R. Powell et al.,
"Studies of Fusion Reactor Blankets with Minimum Radioactive
Inventory and with Tritium Breeding in Solid Lithium Compounds",
BNL - 18236, p. 79, Brookhaven National Laboratory, (1973).
- 55- Z. Al - Rawi,
PhD Thesis, University of Aston in Birmingham, England, (1978).
- 56- L.J. Perkins et al.,
Nucl. Sci. Eng., 78 (1981) 30 .

- 57- F.L. Ribe,
Nucl. Technol., 34 (1977) 179 .
- 58- W.R. Grimes and S. Cantor,
"Molten Solts and Blanket Fluids in Controlled Fusion Reactors",
ORNL - TM - 4047 ., Oak Ridge nathional Laboratory, (1972) .
- 59- L.M. Lidsky,
Nucl. Fusion, 15 (1975) 151.
- 60- D.E. Bartin et al,
Trans. Am. Nucl. Soc., 16 (1973) 8 .
- 61- S. Shani and A. Tsechanski,
Trans. Am. Nucl. Soc., 39 (1981) 791 .
- 62- H. Maekawa etal.,
Nucl. Sci. Eng., 57 (1975) 335.
- 63- W.J. Gray and W.C. Morgan,
"Projection of Graphite Behavior : Comparison of Result on Four
Conceptual Fusion Reactor Designs", Proc. 5 th. Symp. Engineering
Problems of fusion Research, p. 59, Princeton University, (1973) .
- 64- R. Herzing et al.,
Nucl. Sci. Eng., 60 (1976) 189 .
- 65- Y. Seki et al.,
JAERI M - 6220 (NEACRP - L - 136),
Japan Atomic Research Institute, (1975).

- 66- Y. Seki and H. Maekawa,
J. Nucl. Sci. Technol., 14 [3] (1977) 210 .
- 67- Y. Seki et al.,
J. Nucl. Sci Technol., 14 [9] (1977) 680 .
- 68- A.E. Profio et al.,
"Analysis of Fusion Neutron Reactions in Lithium and Graphite",
Final Report, University of California, Santa Barbara, (1979).
- 69- S. Blow,
"The Role of Neutronics Calculations in Fusion Reactor
Technology", Proc. Int. Working Session of Fusion Reactor
Technology, June 28 - July 2, 1971, Oak Ridge, Tennessee, CONF -
710624, p. 43, Oak Ridge National Laboratory, (1971).
- 70- U.P. Jenquin et al.,
Trans. Am. Nucl. Soc., 14 (1971) 447 .
- 71- J.B. Freim and E.L. Draper,
"Calculation of Fusion Spectra in Graphite",
Proc. Int. Symp. Technology of Controlled Thermonuclear Fusion
Experiments and the Engineering Aspects of Fusion Reactors,
Austin, Texas, CONF - 72111, (1972).
- 72- J.B. Freim and E.L. Draper,
Trans. Am. Nucl. Soc., 16 (1973) 9 .
- 73- A. Tsechanski et al.,
Nucl. Sci. Eng., 84 (1983) 226.

- 74- A.P. Fraas,
"Conceptual Design of the Blanket and Shield Region and Related
Systems for a Full Scale Toroidal Fusion Reactor",
ORNL - TM - 3096, Oak Ridge National Laboratory, (1973).
- 75- D. Steiner,
"The Nuclear Performance of Vanadium as a Structural Material in
Fusion Reactor Blankets",
ORNL - TM - 4353, Oak Ridge National Laboratory, (1973).
- 76- J.D. Lee,
"Geometry and Heterogenous Effects on the Neutronics Performance
of a Yin Yang Mirror - Reactor Blanket",
UCRL - 75141, Lawrence Livermore Laboratory, (1973).
- 77- B. Badger et al.,
"UWMAK - I, A Wisconsin Toroidal Fusion Wisconsin, Nuclear
Engineering Department, (1973).
- 78- G. Casini et al.,
12 th Symposium on Fusion Technology, Julich, Germany, Paper
E30673 ORA, Sept. 13 - 17, (1982).
- 79- M.E. Sawan et al.,
Trans. Am. Nucl. Soc., 38 (1981) 575 .
- 80- R.T. Santoro et al.,
Trans. Am. Nucl. Soc., 39 (1981) 798 .

- 81- K. Shin et al.,
J. Nucl. Sci. Technol., 17 [9] (1980) 668 .
- 82- B.K. Malaviya et al.,
Nucl. Sci. Eng., 47 (1972) 329 .
- 83- A. D'Angelo et al.,
Nucl. Sci. Eng., 65 (1978) 477 .
- 84- S. Miyasaka and K. Koyama,
Nucl. Sci. Eng., 73 (1980) 259 .
- 85- L.F. Hansen et al.,
Nucl. Sci. Eng., 60 (1976) 27 .
- 86- R.M. Megahid,
PhD Thesis, University of Aston in Birmingham, England, (1975).
- 87- S.M. Kabir and P.N. Cooper,
J. Nucl. Energy, 26 (1972) 573 .
- 88- Y. Oka et al.,
Nucl. Sci. Eng., 73 (1980) 259 .
- 89- R.B. Leonard,
Nucl. Technol., 20 (1973) 161 .
- 90- L.F. Hansen et al.,
Trans. Am. Nucl. Soc., 32 (1979) 663 .

- 91- S.M. Kabir,
PhD Thesis, University of Aston in Birmingham, England, (1971).
- 92- A.E. Profio et al.,
Nucl, Sci. Eng., 78 (1981) 178 .
- 93- L.Kuijpers et al.,
Nucl. Instr. Meth., 144 (1977) 215 .
- 94- J.V. Sandberg,
Nucl. Instr. Meth., 206 (1983) 227
- 95- A. Tsechanski and G. Shani,
Trans. Am. Nucl. Soc., 45 (1983) 629 .
- 96- W.J. Price,
"Nuclear Radiation Detection",
McGraw-Hill Book Co., Inc., New York, (1958).
- 97- E. Bizard et al.,
"Radiation Handbook, Vol. III, Part B, SHIELDING",
Interscience Publishers, New York, (1962).
- 98- S. Glasstone,
"Principles Of Nuclear Reactor Engineering",
Macmillan & Co. Ltd., London, (1956).
- 99- W.H. Tail,
"Radiation Detection",
Butterworths, London, (1980).

- 100- T.A. Littlefield And N. Thorley,
"Atomic And Nuclear Physics, An Introduction",Third Edition,
Van Nostrand Reinhold Co., New York, (1979).
- 101- J.B. Marion And J.L.Fowler,
"Fast Neutron Physics",Part I,
Interscience Publishers, Inc., New York, (1960).
- 102- H. Etherington,
"Nuclear Engineering Handbook",
McGraw-Hill Book Co., New York, (1958).
- 103- G.F. Knoll,
"Radiation Detection",
John Wiley & Sons, New York, (1979).
- 104- B.E. Eatt,
Physics Rev., 87 (1952) 1037 .
- 105- R.E. Lapp And H.L. Andrews,
"Nuclear Radiation Physics", Fourth Edition,
Prentic - Hall, Inc., (1972).
- 106- M. El - Wakil,
"Nuclear Power Engineering",
McGraw - Hill Book Co., New York, (1962).

- 107- A.R. Foster et al.,
"Basic Nuclear Engineering",
Allyn and Bacon, Inc., Boston, U.S.A, (1973).
- 108- S. Glasstone and A. Sesonske,
"Nuclear Reactor Engineering", Third Edition,
Van Nostrand Reinhold Co., New York, (1981).
- 109- J. Lamarsh,
"Introduction to Nuclear Reactor Theory",
Addison Wesley Publishing Co., (1966).
- 110- R.K. Swank,
Ann. Rev. Nucl. Sci., 4 (1954) 111 .
- 111- C.G. Bell and F.N. Haynes,
"Liquid Scintillation Counting"
Pergamon Press, Oxford, England, U.K., (1957).
- 112- J. Birks,
"The Theory and Practical of Scintillation Counting",
Macmillan, New York, (1964).
- 113- R.B. Owen,
I.R.E. Trans. on Nuclear Science, NS - 5, No. 3 (1958) 198 .
- 114- F.T. Porter et al.,
Nucl. Instr. and Meth., 39 (1966) 35 .

- 115- F.D. Brooks,
Nucl. Instr. and Meth., 4 (1959) 151 .
- 116- T.K. Alexander and F.S. Golding,
Nucl. Instr. and Meth., 13 (1961) 244 .
- 117- W.R. Burrus and V.V. Verbinski,
Nucl. Instr. and Meth., 67 (1969) 181 .
- 118- M. Forte' et al.,
Proc. IAEA Conf., "Nuclear Electronics",
Belgrad, IAEA, Vienna, (1962) .
- 119- V.V. Verbinski et al.,
Nucl. Instr. and Meth., 65 (1968) 8 .
- 120- R.A. Winyard et al.,
Nucl. Instr. and Meth., 95 (1971) 141 .
- 121- R.A. Winyard and G.W. McBeth,
Nucl. Instr. and Meth., 98 (1972) 525 .
- 122- D.M. Glasgow et al.,
Nucl. Instr. and Meth., 114 (1974) 535 .
- 123- P. Kuijper et al.,
Nucl. Instr. and Meth., 42 (1966) 56 .

- 124- B. Sabbah and A. Suhami,
Nucl. Instr. and Meth., 58 (1968) 102.
- 125- D.W. Jones,
IEEE Trans. Nucl. Sci., NS-15, No.3 (1968) 491 .
- 126- M.L. Roush et al.,
Nucl. Instr. and Meth., 31 (1964) 112 .
- 127- C.M. Cialella and J.A. Devanney,
Nucl. Instr. and Meth., 60 (1968) 269 .
- 128- T.G. Miller,
Nucl. Instr. and Meth., 63 (1968) 121 .
- 129- D.A. Gedcke and C.W. Williams,
"High Resolution Time Spectrometry", Ortec, (1968) .
- 130- G.W. McBeth et al.,
"Pulse Shape Discrimination with Organic Scintillators.",
Koch - Light Laboratories Ltd., (1971) .
- 131- C.L. Morris et al.,
Nucl. Instr. and Meth., 137 (1967) 397.
- 132- M. Bertolaccini et al.,
Int. Symp. on Nuclear Electronics, Versailles, (1968) .

- 133- J.M. Adams and G. White,
Nucl. Instr. and Meth., 156 (1978) 459 .
- 134- G. White,
Nucl. Instr. and Meth., 45 (1966) 270 .
- 135- H.W. Broek and C.E. Anderson,
Rev. Sci. Instr., 31 (1960) 1063 .
- 136- H.H. Knox and T.G. Miller,
Nucl. Instr. and Meth., 101 (1972) 519 .
- 137- K. Maier and J. Nitschke,
Nucl. Instr. and Meth., 59 (1968) 227 .
- 138- J. Czirr et al.,
Nucl. Instr. and Meth., 31 (1964) 226 .
- 139- M.M. Wasson,
"The Use of Stilbene, with Decay Time Discrimination, As a Fast
Neutron Spectrometer", AERE Report-4269, (1963) .
- 140- D.L. Garber and R.R. Kinsey,
"Neutron Cross Sections", Volume II ,
BNL 325, New York, (1976) .
- 141- R.J. Schutter,
"Efficiency of Organic Scintillators for Fast Neutrons",
ORNL 3888, (1966).

- 142- M.E. Toms,
IEEE Trans. Nucl. Sci. NS-17, No. 3 (1970) 107 .
- 143- M.E. Toms,
Nucl. Instr. and Meth., 92 (1971) 61 .
- 144- A.E. Lorch,
Int. J. Appl. Rad. Isotopes, 24 (1973) 585.
- 145- L.S. Chuang,
Nucl. Instr. and Meth., 160 (1979) 487 .
- 146- "Technical Bulletin Societe Anonym de Machines Electrostatiques",
Grenoble, France, June (1961) .
- 147- "Catalogue of Radioactive Products",
Amersham International, U.K, (1965) .
- 148- A. Paulsen and H. Liskien,
"An Evaluation for Cross Sections of the Reaction $T(d,n)^4He$ ",
EANDC(E) - 144 "L", Belgium, (1972).
- 149- J. Beneveniste and J. Zenger,
Nucl. Instr. and Meth., 7 (1960) 306 .
- 150- J. Benveniste and J. Zenger,
UCRL - 4266, California, (1954).

- 151- S.J. Bame and J.E. Perry,
Phys. Rev., 107 (1957) 1616 .
- 152- M.D. Coldberg,
"Progress in Fast Neutron Physics",
University of Chicago, (1963).
- 153- E.W. Soker et al.,
S.E.R.L Technical Report No. M - 61 Sept. (1958) .
- 154- T.R. Fewell,
Nucl. Instr. and Meth., 61 (1968) 61 .
- 155- A. Tsechanski and G. Shani.,
Nucl. Sci. Eng. 87(1984) 189 .
- 156- L. Ruby and R.B. Crawford,
Nucl. Instr. and Meth., 24 (1963) 413 .
- 157- E.M. Gunnerson and G. James,
Nucl. Instr. and Meth., 8 (1960) 173 .
- 158- J.L. Fowler et al.,
Nucl. Instr. and Meth., 175 (1980) 449 .
- 159- J.C. Robertson and K.J. Zieba,
Nucl. Instr. and Meth., 45 (1966) 179.

- 160- P. Kuijpep and Spaargaren,
Nucl. Instr. and Meth., 98 (1972) 173 .
- 161- M. Ahmed et al.,
Nucl. Instr. and Meth., 126 (1975) 309.
- 162- J.E. Gaiser et al.,
Nucl. Instr. and Meth., 178 (1980) 249 .
- 163- H.H. Barschall et al.,
Rev. Mod. Phys. 24 (1952) 1 .
- 164- P. Fieldhouse et al.,
Euratom Report EUR 2641 (1966) 179 .
- 165- H. Van Halem et al.,
Nucl. Instr. and Meth. 98 (1972) 175 .
- 166- "Silicon Surface Barrier Radiation Detectors Instruction Manual",
ORTEC Incorporated, U.S.A, (1975) .
- 167- G. Dearnalley and A. Whitehead,
Nucl. Instr. and Meth., 12 (1961) 205.
- 168- F.J. Walter and R.R. Boshart,
Nucl. Instr. and Meth. 42 (1966) 1 .

- 169- R.E. Marshak et al.,
"Introduction to the Theory of Diffusion and Slowing Down of Neutrons", I, II, III and IV, Nucleonics; 4, No. 5 (10 - 22), No. 6 (43 - 49); 5, No. 1 (53 - 60) and no. 2 (59 - 68), (1949).
- 170- H.S. Isbin,
"Introductory Nuclear Reactor Theory",
Reinhold Publishing Corporation, New York, (1963) .
- 171- A.M. Weinberg and L.C. Noderer,
"Theory of Neutron Chain Reactions",
AECD - 3471, (1951) .
- 172- B. Davison,
"Neutron Transport Theory",
Clarendon Press, Oxford, (1957) .
- 173- K.D. Lathrop,
"DTF - IV, A Fortran - IV Programme for Solving the Multigroup Transport Equation With Anisotropic Scattering",
U.S. AEC Report LA-3375, (1965) .
- 174- W.W. Engle,
"User Manual for ANISN A One-Dimensional Discrete Ordinates Transport Code with Anisotropic Scattering",
U.S. AEC Report K - 1693, (1967) .
- 175- W.A. Rhoades and F.R. Mynalt,
"The DOT - III Two - Dimensional Discrete Ordinates Transport Code", U.S. AEC Report ORNL TM.- 4280, (1973) .

- 176- M.B. Emmett,
The MORES Monte Carlo Radiation Transport Code System",
U.S. ARDA Report ORNL - 4972, (1975) .
- 177- B. Carlson,
"Numerical Solution of Transient and Steady State Neutron
Transport Problems", LA - 2260, (1959) .
- 178- G.I. Bell and S. Glasstone,
"Nuclear Reactor Theory"
Van Nostrand Reinhold Co., (1970) .
- 179- J. Spanier and E.M. Gelbard,
"Monte Carlo Principles and Neutron Transport",
Addison - Wesley Publishing Co., (1969).
- 180- B.M. MA,
"Nuclear Reactor Materials and Applications",
Van Nostrand Reinhold Co., (1983).
- 181- A. Takahashi and D. Rusch,
"Fast Rigorous Numerical Method for the Solution of the Anisotropic
Neutron Transport Problem and the NTRAN System for Fusion
Neutronics Application", Part I, KFK - 2832/1, (1979).